REPORT DOCUMENTATION PAGE

AFRL-SR-BL-TR-00-
0671

1. AGENCY USE ONLY *(Leave blank)*

2. REPORT DATE
11/29/00

3. REPORT TYPE AND DATES COVERED
04/01/98 - 09/30/00

4. TITLE AND SUBTITLE
(U) A Numerical Investigation of Sound Generation in Supersonic JET Screech

5. FUNDING NUMBERS
F49620-98-1-0355

6. AUTHOR(S)
Ted A. Manning and Sanjiva K. Lele

7. PERFORMING ORGANIZATION NAME(S) AND ADDRESS(ES)
DEPARTMENT OF AERONAUTICS AND ASTRONAUTICS
Stanford University
Stanford, CA 94305-4035

8. PERFORMING ORGANIZATION REPORT NUMBER
SUDAAR# 727

9. SPONSORING/MONITORING AGENCY NAME(S) AND ADDRESS(ES)
AFOSR
801 N. Randolph St.
Arlington VA 22203-1977

10. SPONSORING/MONITORING AGENCY REPORT NUMBER

11. SUPPLEMENTARY NOTES

20010103 006

12a. DISTRIBUTION AVAILABILITY STATEMENT
Approved for public release; distribution in unlimited.

12b. DISTRIBUTION CODE

13. ABSTRACT *(Maximum 200 words)*

The noise in supersonic jet flows is due in part to the interaction between jet instability waves and the jet shock-cell structure. The emitted shock-cell noise re-excites certain instability wave modes at the nozzle lip and causes resonant feedback to occur. This feedback resonance, known as supersonic jet screech, causes the jet to flap violently at discrete frequencies and generate very strong, narrow-banded tones. Jet screech is a source of acoustic fatigue in the tail and nozzle structures of supersonic aircraft. It is therefore important that methods for predicting the screech amplitude be developed.

In the present research we investigate the screech sound generation process, particularly for high amplitude instability waves. We isolate the interaction of an unsteady shear layer with a single oblique shock. To obtain an overall understanding of the phenomenon with fewest simplifications, we study this problem through the numerical solution of the Navier-Stokes equations. We then consider idealizations to obtain a similar but wider range of results with specially linearbed Euler equations. These results motivate the use of geometric acoustics to describe the screech generation process.

The Navier-Stokes and Euler simulations have revealed important details about the interaction process, how the acoustic field results, and why the screech is so loud.

DTIC QUALITY INSPECTED 4

14. SUBJECT TERMS
Jet screech, shock-associated noise, jet noise, computational aeroacoustics, acoustics

15. NUMBER OF PAGES
202

16. PRICE CODE

17. SECURITY CLASSIFICATION OF REPORT
UNCLASSIFIED

18. SECURITY CLASSIFICATION OF THIS PAGE
UNCLASSIFIED

19. SECURITY CLASSIFICATION OF ABSTRACT
UNCLASSIFIED

20. LIMITATION OF ABSTRACT
UL

A NUMERICAL INVESTIGATION OF SOUND GENERATION IN SUPERSONIC JET SCREECH

A DISSERTATION
SUBMITTED TO THE DEPARTMENT OF AERONAUTICS & ASTRONAUTICS
AND THE COMMITTEE ON GRADUATE STUDIES
OF STANFORD UNIVERSITY
IN PARTIAL FULFILLMENT OF THE REQUIREMENTS
FOR THE DEGREE OF
DOCTOR OF PHILOSOPHY

By
Ted A. Manning
November 1999

I certify that I have read this dissertation and that in my opinion it is fully adequate, in scope and quality, as a dissertation for the degree of Doctor of Philosophy.

Sanjiva K. Lele
(Principal Advisor)

I certify that I have read this dissertation and that in my opinion it is fully adequate, in scope and quality, as a dissertation for the degree of Doctor of Philosophy.

Parviz Moin

I certify that I have read this dissertation and that in my opinion it is fully adequate, in scope and quality, as a dissertation for the degree of Doctor of Philosophy.

M. Godfrey Mungal

Approved for the University Committee on Graduate Studies:

Abstract

The noise of supersonic jet flows is due in part to the interaction between jet instability waves and the jet shock-cell structure. If no counter-measures are taken, the emitted shock-cell noise will re-excite certain instability wave modes at the nozzle lip and cause resonant feedback to occur. This feedback resonance, known as supersonic jet screech, causes the jet to flap violently at discrete frequencies and generate very strong, narrow-banded tones. Jet screech has been shown to be a source of acoustic fatigue in the tail and nozzle structures of supersonic aircraft. It is therefore important that methods for predicting the screech amplitude be developed. While comprehensive screech models will require taking all elements of the feedback loop into consideration, a basic understanding of each element in isolation will also be necessary. Screech sound generation is one such element.

In the present research we investigate the screech sound generation process, particularly for high amplitude instability waves. We isolate the interaction of an unsteady shear layer with a single oblique shock. To obtain an overall understanding of the phenomenon with fewest simplifications, we study this problem through the numerical solution of the Navier-Stokes equations. We then consider idealizations which allow us to obtain a similar but wider range of results with specially linearized Euler equations. The findings of these results motivate the use of geometric acoustics to describe the screech generation process.

The Navier-Stokes and Euler simulations have revealed important details about the interaction process, how the acoustic field results, and why screech is so loud. The mechanism for sound production is found to be fundamentally different and more efficient when the instability waves are the large vortices typical of screech, than when they are small disturbances. At high instability wave amplitude, sound generation process can be regarded as the periodic leakage of the highly perturbed shock through the shear layer as enabled by the passage of the shear layer vortices. The emitted sound levels at one acoustic wavelegth from the apparent source are nearly 10% of the shock strength. As the instability waves are reduced from vortices to small disturbances, the acoustic levels fall exponentially with instability wave amplitude,

and their wave form broadens. Geometrical acoustics can be used to explain the leakage effect at high instability wave amplitude. We conclude that the mechanism for high amplitude screech generation is an unsteady modification to the velocity field by the instability waves that permits the incident shock to refract through the shear layer.

Acknowledgments

Over the course of several years, this research has received funding from a number of sources. Funding was initially provided by the National Science Foundation, with matching funds from the Boeing Commercial Airplane Company, in the form of a Presidential Young Investigator Award, number CTS-9158142, awarded to Professor Sanjiva K. Lele. More recently, funding was provided by the Air Force Office of Scientific Research through the Augmentation Awards for Sciences and Engineering Research Training (AASERT) program under Grants F49620-97-1-0047 and F49620-98-1-0035. Computer time was provided by the Numerical Aerodynamic Simulation Facility (NAS) at the NASA Ames Research Center, by the San Diego Supercomputer Center (SDSC) at the University of California at San Diego, and by the Naval Oceanographic Office (NAVO). Special thanks to program monitor Dr. Stephen Walker of AFOSR.

I would like to thank my advisor, Prof. Sanjiva K. Lele for his guidance over the years. He provided a sense of perspective and inspiration for my work. I would also like to thank the members of my reading committee, Prof. Parviz Moin and Prof. Godfrey Mungal whose advice and guidance proved invaluable. I would also like to acknowledge the time and attention provided by Prof. Daniel Baganoff and Prof. Mark Jacobson for their participation as members of the defense committee.

I would also like to thank Prof. Ganesh Raman, Prof. Christopher K. W. Tam, Dr. Alan Cain, Prof. Michael Howe, Prof. Geoffrey Lilley, Prof. Patrick Huerre, Dr. Karim Shariff, and Prof. Joseph Keller for their technical advice and encouragement.

Of course, there are many other individuals who have devoted time toward my efforts, research and otherwise, whom I must thank... Prof. Edward M. Greitzer and Dr. Choon S. Tan of MIT for encouraging me to pursue my doctorate; Prof. Shojiro Kaji at the University of Tokyo and Dr. Yoshiya Nakamura and others at IHI for enabling me to study jet screech (experimentally) in the first place; and especially members of the Posse, past, present, and honorary, who have helped me enormously through mentorship, code-sharing, and camaraderie: Krishnan Mahesh, Scott Collis, Ganyu Lu, Keith Lucas, Steve Rennich, Sungwon Bae, Steve Timson,

Calvin Lui, Matt McMullen, Takao Suzuki, John Jameson, Matt Barone, Zhongmin "Andy" Xiong, Alexandre Bayen, Dan Bodony, and Karl Dietrich von Ellenrieder.

Finally, I have to thank the members of my family for having infinite patience and maintaining the belief that some day I would stop being a student and get a real job.

Nomenclature

Roman Symbols

A	Amplitude of Stuart mixing layer
a	Streamwise wave number in Stuart mixing layer
a, b, c, d	Coefficient on right hand side of Padé filter
a_1, a_2, a_3	Coefficients in Padé scheme for first derivative
$\tilde{a}_1, \tilde{a}_2, \tilde{a}_3$	Coefficients in Padé scheme for first derivative boundary stencils
$\mathbf{b}$	Wave front phase gradient vector (Ch. 6)
b	Velocity difference coefficient in Stuart mixing layer
b_1, b_2, b_3	Coefficients in Padé scheme for second derivative
C	Stuart vortex coefficient related to A
c	Speed of sound
c_0^*	Reference speed of sound
$c_{ENO}(i, m)$	Coefficient matrix in ENO scheme (§2.2.4)
c_p	Specific heat at constant pressure
c_{ray}	Speed of sound along incident wave-front (Ch. 6)
c_v	Specific heat at constant volume
D_0	Core diameter of free vortex
d_i	Elements of inviscid flux derivative from characteristic analysis ($i = 1, \ldots, 4$)
e	Internal energy per unit mass
E_t	Total energy per unit volume (kinetic and energy)
$\mathbf{F}_1, \mathbf{F}_2$	Inviscid flux vectors in Navier Stokes Equations
f	Forcing and acoustic frequency
f_0	Frequency of most unstable mode
f_i	Solution values at node i, as used in Padé scheme
f_i'	First derivative of solution values at node i, as used in Padé scheme
f_i''	Second derivative of solution values at node i, as used in Padé scheme
$\vec{f}^{+/-}$	Positive/negative split fluxes (§2.2.4)

$\hat{f}^{\pm}_{j+1/2}$	Numerical flux at $j+1/2$ cell face (§2.2.4)
f_r	Buffer zone shape function scaling parameter
$\hat{f}$	Boundary evaluations of Padé filter
h	Enthalpy per unit mass
$h(s)$	Analytic mapping function for stretched mesh
i	index number
k	Thermal conductivity
k	Fourier mode index
$\mathbf{k}$	Acoustic wave number vector (Ch. 6)
K	Instability wave amplitude
k'	Fixed grid wave number $k(\Delta y)_{Ny=291}$ (Appendix B)
k_0	Reference wave number (Ch. 6)
K_u, K_v	Components of instability wave amplitude K
l	Characteristic wave flow length scale (Ch. 6)
L_i	Characteristic variables ($i = 1, \ldots, 4$)
L_0^*	Reference length used to nondimensionalize equations
L_{sponge}	Length of sponge (normal to boundary)
L_y	Height of computational domain
m	index of summation in ENO scheme
$\mathbf{m}$	Velocity-parallel unit vector (Ch. 6)
m_1, m_2, m_3	Grid mapping function slopes
M	High speed stream Mach number
M_0	Reference Mach number
M_c	Instability wave convection Mach number
M_{jet}	Jet Mach number
M_{shock}	Strength of shock measured in terms of normal inflow Mach number
N	Maximum nodal index in grid (Ch. 2)
N	Number of Fourier samples in time
n	Temporal index in Fourier summation

$\mathbf{n}$	Wave-front normal vector
N_{filter}	Time steps between filter applications
Nk	Number of Fourier modes
N_{sponge}	Number of points in a damping sponge (normal to boundary)
Nx, Ny	Number of mesh points in x and y
p	Pressure
p'	Acoustic pressure
p_0^*	Reference pressure
Pr	Prandtl number
r	Distance from apparent source
$\mathbf{R}$	Position vector (Ch. 6)
q	$\partial\Theta/\partial t$ (Ch. 6)
q_i	Heat conduction (Ch. 2)
$\mathbf{Q}$	State variable vector in Navier Stokes equations
$\mathbf{Q}'$	State variable vector in linearized Euler equations
$\mathbf{Q}_{ref}$	Reference solution used in damping sponge
$\mathbf{F}_1$, $\mathbf{F}_2$	Inviscid flux vectors in Navier Stokes Equations
r	Order of ENO scheme (Ch. 2)
r	Distance from acoustic source
r_a, r_b	Grid mapping control points in normalized physical space
$r(s)$	Unscaled grid mapping function
R	Specific gas constant for air
$\mathcal{R}$	Reflection coefficient
Re	Reynolds number based on reference length
$\mathbf{S}$	Viscous terms (generically)
s	Shock cell spacing (Ch. 1)
s	Grid coordinate in computational space (Ch. 2)
s	Coordinate along initial wave-front (Ch. 6)
s_a, s_b	Grid mapping control points in computational space

t	Time
t_n	Time at time-step n
T	Temperature
T	Period of oscillation; $1/f$
T_0^*	Reference temperature
T_∞^*	Inflow farfield temperature
u_0^*	Reference velocity
U	Bufferzone velocity coefficient
U_c	Instability wave convection speed
U_{max}	Maximum value of U, usually at edge of domain
u_i	Velocity component in the i-th direction
$\hat{u}_k$	kth Fourier mode of velocity u
$\mathbf{v}$	Base flow velocity field (Ch. 6)
w	Compression or G-wave width at shear layer
w	Grid wave number $k\Delta x$
w_a, w_b	Grid mapping shape parameters
$\mathbf{x}$	Position vector
x_a, x_b	Boundary zone limits
x_i	Cartesian coordinate in the i-th direction
x_{offset}	Streamwise distance between source and edge of extra sponge
x_{min}, x_{max}	Extent of domain in x-direction
x_{src}, y_{src}	Apparent location sound source
$x_{reflection}$	Streamwise position of shock reflection at shear layer
$\hat{\mathbf{x}}_1$, $\hat{\mathbf{x}}_1$	Component unit normals
y_n	Solution at time-step n in temporal differencing scheme
y_0	y-coordinate of centerline of shear layer
y_{min}, y_{max}	Extent of domain in y-direction

Greek Symbols

α	Coefficient in left hand side of Padé filter

α	Maximum value of $\|u\| + c$ in x-direction (§ 2.2.4)
α_r, α_i	Real and imaginary parts of eigenvalue from stability analysis
α'	$1/\alpha$ (alternate filter coefficient)
α'_x, α'_y	Filter coefficients for each direction
β	Incident shock angle, measured about apparent source
β	$\sqrt{M_1^2 - 1}$ (Appendix A)
γ	Ratio of specific heats
δ	Initial vorticity thickness of shear layer
$\delta(s)$	Streamwise vorticity thickness distribution
δ_{ij}	Kronecker delta tensor
δ_{shock}	Width of shock
δ_{Stuart}	Vorticity thickness of Stuart mixing layer
ΔL	Effective streamwise shift in instability waves forced at different levels
Δp	Compression wave or G-wave amplitude
$\Delta p'$	Mean to peak amplitude of acoustic waveform
$\Delta p_{G-wave}(\xi)$	Pressure distribution of G-wave
Δp_{vortex}	Pressure deficit of free vortex
Δt	Time step
Δx, Δy	Grid node spacings
Δx_{shock}	Streamwise distance over which shock oscillates
Δy_{SL}	Width of grid region devoted to resolving shear layer
$\Delta\omega$	Increment in vorticity contour
ϵ	Small parameter
η	Normalized coordinate in Stuart mixing layer
λ	Acoustic wavelength
λ_i	Instability wavelength
μ	Coefficient of viscosity
${\mu_0}^*$	Reference coefficient of viscosity
$\mu(M)$	Mach angle as function of Mach number

ν	Kinematic viscosity
$\nu(M)$	Prandtl Meyer function
ω	Forcing and acoustic angular frequency
Ω	Characteristic frequency scale of base flow (Ch. 6)
ψ	Bufferzone inner boundary scaling parameter
ρ	Density
ρ_0^*	Reference density
$\sigma(\mathbf{x})$	Damping sponge distribution coefficient
σ_{extra}	Distribution coefficient for "extra" damping sponge
σ_{max}	Maximum value of σ, usually at domain boundary
τ	Characteristic variable (Ch. 6)
τ_{ij}	Viscous stress tensor
θ	Observer angle about acoustic source
θ_{min}	Minimum transmission angle (Ch. 6)
Θ	Phase function of acoustic wave front
θ_{1-2}	Flow turning angle after passing through oblique shock
θ_{2-3}	Flow turning angle after passing through reflected expansion wave
ξ	Normalized coordinate for describing G-wave and extra sponge
ξ	Normalized streamwise coordinate in Stuart mixing layer
ξ_c	Normalized coordinate within compression wave
ξ_e	Normalized coordinate within reflected expansion wave
ζ	Vorticity in Stuart mixing layer
ζ_{peak}	Peak vorticity in Stuart mixing layer

Superscripts and Subscripts

$\hat{(\ )}$	Fourier coefficient
$\vec{(\ )}$	Vector
$\tilde{(\ )}$	Base flow variables (Ch. 4)
$(\ )'$	Fluctuation or perturbation
$(\ )^*$	Dimensional quantity
$(\ )_0$	Reference conditions

$( )_\infty$	Upstream conditions

Abbreviations

CFL	Courant-Friedrichs-Levy number
DNS	Direct Numerical Simulation
ENO	Essentially Non-Oscillatory scheme
RK3	Third Order Runge-Kutta method

Contents

3 Results from Direct Numerical Simulations **56**

4 Linearized Euler Computations: Method **89**

List of Tables

List of Figures

Chapter 1

Introduction

1.1 Motivation and Background

The mechanism by which sound is produced in supersonic jets has been the focus of intense research for several decades. The level of noise generated by supersonic jets far exceeds the levels generated by their subsonic counterparts. The inability to efficiently suppress this noise has been a primary impediment to the development of a modern high speed civil transport. In subsonic jets the mechanism for sound generation is the evolution and decay of turbulent structures; in supersonic jets, there is, besides Mach wave radiation, the additional element of "shock-cell noise", that is, sound generated by the interaction of jet instability waves and the jet's shock-cell structure. The mechanism by which shock-cell noise is produced is not understood in detail. Despite this, accurate predictions of broadband shock-cell noise (*i.e.*, noise arising from the interaction broad-spectrum, turbulent instability waves and the shock-cell structure) have been obtained. Conversely, the acoustic amplitude of a resonant shock-cell noise, supersonic jet screech, has proven difficult to predict.

The resonance in supersonic jet screech arises from a feedback process. Instability waves travel down the jet, imparting motion in the shock-cell structure to produce the shock-cell noise. Part of this sound travels upstream outside the jet and interacts with the thin shear layer at the nozzle lip to excite additional instability waves (see Figure 1.1). The phase relationship necessary for positive reinforcement and feedback

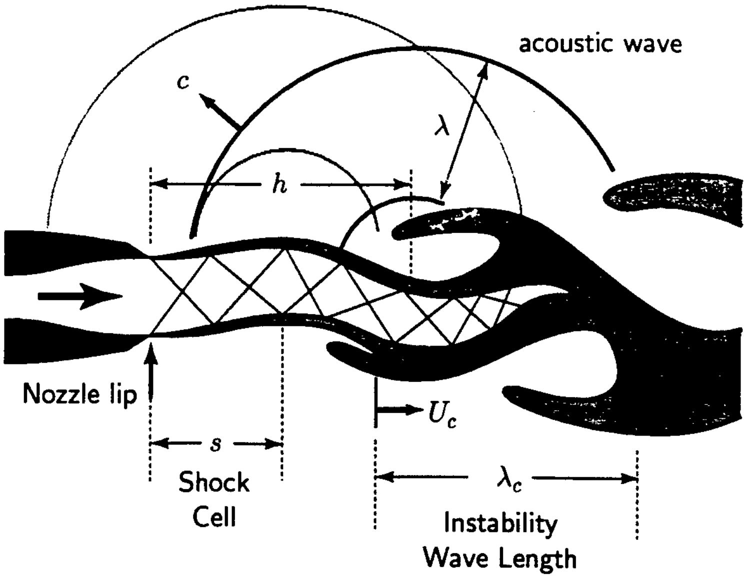

Figure 1.1: Schematic of imperfectly matched jet undergoing supersonic jet screech feedback.

is satisfied only by certain frequencies. As a result, the sound spectrum of a screeching jet is characterized by a discrete tone of an acoustic amplitude which exceeds that of broadband noise (see Figure 1.2). Due to the feedback, it is not uncommon for the instability waves of screeching jets to become very large; such jets exhibit an extreme flapping motion only a few jet diameters downstream of the nozzle.

Although the intensity of screech creates an undesirable noise signature for high speed aircraft, the impact of screech on the aircraft's structural components is the dominant design concern. Screech can cause sonic fatigue in nozzle and tail surfaces when screech frequencies coincide with resonant modes of these structures [10]. Sonic fatigue failures have been observed in aircraft such as the F-15 [54], where cross-coupling of screech in the twin plume jets appear to make the problem even more troublesome. For these reasons the need to understand the mechanisms governing supersonic jet screech is paramount.

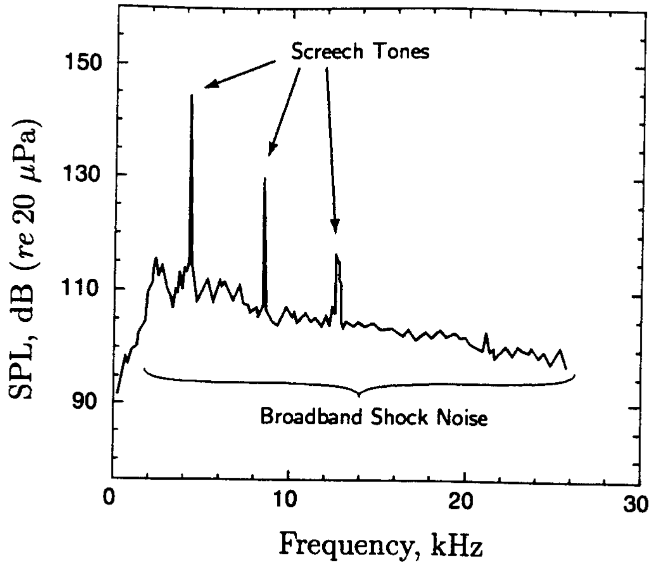

Figure 1.2: Spectrum of noise field from supersonic jet undergoing screech. Jet is rectangular (1.4 x 1.6 cm) with Mach number $M_{jet} = 1.5$. From Raman [44].

The difficulty in predicting screech amplitude stems from the complexity of the feedback dynamics in supersonic jet screech. The components of the feedback loop, namely, instability wave growth, shock-cell noise generation, acoustic propagation, and re-excitation of the instability waves, will affect those dynamics. In the present research, we move away from the overall feedback process and investigate simply the shock-cell noise component, *i.e.*, how the instability-wave shock-cell interaction produces sound. Using a model problem we isolate a portion of the shock-cell structure so as to create a single source. We study the interaction, particularly for the high amplitude instability waves typical of screech, with numerical simulations and simplified analyses. We conclude that the mechanism for sound generation at high instability amplitude is much more efficient than the mechanism at low instability wave amplitude. The jet shear layer is sufficiently distorted by high amplitude instability waves to allow portions of the confined shock waves to escape. We propose that this finding explains in part how screech tone levels can exceed broad-band shock associated noise levels by orders of magnitude.

1.2 Review of Past Work

In this literature review, we survey past work in supersonic jet screech and, more generally, shock-cell noise. While the focus of the work in this thesis does not cover the overall screech process, the issues encountered in jet screech help motivate and guide the present work. We begin with a review of the initial discovery of screech, which we follow with modern interpretations.

1.2.1 Screech: Powell's early work

The discovery and basic description of the screech phenomenon are credited to Powell [40, 39, 41] for his work on rectangular and round choked jets in the 1950s. This discovery also constitutes the discovery of shock-cell noise in general. In these experiments, Powell utilized spark schlieren visualization and basic acoustic sampling techniques to deduce the existence of feedback and describe the directivity of the sound field. It is instructive to review his basic findings as they remain largely valid in our present understanding. In these works, Powell's most important contributions consist of the following findings:

1. The screech frequency is related to the regular shock wave spacing.
2. The sound field is highly directional and can be explained in terms of a phased array of stationary sources.
3. Round jets exhibit a frequency "staging" behavior; *i.e.*, a propensity to occasionally experience large jumps in screech frequencies with a small changes in nozzle pressure ratio.
4. A gain criterion must be satisfied for screech to exist.

Powell reasoned that the narrow frequency band he observed in the acoustic field of supersonic, choked jets requires that there be some mechanism for frequency selection. Having studied the edge-tone phenomenon at length [38], he was aware that acoustic feedback and re-excitation of the instability waves could provide a mechanism for this selection. For feedback to exist, a phase relation about the feedback loop must be preserved over a wide range of operating conditions. The jet shear layer instability wave was identified as the likely mechanism for transporting the disturbance signal downstream. The interaction of these waves with the ends of the shock cells, which were spaced quasiperiodically, was observed to generate the sound. The emitted sound would then transport the signal back upstream, outside the jet, to the nozzle lip, where it would re-excite the instability waves. Powell verified the existence of feedback in supersonic jet screech by showing the following phase condition for screech frequency to be valid:

$$\frac{N+\phi}{f} = \frac{h}{U_c} + \frac{h - l\lambda}{c}^{\dagger} \tag{1.1}$$

Powell also observed in his experiments that the acoustic waves at the fundamental frequency appeared strongest in the upstream direction; at the harmonic frequency he found a strong beaming to the side of the jet. Given the quasiperiodic nature of the shock cell structure, Powell proposed that the acoustic field was made up of a series of monopole sources, emitting sound in phase delayed fashion such that sound emitted at the fundamental frequency interferes constructively in the upstream direction. The directivity pattern which results from this analysis for three equally spaced, equal strength sources is given for the fundamental mode by

$$D_f = \frac{1}{3} + \frac{2}{3}\cos\left[\frac{2\pi s}{\lambda_c}(1 - M_c\cos\theta)\right] \tag{1.2}$$

and for the harmonic by

$$D_h = \frac{1}{3} + \frac{2}{3}\cos\left[\frac{4\pi s}{\lambda_c}(1 - M_c\cos\theta)\right] \tag{1.3}$$

[†] The left hand side represents some multiple of the acoustic period $1/f$; N is a positive integer and $0 \leq \phi < 1$ represents phase lags which may occur at the source site or the nozzle lip during re-excitation. The first term on the right hand side represents the instability wave travel time from nozzle lip to the source site (traveling distance h at speed U_c), while the second term represents the minimum time between the time of production of a given phase of an acoustic wave and the time an acoustic wave of the same phase reaches the nozzle lip. l is the integer number of acoustic wavelengths λ spanning the distance h. h itself is approximately an integer multiple of the shock cell length s for overexpanded jets, as one would obtain for a choked nozzle.

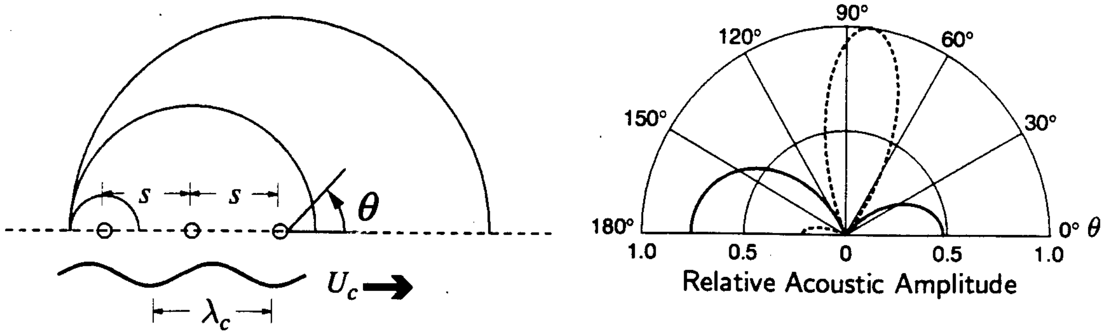

Figure 1.3: *Left*: Schematic of phased array of monopole sources, spaced at shock cell interval s. Source phase is triggered by passage of instability waves of wavelength λ_c and phase speed U_c. *Right*: farfield relative directivity given by fundamental frequency (——, Equation 1.2) and harmonic (– – –, Equation 1.3) for $s/\lambda_c = 0.538$, $M_c = 0.6$ (see [40]).

λ_c is the wavelength and M_c is the Mach number of the jet disturbances; s is the shock cell length; and θ is the observer angle measured from the downstream direction. The phased array of sources and the resultant directivity are depicted in Figure 1.3.

The phased array source model also yields a prediction for the screech frequency. If one requires maximum constructive interference in the upstream direction, then one can obtain the amplitude condition for screech frequency:

$$f = \frac{U_c}{s(1+M_c)} \tag{1.4}$$

where M_c is U_c/c. Equation 1.4 is a more restrictive version of Equation 1.1.

The basic screech findings were found to apply to both rectangular and round jets. In addition to flapping modes, however, Powell [38] also observed axisymmetric and helical modes in round jets. Further, the transitions among these modes, as nozzle pressure is raised, were found to occur abruptly and exhibit hysteresis (see Figure 1.4) or to be indeterminate. Powell referred to this mode switching phenomenon as "staging". He suggested that the mode switching occurred to favor oscillation modes which satisfy both feedback phase (Equation 1.4) and gain criteria (described below).

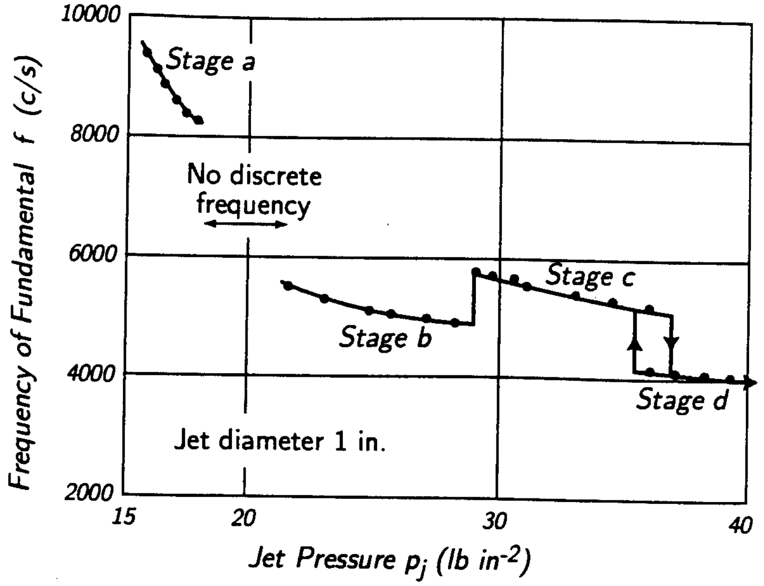

Figure 1.4: Dominant screech frequency as function of nozzle pressure in round jet, from Powell [39].

Powell identified the components that make up the feedback loop, and formulated a feedback gain criterion. The condition for screech to be self-sustained is

$$q\eta_s\eta_t\eta_d \geq 1. \tag{1.5}$$

Here, q is the gain associated with the propagation of eddies in the jet, η_s is efficiency of the interaction of these eddies with the shock cell structure in producing sound, η_t is efficiency associated with the propagation of the sound upstream, and η_d is the efficiency by which the sound waves excite additional eddies at the nozzle lip. In modern terminology, we refer to the last process as acoustic receptivity. These concepts are particularly important because they lay the foundation for formulating a prediction of screech amplitude. With regard to the objectives in the present work, we are interested most in understanding the mechanisms that influence η_s.

1.2.2 Screech: Modern interpretation of Powell's early work

The body of research devoted to understanding screech is large. After Powell, the focus of the much of the early experimental work [4, 5, 7, 37, 77] has been based on visualizing the jet and the acoustic field. Seiner and others conducted numerous experiments in supersonic jets [30, 56, 80] to accurately characterize the shock-cell structure and acoustic field. Others have investigated screech under conditions which may more closely approximate realistic flight configurations. These include the effects of forward flight [10], hot jet cores [17], and coaxial jets [3]. The twin jet configuration has been studied [49, 50, 55] and has been shown to result in screech of increased intensity. The effects of unusual nozzle geometry on screech have been studied by several [29, 34, 45, 72, 75], including beveled, elliptical, and triangular nozzle geometries.

Much progress has been made in the understanding of jet screech, particularly in the prediction of the screech frequency over a wide range of operating conditions. The prediction of screech amplitude has been elusive. The eventual saturation of the feedback mechanism involves many processes throughout the feedback loop, and most of these processes and their dependence on each other are still poorly understood. Raman [46, 47] gives a comprehensive overview research in jet screech and the state of our current understanding, and provides an assessment of the direction the research needed to make screech amplitude prediction a reality. Tam [65, 64] gives broader reviews of supersonic noise, including screech and broadband shock-cell noise.

The factors affecting the screech frequency of round and rectangular jets under a variety of operating conditions are now well understood within a single oscillation mode type. Tam *et al.* [71] have developed a reliable prediction of screech frequency f_s based on amplitude condition (Equation 1.4). They refine estimates of shock cell length, incorporate empirical factors, and accommodate "hot core" jets. The screech frequency for a round jet operating in the helical oscillation mode is given by:

$$\frac{f_s D_j}{u_j} \approx \frac{0.67}{\left(M_j^2 - 1\right)^{1/2}} \left[1 + \frac{0.7 M_j}{\left[1 + (\gamma - 1) M_j^2/2\right]^{1/2}} \left(\frac{T_r}{T_\infty}\right)^{1/2} \right]^{-1} \tag{1.6}$$

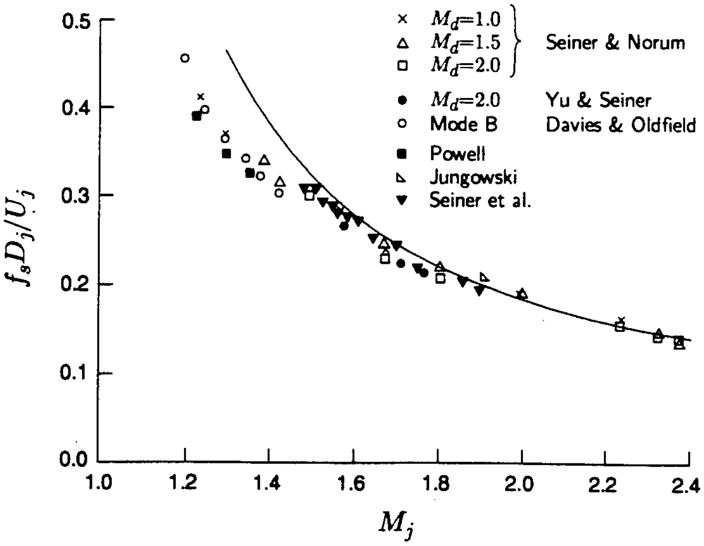

Figure 1.5: —— Prediction of screech frequency due to Tam *et al.* [71] (Equation 1.6) compared to experimental results of of Seiner and Norum [56], Yu and Seiner [80], Davies and Oldfield [4, 5], Powell [39], Jungowski [15], and Seiner *et al.* [55]. (Originally compiled by Tam [65].)

D_j is the fully expanded jet diameter, obtained by conserving mass flux in the off-design condition [73], and is related to the shock cell length through fully expanded jet Mach number M_j. Tam *et al.* use the approximation $U_c = 0.7u_j$ (jet velocity) based on experiment. T_r/T_∞, the ratio of the reservoir temperature to the ambient temperature, compensates for the modification to the jet velocity at higher jet temperatures for given Mach number. In Figure 1.5 we reproduce from Tam *et al.* [71] the comparison of Equation 1.6 to experimental results.

The superposition of a phased array of sources appears to offer the best explanation for screech directivity in round jets. Norum [29] verified the directivity result of Powell's simple source model using parameters obtained from round jet experiments. His directivity measurements (fundamental and harmonic modes) agreed well with a Powell-type source model made up of nine sources following a parabolic amplitude distribution. However, he also found the distribution to be largely insensitive to the distribution; further, three sources were sufficient to capture the dominant features.

In rectangular jets of high aspect ratio, the superposition of sources may be unimportant. Raman [46] notes that in such jets, the screech field often consists of a "feedback shock", or sound waves with a compact wave forms, which appear to originate from a single source. They are visible in photographs appearing in Raman [44, 46], Poldervaart *et al.* [37], Hammitt [7], and Krothapalli *et al.* [18], all of which were based on high aspect ratio supersonic jet flows. The dominance of a feedback shock is also clear in the acoustic measurements of Krothapalli *et al.* [18]; the fundamental frequency is dominant in all directions, suggesting the absence of multiple sources. The dominance of a single source is attributed to the rapid growth of instability waves in these jets. Only at a certain streamwise location would conditions be optimal for sound generation. Upstream of this point the instability waves are much weaker; downstream, the shock cell structure is mixed out.

The basic mechanisms underlying the staging phenomenon are better understood. Tam *et al.* [66] show compelling evidence that the frequency jump in staging can be attributed to changes in jet instability as operating conditions change. They examined the inviscid linear stability characteristics of the axisymmetric and helical jet oscillation modes (based on the stability analyses presented in Tam and Burton [67] and Tam and Hu [69]) and found that for low jet Mach number the peak growth rate of the axisymmetric mode is larger than any helical mode. Conversely, the peak growth rate of the first helical mode is dominant at higher jet Mach number ($M_j > 1.3$). This is consistent with the observed mode switch.

It is clear, however, that a frequency prediction of screech which includes staging may not be easily realized. Staging has been observed over a broad range of operating conditions, including in rectangular jets [61], and the dominant modes have been classified [29]. But staging has been shown to exhibit a great sensitivity to facility design, such as the size and placement of surfaces at the nozzle exit [29]. Under certain conditions the screech frequency is unstable; under others, frequency hysteresis has been observed. These are manifestations of the complexity introduced by the nonlinearity of the feedback process.

Although Powell's gain criterion (Equation 1.5) has yet to form the basis of much work in jet screech, the work of Cain *et al.* [1, 2, 16] represents one exception. Cain *et al.* formulated a component-based model to predict the amplitude of screech by forming simplified models of the four elements comprising the screech feedback loop. These therefore included separate models for instability wave growth in jets, shock instability wave interaction to generate sound, acoustic wave propagation, and shear layer receptivity to sound at the nozzle trailing edge. The basis of these models are a mixture of theoretical analyses and empirical data. The combined models are implemented via a neural-net algorithm. Although their preliminary results were encouraging, wherein they obtained the correct screech frequency and and amplitude of the fundamental mode, the general applicability of these results was unclear.

Much of the analysis of screech to date has been based on linear and only weakly nonlinear concepts. The feedback process and the high jet oscillation amplitudes indicate that the process is strongly nonlinear. One assumption implicit in the screech gain analysis is that an oscillation mode will occur in isolation. There is ample evidence instead that multiple simultaneous screech modes are possible [4, 5, 39]. Walker *et al.* [76] make use of nonlinear spectral analysis to show the presence of nonlinear phase locking between modes in a two-dimensional, screeching jet. Another example of nonlinear phenomena occurring in screech includes the modulation of the instability waves by the shock cell structure [48], both in terms of fluctuation amplitude and propagation speed. It is clear that more work characterizing the nonlinear aspects of the screech process needs to be carried out before a reliable screech model is obtained.

1.2.3 The role of fine scale turbulence in screech

The screech mechanism has been linked to the formation and growth of large scale disturbances in the jet shear layer which interact with the shock cell structure to produce sound. However, in most experiments, where the jet Reynolds numbers based on jet width are of the order of 10^6, fine scale turbulence will be present. Indeed, most of these experimental results exhibit the broad-band shock noise, which arises from the interaction of fine scale, comparatively random turbulence and the shock cell structure. Hu and McLaughlin [13] show definitively that the fine scale turbulence is extraneous to the basic screech phenomenon. They studied low Reynolds number (Re = 8000), underexpanded, supersonic jets issuing from round nozzles. Their jets are shown to contain shock cell structures typical of high Reynolds number jets, with only a small deviation in shock cell spacing. Their acoustic spectra are dominated by the screech tone but do not contain broad-band shock noise. The screech frequencies agree well with their high Reynolds number counterparts.

Although secondary, the presence of fine scale turbulence should subtly influence screech behavior. First, turbulence will modify the mean jet profile and thereby alter its stability characteristics; the growth rate of instability waves influence the feedback criterion for screech (Equation 1.5). Secondly, the modification in growth rate will modify the shock cell spacing and core length. Screech frequency depends on shock-cell spacing (Equation 1.4). Finally, the presence of turbulence will tend to diffuse the shock strength with each successive reflection down the jet; this will modify the sound generated.

1.2.4 Numerical Simulations

The direct simulation of screech is a formidable challenge. The problem is characterized by disparate length scales and disturbance amplitudes. The acoustic wavelength is typically over 20 times larger than the initial thickness of the jet mixing layer [63]. The sound pressure levels can be five or six orders of magnitude below the hydrodynamic fluctuations associated with the instability waves. Furthermore, the computational demands of shock capturing and boundary conditions add to the cost of carrying out such a simulation. With the dramatic rise in computational power of computers recently, complex simulations of screech have become increasingly a practical reality.

Shen and Tam [57] have conducted simulations of an axisymmetric jet undergoing screech and report good agreement with experiments. They solve the compressible Navier-Stokes equations using the dispersion-relation preserving (DRP) scheme on a multi-block domain of discontinuous grid density. An artificial damping scheme is required to suppress numerical instabilities which arise at the sub-block boundaries.

The k-ϵ turbulence model is added to obtain Reynolds numbers comparable to those in experiments. The time averaged results for velocity profiles and the shock cell spacing agree very well with experiments. The acoustic field is found to compare favorable in terms of directivity and intensity. In particular, the strong upstream directivity of the screech tone is predicted.

Rona and Zhang [52] adopt a hybrid computational approach to obtain far-field estimates of the radiated screech field. The advantage of this approach is that the region over which time-accurate viscous computations must be carried out is limited to the aerodynamic region immediately around the jet. Using the k-ω turbulence model, Rona and Zhang solve the short-time Reynolds averaged Navier-Stokes (RANS) equations to compute the source terms in Lighthill's acoustic analogy [21]. They then integrate these source terms to solve a short-time averaged version of Lighthill's equation. The RANS equations are solved using a second order finite volume spatial discretization and the four-step Runge-Kutta time advancement scheme, whereas the Lighthill equation source volume is integrated with a second-order central difference method. An axisymmetric, over-expanded, Mach 2 jet is found to experience screech feedback with some frequency jitter, possibly due to the dynamic modulation of instability waves by the shocks. The shock motion is observed to radiate sound as the shocks jump upstream from one instability wave vortex to the next. This is in agreement with the findings of Manning and Lele [26, 27], which we report in detail in Chapter 3. Finally, the overall sound pressure level in the forward arc of the far field is found to agree well with the measurements of Norum and Seiner [30], although the screech frequency is underpredicted.

1.2.5 Shock Instability-wave Interaction as a Source of Sound

Powell and others offer sufficient evidence to conclude that the interaction of disturbances in the imperfectly expanded supersonic jet and its enclosed shock cell structure give rise to stationary sources of sound. Shock-cell noise may be made up of a wide band of frequencies, as in broadband shock noise, or a narrow band, as in screech, and the two forms usually co-exist (see, *e.g.*, Figure 1.2). An understanding of the shock noise generation process requires one to understand the nature of the jet disturbances, the shock cell structure, and how they interact to produce sound. In this section we recount past observations of shock motion associated with supersonic jet screech. We then survey the evolution of shock instability wave interaction models for both broadband shock-cell noise and screech. We note that in screech, shock motion is generally observed to be large, whereas in shock-cell noise modeling, the jet instability waves have been assumed to be small.

Shock-cell structure and motion

The shock cell structure in a supersonic jet arises from the pressure mismatch that occurs at the nozzle exit when the jet is not fully expanded. For weak under- or over-expansion, a simple shock cell system develops whereby oblique shocks or expansions emanate from the nozzle lip, cross the jet centerline and impinge on the jet shear layer opposite the original nozzle lip. The waves then reflect as the waves of the opposite type (*i.e.*, compression waves reflect as expansion waves and vice versa) to maintain pressure continuity at the jet boundary. The process then repeats itself in a periodic manner down the jet to produce the familiar shock-cell, or shock-diamond, pattern until turbulent mixing destroys the supersonic jet core. The jet flow behaves as a waveguide for the disturbances that form the shock cells [65]. For stronger under- or over-expansion, the expansion waves spread in a Prandtl-Meyer fan. Their reflection from the sonic boundary is distributed and results in a curved shear layer. The reflected compression waves coalesce to form oblique shocks at the ends of the shock cells. At even stronger over- or under-expansion, local features such as Mach disks will form between the shock cells, but the pattern remains essentially periodic.

For unsteady jets such as those oscillating in supersonic jet screech, the shock-cell structure is vigorously disturbed. The mechanism by which the motion of the shocks produce sound is not known in detail. However, the shock motions in screech themselves have been documented.

Based on extensive stroboscopic spark schlieren and shadowgraph visualization, Westley and Woolley [77] have observed significant shock motion within a round choked jet. In Figure 1.6 we reproduce their depiction of downstream shock propaga-

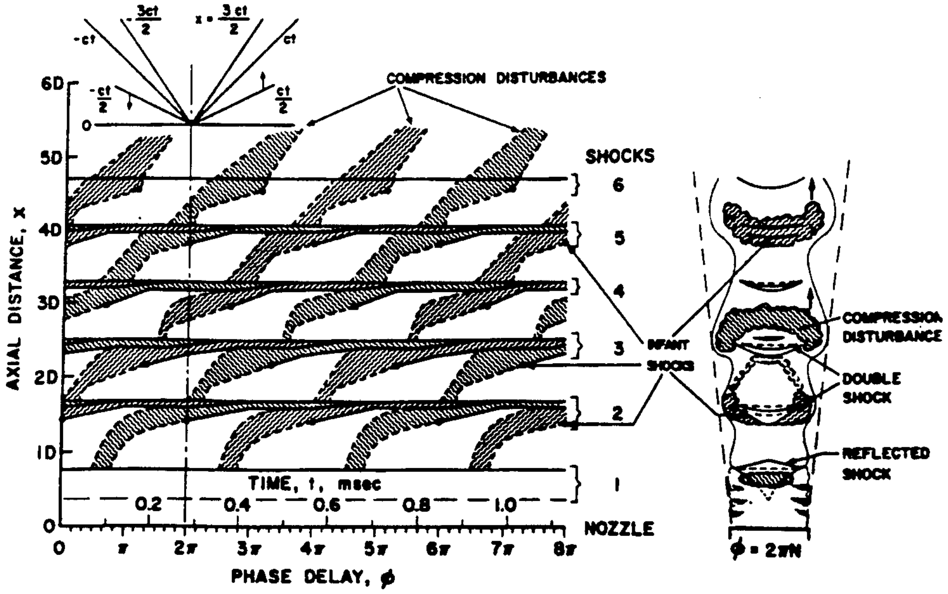

Figure 1.6: Disturbance and shock motions during oscillation cycle, Mode B_1 (axisymmetric mode), from Westley and Woolley [77].

tion in a jet screeching in the axisymmetric mode, wherein the instability waves are toroidal. With the passage of the toroidal disturbances they observe the formation of shocks, which travel the length of shock cell but disappear as they approach the end of the shock cell; at times double shocks exist. This "staircase" shock motion was also observed by Panda [33]. Westley and Woolley also studied the shock oscillations in a screeching jet experiencing the helical oscillations. As the jet disturbances are no longer axisymmetric, the shocks undergo changes in orientation, as graphed in 1.7. The magnitude of these changes increase with downstream distance; this is consistent with the growth of jet instability waves in this direction. They also note in that the oblique shocks appear to strengthen just as the disturbances pass, and weaken at other times.

Suda *et al.* [61] report visualizations from a rectangular jet which is undergoing anti-symmetric flapping oscillations about the long cross-sectional axis. The jet contains a single dominant screech source centered about the third shock cell, as is typical of rectangular jets of high aspect ratio. As shown Figure 1.8, the oblique shocks in

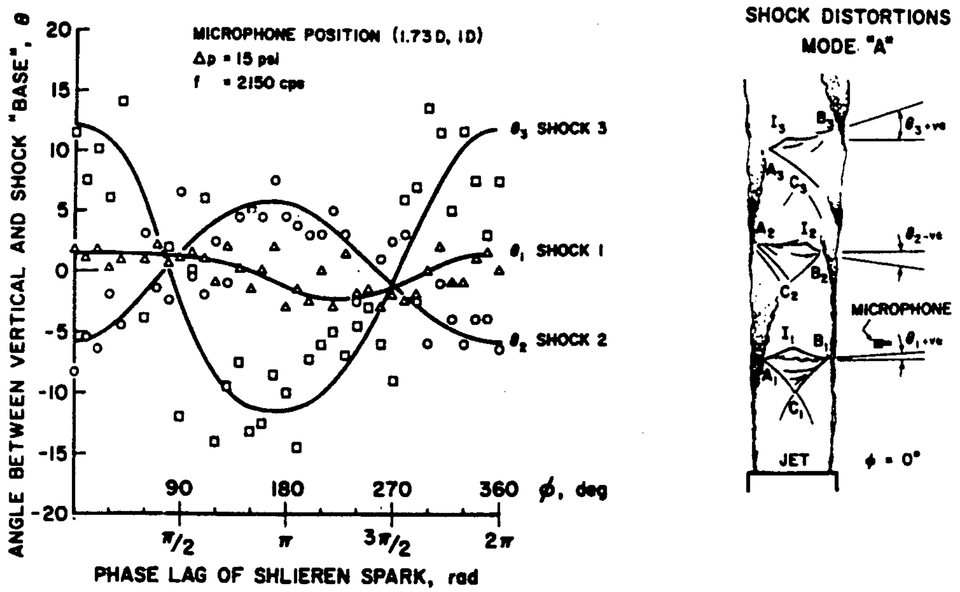

Figure 1.7: Tilt angle of shock bases during screech cycle Mode A (helical mode), from Westley and Woolley [77].

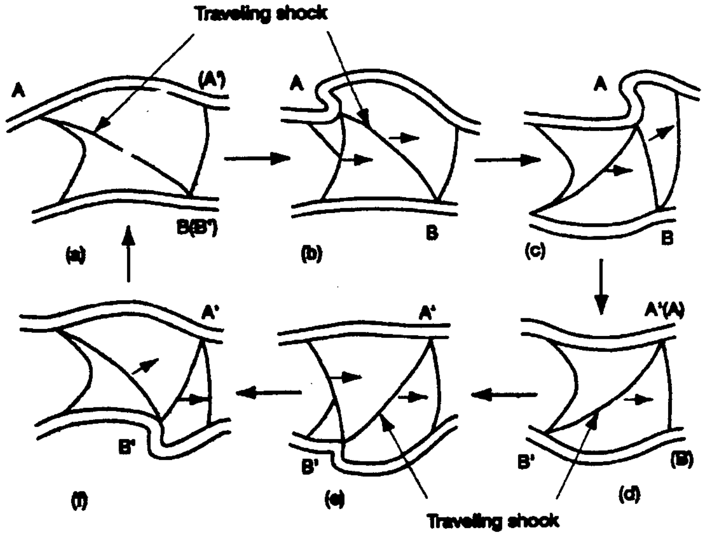

Figure 1.8: Motion of traveling shock in third shock cell of rectangular jet (from Suda *et al.* [61]).

the third shock cell appear to travel downstream with the shear layer vortex and coalesce into shocks at the end of the cell, during which the shock experiences significant changes in orientation. They propose that this motion results in the screech sound, but offer no direct evidence.

Shock noise modeling

Powell, having discovered screech and therefore shock-cell noise, also devised the first shock-cell noise model with his phased array of monopole sources [40]. However, this model offered no basis for predicting screech amplitude, beyond its relative directivity. Lighthill [22] set out to understand the shock-cell noise phenomenon from first principles by considering the shock-turbulence interaction as a model problem, wherein a linear analysis yields the acoustic field scattered from vorticity waves convecting through a normal shock. Others [28, 51] have generalized the vorticity waves to free vortices to approximate large amplitude instability waves. This unbounded shock model has yet to offer practical results for shock-cell noise; the jet shear layer and the bounded shock-cells, which this approach ignores, may be critical to a successful model.

Harper-Bourne and Fisher [8] were the first to establish that broadband shock-cell noise arises from the interaction between the random, fine scale turbulence in jet shear layers and the shock cell structure. They further showed that the overall intensity is of this sound is independent of observer angle and is a function only of the shock cell strength. They developed a model for the peak frequency of this noise based on a phased array of equally spaced sources (based on that of Powell's), whereby peak frequency f_p depends on observer angle θ according to the following:

$$f_p = \frac{U_c}{s(1 - M_c \cos\theta)} \tag{1.7}$$

As Tam *et al.* [71] observe, setting $\theta = 180°$ recovers Equation 1.4. They show that screech frequency is in fact the limiting case of broad band shock noise in the upstream direction. Like Powell's source model, Harper-Bourne and Fisher's [8] source model does not consider the mechanism by which shock-cell noise is produced but instead only the sound field that results from a phased array of such sources.

Howe and Ffowcs Williams [12] devised simple model for the imperfectly expanded, supersonic jet to obtain some basic insight into acoustic energy flux in the production of the shock-cell noise. The model utilizes the streamwise-invariant, vortex sheet approximation to the round jet and the streamwise-periodic shock cell structure based on the linear description first developed by Prandtl [42] and later refined by Pack [32]. In their model, they construct acoustic source terms in the spirit of Lighthill's [21] acoustic analogy by considering the weak interactions between random, axisymmetric disturbances in the vortex sheet and the shock cell structure. They find that the dominant convection velocity of the large-scale eddies is "a principal factor determining the total radiated sound power, essentially independently of the details of the interaction mechanism." Hence, within the regime of this model (small fluctuations) details of the shock-cell noise generation mechanism may not be important.

Tam [62] builds upon Howe and Ffowcs Williams' model by refining the description of the shock cell structure and jet disturbances. He devises a shock cell model composed of time-independent waveguide modes of the jet flow using the multiple scales expansion of Tam *et al.* [70]. The turbulence structures are modeled by superimposing jet instability wave modes, which are initiated by random white noise excitations based on the similarity arguments (see Tam and Chen [68]). The weak interaction of these two components then give rise to the broadband sound field. Tam's near- and far-field contour and directivity maps agree well with the experimental measurements of Norum and Seiner [30], predicting both the shift in peak frequency and the narrowing of the peak's spectral width as observer angle moves from downstream to upstream.

Motivated by the supersonic jet screech problem, Kerschen and Cain [16] developed a shock instability-wave interaction model for a single source. Their consideration of a single source arises from the observation that in jet screech, the shock-cell structure is short due to rapid mixing and therefore contains only a few dominant sources, which furthermore vary significantly in amplitude. Understanding the properties of a single source, such as directivity, therefore becomes important. Their

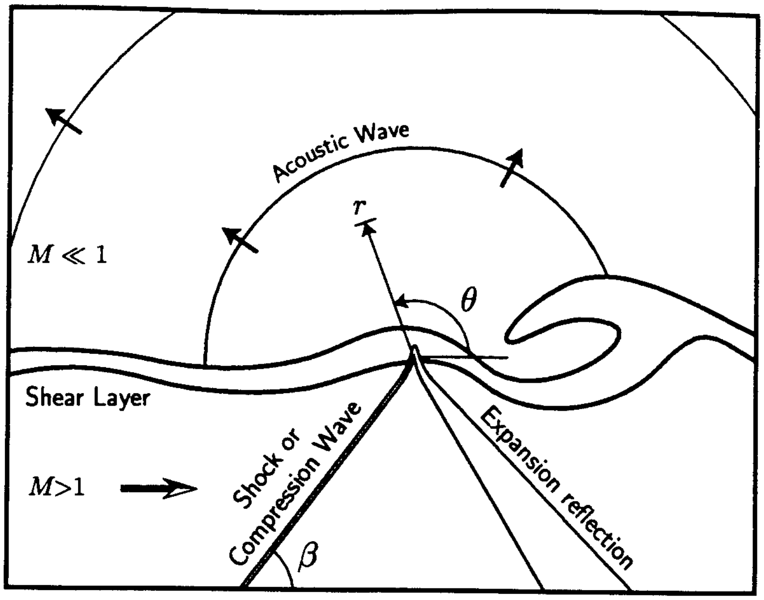

Figure 1.9: Schematic of the model problem. (r, θ) coordinate system defines acoustic field observer coordinates relative to approximate location of acoustic source.

idealized flow consists of a vortex sheet, on which small disturbances are propagated, and an stationary, oblique Mach wave (and its reflection from the vortex sheet). As with the broadband shock-cell noise models above, the sound field resulting from the weak interaction of the vortex sheet disturbances and the Mach wave system is considered. The Wiener-Hopf technique is used to accommodate the singularity at the interaction site. Kerschen and Cain predict that the radiation field of a single source peaks at 48° from the downstream direction, and decays rapidly in the upstream direction. They suggest that the apparent contradiction with the directivity typically observed in screech is corrected when multiple sources are superimposed in a phased array.

1.3 Model Problem

To study the mechanism by which screech is generated, we have devised a model problem that consists of an isolated shock reflection and a single shear layer (Figure 1.9). We have reduced the shock-cell noise (and therefore, screech) source to its fundamental elements. Its physical scope is similar to that considered in Kerschen and Cain [16]. However, within the context of this model, we admit shear layers of finite thickness and instability waves and shocks whose amplitude may be large. We have therefore retained sufficient generality to allow us to explore fully nonlinear interactions.

In studying the screech source at this level we are omitting a number of phenomena which readily occur in screech. These are:

1. *Feedback*—we wish to explore the relationship between instability amplitude and acoustic amplitude; feedback is eliminated to give us direct control over instability wave amplitude.
2. *Three-dimensional effects*—the occurrence of screech in high aspect ratio jets demonstrates that the overall screech phenomenon, and therefore the screech generation mechanism, can be encapsulated in two dimensions; furthermore, the role of turbulence in screech is minor [13].
3. *Full jet effects*—these include cross-jet interactions such as antisymmetric oscillation modes, disturbance propagation down the shock cell structure, and interference effects among multiple sources; these are extraneous to the basic screech generation mechanism.

1.4 Overview of Thesis

The overall objective of this study is to improve our understanding of the shock-cell noise generation mechanism, particularly at the high instability wave amplitudes typical of screech. We carry out direct numerical simulations to establish the noise generation behavior. We employ linearized Euler simulations to explore the dependence of the acoustic field on instability wave amplitude. Finally, we make use of geometric acoustics to verify the appropriate framework for understanding the sound generation process.

The principal accomplishments and findings of this work are listed as follows:

- The passage of instability wave vortices across an incident shock result in large fluctuations in the position and orientation of the shock. Coupled with these fluctuations is the generation of the sharp compression front of the acoustic wave, which occurs precisely as the shock travels upstream between the vortices in its oscillation cycle. The shock itself "leaks" through the shear layer at this point to become the sound wave.
- The sound generated by the interaction exhibits significant upstream directivity, to the extent that the upstream traveling sound wave creates an oblique Mach wave in the supersonic stream.
- The instability-wave shock interaction and sound emission behavior is essentially reproduced for weak compression waves, indicating that the nonlinearity of the shock is not required for the process to occur. The amplitude of the acoustic field is found to scale with the compression wave amplitude.
- Slow, downstream-traveling waves are found to appear and persist in the supersonic stream and serve as secondary sources of sound via essentially the same interaction mechanism.
- Numerical solutions of the Euler equations, linearized about an unsteady base flow obtained from DNS, are used to show that the sound generation process can be regarded as the scattering of incident standing wave into propagating waves by shear layer disturbances. This may represent the first instance in which an unsteady base flow is used with the linearized Euler equations to study supersonic jet noise.
- The linearized Euler simulations are used to show that the sound generation process is governed by a thresholding phenomenon, whereby the acoustic amplitude rises exponentially with instability wave amplitude until a saturation state is reached. There is also evidence of a third regime of dependence at low instability wave amplitude.

- The velocity field is shown to be the critical feature of instability waves which result in the sound generation. Replacing the the DNS base flow with an incompressible vortex mixing layer solution with thermodynamic variations omitted is shown to reproduce much of the sound generation behavior, including the thresholding phenomenon.
- The sound generation process is reproduced with geometric acoustics by integrating ray paths through a vortex laden shear flow. This result shows that the high amplitude screech generation process is fundamentally driven by the unsteady refraction of the incident shock and that "leakage" is an appropriate characterization.

This thesis is organized as follows. Chapters 2 and 3 cover the numerical simulations. In Chapter 2 we focus on the details of the numerical methods, from the basic scheme, boundary conditions, to special considerations (shock capturing and filtering) and postprocessing. In Chapter 3, we outline the details of the actual implementation of the simulations and present the results of the simulations. In Chapters 4 and 5, we show that the basic results found in the Navier-Stokes simulations can be reproduced and expanded upon using specially linearized Euler equations. In Chapter 6 we consider the efficacy of a model based on geometric acoustics. Chapter 7 consists of conclusions and recommendations for future work.

Chapter 2

Numerical Simulations: Method

2.1 Introduction

In this chapter we discuss the numerical methods used to solve the Navier-Stokes equations when applied to the model problem for a screech-type source. Studying the model problem with solutions to the Navier-Stokes equations permits us to investigate the screech generation phenomenon with fewest *a priori* assumptions about the nature of the sound source. We refer these computations as "direct numerical simulations", or DNS, to indicate that on the interior of the solution domain, the Navier-Stokes equations are solved without modeling any of its terms. Because the screech phenomenon is not inherently linked to turbulence but instead to the large scale instability waves of the shear layer, it is acceptable to carry out these simulations at Reynolds numbers substantially below those of experiments and actual jet engine exhaust flows.

In the following sections, we begin by summarizing the numerical methods. We then focus on the equations of motion, and the time and space discretization schemes, including those for shock capturing. This is followed by a discussion of the boundary conditions methods, where we also discuss inflow forcing and shock prescription. Finally we describe the computational mesh distribution.

2.2 Numerical Method

In the screech-type source model problem, shear-layer instability waves and vortices interact with an isolated region of the shock-cell structure. The model allows independent control over the amplitude and frequency of shear-layer disturbances as well as the strength and orientation of the shock. To simulate the shock-vortex interaction and the resulting sound, it is necessary to use accurate space and time discretization schemes.

The simulations are based on a numerical solution to the unsteady compressible Navier Stokes equations in conservative variables [24]. The scheme uses the compact, sixth-order Padé scheme [20] for computing spatial derivatives. It also makes use of the ENO scheme [58, 59] to capture discontinuities when necessary. Time advancement is performed using the third-order Runge-Kutta scheme [79]. Boundary treatment consists of Thompson-type non-reflecting boundary conditions [36], and is augmented by damping-sponges [14] and buffer-zones [6].

2.2.1 Equations of Motion

The simulations are based on numerical solutions to the unsteady compressible Navier-Stokes equations. In conservation form, the Navier-Stokes Equations are

$$\frac{\partial \rho^*}{\partial t^*} + \frac{\partial}{\partial x_i^*}(\rho^* u_i^*) = 0 \tag{2.1}$$

$$\frac{\partial}{\partial t^*}(\rho^* u_i^*) + \frac{\partial}{\partial x_j^*}(\rho^* u_i^* u_j^* + p^* \delta_{ij}) = \frac{\partial \tau_{ij}^*}{\partial x_j^*} \tag{2.2}$$

$$\frac{\partial E_t^*}{\partial t^*} + \frac{\partial}{\partial x_i^*}[(E_t^* + p^*)u_i^*] = -\frac{\partial q_i^*}{\partial x_i^*} + \frac{\partial}{\partial x_j^*}(u_i^* \tau_{ij}^*) \tag{2.3}$$

where the superscript $(\ )^*$ indicates dimensional quantities. Note that the Einstein convention of summing over repeated indices is observed for brevity. The energy equation is expressed in terms of the total energy E_t^*, which is comprised of the internal and kinetic energy per unit volume:

$$E_t^* = \rho^*(e^* + \frac{u_i^* u_i^*}{2}) \tag{2.4}$$

The constitutive relations close the system of equations. We assume Stokes hypothesis holds so that the viscous stress is given by

$$\tau_{ij}^* = \mu^*\left(\frac{\partial u_i^*}{\partial x_j^*} + \frac{\partial u_j^*}{\partial x_i^*} - \frac{2}{3}\frac{\partial u_k^*}{\partial x_k^*}\delta_{ij}\right) \tag{2.5}$$

The Fourier law for heat conduction gives q_i^* as

$$q_i^* = -k^*\frac{\partial T^*}{\partial x_i^*} \tag{2.6}$$

where k^* is the thermal conductivity. The coefficient of viscosity and the thermal conductivity are not assumed to be constant (see below). The fluid is taken to be an ideal gas so that

$$p^* = \rho^* R^* T^* \tag{2.7}$$

R^* is the specific gas constant.

The viscosity is assumed to vary only with temperature according to a power law,

$$\mu^* \propto (T^*)^n \tag{2.8}$$

where $n = 0.67$ (see White [78]). The thermal conductivity k^* is related to the coefficient of viscosity μ^* through the Prandtl number

$$Pr = \frac{\mu^* c_p^*}{k^*} \tag{2.9}$$

which is assumed to be constant.

The specific internal energy is related to the temperature through the specific heat at constant volume c_v^*,

$$e^* = c_v^* T^*; \tag{2.10}$$

similarly the specific enthalpy is related to temperature through the specific heat at constant pressure

$$h^* = c_p^* T^*. \tag{2.11}$$

The ratio of specific heats $\gamma = c_p^*/c_v^*$ is assumed to be 1.4.

The solutions to the equations of motion are carried out in nondimensional form. The nondimensionalizations of the flow quantities are based on a reference length (L_0^*), velocity (u_0^*), density (ρ_0^*), and viscosity (μ_0^*). There is also a reference Mach number $M_0 = u_0^*/c_0^*$.

$$x_i = \frac{x_i^*}{L_0^*},\ t = \frac{t^*}{L_0^*/u_0^*},\ u_i = \frac{u_i^*}{u_0^*},\ \rho = \frac{\rho^*}{\rho_0^*},\ \mu = \frac{\mu^*}{\mu_0^*}, \tag{2.12}$$

$$p = \frac{p^*}{\rho_0^* u_0^{*2}} = \frac{p^*}{\gamma M_0^2 p_0^*},\ T = \frac{T^*}{u_0^{*2}/c_p^*} = \frac{1}{(\gamma-1)M_0^2}\frac{T^*}{T_0^*},\ e = \frac{e^*}{u_0^{*2}} \tag{2.13}$$

where $p_0^* = \rho_0^* u_0^{*2}/(\gamma M_0^2)$ and $T_0^* = p_0^*/\rho_0^* R^* = u_0^{*2}/[(\gamma-1)c_p^* M_0^2]$. Substituting these definitions into the Navier-Stokes equations allows one to obtain the nondimensional set of equations.

$$\frac{\partial \rho}{\partial t} = -\frac{\partial}{\partial x_i}(\rho u_i) \tag{2.14}$$

$$\frac{\partial}{\partial t}(\rho u_i) = -\frac{\partial}{\partial x_j}(\rho u_i u_j + p\delta_{ij}) + \frac{\partial \tau_{ij}}{\partial x_j} \tag{2.15}$$

$$\frac{\partial E_t}{\partial t} = -\frac{\partial}{\partial x_i}[(E_t + p)u_i] - \frac{\partial q_i}{\partial x_i} + \frac{\partial}{\partial x_j}(u_i \tau_{ij}) \tag{2.16}$$

If one defines Reynolds number

$$Re = \frac{\rho_0^* u_0^* L_0^*}{\mu_0^*} \tag{2.17}$$

the constitutive relations are similarly nondimensionalized:

$$\tau_{ij} = \frac{\mu}{Re}\left(\frac{\partial u_i}{\partial x_j} + \frac{\partial u_j}{\partial x_i} - \frac{2}{3}\frac{\partial u_k}{\partial x_k}\right), \tag{2.18}$$

$$q_i = -\frac{\mu}{Re Pr}\frac{\partial T}{\partial x_i}, \tag{2.19}$$

$$p = \frac{\gamma - 1}{\gamma} \rho T. \tag{2.20}$$

2.2.2 Spatial Differencing Scheme

The spatial discretization implemented in the simulations is based on the compact finite difference schemes studied by Lele [20]. These schemes are modified Padé methods, *i.e.*, they use an implicit formulation to achieve high accuracy on a relatively small stencil. The schemes have also been shown to have low dispersion error, an important feature for aeroacoustic simulations.

The first derivative of $f(s)$ is approximated at s_i by

$$f'_{i-1} + a_1 f'_i + f'_{i+1} = a_2 \frac{f_{i+1} - f_{i-1}}{\Delta s} + a_3 \frac{f_{i+2} - f_{i-2}}{\Delta s} \tag{2.21}$$

where Δs, the grid spacing, is assumed to be uniform. To accommodate non-uniform grids, a mapping function $h(s)$ is defined; see below. The coefficients are defined

$$a_2 = \frac{1 + 2a_1}{3}, \quad a_3 = \frac{4 - a_1}{12} \tag{2.22}$$

where a_1 is taken to be 3. This stencil is applied to the interior of the domain, from $i = 4$ to $i = N - 3$, where N is the number of grid points in the s-direction. Near the boundary, the following stencils are used:

$$2f'_1 + 4f'_2 = \frac{-5f_1 + 4f_2 + f_3}{\Delta s}; \quad i = 1 \tag{2.23}$$

$$f'_1 + 4f'_2 + f'_3 = 3\frac{f_3 - f_1}{\Delta s}; \quad i = 2 \tag{2.24}$$

$$f'_2 + \tilde{a}_1 f'_3 + f'_4 = \tilde{a}_2 \frac{f_4 - f_2}{\Delta s} + \tilde{a}_3 \frac{f_5 - f_1}{\Delta s}; \quad i = 3 \tag{2.25}$$

where $\tilde{a}_1$, $\tilde{a}_2$, and $\tilde{a}_3$ are defined:

$$\tilde{a}_1 = 16\frac{1 + 2a_1}{40 - a_1}; \quad \tilde{a}_2 = \frac{1 + 2\tilde{a}_1}{3}; \quad \tilde{a}_3 = \frac{4 - \tilde{a}_1}{12} \tag{2.26}$$

Analogous stencils are obtained for the points $i = N-2,\ N-1$, and N. The differencing scheme is sixth-order accurate for the interior points ($4 \leq i \leq N-3$), fourth-order accurate at $i = 2, 3, N-2, N-1$, and third-order accurate at $i = 1, N$.

When the computational grid is non-uniform, it is possible to retain the accuracy of differencing provided the grid is defined in terms of an analytic mapping function h such that $h(s) = \mathrm{d}x/\mathrm{d}s$. The approximation to the first derivative on the nonuniform grid is then

$$\frac{\partial f}{\partial x} = \frac{1}{h(s)}\frac{\partial f}{\partial s} \tag{2.27}$$

Second derivatives are also approximated in an implicit fashion:

$$f''_{i-1} + b_1 f''_i + f''_{i+1} = b_2 \frac{f_{i+1} - 2f_i + f_{i-1}}{\Delta s^2} + b_3 \frac{f_{i+2} - 2f_i + f_{i-2}}{\Delta s^2} \tag{2.28}$$

where

$$b_2 = 4\frac{b_1 - 1}{3}; \quad b_3 = \frac{10 - b_1}{12} \tag{2.29}$$

b_1 is set to 11/2 to achieve 6th order accuracy. The boundary stencils are

$$f''_1 + 11 f''_2 = \frac{13f_1 - 27f_2 + 15f_3 - f_4}{\Delta s^2}; \quad i = 1 \tag{2.30}$$

$$f''_1 + 10 f''_2 + f''_3 = \frac{12(f_3 - 2f_2 + f_1)}{\Delta s^2}; \quad i = 2 \tag{2.31}$$

To obtain the second derivative on a non-uniform mesh, one simply differentiates Equation 2.27 with respect to x.

$$\frac{\partial^2 f}{\partial x^2} = \frac{1}{h^2}\frac{\partial^2 f}{\partial s^2} - \frac{h'}{h^2}\frac{\partial f}{\partial x} \tag{2.32}$$

For both first and second order derivatives, a system of linear equations is obtained. Matrix inversion is carried out with *LDU* factorization using the Thomas algorithm for tri-diagonal matrices.

2.2.3 Temporal Differencing Scheme

The solution is advanced in time in an explicit fashion using the compact storage, third-order accurate Runge Kutta method of Wray [79]. The scheme, when applied to the model equation $\mathrm{d}y/\mathrm{d}t = f(y,t)$, has the following predictor-corrector form:

$$y_{n+1/3} = y_n + \frac{8}{15}\Delta t f(y_n, t_n) \tag{2.33}$$

$$y_{n+2/3} = y_n + \frac{1}{4}\Delta t f(y_n, t_n) + \frac{5}{12}\Delta t f(y_{n+1/3}, t_{n+1/3}) \tag{2.34}$$

$$y_{n+1} = y_n + \frac{1}{4}\Delta t f(y_n, t_n) + \frac{3}{4}\Delta t f(y_{n+2/3}, t_{n+2/3}) \tag{2.35}$$

where

$$t_{n+1/3} = t + \frac{8}{15}\Delta t; \quad t_{n+2/3} = t_n + \frac{2}{3}\Delta t. \tag{2.36}$$

Flows considered herein are dominated by inviscid, rather than viscous, behavior. Mahesh *et al.* [24] documents the convective and viscous stability criteria for the RK3–Padé scheme. Based on these criteria, we show here that the time step is constrained more by a convective numerical instability than by a viscous numerical instability. The stability limits are deduced from model convection and diffusion equations, which approximate the convective and viscous terms of the Navier-Stokes equations, respectively. The convective stability limit, expressed in terms of CFL number, is

$$CFL = \left[\frac{|u_1| + c}{\Delta x_1} + \frac{|u_2| + c}{\Delta x_2}\right]_{max} \Delta t < 0.871. \tag{2.37}$$

In practice the CFL number is limited to around 0.5 for accuracy reasons. Time step Δt is often held fixed to accommodate post-processing methods which require equal time-spacing. The viscous stability limit is given by

$$\frac{\Delta t}{Re}\left(\frac{1}{\Delta x_1^2} + \frac{1}{\Delta x_2^2}\right)_{\max} < 0.365. \tag{2.38}$$

For a $CFL = 0.5$, $Re = 1000$, $\Delta x_1 = 1/10$, and $(\Delta x_2)_{\min} = 1/15$, which are typical values for simulations we have run, the left hand side of Equation 2.38 evaluates to approximately to 3.6×10^{-3}, *i.e.*, well within the viscous stability limit.

2.2.4 Shock Capturing

Resolving shocks with the spatial differencing scheme given above would require extremely dense grid spacing in regions where shocks are expected to arise. When the shocks move, the region of high grid density must be expanded to cover a larger region. For an explicit time advancement scheme, the small grid spacing imposes a high cost not only through increased grid sizes but also through a comparable reduction in the time step necessary to maintain numerical stability. It is therefore important to employ a shock-capturing scheme to accommodate discontinuities of interest in the numerical solution. In this section we describe the implementation of the essentially non-oscillatory (ENO) shock capturing scheme. The ENO schemes were first developed by Harten and Osher [9]. The scheme described here is based on the improved versions of Shu and Osher [58, 59].

The ENO shock capturing method uses the traditional Lax-Friedrichs splitting of the inviscid fluxes,

$$\vec{f}(\vec{q}) = \vec{f}^{+}(\vec{q}) + \vec{f}^{-}(\vec{q}) \tag{2.39}$$

where

$$\vec{f}^{\pm} = (\vec{f} \pm \alpha\vec{q})/2 \tag{2.40}$$

and α is the maximum value of $|u| + c$ in the x direction within the ENO zone (along fixed y). We consider each direction in a quasi-one-dimensional fashion. In the Navier-Stokes equations the inviscid fluxes appear in the form $\partial f/\partial x$. The derivative of these fluxes are then

$$\left.\frac{\partial \vec{f}^{\pm}}{\partial x}\right|_{x=x_j} = \frac{\hat{\vec{f}}^{\pm}_{j+1/2} - \hat{\vec{f}}^{\pm}_{j-1/2}}{\Delta x} \tag{2.41}$$

The numerical fluxes are defined using an expression which is general for arbitrary order r. If index i is the leftmost point in the stencil, then the numerical fluxes are

$$\hat{\vec{f}}^{\pm}_{j+1/2} = \sum_{m=0}^{r} c_{ENO}(i-j,m)\vec{f}^{\pm}[i,m] \tag{2.42}$$

$$\hat{\vec{f}}^{\pm}_{j-1/2} = \hat{\vec{f}}^{\pm}_{(j-1)-1/2} \tag{2.43}$$

where $c_{ENO(s,m)}$ is the coefficient matrix for the stencil of general order,

$$c_{ENO}(s,m) = \frac{1}{(m+1)!} \sum_{l=s}^{s+m} \prod_{p=s,p\neq l}^{s+m} (-p+1) \tag{2.44}$$

and $\vec{f}^{\pm}[j,k]$ are differences of $\vec{f}^{\pm}$:

$$\vec{f}[j,k] = \begin{cases} \hat{\vec{f}}^{\pm}(u_j), & k=0 \\ \vec{f}^{\pm}[j+1,k-1] - \vec{f}^{\pm}[j,k-1], & k=1,\ldots,r \end{cases} \tag{2.45}$$

An adaptive procedure is used to determine i (the leftmost point of the stencil); the purpose of the procedure is to strongly inhibit the differencing across the discontinuity:

$$i = i-1 \ \text{ if } \ 2|\vec{f}^{\pm}[i,k]| > |\vec{f}^{\pm}[i-1,k]|; \quad k=1,\ldots,r. \tag{2.46}$$

The factor of 2 left of the inequality is a scaling which reduces the likelihood of instability. The same scheme is applied for the x_1 and x_2 directions.

The "ENO zone" is a rectangular region in which the shock is expected. The ENO scheme is used to compute inviscid fluxes within this zone; the Padé scheme is used elsewhere. The extent of this zone for which ENO scheme is applied is indicated in Figure 2.1. The left boundary of the zone was designated to be 2δ to the left of the entry point of the shock on the lower boundary and 6δ to the right of the mean shock reflection site (*e.g.*, $x_{src}/\delta = 20$ for Case A as reported in Chapter 3). The lower boundary of the ENO zone coincides with the lower boundary of the computational domain, whereas the upper boundary was located 5δ above y_{src}. δ is the initial vorticity thickness of the shear layer. See Section 2.5 for implementation of oblique shock boundary condition. Note that the ENO scheme is used only for a small subset of simulations as indicated in Table 3.4.

2.2.5 Numerical Filtering

The appearance of shocks in an unsteady, supersonic flow is often unavoidable. When shock capturing as outlined above is used in a simulation, it is directed toward specific

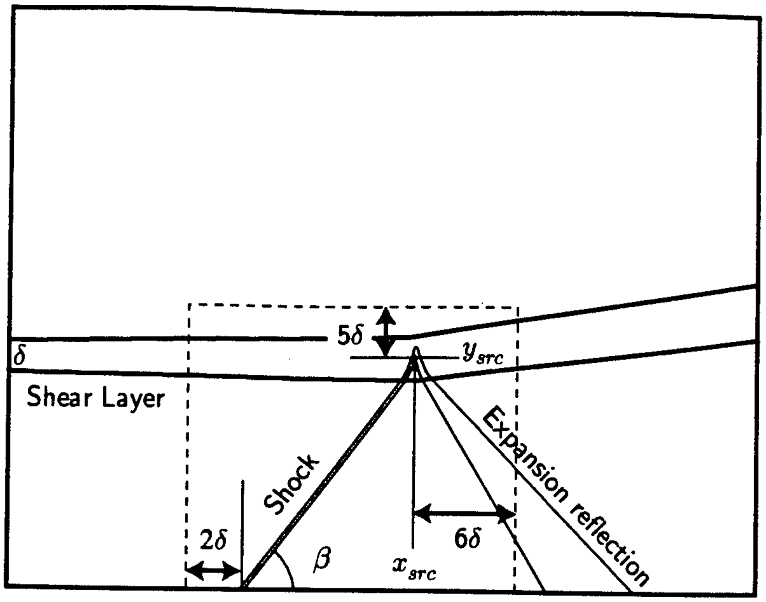

Figure 2.1: Approximate typical placement of ENO zone relative to shock position. ENO zone is located within the dashed line.

zones within which the shocks are known to be strong. Due to its computational expense, shock capturing cannot be efficiently applied throughout the domain. A growing unsteady shear layer at sufficiently high convective Mach number gives rise to traveling shocks (*e.g.*, eddy shocklets), which, if left untreated, would lead to an unstable solution. In recognition of these effects, we apply a filtering scheme which eliminates the high wave number (primarily 2-delta wave) numerical errors from the solution.

We apply the sixth order Padé filter, as documented in Lele [20]. Setting β in [20] to zero, the general form of the function is

$$\alpha \hat{f}_{i-1} + \hat{f}_i + \alpha \hat{f}_{i+1} = a f_i + \frac{d}{2}(f_{i+3} + f_{i-3}) + \frac{c}{2}(f_{i+2} + f_{i-2}) + \frac{b}{2}(f_{i+1} + f_{i-1}) \quad (2.47)$$

where $\hat{f}_i$ is the filtered value at x_i. Formulated in terms of a low pass transfer function, we have

$$T(w) = \frac{a + b\cos(w) + c\cos(2w) + d\cos(3w)}{1 + 2\alpha\cos(w)} \quad (2.48)$$

where $w = k\Delta x$ is the wave number normalized to the grid element size and

$$a = \frac{1}{8}(5 + 6\alpha + 16d) \tag{2.49}$$

$$b = \frac{1}{2}(1 + 2\alpha - 2d) \tag{2.50}$$

$$c = -\frac{1}{8}(1 - 2\alpha + 16d) \tag{2.51}$$

If we take $d = 0$, we obtain a reasonable low-pass filter for $\alpha < 0.5$. Rearranging the coefficients, we obtain:

$$\hat{f}_{i-1} + \frac{1}{\alpha}\hat{f}_i + \hat{f}_{i+1} = \frac{a}{\alpha}f_i + \frac{c}{2\alpha}(f_{i+2} + f_{i-2}) + \frac{b}{2\alpha}(f_{i+1} + f_{i-1}) \tag{2.52}$$

or

$$\hat{f}_{i-1} + \alpha'\hat{f}_i + \hat{f}_{i+1} = a'f_i + b'(f_{i+1} + f_{i-1}) + c'(f_{i+2} + f_{i-2}) \tag{2.53}$$

where $\alpha' = 1/\alpha$ and

$$a' \equiv \frac{a}{\alpha} = \frac{1}{8}(5\alpha' + 6) \tag{2.54}$$

$$b' \equiv \frac{b}{2\alpha} = \frac{1}{4}(\alpha' + 2) \tag{2.55}$$

$$c' \equiv \frac{c}{2\alpha} = -\frac{1}{16}(\alpha' - 2) \tag{2.56}$$

Boundary treatment for non-periodic boundary conditions are as follows (explicit fourth order accuracy with exact filtering of $w = \pi$):

$$\hat{f}_1 = \frac{15}{16}f_1 + \frac{1}{16}(4f_2 - 6f_3 + 4f_4 - f_5) \tag{2.57}$$

$$\hat{f}_2 = \frac{3}{4}f_2 + \frac{1}{16}(f_1 + 6f_3 - 4f_4 + f_5) \tag{2.58}$$

Similarly, for the opposite boundary:

$$\hat{f}_N = \frac{15}{16}f_N + \frac{1}{16}(4f_{N-1} - 6f_{N-2} + 4f_{N-3} - f_{N-4}) \tag{2.59}$$

$$\hat{f}_{N-1} = \frac{3}{4}f_{N-1} + \frac{1}{16}(f_N + 6f_{N-2} - 4f_{N-3} + f_{N-4}) \tag{2.60}$$

In Figure 2.2 we show the transfer function for $\alpha' = 2.222$. The second graph in the figure gives an indication of the wave number range over which the modification by the transfer function exceeds 1% In practice the filter is applied only every tenth time-step. Therefore the filtering should have little impact on features for which $w = k\Delta x < \pi/2$. In Appendix B we demonstrate that this choice of filter parameter has little impact on the accuracy of the results.

2.3 Boundary Conditions

The boundary conditions are considered in the context of their application, namely, an aero-acoustic flow simulation. The flow consists of a supersonic shear layer of finite thickness, bounded on the top by an essentially quiescent region (see Figure 1.9). An oblique shock or compression wave, which impinges on the shear layer, is introduced from the lower boundary of the domain. Instability waves are generated by forcing the inflow at the left of the domain. The instability waves grow and evolve into vortices, which then must exit the domain through the outflow boundary at the right. The interaction between the unsteady shear layer and the oblique shock results in acoustic waves which radiate in most directions, including back into the supersonic stream.

To simulate this flow it is crucial that highly accurate numerical boundary conditions are employed. These boundary conditions must allow the following: (1) a controlled inflow perturbation without spurious numerical feedback (*i.e.*, avoid spurious numerical receptivity), (2) oblique shocks to be prescribed and anchored at the computational boundary, (3) large-scale vortical disturbances to exit from the outflow boundary without creating significant reflection, and (4) acoustic disturbances to propagate out of the computational boundary without significant reflection.

Three types of boundary conditions are used: 1) Thompson-type nonreflecting boundary conditions [74], 2) the damping sponge [14], and the buffer-zone [6]. The boundary conditions are either used alone or in combination. The Thompson boundary conditions are applied at the boundary directly, whereas the other two methods

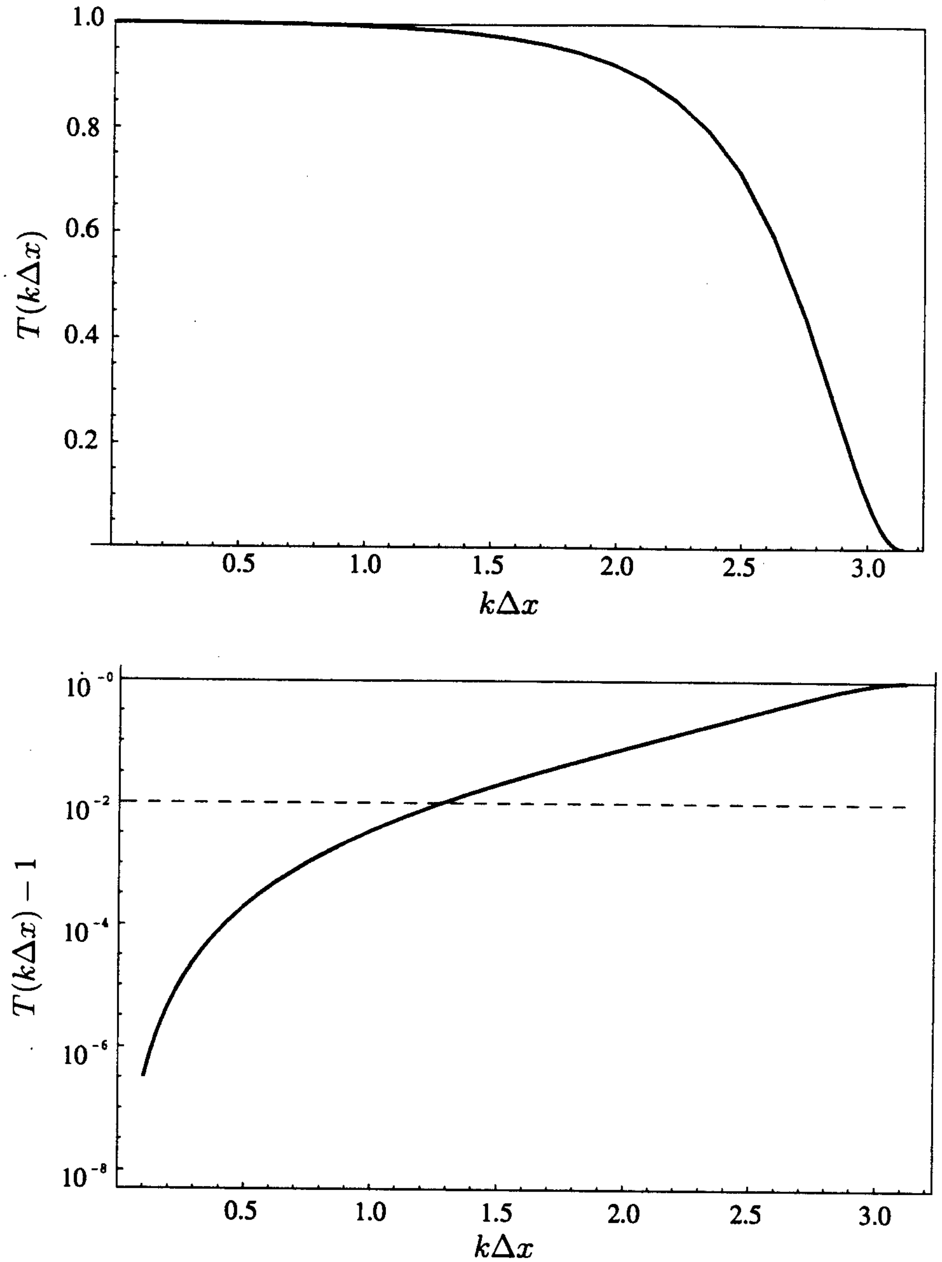

Figure 2.2: Top: Transfer function $T(k\Delta x)$ for Padé filter. Bottom: Relative change due to filter function. Filter parameter $\alpha' = 2.222$. Plotted against grid wave number $k\Delta x$.

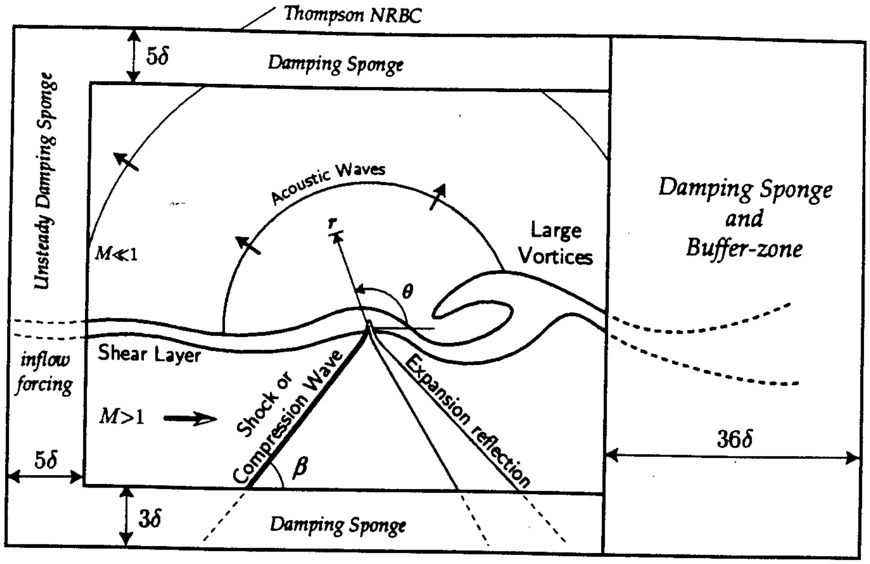

Figure 2.3: Boundary zones for the numerical simulations.

are applied over a region adjacent to the boundary, which we call the "boundary zone". As shown in Figure 2.3, the Thompson boundary condition is applied only to the upper boundary. The damping sponge is applied at all four boundaries, and the buffer-zone is applied only at the outflow.

The Thompson-type boundary conditions are based on a one-dimensional characteristic analysis, where incoming characteristics are set to zero so as to eliminate reflections. The damping sponge method [14] involves the addition of a source term to the equations of motion; in the boundary zone, this source term drives the solution toward a prescribed solution. The distribution of the source strength is varied from zero to a maximum value across the boundary zone, thereby damping out unwanted disturbances as they exit the computational domain. The buffer zone [6] changes the convective terms of the Navier-Stokes equations such that characteristics associated with traveling disturbances become entirely outward-going at the boundary. At inflows, this permits one to prescribe all quantities, whereas at outflows, one need not prescribe any.

The rationale for using the various boundary conditions in combination is several fold. The first reason is to satisfy well-posedness: even the Thompson BC should be used with the damping sponge when the flow crossing the boundary is subsonic. However, in the case of the buffer-zone, the Thompson boundary conditions are no longer necessary since the characteristics have been modified to be entirely outgoing or incoming; on the other hand, a damping sponge remains necessary for the purpose of damping a persistent steady-state error.

2.3.1 Computational Methodology

Thompson-type non-reflecting

The Thompson boundary conditions fall in the class of characteristic-based boundary conditions for hyperbolic systems. These boundary conditions make use of information transported along characteristics to predict the boundary values in a numerical solution. These methods typically invoke the assumption that disturbances propagate only normal to the boundary. The Thompson boundary condition modifies boundary terms associated with inviscid transport in Navier Stokes equations. These transport mechanisms consist of acoustic wave propagation and the advection of vorticity and entropy.

Consider the two-dimensional Navier-Stokes equation expressed in conservation form.

$$\frac{\partial \mathbf{Q}}{\partial t} + \frac{\partial \mathbf{F}_1}{\partial x_1} + \frac{\partial \mathbf{F}_2}{\partial x_2} = \text{viscous terms} \tag{2.61}$$

For a boundary normal to the x_i-direction, $i = 1$ or 2, only the terms contained in the inviscid flux expression $\partial \mathbf{F}_i / \partial x_i$ are approximated using characteristic variables. The amplitude variation of characteristic waves for the x_1 direction are [74]

$$L_1 = (u_1 - c)\left(\frac{\partial p}{\partial x_1} - \rho c \frac{\partial u_1}{\partial x_1}\right) \tag{2.62}$$

$$L_2 = u_1 \left(c^2 \frac{\partial \rho}{\partial x_1} - \frac{\partial p}{\partial x_1}\right) \tag{2.63}$$

$$L_3 = u_1 \frac{\partial u_2}{\partial x_1} \tag{2.64}$$

$$L_4 = (u_1 + c)\left(\frac{\partial p}{\partial x_1} + \rho c \frac{\partial u_1}{\partial x_1}\right) \tag{2.65}$$

where c is the local speed of sound. The coefficients $(u_1 - c)$, u_1, and $(u_1 + c)$ are the characteristic velocities. Based on these velocities, the variables L_m associated with outgoing characteristics are evaluated based on interior points, whereas those associated with incoming characteristics are zeroed so as to eliminate the reflection of the inviscid normal disturbances. These characteristic variables are then rearranged to obtain the terms that appear in the flux expression $\partial \mathbf{F}_1/\partial x_1$:

$$d_1 = \frac{\partial(\rho u_1)}{\partial x_1} = \frac{1}{c^2}\left(L_2 + \frac{L_4 + L_1}{2}\right) \tag{2.66}$$

$$d_2 = \frac{\partial(c^2 \rho u_1)}{\partial x_1} = \frac{L_4 + L_1}{2} \tag{2.67}$$

$$d_3 = u_1 \frac{\partial u_1}{\partial x_1} = \frac{L_4 - L_1}{2\rho c} \tag{2.68}$$

$$d_4 = u_1 \frac{\partial u_2}{\partial x_1} = L_3 \tag{2.69}$$

While this boundary condition scheme is well suited for planar acoustic disturbances traveling in the x_1 direction, acoustic waves traveling obliquely to the x_1 axis and features corresponding to large disturbances in vorticity, such as disturbed shear layers, result in large reflections. To address these, the following additional boundary treatments have been implemented.

Damping Sponge

Consider a system of equations of the form

$$\frac{\partial \mathbf{Q}}{\partial t} = L(\mathbf{Q}) \tag{2.70}$$

where $\mathbf{Q} = \mathbf{Q}(\mathbf{x}, t)$ and L is a general nonlinear operator. Then we can modify these equations by adding a source term to the right hand side which provides a negative feedback:

$$\frac{\partial \mathbf{Q}}{\partial t} = L(\mathbf{Q}) - \sigma(\mathbf{x})(\mathbf{Q} - \mathbf{Q}_{ref}) \tag{2.71}$$

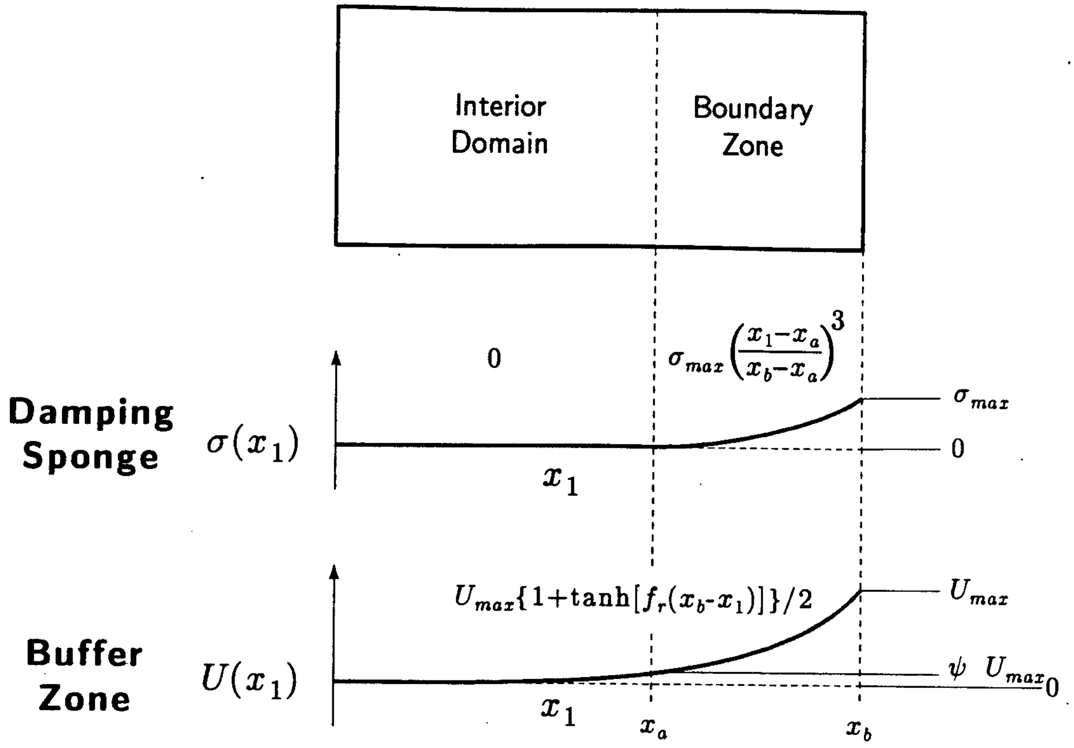

Figure 2.4: Schematic of boundary zone shape functions for damping sponge and buffer-zone.

where the prescribed reference solution, $\mathbf{Q}_{ref} = \mathbf{Q}_{ref}(\mathbf{x}, t)$, may be unsteady. The sponge coefficient, $\sigma(\mathbf{x})$, is non-negative everywhere. The boundary zone is defined for regions in which $\sigma \geq 0$. Following Mahesh *et al.* [24] the sponge coefficient is given a cubic distribution,

$$\sigma(x) = \begin{cases} \sigma_{max}\left|\frac{x_1-x_a}{x_b-x_a}\right|^3 & \text{if } x_a < x_1 < x_b \\ 0 & \text{otherwise} \end{cases} \tag{2.72}$$

where $\sigma_{max} > 0$ is the maximum sponge strength, at the computational boundary, and x_a and x_b demark the inner and outer edges of the boundary zone, respectively, and x_1 is the coordinate perpendicular to the boundary (see Figure 2.4). In practice, individual sponge functions are defined for each boundary; in the vicinity of corners, the boundary zones overlap, and a combined sponge function is defined. For instance, in a two-dimensional domain, such a sponge function may have the form

$$\sigma(x_1, x_2) = \sigma_1(x_1) + \sigma_2(x_2) \tag{2.73}$$

The reference solution is prescribed by the implementer, usually using information and assumptions known before carrying out the computation. In many circumstances, a good prescribed solution is not known outright. For instance, if the damping sponge solution were to be used to absorb outgoing shear layer vortices, it would be difficult to know the unsteady solution at the boundary *a priori*. The usual alternative is to provide a mean flow reference solution which sustains the overall mean structure of the flow, but does not accommodate the unsteady feature, other than to damp them. There are instances where it is desired that the reference solution be imposed in an unsteady fashion. In the present application, such a reference solution is imposed in the inflow sponge with the intent that the instability waves prescribed at the inflow are not damped or otherwise modified as they pass through the sponge. The inflow forcing is described in more detail in Section 2.4.

Buffer Zone

The buffer zone boundary treatment, like the damping sponge, is comprised of a modification to the equations of motion in the vicinity of the boundary. Instead of damping outgoing disturbances, however, the buffer zone method modifies the characteristics variables associated with traveling disturbances such that they resemble characteristics one would encounter in supersonic flow. In so doing, the characteristic variables may either be completely specified (as at a supersonic inflow) or completely unspecified (as at a supersonic outflow).

Here we visit the basics of the formulation; a more complete description is available in Freund [6]. Generically speaking, the Navier-Stokes equations can be expressed in conservative form as:

$$\frac{\partial \mathbf{Q}}{\partial t} + \frac{\partial \mathbf{F}_i}{\partial x_i} = \mathbf{S} \text{ (viscous terms)} \tag{2.74}$$

The characteristics in the streamwise direction (the x_1) direction are modified by the addition of a "convective" term

$$\frac{\partial \mathbf{Q}}{\partial t} + \frac{\partial \mathbf{F}_i}{\partial x_i} + \rho U(x_1)\frac{\partial \mathbf{Q}}{\partial x_1} = \mathbf{S} \text{ (viscous terms)} \tag{2.75}$$

Similar to the damping sponge coefficient $\sigma(x_1)$, the coefficient $U(x_1)$ is prescribed according to a distribution in the boundary-normal direction. A characteristic analysis will show that the characteristics (in the x_1-direction) will propagate at speeds $u_1 + U + c$, $u_1 + U - c$, and $u_1 + U$ (two characteristics). Therefore, to ensure that all characteristics are either incoming at the inflow or outgoing at the outflow, it is necessary to set at the boundary such that $u_1 + U - c > c$ for a mean flow to the right. There are some issues with regard to how the function $U(x_1)$ is distributed; in the present study we follow Freund [6] and make use of a hyperbolic tangent distribution which is centered at the outflow boundary, and decaying toward the interior:

$$U(x_1) = \frac{U_{max}}{2}\left\{1 + \tanh\left[f_r(x_1 - x_b)\right]\right\} \tag{2.76}$$

where x_b is, again, the outflow boundary coordinate (see Figure 2.4). f_r is a parameter which is chosen such that $U(x_a) = \psi U_{max}$, $0 < \psi < 1$, where x_a is the boundary zone interior coordinate. Therefore, as implemented, the buffer zone term acts on the entire domain. For $\psi \lll 1$, though, the influence of the buffer zone terms for $x_1 < x_a$ are minimal. Values for x_a, x_b, and ψ are given in or can be deduced from Table 3.2.

In practice, according to Freund, it is also necessary to combine the use of the damping sponge with the buffer zone. The sponge damps steady-state error which persist in the buffer zone region. (The steady-state error is thought to be caused by disturbances traveling according to characteristics of zero velocity somewhere within the sponge.)

Validation of outflow boundary conditions

The outflow boundary condition consists of the buffer zone and the damping sponge. To determine satisfactory boundary condition coefficient settings, we carried out a

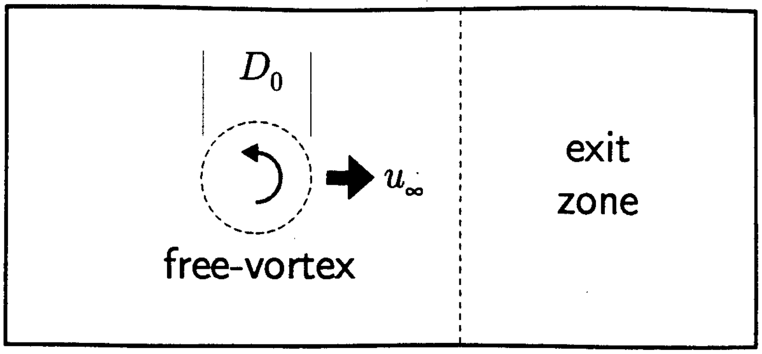

Figure 2.5: Schematic of exit boundary treatment tests with free vortex in uniform flow.

series of test computations in which we placed a free vortex in a uniform flow (Figure 2.5). The Mach number of the flow $M_\infty = 0.75$ approximates the convection Mach number of instability waves in a shear layer of $M_1 = 1.5$ (the Mach number in the simulations is $M_1 = 1.2$, chosen after these tests were carried out). The swirl velocity of the vortex is $0.8u_\infty$, and was chosen to represent a saturated shear-layer vortex computed in a simulation. The diameter $D_0 = 5\delta$.

The reflection coefficient is defined as

$$\mathcal{R} = \frac{|p_{max} - p_{min}|_{max}}{\Delta p_{vortex}} \tag{2.77}$$

where p_{min} and p_{max} are the minimum and maximum pressure observed in the interior domain (excluding the exit zones) at a given time, and Δp_{vortex} is the pressure deficit associated with the vortex. $|p_{max} - p_{min}|_{max}$ is then the maximum pressure difference after the vortex has completely departed the interior domain.

In Figure 2.6 we show the time trace of instantaneous $|p_{max} - p_{min}|/\Delta p_{vortex}$ for a number of boundary conditions, including:

1. the Thompson boundary condition alone,
2. the damping sponge with the Thompson boundary condition,
3. the buffer zone alone, and
4. the buffer zone with the damping sponge.

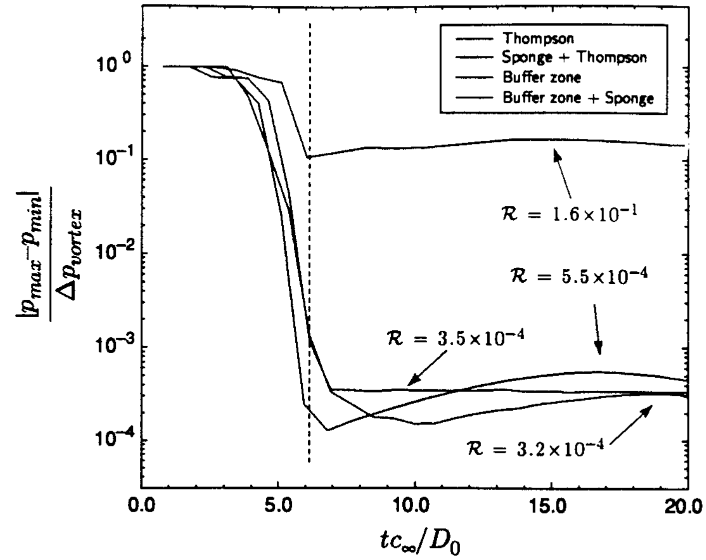

Figure 2.6: Instantaneous measure of maximum pressure difference in interior domain compared to original vortex pressure deficit in free vortex tests of four boundary conditions. Reflection coefficients for each case are indicated.

The specifics of the exit zone parameters for these configurations are as follows. The length of the exit zone is 36δ except in configuration 1. For the cases which employ the damping sponge (2 and 3), $\sigma_{max} = 0.15$. This value was arrived upon in the optimization survey depicted in Figure 2.7. The value of the buffer zone function at the domain exit is $U_{max}/U_1 = 1.2$, where U_1 is the high speed stream velocity in the simulations. $\psi = 10^{-3}$. The grid spacing is uniform in x_1 at $\Delta x/\delta = 0.2$.

As determined by the plots in Figure 2.6, there is marked reduction in the reflection coefficient due to a free vortex when one considers either the buffer zone or the optimized damping sponge, compared to the Thompson condition alone. The performance of the buffer zone alone is only marginally better than the damping sponge alone. The use of the buffer zone eliminates the need for Thompson boundary conditions out the boundary zone outflow. The addition of the damping sponge to the buffer zone was found to result in only a modest further improvement in reflection coefficient within the time sample of this test. However, as can be seen in Figure 2.6

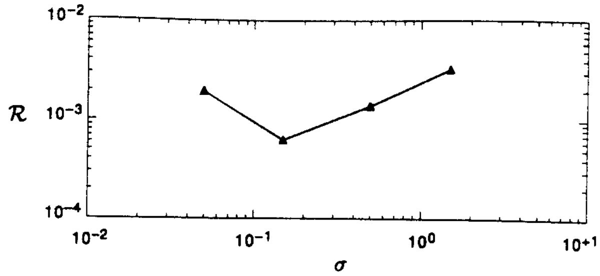

Figure 2.7: Damping sponge coefficient σ optimization at fixed sponge length for free vortex boundary condition test problem.

the buffer zone reflection error is slow to disperse and may be cumulative as additional vortices pass into the boundary zone. The cases with combined buffer zone and damping sponge indicate a more rapid decay in the reflection.

2.4 Inflow Forcing

The instability wave disturbances are introduced at the inflow boundary. The disturbances are forced harmonically according to eigenfunctions obtained from a linear stability analysis. For the inflow disturbances to remain undamped as they pass through the inflow damping sponge, we must define a reference solution based on a prediction of the convection and growth of the instability waves over the width of the sponge. The linear stability theory provides an adequate prediction if we assume that, within the sponge, the amplitude of these waves remains within the limits of the linearized theory.

We decompose the reference solution into a steady component, the mean shear layer, and an unsteady component, the predicted instability wave.

$$\mathbf{Q}_{ref} = \overline{\mathbf{Q}}_{ref}(\mathbf{x}) + \mathbf{Q}'_{ref}(\mathbf{x}, t) \tag{2.78}$$

The steady component $\overline{\mathbf{Q}}_{ref}$ is described in the following section (2.4.1), whereas the details of the unsteady component are outlined in the subsequent section (2.4.2). According to the stability theory, the description of the instability wave in space and time can be decomposed into a product of terms corresponding to the shear-layer-normal variation (the eigenfunction), the streamwise growth, and the streamwise convection:

$$\mathbf{Q}'_{ref} = \hat{\mathbf{Q}}'_{ref}(x_2)e^{-\alpha_i x_1}e^{i(\alpha_r x_1 - \omega t)} \tag{2.79}$$

$-\alpha_i$, α_r, and ω are respectively instability wave growth rate, wave number, and frequency.

2.4.1 Inflow profile and initial condition

The mean inflow profile is based on a similarity solution to the compressible boundary layer equations. The procedure for obtaining this profile is documented in detail in Lu and Lele [23]. It is based on the Howarth transformation (see Schlichting [53]) of similarity solutions to the incompressible boundary layer equations and is generalized by Lu and Lele [23] to accommodate skewed shear layers; here the skew angle is set to zero. A system of ordinary differential equations are solved numerically, with a far-field temperature ratio of unity. Figure 2.8 depicts the velocity, density, and temperature profiles of the inflow for $M = 1.2$.

2.4.2 Stability Analysis

The eigenfunctions for the inflow forcing are obtained from a linear stability analysis, with the inflow profile obtained above as the base flow (the parallel flow assumption is invoked for the stability analysis). Only the inviscid linearized disturbance equations are considered, since the instability mechanism of the shear layer is inviscid. In the spatial stability analysis (as carried out as in Lu and Lele, again with the skew angle set to zero), the normal mode assumption is made for disturbances in the streamwise direction, yielding a system of ordinary differential equations in the transverse coordinate. The dispersion relation which arises from the numerical solution of these equations gives a relationship between disturbance stream-wise growth rate and instability wave-number; and a relationship between instability wave frequency and instability wave number. Based on the dispersion relation, a specific frequency (or

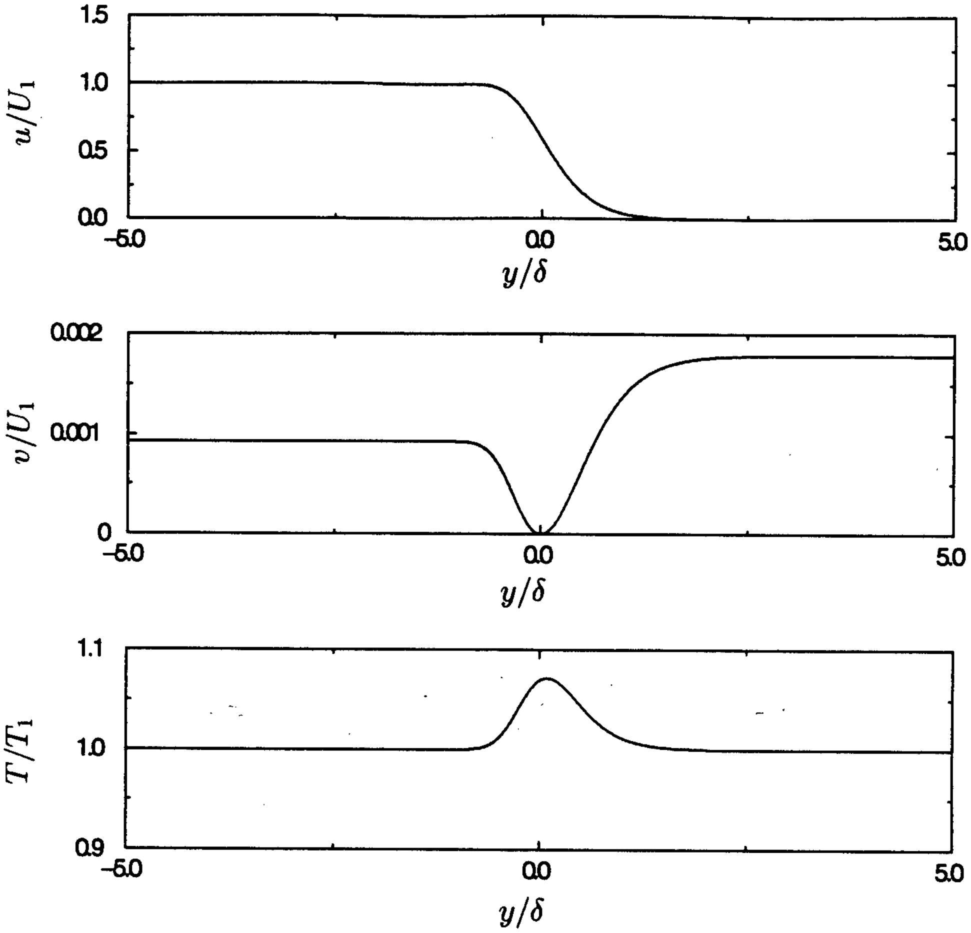

Figure 2.8: Mean inflow profile for Mach number $M = 1.2$, $Re = 1000$. Pressure is uniform; density is obtained through ideal gas law.

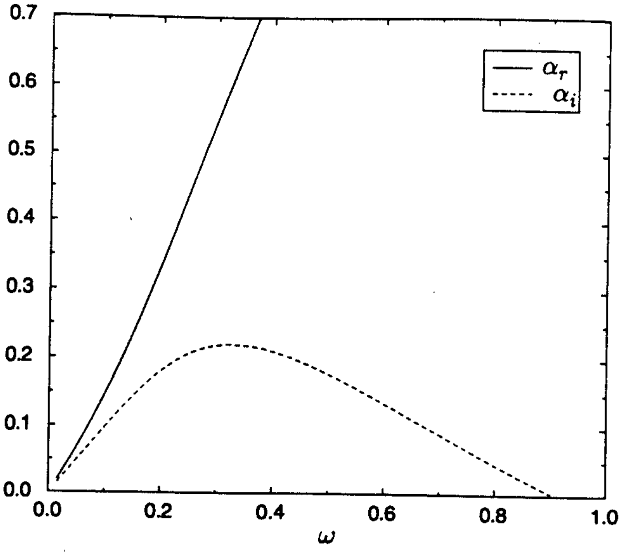

Figure 2.9: Dispersion relation for stability analysis based on shear layer given in Figure 2.8. Simulations are carried out at the most unstable frequency and at its sub-harmonic. — instability wave number α_r, - - - growth rate $(-\alpha_i)$.

f/f_0	ω	α_r	$-\alpha_i$	λ_i	*Shear Layer*
1.0	0.328690	0.616465	0.212204	10.1923	SL0
0.5	0.164345	0.268053	0.150150	23.4401	SL1, SL2, SL3

Table 2.1: Eigenvalues used in instability wave forcing at inflow; shear layer cases are SLn are given in Table 3.3.

"eigenvalue") is chosen and substituted back into the system of equations to obtain eigenfunctions. These eigenfunctions describe the dependence of the relative disturbance magnitude and phase on the transverse coordinate. Unique eigenfunctions are obtained in this manner for streamwise and transverse velocity fluctuations and the density and temperature fluctuations.

Figure 2.9 illustrates the dependence of frequency and disturbance streamwise growth rate as functions of streamwise wave-number for the mean flow profile shown above. The forcing frequencies chosen for the simulations described below are indicated. Figure 2.10 shows the eigenfunctions for velocity and temperature fluctuations.

Real Part

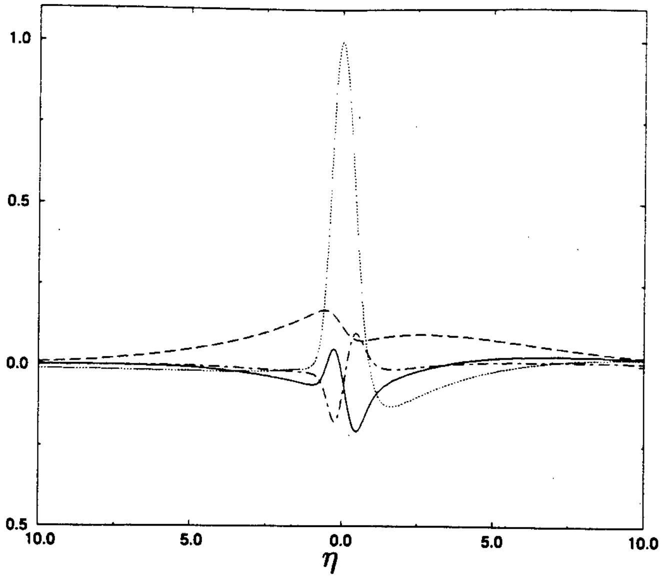

Imaginary Part

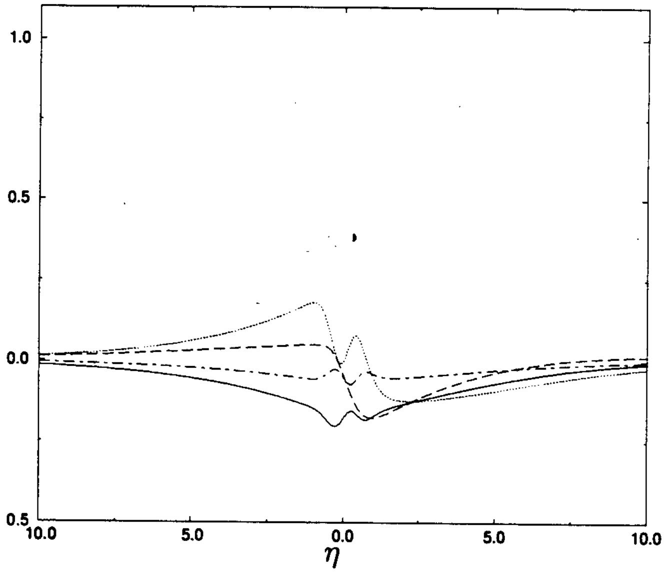

Figure 2.10: Real and imaginary parts of instability wave eigenfunction distributions corresponding to eigenvalue $\omega/(U/\delta) = 0.164345$ (subharmonic of most unstable mode). —— ρ'/u'_{max}, - - - - u'/u'_{max}, — — — v'/u'_{max}, – - – T'/u'_{max}. u'_{max} is the amplitude of the streamwise velocity fluctuation and serves as the scaling parameter for the instability wave mode. Note that the nondimensionalization for temperature given here is $T' = T'^{*}/T^{*}_{\infty}$.

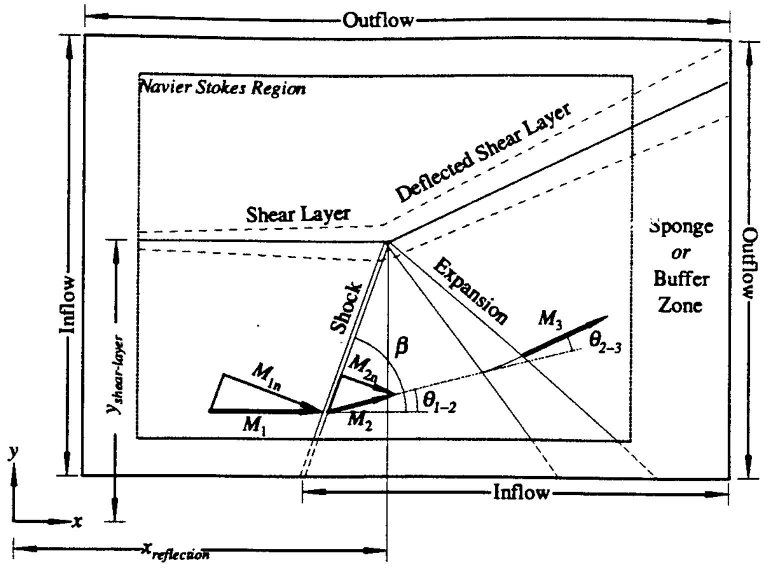

Figure 2.11: Schematic of how oblique shock is introduced by lower sponge into computational domain, and its effect on the mean flow.

2.5 Incident Wave

Depending on the case, either an oblique shock or compression wave is imposed on the lower boundary. Figure 2.11 depicts schematically how the shock is imposed upon the flow through the lower boundary sponge, and how it reflects from the shear layer in the form of an expansion wave fan. The flow passing through this wave system turns toward the shear layer successively twice, thereby deflecting the shear layer away from the supersonic stream. The sponge must also accommodate and absorb the expansion waves. The sponge serves the purpose of holding the shock and absorbing unsteady disturbances which travel down the expansion waves during the shock vortex interaction.

Whereas the shock is by definition a thin feature through which entropy increases as flow variables make a significant jump, the compression wave consists of a similar transition, except that the wave profile is widened and the jump is reduced to the extent that the wave remains essentially isentropic. The motivation for considering these weaker, wider compression waves consists of the following: 1) the elimination of the thin shock permits computations without discontinuity-capturing schemes, which are computationally expensive; 2) the weaker and wider compression wave is found to result in a radiated acoustic wave profile whose features can be resolved on a coarser mesh; and 3) the weaker compression wave deflects at a smaller angle, thereby increasing the effectiveness of the subtraction technique for obtaining the acoustic field; 4) the weaker waves are more amenable to small-disturbance modeling.

As it was necessary to verify that the compression waves produce interactions which retain the gross behavior of the shock instability wave interactions, we carry out both simulations with shocks and with compression waves.

2.5.1 Shock and Prandtl-Meyer Expansion

In the case of the shock, the jump in the flow variables is a significant fraction of the mean, and the width of the shock is thin enough to require shock-capturing. The jump conditions are the Rankine-Hugoniot conditions for a normal shock, with velocities modified appropriately to accommodate the obliqueness. At the lower boundary and in the sponge, the width δ_{shock} of the imposed profile is estimated based on the expression for the thickness of a weak laminar shock (see the Taylor analysis in Mahesh *et. al* [24]:

$$\frac{c_1 \delta_{shock}}{\nu_1} = \frac{6.89}{M_1 - 1} \tag{2.80}$$

where M_1 is the upstream normal Mach number, c_1 the upstream speed of sound, and ν_1 the upstream kinematic viscosity. The profile itself is imposed in the shape of a hyperbolic tangent.

The imposed boundary and sponge profiles for the reflected expansion are based on the idealized Prandtl-Meyer expansion emanating from the point at which the shock would intersect the centerline of the shear layer (discounting shear-layer thickness effects). Providing a precise description of the reflection is not critical given the unsteady nature of the disturbances which interact with the compression wave; most important is that the overall mean flow changes be accommodated. Figure 2.12 illustrates the details of expansion fan system approximation.

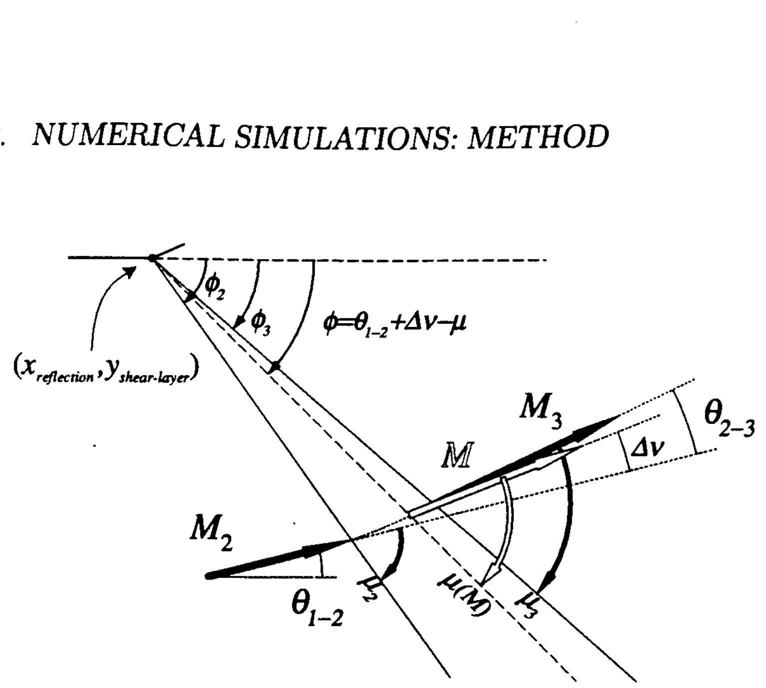

Figure 2.12: Detail of P-M expansion, which arises from the reflection of the shock off the shear layer.

2.5.2 Compression Wave Prescription

The compression waves, though imposed with strengths somewhat weaker than in the shock cases investigated, are still of magnitude where convergence of Mach lines must be accommodated, particularly to avoid the formation of a thin shock. The width of the oblique compression wave, denoted w, corresponds to the theoretical separation of the leading and trailing Mach waves at the center-line of the mean shear layer (discounting finite shear layer width effects; see Figure 2.13). This separation is denoted w . The details of the geometry are given in Appendix A.

2.6 Computational Mesh

In order to reduce overall computational costs while retaining numerical accuracy, it is necessary to reduce the density of grid points away from the shear layer by using a nonuniform mesh. As described earlier, the numerical method relies on an analytic mapping function $h(s) = dx/ds$ to compute first and second derivatives on a generally nonuniform mesh. In the direction perpendicular to the shear layer, the analytic function is defined for the present simulations in terms of three distinct

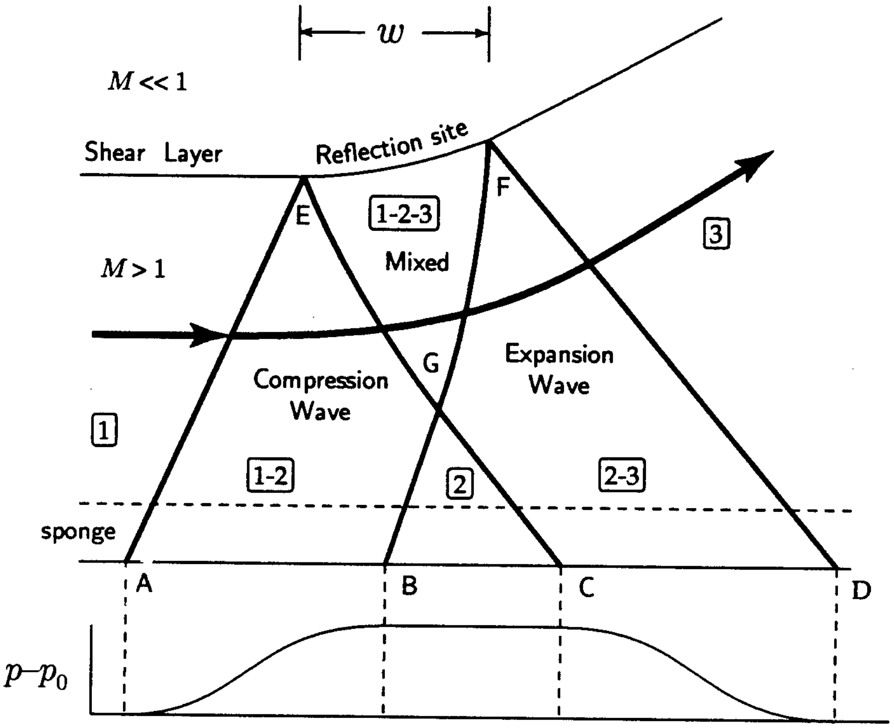

Figure 2.13: Schematic of compression wave system, with width w defined as indicated. Further detail of geometry is given in Appendix A, Figure A.1.

zones: the shock region, the shear layer, and the outer flow. The grid is uniform in the stream-wise direction.

As shown in the left side of Figure 2.14, we define the function $r(s)$ which defines a mapping from the computational domain to the unscaled physical domain (mapping from $[0,1]$ to $[0,1]$). Two control points, s_a and s_b, demarcate the borders of the three regions in the computational domain, and the corresponding control points r_a and r_b indicate where the borders will lie in the (unscaled) physical domain. Through these points, the slopes of the line segments (m_1, m_2, and m_3, respectively) are defined:

$$m_1 = \frac{r_a}{s_a}, \quad m_2 = \frac{r_b - r_a}{s_b - s_a}, \quad m_3 = \frac{1 - r_b}{1 - s_b} \tag{2.81}$$

these slopes are proportional to the grid element size Δy for each region. To construct the function with smooth transitions between the line segments, we define its derivative as follows:

$$r'(s) = m_1 + \frac{1}{2}(m_1 - m_2)\left[1 + \tanh\left(\frac{s - s_a}{w_a}\right)\right] + \frac{1}{2}(m_2 - m_3)\left[1 + \tanh\left(\frac{s - s_b}{w_b}\right)\right] \tag{2.82}$$

where w_a and w_b control the transition width between the regions. The unscaled grid mapping function is then obtained by integrating Eq. 2.82 from $s = 0$ to s:

$$\begin{aligned} r(s) = \frac{1}{2}(m_1 + m_3) \quad & +(m_2 - m_1)w_a \ln\left[\cosh\left(\tfrac{s-s_a}{w_a}\right)\right] + (m_1 - m_2)w_a \ln\left[\cosh\left(\tfrac{x_a}{w_a}\right)\right] \\ & +(m_3 - m_2)w_b \ln\left[\cosh\left(\tfrac{s-s_b}{w_b}\right)\right] + (m_2 - m_3)w_b \ln\left[\cosh\left(\tfrac{s_b}{w_b}\right)\right] \end{aligned}$$

$y(s)$ is found by scaling $r(s)$,

$$y(s) = r(s)(y_{max} - y_{min}) + y_{min} \tag{2.83}$$

and $h(s)$ is obtained by scaling $r'(s)$,

$$h(s) = r'(s)(y_{max} - y_{min}). \tag{2.84}$$

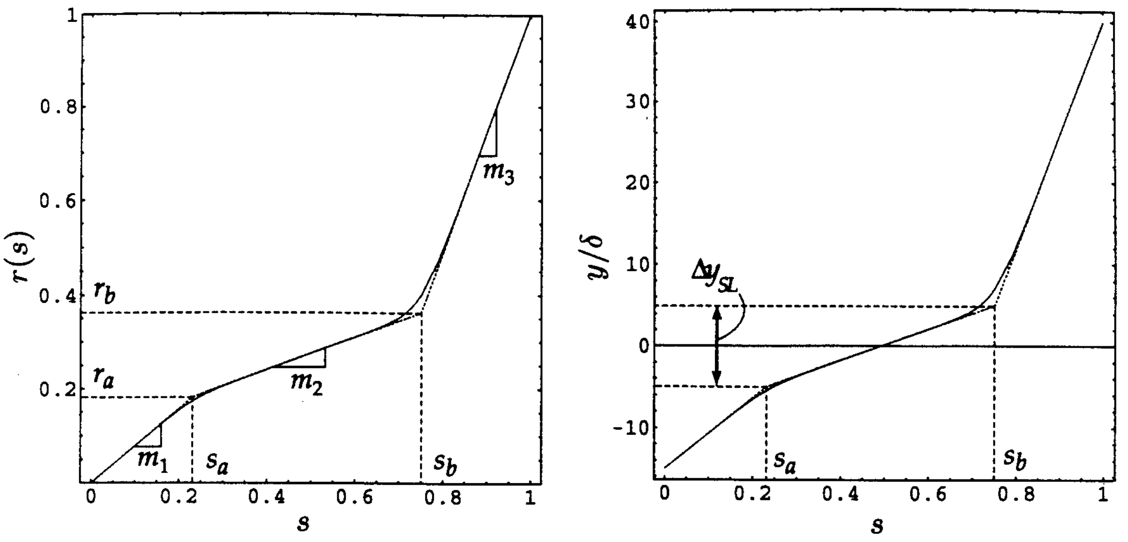

Figure 2.14: *Left*: unscaled grid mapping function for the vertical mesh direction, showing the three regions (from the left) of shock, shear layer, and outer. *Right*: scaled grid mapping function $y(s)$ used in actual simulations. Δy_{SL} is the the width of the shear layer region.

The mapping function $y(s)$ used in simulations documented in the next chapter is shown on the right in Figure 2.14. In this grid, we have set

$$s_a = 0.23, \quad s_b = 0.75, \quad \text{and} \quad w_a = w_b = 0.05 \tag{2.85}$$

and

$$r_a = \frac{(y_0 - \Delta y_{SL}) - y_{min}}{L_y} \quad \text{and} \quad r_b = \frac{(y_0 + \Delta y_{SL}) - y_{min}}{L_y}, \tag{2.86}$$

where $y_0 = 0$ is the nominal center of the shear layer, $\Delta y_{SL} = 10\delta$ is the width of the shear layer region, and $L_y = y_{max} - y_{min}$ is the height of the domain. The analytic mapping function $h(s)$ and physical distribution of grid density $\delta/\Delta y(y)$ is shown for these parameter settings in Figure 2.15. The y-mapping described by these parameters is used in all of the Navier-Stokes (Chapter 3) and linearized Euler (Chapter 5) simulations discussed in this work.

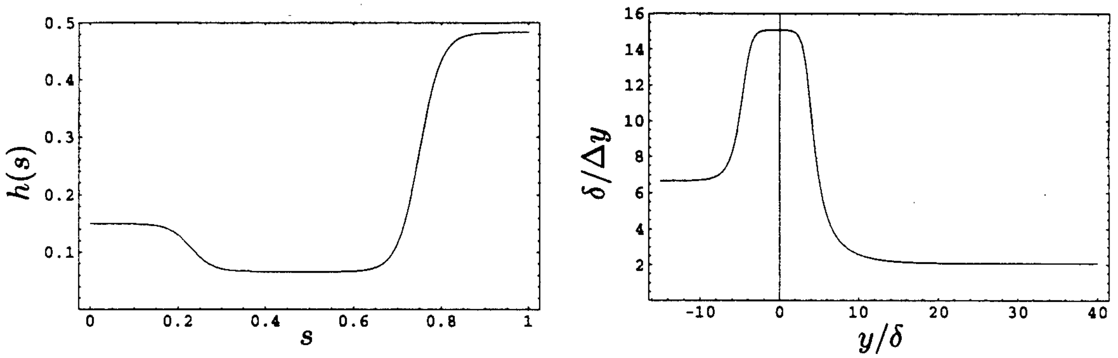

Figure 2.15: *Left*: analytic mapping function $h(s)$ for actual grid in y-direction, which is also $\Delta y(s)$.*Right*: Grid density (elements per reference length δ).

Chapter 3

Results from Direct Numerical Simulations

3.1 Introduction

In this chapter we present the results of the direct numerical simulations, using the numerical methods for solving the Navier-Stokes equations described in the previous chapter. We will demonstrate that the sound generation process of a screech-type source is best described as "leakage" of the incident shock or compression wave through the shear layer as enabled by the passage of the instability wave vortices. We also explore the dependence of the radiated acoustic field on the parameters of shock (or compression-wave) strength, width, and instability wave amplitude.

We begin our discussion of the simulations by presenting results for a free shear layer in absence of any incident shock or compression wave. We document its behavior and measure instability wave amplitude as a function of streamwise coordinate over a range of forcing conditions. These reference flows are used both to help extract the acoustic field in simulations containing incident shocks or compression waves and to provide basic instability wave data for theoretical analyses described in later chapters. We then present the results for a shock incident on a steady shear layer to illustrate the mean effects of the interaction. In Section 3.4 we describe the basic nature of the shock instability-wave vortex interaction and the resultant sound generation. We then

Grid Size	$Nx \times Ny$	$901/721^* \times 291$
Complete Domain Size	$(x_{min} : x_{max}) \times (y_{min} : y_{max})$	$(0 : 90/72^*) \times (-15 : 40)$
Interior Domain Size	$(x_{min} : x_{max}) \times (y_{min} : y_{max})$	$(5/10^\dagger : 54/36^*) \times (-11.8 : 30)$
Time Step	Δt	0.0119474
Filter Coeff.	α'	2.222
Filter Period	N_{filter}	every 10 Δt

Table 3.1: Parameters for numerical simulations. Exceptions for: *Case A1. †Cases SL1 and D1; see Tables 3.3 and 3.4 for case designations. Interior domain refers to computational domain excluding boundary zones.

	Inflow	*Outflow*	*Top*	*Bottom*
U_{max}	—	0.7677	—	—
ψ	—	10^{-3}	—	—
σ_{max}	10.0	0.15	5.0	5.0
N_{sponge}	50/100*	360	10	24
L_{sponge}	5.0/10.0*	36.0	5.0	3.2

Table 3.2: Boundary zone: Buffer zone and damping sponge settings. *Alternate settings for weakly forced cases (SL3 and D1; see Tables 3.3 and 3.4 for case designations).

demonstrate in Section 3.5 that the interaction and radiation behavior is essentially reproduced when incident waves of lower amplitude and broader profile than those of shocks impinge on the shear layer. The improved quantitative results afforded by these simplifications are presented.

A summary of the parameter settings used in the numerical simulations presented in this chapter are given in Table 3.1. Boundary zone parameters are given in Table 3.2.

3.2 Free Shear Layer

In this section we carry out a limited study of the forced shear layer alone. In particular, we document the amplitude of the instability waves as a function streamwise distance for several forced shear layers. These shear layers are later subject to shock and compression wave interaction, and further form the base flow for linearized Euler simulations described in the next two chapters.

All shear layers explored in this study have a Mach number of 1.2, a choice which represents a tradeoff between conditions sufficient to impose a reasonably strong shock and the need to eliminate other sources of sound. At minimum, a supersonic flow is of course necessary to support a standing oblique shock or compression wave in the high speed stream. There is also an upper limit on the Mach number. Above a certain Mach number the instability waves move at speeds supersonic relative to the quiescent side of the shear layer and emit Mach waves. However, it was found that even for Mach numbers such as 1.4 or 1.5, strong eddy shocklets readily form above and below the saturated vortices. As these shocklets require high resolution and because they can also serve as unintended sources of sound, the flow Mach number was reduced to 1.2. The steeper shock or compression wave angle at this Mach number also conveniently reduces the necessary length of the computational domain.

The Reynolds number of the shear layers studied is 1000 based on initial vorticity thickness δ and the velocity of the high speed stream, U_1. At this Reynolds number and at a grid density of 15 nodes per vorticity thickness in the direction across the shear layer, the entire instability-wave vortex evolution was sufficiently resolved.

The forced shear layers presented in this work are summarized in Table 3.3. The forcing frequency is obtained from linear stability analysis of the inflow profile, as described in Section 2.4.2. Case SL0 was obtained by forcing the inflow at the most unstable frequency. Because of a spurious, rapidly growing subharmonic mode that leads to vortex pairing, only one case involving an incident wave interaction was carried out for this shear layer (Case A1; see Table 3.4). A reduction in the forcing frequency to half the most unstable frequency was found to satisfactorily suppress the subharmonic mode and prevent vortex pairing within the computational domain. The remaining shear layer cases (SL1 through SL3) are carried out at this frequency.

cases	f/f_0	$\lvert\hat{u}\rvert_{max}/U_1$	λ_i/δ	λ/δ
SL0	1.0	2.00×10^{-2}	10.2	15.9
SL1	0.5	2.00×10^{-2}	23.4	31.9
SL2	0.5	6.32×10^{-3}	23.4	31.9
SL3	0.5	2.00×10^{-3}	23.4	31.9

Table 3.3: Summary of free shear layers cases reported. f/f_0 is the forced frequency normalized by the most unstable frequency of the shear layer, $f_0 = f^*{}_0/(U^*{}_1/\delta^*) = 0.328690/2\pi$. λ_i is the instability wave length. Other parameters are defined is Section 3.3

3.2.1 Instability Wave Amplitude

A measure of shear layer amplitude is based on fluctuation velocity magnitude, sampled at stations in the streamwise coordinate x. In terms of the square of the fluctuation velocity magnitude, we define the square of an instability wave amplitude as

$$K^2 = \int_{-\infty}^{+\infty} \frac{\left(\overline{u'^2} + \overline{v'^2}\right)}{2} dy \tag{3.1}$$

where for any $f(t)$, its average over fundamental oscillation period T is $\overline{f} \equiv T^{-1} \int_0^T f(t)dt$. We can decompose this measure of instability wave amplitude (squared) into the contributions due to the streamwise and transverse velocity fluctuations:

$$K^2 = K_u^2 + K_v^2 \tag{3.2}$$

where

$$\begin{aligned} K_u{}^2 &= \int_{-\infty}^{+\infty} \frac{\overline{u'^2}}{2} dy \\ K_v{}^2 &= \int_{-\infty}^{+\infty} \frac{\overline{v'^2}}{2} dy \end{aligned} \tag{3.3}$$

In later chapters, we will examine the dependence of acoustic radiation levels on K, K_u, and K_v.

If the time interval T is taken to be the fundamental sampling period for a discrete Fourier series representation of the velocity field in time, we can represent the instability amplitude (squared) as the sum the velocity magnitudes of each Fourier mode

$$K^2 = \sum_{k=-Nk/2}^{Nk/2+1} K_k^2 = \sum_{k=-Nk/2}^{Nk/2+1} \int_{-\infty}^{+\infty} \frac{(|\hat{u}_k|^2 + |\hat{v}_k|^2)}{2} dy \tag{3.4}$$

where $\hat{u}_k$ and $\hat{v}_k$ are the Fourier velocity coefficients:

$$\hat{u}_k(x, y) = \frac{1}{N} \sum_{n=1}^{N} u(x, y, t_n) e^{i2\pi kn/N} \tag{3.5}$$

N is the number of evenly spaced points in time sampled in over the period corresponding to fundamental frequency ω.

In Figure 3.1 we show K^2 for the three shear layer forcing amplitude. For each case we show the fluctuation velocity magnitude for the fundamental mode ($k = 1$), the fundamental and first harmonic combined ($k = 1, 2$), and the fundamental, first harmonic, and second harmonic combined ($k = 1, 2, 3$). The plots indicate that K^2 is represented almost entirely by the fundamental mode. Each shear layer initially grows exponentially at approximately the predicted growth rate based on linear instability theory, followed by nonlinear saturation. This saturation process is associated with the formation of the vortex, and occurs progressively farther downstream at intervals consistent with the inflow forcing. The streamwise shift between each case is approximately $L/\delta = 8.5$. We verify that these instability wave amplitude trends for the SL1 shear layer are independent of grid resolution and filter coefficient in Appendix B.

In Figure 3.2 we show K^2 and its components ${K_u}^2$ and ${K_v}^2$ from the SL1 shear layer. While the growth rate remains exponential, ${K_u}^2$ is the dominant component; however, as the instability wave saturates, the growth in ${K_u}^2$ diminishes and is overtaken by K_v^2. In Figure 3.3 we show the same data on a linear scale. K_u^2 exhibits a localized leveling at $x/\delta = 30$, corresponding to the formation of the shear layer vortex, before continuing to its maximum value at approximately $x/\delta = 40$. The amplitude associated with the vertical velocity component ${K_v}^2$ continues to grow during the leveling of K_u^2. After $x/\delta = 40$, it decays slightly and reaches a local minimum when ${K_u}^2$ reaches its maximum. The absence of these features in the sum K^2 of

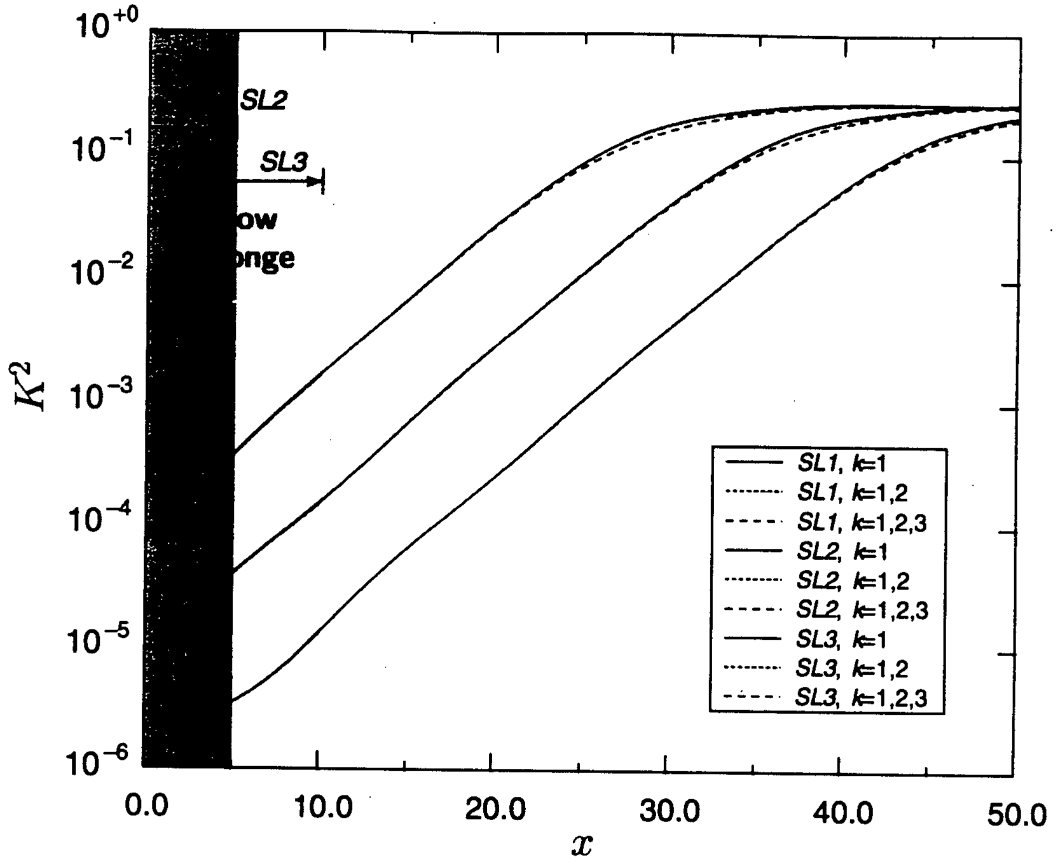

Figure 3.1: Instability wave amplitude (squared). Shear layer designations SL1-3 are given in Table 3.3.

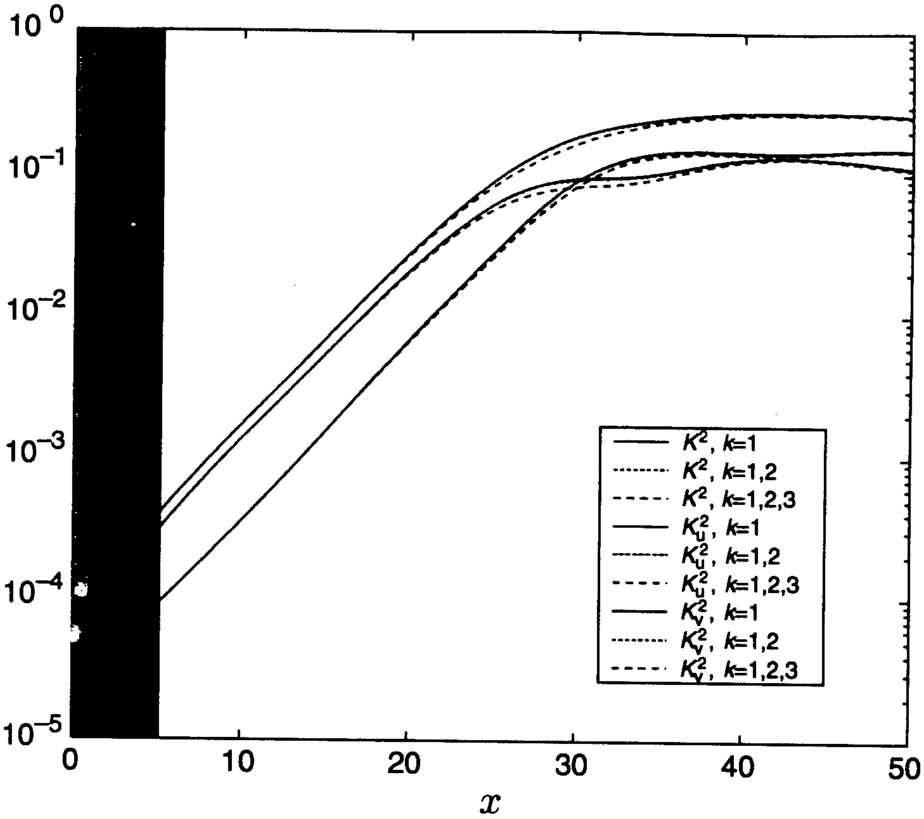

Figure 3.2: Semi-log plot of instability wave amplitude squared for shear layer SL1, broken down by component and Fourier mode.

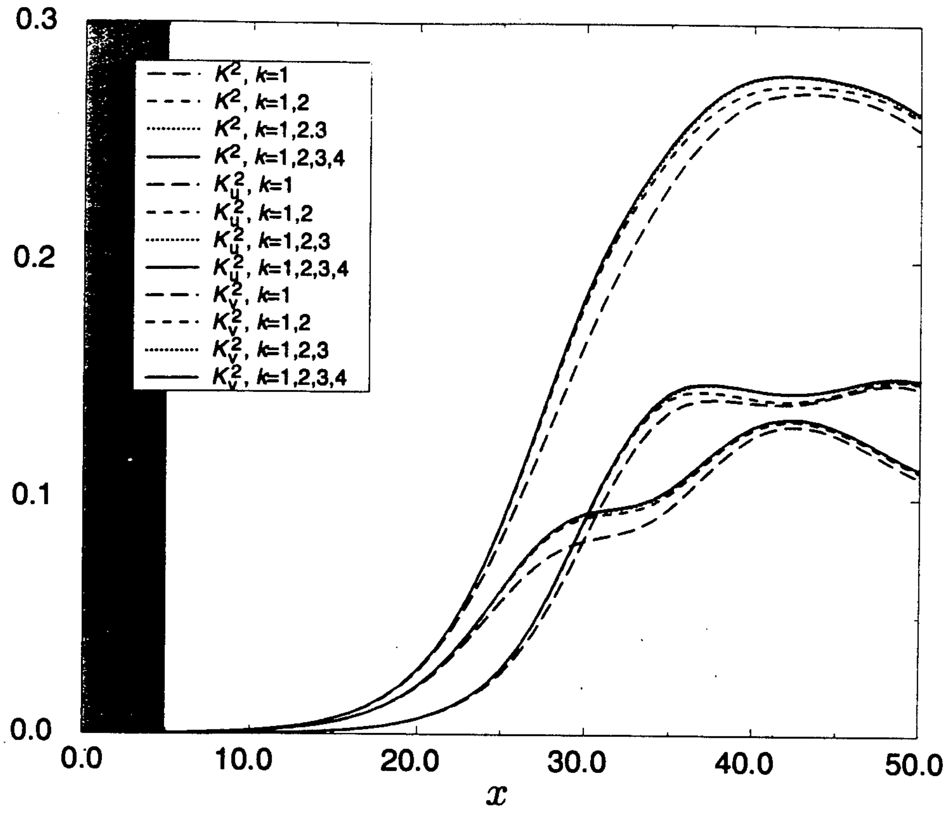

Figure 3.3: Linear plot of instability wave amplitude squared for shear layer SL1, broken down by component and Fourier mode.

the components suggests that this behavior arises from an energy exchange between different velocity components of the nonlinear instability wave.

3.2.2 Other free-shear layer results

We next compare the three shear layers (SL1 through SL3) in more detail. As one can deduce from Figure 3.1, the primary effect of reducing the inflow forcing level is that of delaying the onset of saturation farther downstream. This notion is important because one may modify the shear layer amplitude at a point of interest (*e.g.* where a

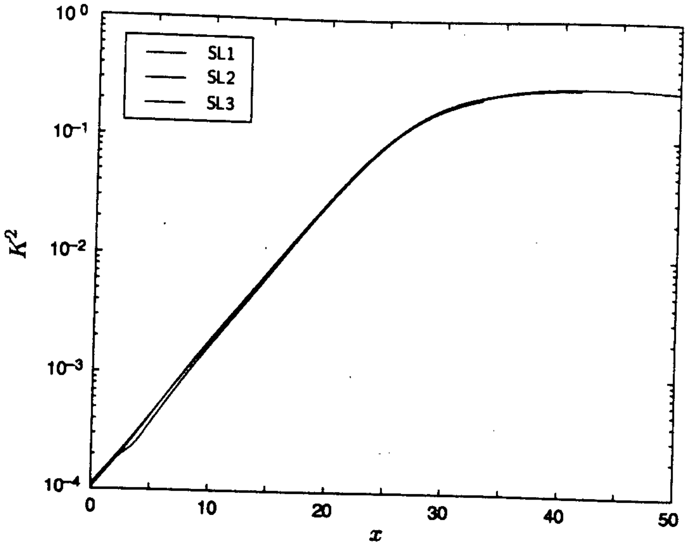

Figure 3.4: Comparison of instability wave amplitude from different shear layer cases after shifting x by 0 (SL1), 8.5 (SL2), and 17.0 (SL3). Note that the dip in SL1 (blue) case is due to inflow sponge.

shock interacts) either by changing the inflow forcing level, so as to modify the entire shear layer, or by moving the point of interest to the position of the desired amplitude without modifying the forcing level. This property will be exploited in Chapter 5.

Were the shear layer to grow as predicted by linear stability theory, that is, based on the inflow profile, a factor of 10 reduction in the inflow forcing level would be equivalent to shifting the shear layer downstream by $\Delta L/\delta = 15.34$. However, because of shear layer spreading due to viscous diffusion, the growth rate decreases with streamwise distance. The actual streamwise shift is approximately $\Delta L/\delta = 17.0$. Using this measured shift, we superimpose the instability wave amplitude of the three shear layers K^2, as shown in Figures 3.4 and 3.5. The amplitudes agree well over the entire range, with a small shortfall near the maximum values for the more weakly forced shear layers. We attribute this discrepancy again to viscous diffusion within the shear layer. The more weakly forced shear layers saturate farther downstream and therefore are subject to the viscous spreading of the shear layer over a greater streamwise distance.

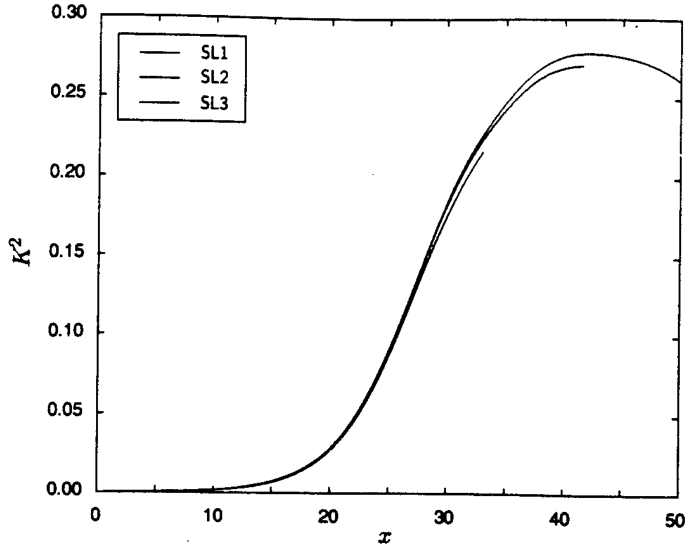

Figure 3.5: Comparison of instability wave amplitude from different shear layer cases after shifting x by 0 (SL1), 8.5 (SL2), and 17.0 (SL3).

In Figure 3.6 we monitor shear layer growth rate among the three cases. We evaluate growth rate by using the derivative of the logarithm of instability wave amplitude K with respect to streamwise coordinate. We observe that for much of the inflow sponge, the growth rate falls below the theoretical target of $-\alpha_i = 0.15015$, then recovers near the exit of the sponge. Note that the sponge width for SL3 is twice that of SL1 and SL2. There is evidence that we underestimated the viscous spreading rate in the inflow sponge reference solution. These discrepancies are however not significant for the development of the shear layer; further, the present studies rely on direct measures of instability wave amplitude, are therefore not sensitive to small departures from theoretical development. Beyond the sponge, the reduction in growth rate observed in Figure 3.6 is attributed to the viscous thickening of the shear layer, followed by the further reduction associated with shear layer growth and saturation due to vortex roll-up. As with instability wave amplitude, we verify that shear layer growth rate is insensitive to our choice of grid resolution and filter coefficients in Appendix B.

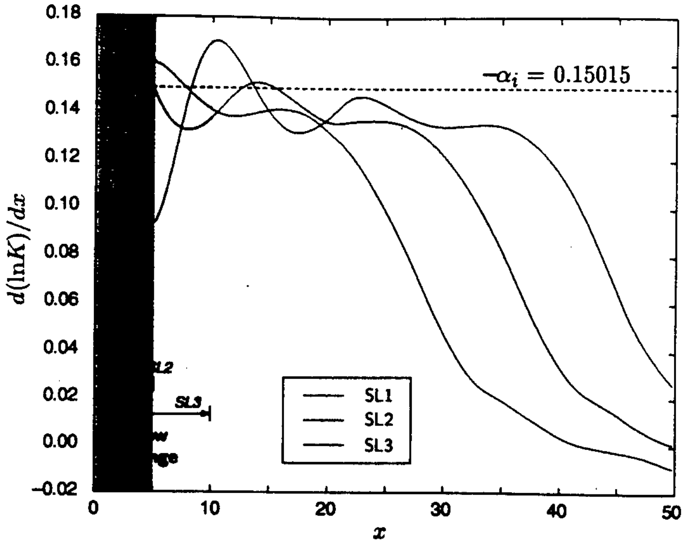

Figure 3.6: Growth rate of instability wave amplitude K compared to theoretical growth rate $-\alpha_i$ obtained from linear stability analysis of inflow profile.

Finally we document the shear layer width, in terms of mean vorticity thickness, as function of streamwise coordinate (Figure 3.7). We note the three distinct regions of growth: a weak growth due viscous diffusion, the rapid growth due to nonlinear instability waves, and saturation. The fully saturated layer has an effective width four times that the weakly disturbed shear layer. Much of the shock-instability wave interaction we consider in later chapters occurs in this region.

3.3 Parameters

To clarify the presentation of the results in the following sections, we summarize all parameters at this point. The Mach number of the high speed stream, which approximates the jet below the shear layer (Figure 1.9), is denoted M. The Mach number of the low speed stream is essentially zero. The Reynolds number Re is based on the initial vorticity thickness δ of the shear layer and the velocity U_1 in the high speed stream. The pressure rise across the incident shock or compression wave is Δp, and we normalize this by the mean inflow pressure p_∞. The width of the

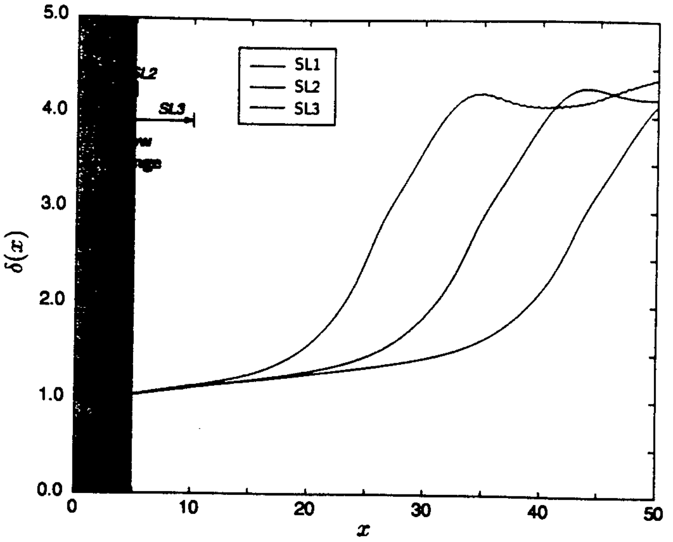

Figure 3.7: Mean vorticity thickness of SL1, SL2, and SL3 shear layers.

shock or compression wave profile, w, is based on the distance between the points at which the pressure departure from its asymptotic values decreases to 1% of Δp. The compression wave profile we impose is based on the hyperbolic tangent function. p' is the amplitude of the radiated acoustic wave. Two relevant angles are the shear layer mean deflection angle ϕ (Figure 3.8) and the observer angle θ (Figure 1.9). Both are measured counter-clockwise from the downstream direction about the point at which the mean center-line of the shock or compression wave meets the sonic line of the mean shear layer. This point coincides approximately with the "acoustic source". r refers to the radial distance from this location, and we normalize it by the acoustic wavelength λ.

3.4 Shock Shear-layer Interaction

In this section we establish the basic behavior of the shock shear-layer instability wave interaction and the resultant acoustic field. Only a single set of operating conditions for the shock is considered due to the computational expense associated with shock capturing. The cases here make use of a "real" shock in the sense that the

cases	*wave type*	*shear layer*	$\Delta p/p_\infty$	w/δ	ϕ
A1	shock	SL0	0.25	ENO	10°
A2	shock	SL1	0.25	ENO	10°
B1	weak compression	SL1	0.05	2	2°
B2	weak compression	SL1	0.10	2	4°
B3	weak compression	SL1	0.05	4	2°
B4	weak compression	SL1	0.05	8	2°
C1	weak compression	SL2	0.05	2	2°
D1	weak compression	SL3	0.05	2	2°

Table 3.4: Summary of cases reported. "ENO" indicates use of shock capturing. Other parameters are defined is Section 3.3

imposed shock is of significant pressure rise (25% above the mean) and of a thickness (less than $\delta/2$) that requires the use of a shock-capturing scheme for the numerical solution to remain stable. These cases were run with the ENO shock-capturing treatment activated. Although the ENO scheme is applied zonally to a rectangular region containing little more than the oblique shock, its application was found to increase the computational expense significantly. Furthermore, the scheme was found to produce spurious oscillations of the order of 1% of the pressure jump. These disturbances where found to convect downstream with the flow. The recent work of Lee and Zhong [19] corroborates our observed deficiencies with the ENO scheme. For these reasons and due to accuracy concerns regarding the acoustic field outside the shock-capturing zone, the number of runs using the shock were limited. These cases therefore serve as a reference for establishing the relevance of the later cases, in which we substitute the shock with weakened compression waves with broadened profiles.

3.4.1 Interaction of an Oblique Shock with Steady Shear Layer

As anticipated in Section 2.5, the introduction of an oblique shock results in the deflection of the shear layer in the direction away from the high speed stream. An example of this phenomenon is shown in Figure 3.8, wherein a steady shear layer at the standard conditions of $M = 1.2$ is subjected to an oblique shock. The pressure

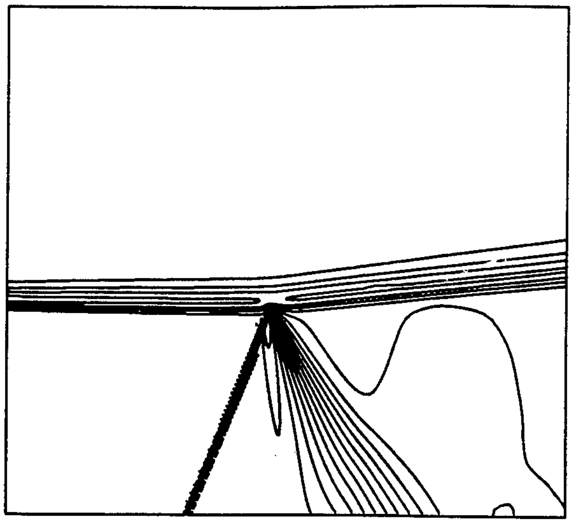

Figure 3.8: Deflection of unforced shear layer by incident shock and reflected expansion. Shown in contours of density. Deflection angle $\phi = 10°$. The distorted contour in the reflected expansion wave is due to bottom boundary conditions (damping sponge, $\sigma_0 = 5$, sponge width $= 3\delta$).

rise across the shock is 25% above the ambient pressure, corresponding to a normal Mach number of 1.1. The shock meets the shear layer and reflects as a Prandtl-Meyer expansion fan, which is absorbed by the damping sponge boundary zone along the lower edge of the domain. The resultant deflection turns the shear layer approximately 10° from its undisturbed position. Because the flow above the shear layer is quiescent, the deflection has only a small impact on the pressure field there. However, the deflection does impact pressure disturbances associated with instability waves.

3.4.2 Shock Evolution and Acoustic Wave Generation

The results described here correspond to the flow conditions given by Case A1 in Table 3.4. To illustrate the overall interaction and sound generation process, we plot the dilatation and vorticity fields of the flow in Figure 3.9 over one instability wave oscillation.

The shear layer, as indicated by the green contour lines of vorticity, is forced upstream of the left edge of the visualized region. Instability waves grow and convect

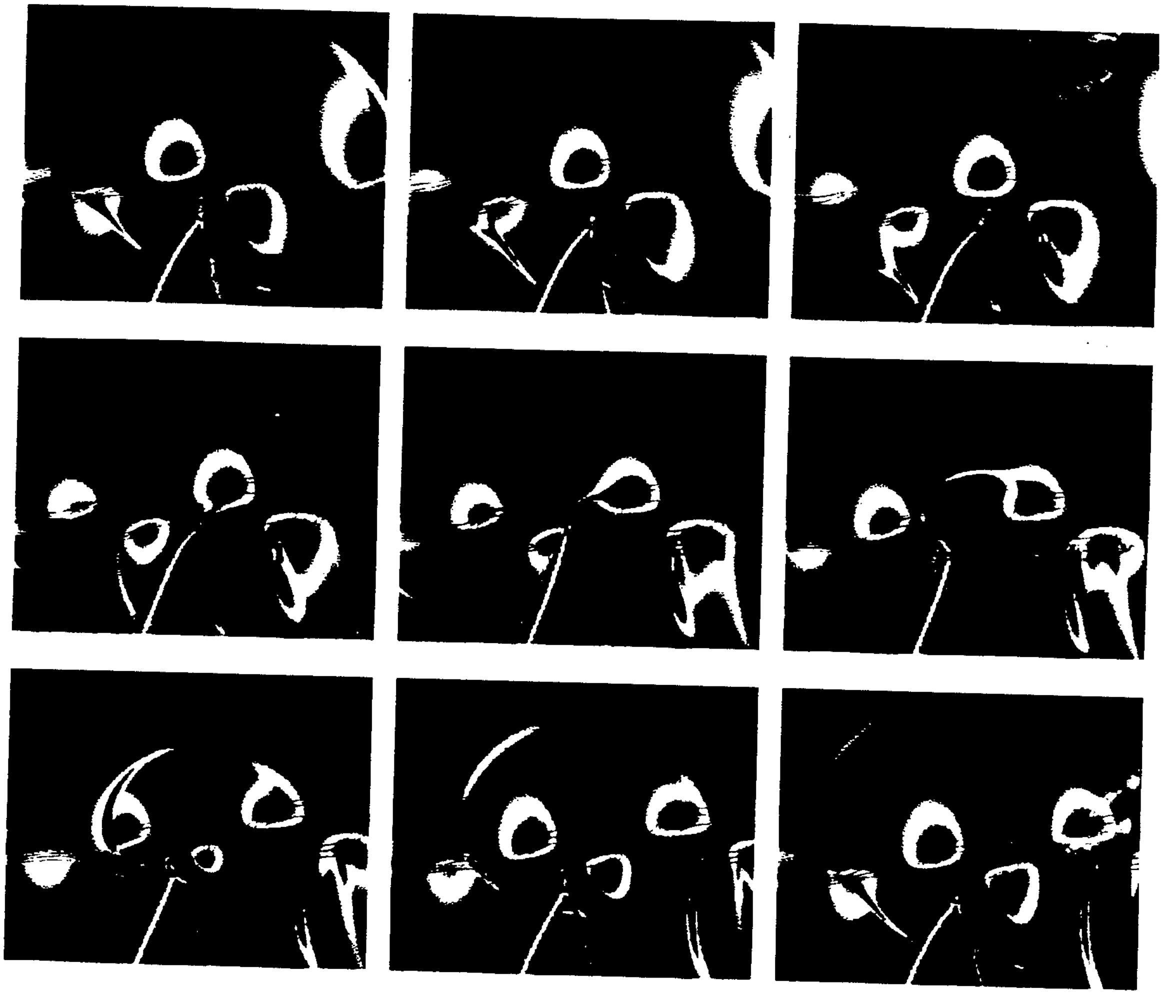

Figure 3.9: Shear layer instability wave / shock interaction and the acoustic wave generation for Case A1, shown at intervals of $t/T_{oscillation} = 1/8$. Smooth colors are dilatation (from compression : very strong—yellow, strong—red, weak—white; to expansion: weak—black, strong—blue), superimposed by contours of vorticity $(\Delta\omega/(U_\infty/\delta) = 2 \times 10^{-1})$. $M = 1.2$, $M_{normal} = 1.1$.

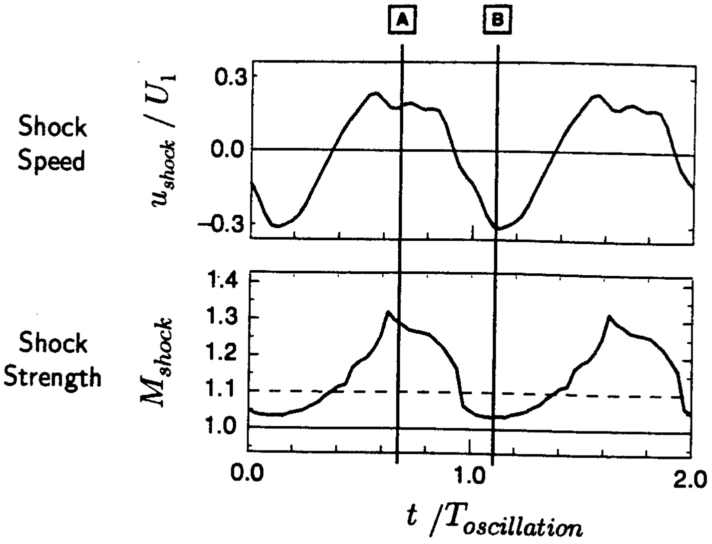

Figure 3.10: Time evolution of Shock in Case A1. Time traces indicate speed of shock in streamwise direction and strength of shock as sampled at $y/\delta = -2.4$. Local shock strength M_{shock} is based pressure ratio across shock. - - - - $M_{shock} = 1.1$ prescribed mean shock strength ⇔ $\Delta p/p_{\infty} = 0.25$. Spatial variation in Figure 3.11 occur at time slices $\boxed{\text{A}}$ and $\boxed{\text{B}}$.

downstream to the right, evolving into vortices. The oblique shock, indicated in yellow in the dilatation field, oscillates as the instability waves pass. A compression front of a cylindrical acoustic wave is emitted from this interaction site during each period. The shock is deformed near its reflection point, or forms a "tip", as the vortices pass, such that the tip follows a counter-clockwise circular path (*i.e.*, the same sense of rotation as that of the vortices).

The speed, orientation, and strength of the shock vary through this cycle, as illustrated in Figure 3.10 and Figure 3.11. To obtain the time evolution (Figure 3.10) we locate the pressure jump associated with the shock and track its x-component of velocity at fixed y. The spatial variation plots (Figure 3.11) show shock strength as a function of vertical coordinate y. The pressure ratio is converted to equivalent normal Mach number based on the Rankine-Hugoniot shock jump conditions. We find that the shock translation rate is greater as the tip travels upstream through the braid between the vortices and less as it travels downstream through the vortex. The

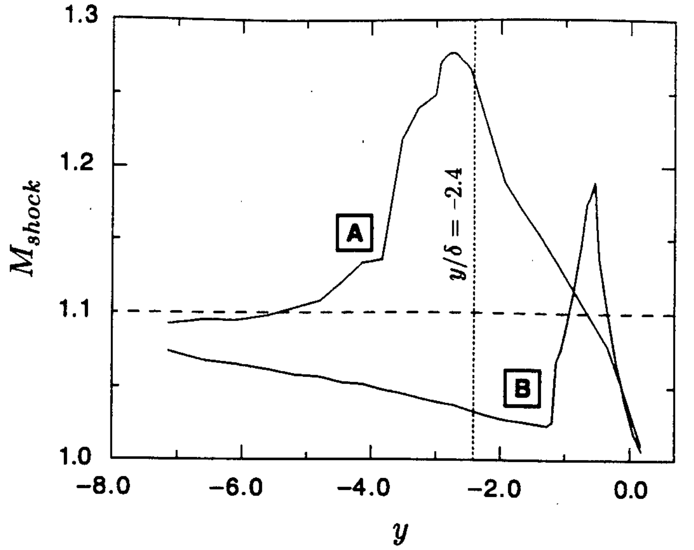

Figure 3.11: Spatial evolution of Shock in Case A1. Spatial variation of shock strength follows shock at time slices $\boxed{\text{A}}$, $\boxed{\text{B}}$, as shown in Figure 3.10. Acoustic wave is released near time $\boxed{\text{B}}$.

compression associated with the acoustic wave is found to be generated during the upstream travel of the shock. The compression region of the acoustic wave profile is substantially shorter than the acoustic wavelength. This result is seen in the narrow dilatation distributions in the acoustic waves shown in Figure 3.9.

There other wave-like features which appear only inside the supersonic flow, such as the extension of the acoustic pulse back into the supersonic flow upstream of the shock. Another is a structure which forms when a region of compression convecting with the vortex passes through the shock and is amplified. The latter feature subsequently evolves into acoustic waves oriented upstream but, in net, traveling downstream in the supersonic flow. It resembles the wave-like structures propagating downstream inside a screeching jet observed by Suda *et al.* [61].

In Figure 3.12 we show Case A2 visualization detail of interaction between the SL1 shear layer (forced at one half the most unstable frequency) and a $M_{normal} = 1.1$ shock. We moved the point of interaction downstream to $x/\delta = 40$ to accommodate the reduced instability wave growth rate. The increased instability wave size results

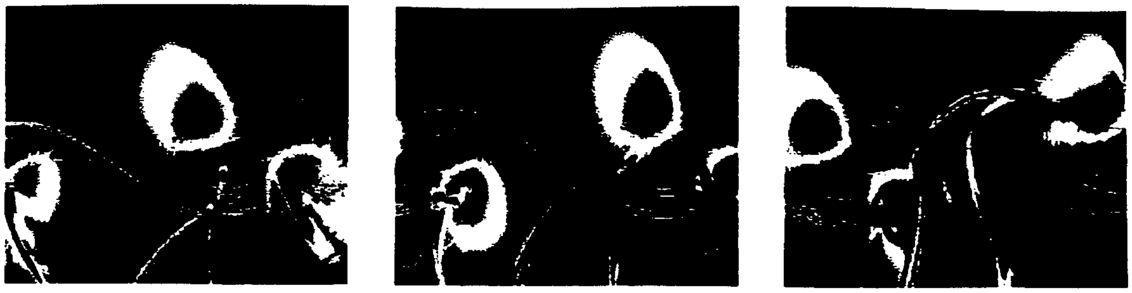

$t/T = 0/32$ $t/T = 6/32$ $t/T = 12/32$

Figure 3.12: Visualization of Case A2; dilatation field superimposed by contours of vorticity.

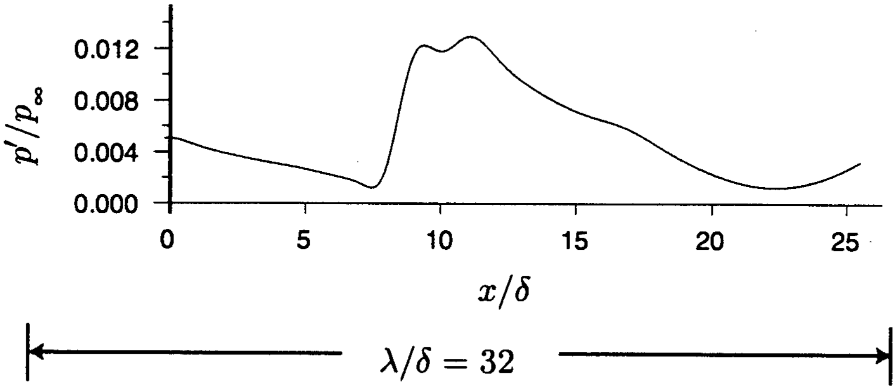

Figure 3.13: Sampling of acoustic field at $r/\lambda = 1.5$, $\theta = 170°$.

in larger excursions in the shock motion. At $t/T = 0$, the incident shock (yellow) and a reflected *compression* wave (red) appear to meet at a triple point with a shock that extends into the vortex. The reflected expansion fan is visible in blue to the right of the reflected compression wave. Both the incident shock and its reflection appear to penetrate the shear layer in the braid region ($t/T = 6/32$), eventually to escape together (at $t/T = 12/32$). The acoustic field sample at 1.5 acoustic wavelengths upstream from the source is shown in Figure 3.13. The acoustic trace exhibits a characteristically sharp compression, followed by a slow decay. From this measurement, we find a pressure amplitude of approximately $p'/p_\infty = 5 \times 10^{-3}$ (or SPL of 140 dB).

3.4.3 Resolution Considerations and the Compression Wave

The instability-wave shock interaction results of Cases A1 and A2 readily capture the intrinsic phenomenon of screech-type sound generation. However, the compact wavefront of the acoustic field was found to be insufficiently resolved. The numerical dissipation which arises from this under-resolution would lead one to underpredict the acoustic levels. The sound pressure level reported above therefore represents a conservatively low estimate. To obtain satisfactory acoustic measurements, we recognized that we would be forced to either dramatically increase grid resolution in the far field to permit adequate resolution, or make use of ENO shock capturing over the entire domain. Both options were rejected on the basis of computational expense.

To address this problems in subsequent simulations, we chose instead to replace the oblique shock with oblique compression waves. The profile of the incident compression wave is distributed over a wider region so as to be nearly isentropic, and its amplitude is much reduced from that of the shock. The radiated acoustic waves generated in these later cases (B1–B4, C1, D1) have broadened, resolvable profiles.

3.4.4 Acoustic Measurements

The pressure field typical of a computation such as that described above is shown in Figure 3.14. Extracting the acoustic pressure amplitude cannot be accomplished at every point in the field due to interference with fluctuations in pressure associated with the instability waves. The sound pressure level measurement given above for Case A2 was sampled just inside the inflow to minimize this contamination. The strategy we utilize for extracting the sound field requires us to compute two forced shear layers in which the forcing is synchronized: one case contains the incident shock wave and the other does not. The acoustic fluctuations are then obtained by subtracting the dependent field variable of choice between the two fields. An example of the acoustic extraction is illustrated in Figure 3.15. The method is attractive because in addition to eliminating the hydrodynamic fluctuations common to both fields, the method in theory permits one to eliminate sound sources which are common to both fields, thereby isolating the sound due to the interaction. The method is not faultless,

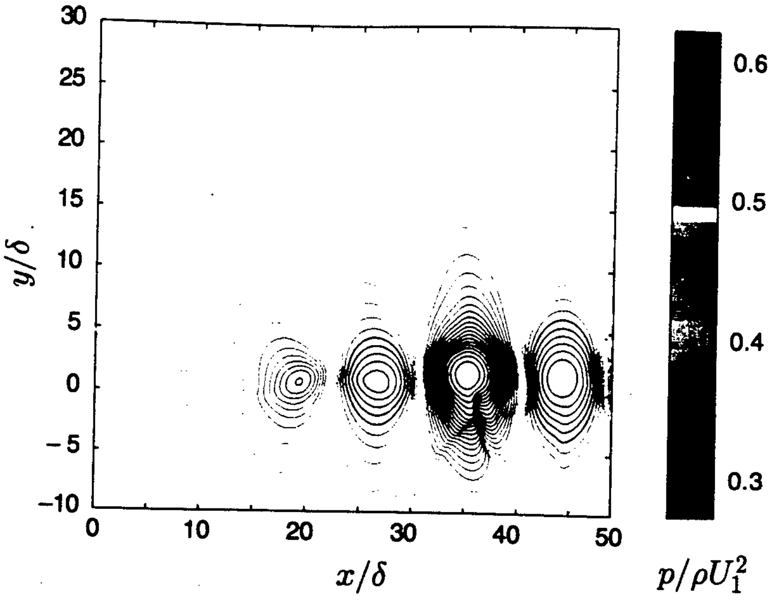

Figure 3.14: Pressure field from Case B1.

as the deflection of the shear layer in the presence of the shock or compression wave distorts the field so as to cause some degree of misalignment and imperfect cancellation between the fields. This effect is most severe downstream of the interaction site; as we are most interested in the upstream directivity of the sound generation, useful results can still be obtained.

3.5 Weak Compression Wave Interaction

In the following we present the results of *weak compression wave* – vortex interactions, cases for which we have confidence in the numerical accuracy of the acoustic field. We investigate the dependence of the acoustic field on variations in compression wave amplitude, compression wave profile width, and instability wave forcing amplitude as outlined in Table 3.4. Although forcing frequency remains fixed through these cases, its value is half that used in Case A1. At this lower frequency, we found that the onset of vortex pairing downstream of the interaction site is suppressed.

The computations use a mesh of 900 by 290 points. The mesh is uniform in the streamwise direction, where the grid spacing $\Delta x/\delta = 0.10$. In the transverse

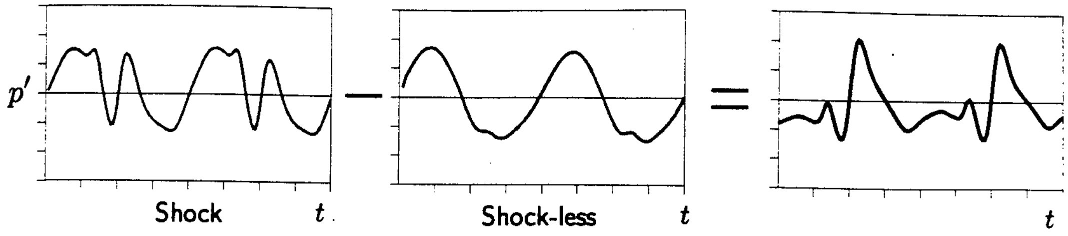

Figure 3.15: Subtraction technique for extracting acoustic field. Method involves subtracting pressure field of shockless shear layer with shear layer with shock. Raw pressure traces of two shear layers, and their resultant difference. Sampled from Case B1 at $r/\lambda = 1.3$, $\theta = 135°$.

direction, the grid spacing $\Delta y/\delta$, which is non-uniform, extends from 0.067 in the region 4δ on either side of the center-line of the shear layer to 0.50 near the upper boundary and 0.13 near the lower boundary. The computational domain (excluding boundary treatment regions) extends 50 vorticity thicknesses δ in the streamwise direction, and 35δ above the shear layer center-line and 10δ below. The compression wave profile we impose is based on the hyperbolic tangent function.

3.5.1 Overall Interaction Behavior for Compression Wave Cases

The behavior of the weak compression wave – vortex interaction is found to closely follow the shock-vortex interaction. In Figure 3.16 from Case B1, we show the weak compression wave counterpart to Figure 3.9 of Case A1 (or A2). Note, however, that the field-subtraction method is now employed to bring out the dilatation field associated with the generated sound waves. This is necessary to visualize the weaker acoustic waves amongst the dilatation field convecting with the vortices.

As the instability wave vortices pass over it, the oblique compression wave (visualized in red and yellow at the bottom of each plot) undergoes a periodic deformation that resembles, both in extent of oscillation and phase, the shock motion for case A1. The visualization also shows, however, that during each period, circular acoustic waves from two different points of origin are produced such that their wave fronts coincide in the upstream direction. The lagging wave front of smaller radius is the primary acoustic wave of interest, as it is generated by the oblique compression wave with the instability wave vortex. The leading wave front of larger radius is produced farther downstream by a downstream traveling compression wave in the previous cycle of forcing. This secondary wave is weaker, as will be shown in results below. The constructive interference in the upstream direction is regarded as a coincidence and shall not be confused with the constructive interference of the phased sources that arise in full screech.

The traveling compression wave is observed in all weak compression wave cases at large forcing(B1–B4), although the phase of the secondary sound wave appears to vary with compression amplitude. This traveling compression wave is also observed in Case A1, but the secondary acoustic wave is not. In that case, however, the traveling wave is much weaker than the shock, whereas in B1-B4 it is of the same order of magnitude.

3.5.2 Directivity

Next we consider the directivity of the radiated sound field. For Case B1, Figure 3.17 illustrates the variation of the temporal profile of the acoustic pressure perturbation at various angles along an arc centered about the source location. In Figure 3.18 we show detail of the temporal profiles across the shear layer. The radius of this arc is equal to an acoustic wavelength λ, or 32δ. The field differencing method for extracting the acoustic field as described above is applied to the pressure variable. In terms of the acoustic pressure amplitude, the pressure rise across the short compression region p'/p_∞ is consistently about 0.002 (0.2%) for most of the angles shown. Hence, within the forward arc, the directivity of the acoustic field is found to be somewhat uniform, except for a small decay across the shear layer itself. The shift in the profile peak at angles below the shear layer result from the refraction of the acoustic wave by the mean (supersonic) flow. However, there is clearly no decay to zero, as would be suggested by the model of Kerschen and Cain [16]. Indeed, the acoustic waves are found to easily propagate into the supersonic shear layer, behaving as oblique Mach

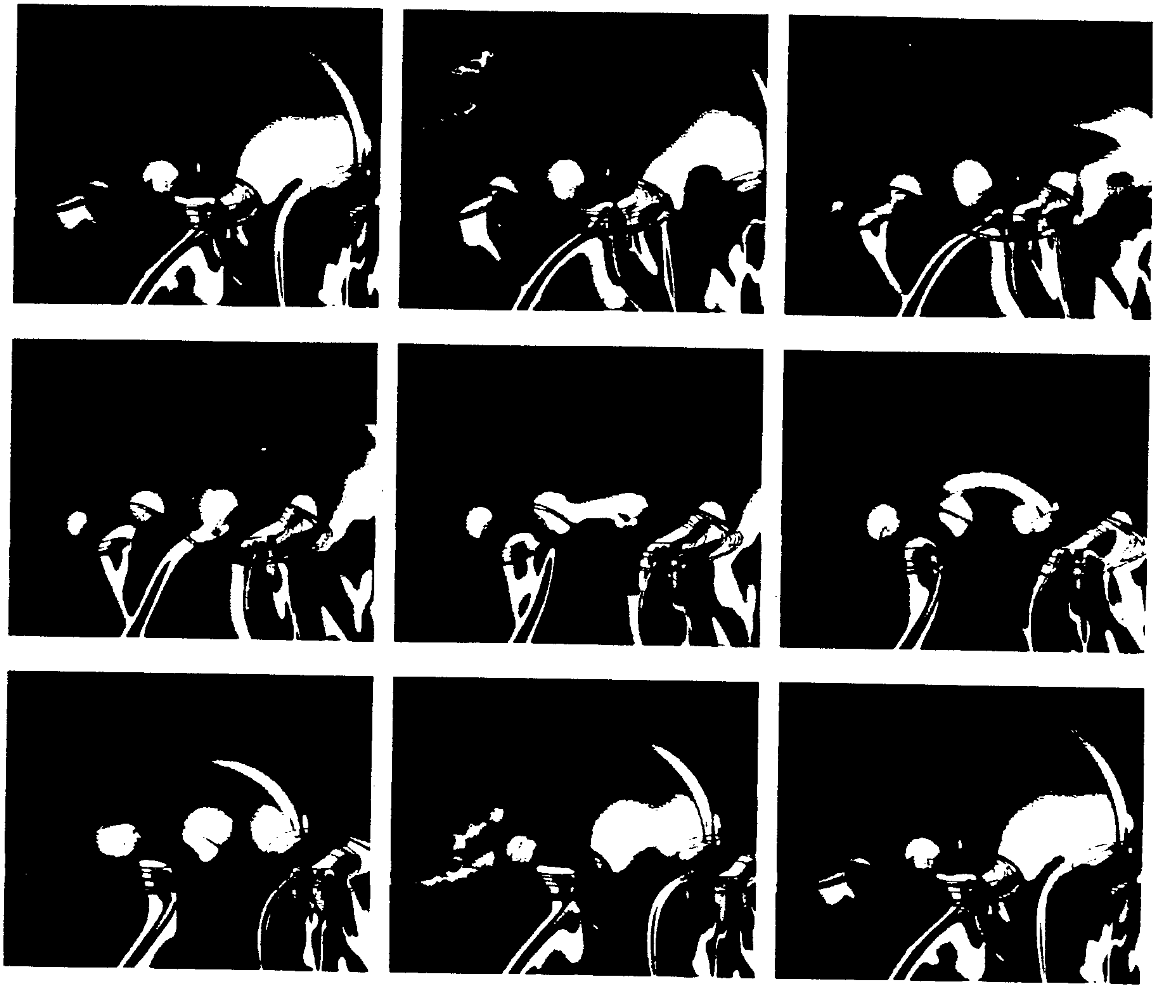

Figure 3.16: Shear layer instability wave / weak compression wave interaction and acoustic wave generation for Case B1, shown at intervals of $t/T_{oscillation} = 1/8$. Smooth colors are fluctuations in dilatation (from compression: very strong—yellow, strong—red, weak—white; to expansion: weak—black, strong—blue), superimposed by contours of vorticity ($\Delta\omega/(U_\infty/\delta) = 2 \times 10^{-1}$). The fluctuating dilatation field was obtained using the field subtraction technique. A secondary wave can be seen leading the primary acoustic wave.

waves generated by an upstream traveling disturbance. Such upstream propagating acoustic waves are readily apparent in still images (*e.g.* Figure 3.22, left column) and in animations based on these simulation results. The slight decay may be attributable to local distortion by the mean shear flow. The distortion of the profile near $\theta = 90°$ is attributed to a misalignment of "hydrodynamic" fields in the field subtraction method. The misalignment renders the acoustic amplitude to be less reliable in the downstream arc.

We next consider details of the acoustic profiles directly and their dependence on the compression wave parameters. (In our discussion here we freely interchange the use of temporal and spatial profiles, given that the acoustic waves travel at a fixed speed and that their decay ($\sim r^{-1/2}$) is small over the length scales we are considering.) The profile of the acoustic wave is consistent with the profiles observed in the shock interaction cases: compression occurs over a short time compared to the acoustic wave-length, whereas expansion occurs over a somewhat longer time.

3.5.3 Variation with compression wave amplitude

The effect of varying the compression wave amplitude is illustrated in time traces of the acoustic pressure fluctuation. As shown in Figure 3.19, where we compare Case B1 to Case B2 at two observer angles θ, a doubling in the compression wave amplitude doubles the acoustic amplitude while retaining the profile shape of the primary acoustic wave. The notion that profile shape is preserved is further reinforced when we scale the acoustic amplitude p' with the compression wave amplitude Δp, as shown in Figure 3.20. The secondary wave peaks are not in phase. Visualization studies of Case B2, which are not presented here, show that the traveling compression wave responsible for producing the secondary wave is farther upstream than in Cases B1 and B3 when the vortex passes. This results in the earlier emission observed in B2. The reason for the position of the traveling wave to vary with the strength of the prescribed wave is not understood at this point.

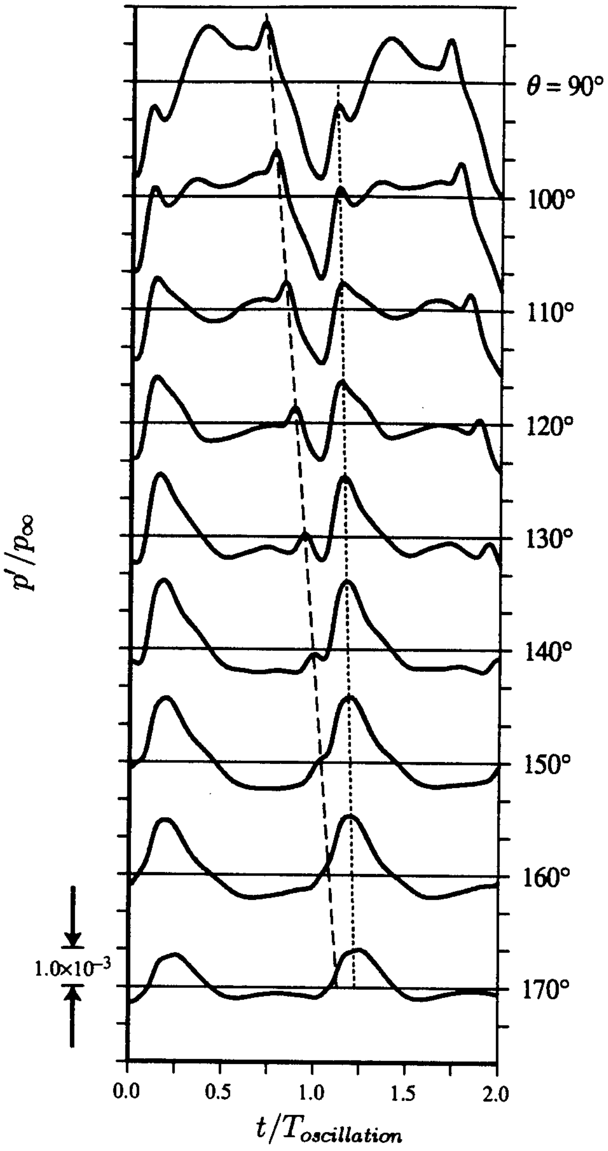

Figure 3.17: Acoustic fluctuation trace at various observation angles θ, $r/\lambda = 1.0$ for Case B1. - - - - Peak of primary acoustic wave, produced by oblique compression wave – vortex interaction. — — Peak of secondary acoustic wave, produced by traveling compression wave – vortex interaction. Amplitude of primary wave is determined from change in height of sharp compression immediately preceding primary wave peak.

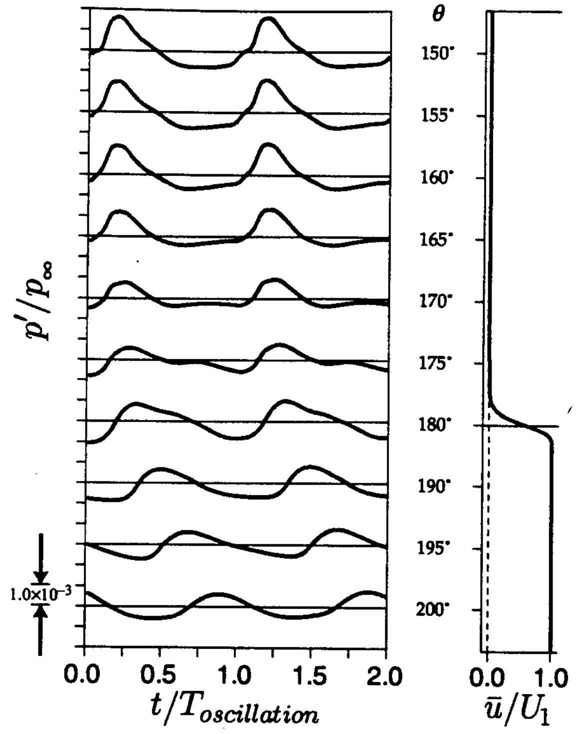

Figure 3.18: Acoustic fluctuation trace at various observation angles θ, $r/\lambda = 1.0$ for Case B1. Mean streamwise velocity profile is given at right.

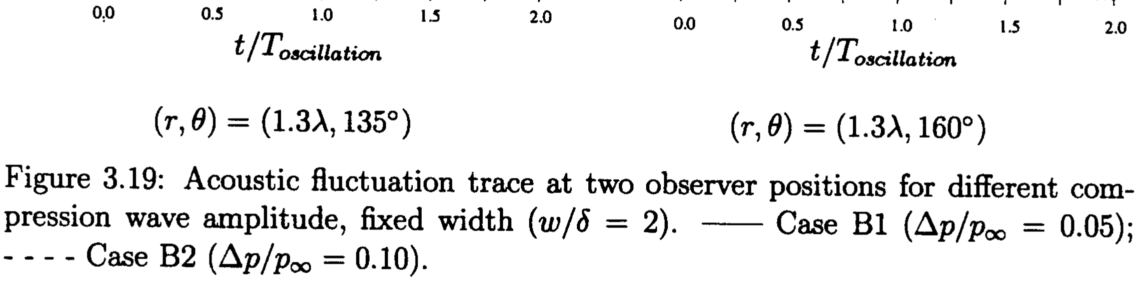

$(r,\theta) = (1.3\lambda, 135^\circ)$ $(r,\theta) = (1.3\lambda, 160^\circ)$

Figure 3.19: Acoustic fluctuation trace at two observer positions for different compression wave amplitude, fixed width ($w/\delta = 2$). —— Case B1 ($\Delta p/p_\infty = 0.05$); - - - - Case B2 ($\Delta p/p_\infty = 0.10$).

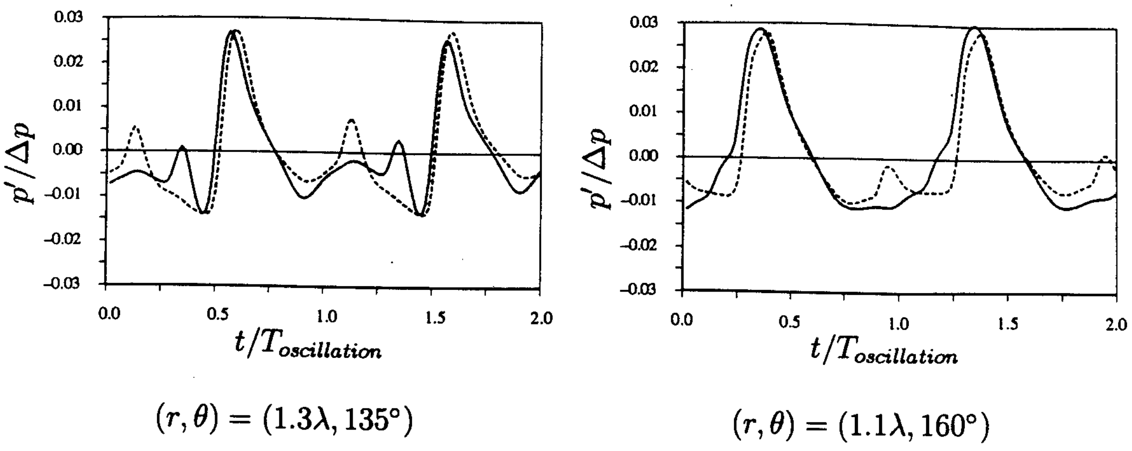

$(r, \theta) = (1.3\lambda, 135°)$ $(r, \theta) = (1.1\lambda, 160°)$

Figure 3.20: Same as Figure 3.19 except acoustic amplitude is renormalized to respective compression wave amplitudes. —— Case B1 ($\Delta p/p_\infty = 0.05$); - - - - Case B2 ($\Delta p/p_\infty = 0.10$).

3.5.4 Variation with compression wave width

The effect of increasing the compression wave width on the acoustic wave-form is explored through a comparison among cases B1 and B3, and B4. The parameter w is set to 2δ, 4δ, and 8δ, respectively. The purpose of investigating the dependence of the acoustic field on compression wave width is to determine the role compression wave gradients and spatial extent of the profile. The width of the compression wave imposed in Case B4 is 40% of the instability wave length (or, alternatively, 25% of the acoustic wavelength) and therefore non-compact. In Figure 3.21 we show time traces of acoustic pressure fluctuation over two periods as observed at two locations upstream of the compression-wave – instability-wave interaction site. Contributions from both primary and secondary sources are present. The peak value of the primary acoustic wave decreases with increased compression wave width, as shown in the first plot in Figure 3.21. However, the location of the peak does not shift with increased width.

One should note that although the amplitude of the incident compression wave does not change with compression wave width, the region of overlap between the compression wave and the reflected expansion wave (region 1-2-3 in Figure 2.13) does increase with width. The lower extent of this region of overlap (point G in Figure 2.13)

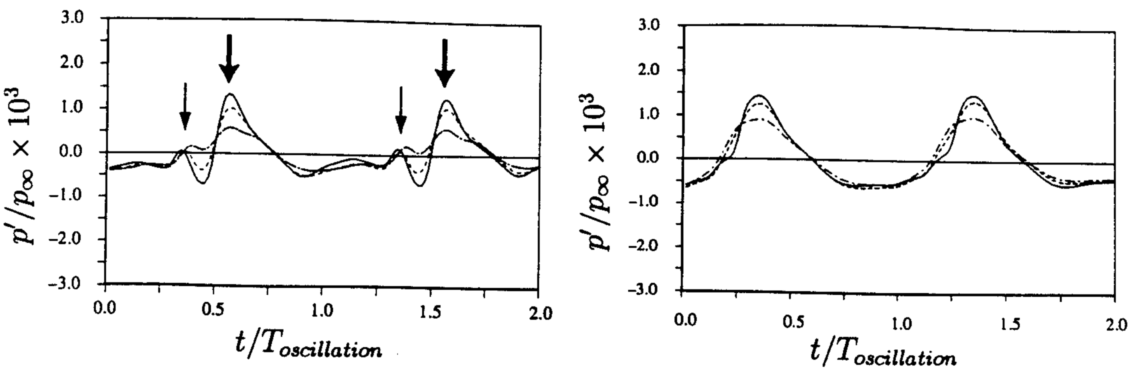

$(r,\theta) = (1.3\lambda, 135°)$ $(r,\theta) = (1.1\lambda, 160°)$

Figure 3.21: Acoustic fluctuation trace at two observer positions for different compression wave width, fixed amplitude ($\Delta p/p_\infty = 0.05$). —— CASE B1 ($w/\delta = 2$); - - - - CASE B3 ($w/\delta = 4$); — - — CASE B4 ($w/\delta = 8$). Thick arrow: primary acoustic wave; thin arrow: secondary acoustic wave. Primary and secondary waves have coalesced in second plot.

moves from approximately $y/\delta = -0.75$ to -3.0 as the width changes from $w/\delta = 2$ to 8 in the steady case. Hence, the nearest approach of the full scale of the incident compression wave moves away from the centerline of the shear layer as the width of the compression wave is increased.

3.5.5 Variation with instability wave amplitude

As mentioned above, we have found previously that the acoustic amplitude scales directly with the pressure rise of the compression wave. Theoretical analyses such as [16] and [62] take the approach that the acoustic field arises from the product of fluctuations due to the instability waves and the compression wave. Such an approach is consistent with a direct scaling with compression wave amplitude. The approach would also suggest a linear dependence on instability wave amplitude. To test this hypothesis, we carried out the series of cases B1, C1, and D1, over which the shear-layer forcing amplitude was reduced by an order of magnitude (see Tables 3.3 and 3.4).

Although in all three cases the location of the compression-wave instability-wave interaction site is the same, at approximately $x/\delta = 40$ from the domain inflow, the development of the shear layer is different. In Case B1 (shear layer SL1), the interaction site is located downstream of the point at which the instability wave amplitude K reaches its maximum value (see Figure 3.1). However, in Case D1 (shear layer SL3), the interaction site lies upstream of this point, though still in the region in which instability wave evolution has become non-linear. Therefore, the instability wave "amplitude" at the interaction site does not decrease by the same amount the inflow forcing is reduced.

The result of this reduction in instability wave amplitude is the apparent elimination of the acoustic emission. Figure 3.22 shows a sequence of visualizations of both Case B1 and Case D1 over one cycle. The region over which the compression wave in Case D1 is perturbed is dramatically reduced; the expansion reflection remains visibly "attached", unlike in Case B1 where the analogous feature is shed downstream during each oscillation. The circular arc of the dominant acoustic wave of Case B1 does not exist in D1. There is a very weak acoustic wave emitted by the flow in D1. However, its origin is far downstream of the interaction site. Its frequency, at the sub-harmonic of the forced frequency, suggests that its generation is associated with the vortex pairing which begins to occur near the domain outflow. We show further detail of the compression wave motion and initial formation of the acoustic compression front (where visible) in Figure 3.23.

The acoustic measurements taken in these flow fields indicate that the dependence of the acoustic amplitude instability wave amplitude is nonlinear. In Figure 3.24 we show acoustic pressure traces sampled at $r/\delta = 1.3$, $\theta = 135°$. Although the trace for the intermediate case C1 retains most of the characteristics observed in the trace for Case B1, namely the sharp compression and gentler expansion, these features are lost in the trace for Case D1. The subharmonic disturbance observed in the visualization is quite evident; only an upper bound for acoustic amplitude can be given for this case. In Figure 3.25 we plot the mean-to-peak amplitude of the acoustic pressure ($\Delta p'$) against the three measures of instability wave amplitude, K, K_u, and K_v. A linear scaling of acoustic amplitude with instability wave amplitude is clearly not observed

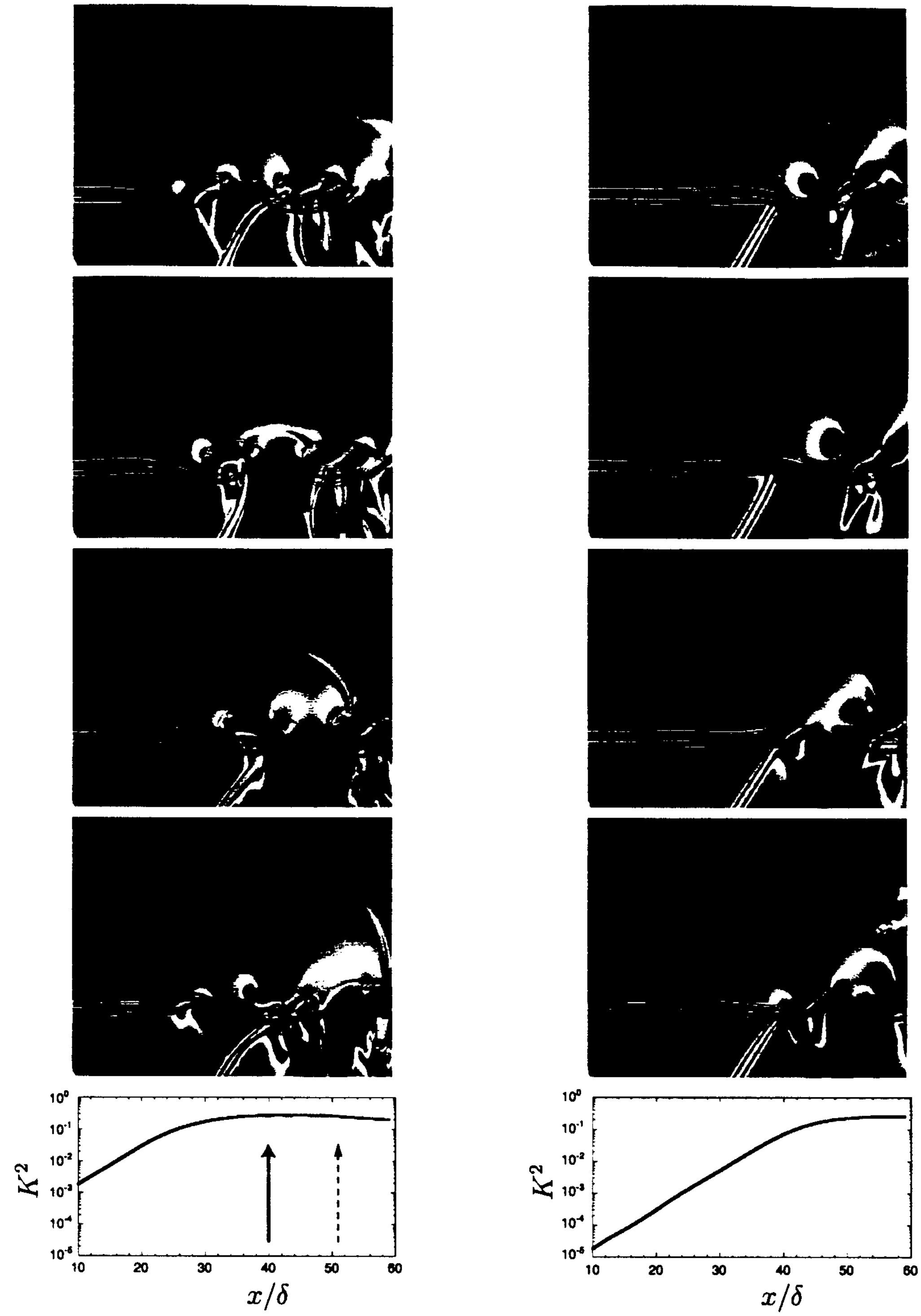

Figure 3.22: Case B1 (left) and Case D1 (right), at intervals of $t/T_{osc} = 1/4$. Colors are dilatation (from compression: very strong—yellow, strong—red, weak—white; to expansion: weak—black, strong—blue), and vorticity ($\Delta\zeta/(u_\infty/\delta) = 2 \times 10^{-1}$). In third frame of Case B1, primary acoustic wave is solid line, secondary is dashed. Solid arrow—primary source; dashed arrow—secondary source .

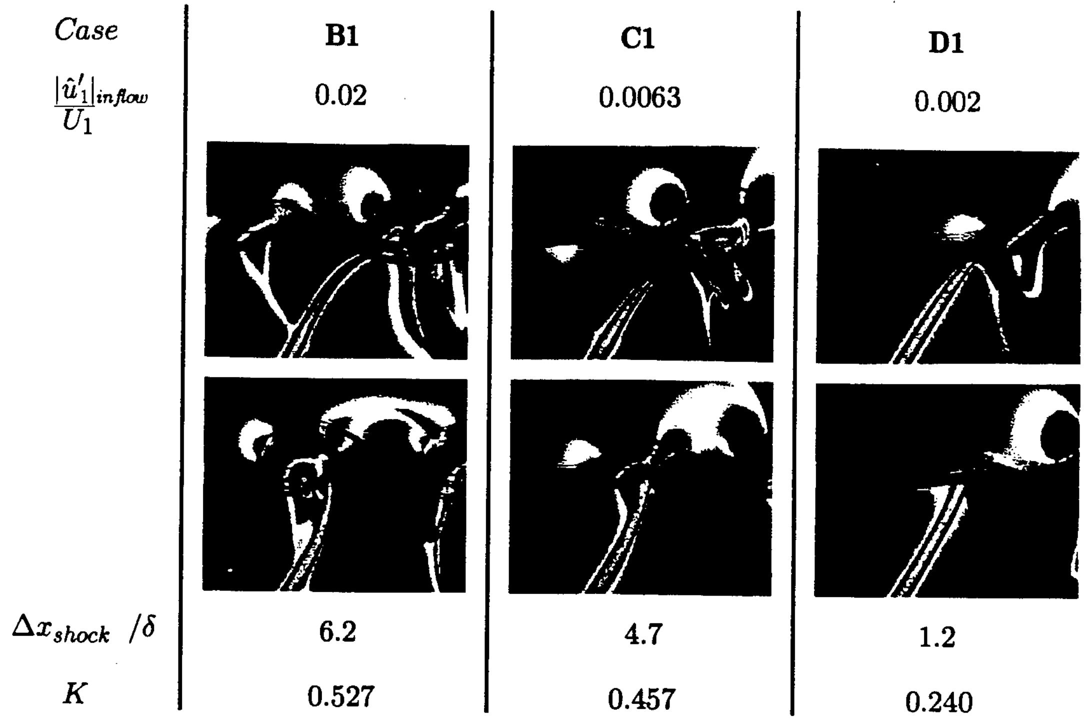

Figure 3.23: Detail of interaction region for Cases B1, C1, and D1. Extent of compression wave motion in the streamwise direction is denoted Δx_{shock}.

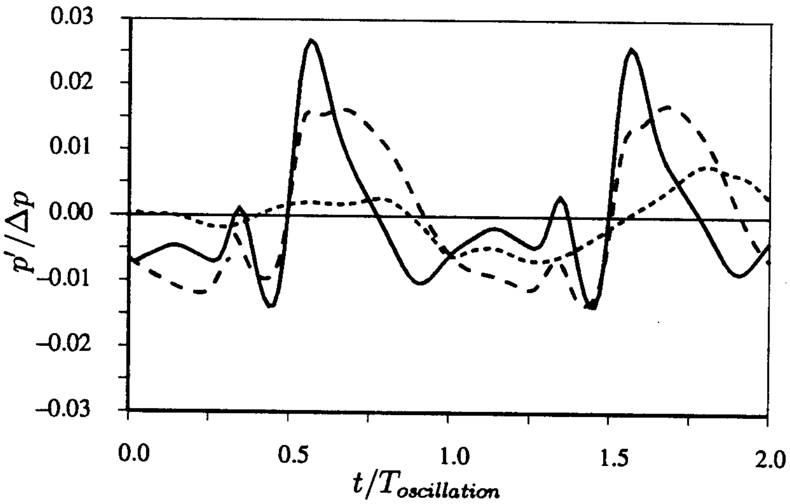

Figure 3.24: Acoustic pressure traces sampled at $r/\lambda = 1.3$, $\theta = 135°$, for Cases B1 (——), C1 (– – –), and D1 (- - - - -).

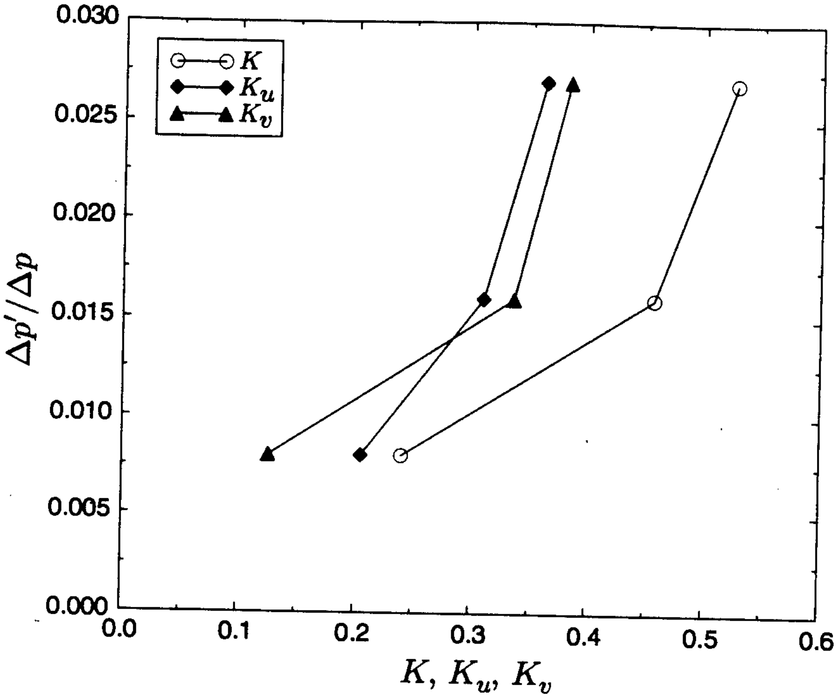

Figure 3.25: Acoustic pressure amplitude (mean to peak acoustic pressure $\Delta p'$ normalized to compression wave amplitude Δp) plotted against instability wave amplitude(s) measured at the interaction site.

at the higher instability wave amplitudes. At the lower amplitude the uncertainty in the acoustic results precludes definite conclusions; however, as the dominant signal in Case D1 has been identified to originate from a location other than the compression-wave instability-wave interaction site, and no other disturbance is identifiable in the visualization, one may conclude that the acoustic signal of interest is significantly weaker than the upper bound of $\Delta p'/\Delta p = 0.008$ given in Figure 3.25.

3.6 Summary of results from direct numerical simulations

In this chapter we have presented the results from numerical simulations of the interaction between shear-layer instability waves and shocks or compression waves. We have shown that in the case of large amplitude instability waves, the passing of the shear-layer vortices imparts large distortions in the shock position. We have shown evidence that the sound generation process is analogous to the leakage of the shock at specific phases in the interaction process, namely, as the shock travels upstream between the vortices. This process is reproduced even for compression waves of significantly reduced strength. Interactions involving weaker compression waves enabled more accurate acoustic measurements to be carried out, where the acoustic field was found to scale directly with compression wave strength. Finally, an investigation into the dependence of acoustic amplitude on instability wave amplitude reveals the first evidence that the relationship between the two is nonlinear. Exploiting the success of the compression wave results, in the following chapter we introduce simplifications to the governing equations in order to study the sound generation process more thoroughly.

Chapter 4

Linearized Euler Computations: Method

4.1 Background

In the previous sections we have discussed the interaction of the shear-layer instability-waves with the oblique compression-wave, and the resulting sound. All components of the flow, namely, the unsteady shear layer, the incident compression-wave, and the acoustic field, were computed together by solving the full Navier-Stokes equations. For sufficiently large instability waves, we have shown that the incident compression-wave and the compression-front of the acoustic wave to be continuous, and have suggested that the sound generation process may be analogous to the propagation of acoustic waves through an unsteady shear layer. To explore this possibility, we consider the propagation of linearized, inviscid disturbances through an unsteady transonic shear layer. This analysis is carried out by solving the Euler equations linearized about an unsteady base-flow.

In this chapter we discuss the derivation and implementation of this linearized approach. We will show in the next chapter that this method reproduces the sound field for weak compression waves interacting with weak or strong instability waves. We will use this method to reveal a number of important dependencies between acoustic amplitude and the instability wave field. Although solutions to the linearized Euler equations have previously been utilized to investigate supersonic jet noise (see for instance Mankbadi *et al.* [25] and Dahl and Morris [3]), those studies involved linearizations which were performed about a steady base flow. The present investigation represents the first use of the Euler equations linearized about an unsteady base flow to obtain jet noise results.

4.2 Equations of Motion

The flow we consider is divided into two components: the base flow and the perturbation field. The base flow is prescribed and is therefore unmodified by the perturbations. Conversely, the evolution of the perturbation field, whose magnitude is assumed to be much smaller than that of the base flow, depends strongly on the base flow. In the context of the instability-wave oblique-shock interaction problem, the unsteady shear layer forms the base flow. The perturbation field is made up of the incident shock (or, more precisely, an incident Mach wave), the acoustic field, and any other inviscid disturbances that results from the interaction.

The physical flow variables are decomposed into the base flow (tilde) and perturbation components (primed) as follows.

$$\rho(\mathbf{x},t) = \tilde{\rho}(\mathbf{x},t) + \epsilon\rho'(\mathbf{x},t) \quad (4.1)$$

$$p(\mathbf{x},t) = \tilde{p}(\mathbf{x},t) + \epsilon p'(\mathbf{x},t) \quad (4.2)$$

$$u_i(\mathbf{x},t) = \tilde{u}_i(\mathbf{x},t) + \epsilon u_i'(\mathbf{x},t) \quad (4.3)$$

$$E_t(\mathbf{x},t) = \tilde{E}_t(\mathbf{x},t) + \epsilon E_t'(\mathbf{x},t) \quad (4.4)$$

$$\tau_{ij}(\mathbf{x},t) = \tilde{\tau}_{ij}(\mathbf{x},t) + \epsilon\tau_{ij}'(\mathbf{x},t) \quad (4.5)$$

where $\epsilon \ll 1$. Note that the base-flow is generally unsteady.

To obtain the linearized equations, we take the following steps. We substitute the full variables into the Navier-Stokes equations. We collect the terms according to their order in the small parameter ϵ. We assume that the base-flow variables alone satisfy the Navier-Stokes equations; as a consequence all $O(1)$ terms can be removed. The terms of $O(\epsilon^2)$ are neglected. The remaining terms are of $O(\epsilon)$. Finally, we observe that for Reynolds numbers of the order we consider ($Re = 1000$), the terms of $O(\epsilon)$ containing the viscous shear stress tensor and heat flux vector will be small, will not a play a major role in the propagation of acoustic waves, and thereby may be neglected. We note that the viscous shear-stress terms are still retained in the base-flow variables, allowing us to utilize viscous, heat conducting base flows.

Thus, substituting Equations 4.1 and 4.3 into the continuity equation, and collecting terms according to the order in ϵ, we obtain,

$$\left[\frac{\partial\tilde{\rho}}{\partial t}+\frac{(\tilde{\rho}\tilde{u}_i)}{\partial x_i}\right]+\epsilon\left[\frac{\partial\rho'}{\partial t}+\frac{\partial}{\partial x_i}\left(\tilde{\rho}u_i'+\rho'\tilde{u}_i\right)\right]+O(\epsilon^2)=0. \tag{4.6}$$

The analogous result for the momentum equation is,

$$\begin{aligned}
&\left[\frac{\partial}{\partial t}(\tilde{\rho}\tilde{u}_i)+\frac{\partial}{\partial x_j}(\tilde{\rho}\tilde{u}_i+\delta_{ij}\tilde{p})-\frac{\partial\tilde{\tau}_{ij}}{\partial x_j}\right]\\
+\;&\epsilon\left[\frac{\partial}{\partial t}(\tilde{\rho}u_i'+\rho'\tilde{u}_i)+\frac{\partial}{\partial x_j}\left(\tilde{\rho}\tilde{u}_iu_j'+\tilde{\rho}u_i'\tilde{u}_j+\rho'\tilde{u}_i\tilde{u}_j+\delta_{ij}p'\right)-\frac{\partial\tau_{ij}'}{\partial x_j}\right]\\
+\;&O(\epsilon^2)=0.
\end{aligned} \tag{4.7}$$

And for energy, it is,

$$\begin{aligned}
&\left[\frac{\partial\tilde{E}_t}{\partial t}+\frac{\partial}{\partial x_j}\left[\left(\tilde{E}_t+\tilde{p}\right)\tilde{u}_i\right]+\frac{\partial\tilde{q}_i}{\partial x_i}-\frac{\partial}{\partial x_j}\left(\tilde{u}_i\tilde{\tau}_{ij}\right)\right]\\
+\epsilon&\left[\frac{\partial\tilde{E}_t}{\partial t}+\frac{\partial}{\partial x_j}\left[\left(\tilde{E}_t+\tilde{p}\right)u_j'+\left(E_t'+p'\right)\tilde{u}_j\right]+\frac{\partial q_i'}{\partial x_i}-\frac{\partial(\tilde{u}_i\tau_{ij}')}{\partial x_j}-\frac{\partial}{\partial x_j}\left(u_i'\tilde{\tau}_{ij}\right)\right]\\
&+O(\epsilon^2)\;=\;0.
\end{aligned} \tag{4.8}$$

We also omit terms of order ϵ/Re, namely $\partial\tau_{ij}'/\partial x_j$, $\partial q_i'/\partial x_i$, and $\partial(\tilde{u}_i\tau_{ij}' + u_{ij}'\tilde{\tau}_{ij})/\partial x_j$. We now find it convenient to define small disturbance conservative variables,

$$\begin{aligned}
Q_i' &= \tilde{\rho}u_i'+\rho'\tilde{u}_i,\ i=1,2\\
Q_3' &= \rho'
\end{aligned}$$

$$Q'_4 = E'_t \tag{4.9}$$

These variables $Q'_m \equiv Q_m - \tilde{Q}_m$, $m = 1, 2, 3, 4$ represent the departure from the base state, as expressed in terms of the full conservative variables ($Q_1 = \rho u_1, Q_2 = \rho u_2$, $Q_3 = \rho$, $Q_4 = E_t$). We also find it convenient to define some inverse relations, $u'_i = \frac{Q'_i - \tilde{u}_i Q'_3}{\tilde{\rho}}$ and $p' = (\gamma - 1)\left[Q'_4 - \left\{\tilde{u}_k Q'_k - \frac{1}{2}\tilde{u}_k \tilde{u}_k Q'_3\right\}\right]$. Substituting these definitions into the above expressions for mass, momentum, and energy (Equations 4.6, 4.7, and 4.8), we obtain the Euler equations linearized about an unsteady base flow.

$$\begin{aligned}
\frac{\partial Q'_3}{\partial t} &= -\frac{\partial Q'_i}{\partial x_i} && (4.10)\\
\frac{\partial Q'_i}{\partial t} &= -\frac{\partial}{\partial x_j}\left(\tilde{u}_j Q'_i + \tilde{u}_i Q'_j - \tilde{u}_i \tilde{u}_j Q'_3 + \delta_{ij} p'\right) \qquad i = 1, 2 && (4.11)\\
\frac{\partial Q'_4}{\partial t} &= -\frac{\partial}{\partial x_i}\left[\left(\tilde{E}_t + \tilde{p}\right) u'_i + \left(Q'_4 + p'\right) \tilde{u}_i\right] && (4.12)
\end{aligned}$$

4.3 Numerical Solution to the Small Disturbance Equations

The equations 4.10 through 4.12 are solved numerically in much the same way the Navier-Stokes equations are solved in the direct numerical simulations. The spatial derivatives are found using the sixth-order compact Padé method, and the right-hand side is advanced in time using the third order compact storage Runge-Kutta scheme. Damping sponges and buffer zones are again used as boundary treatment methods; however, as the disturbances in the solution variables are significantly smaller, these boundary zones can be more compact. However, a nonreflecting boundary condition linearized about an unsteady base flow is currently unavailable. The Thompson nonreflecting boundary conditions discussed in Section 2.3.1 do not simply accommodate the separation between base flow and perturbation field in the instance that the base flow is unsteady. Instead, we use simple characteristic boundary conditions based on Riemann invariants to maintain well-posedness. The Riemann invariants are evaluated using the base flow. The compression wave boundary condition is imposed in the perturbation variables in a fashion similar to that described in Section 2.5.2. The difference is that because the equations are linear in the fluctuations, the compression waves will orient themselves according to Mach angles in the base flow. Their specification therefore does not account for nonlinear effects. We verify that the numerical solutions to the linearized Euler equations behave linearly in Appendix B, Section B.3. Numerical filtering is again used, in this case to counter-act numerical instabilities whose exact origin is not known. We note that our method solves inviscid equations using a central differencing method, and thereby contains little physical or numerical dissipation. Details of the choice of filtering parameters are given in Appendix B, Section B.2.

4.3.1 Base Flow

The base flow terms are prescribed. In practice, they are supplied either analytically through a model for the unsteady shear layer, or from data obtained from numerical simulations. For the latter case, it is be assumed that the base flow is periodic in time, so that it can be represented with a temporally limited data set. Furthermore, to take advantage of the periodicity, the base flow is furnished to the solver in terms of Fourier coefficients, rather than in a "time accurate" fashion. This strategy enables us to accurately represent the base flow in time without significant memory usage. With Fourier series reconstruction, it also provides a simple means for accurately interpolating in time, allowing us to freely decouple (within stability limits) the time step of the computation from the base flow data.

The Fourier coefficients of the base flow variable are computed from real data. Therefore, the coefficients will consist of complex conjugate pairs, except for the mean flow coefficients; we can reduce the memory storage of the base flow by near half. Suppose the coefficients of the base flow were obtained through discrete Fourier transform in time using N equally spaced samplings over one flow oscillation. The Fourier coefficients obtained would then have indices $n = -N/2$ to $N/2 + 1$ and be related to the original data as

$$\tilde{Q}(x, y, t) = \sum_{n=-N/2}^{N/2+1} \hat{\tilde{Q}}_0(x, y) \exp(-in\omega t) \tag{4.13}$$

which will be real, since $\hat{\tilde{Q}}_{-n} = \hat{\tilde{Q}}_n^*$. ω is the fundamental frequency of the base flow data. Hence, we can obtain the same temporal data by taking the following sum:

$$\tilde{Q}(x, y, t) = \hat{\tilde{Q}}_0 + \sum_{n=1}^{N/2} \left[\hat{\tilde{Q}}_n \exp(-in\omega t) + \hat{\tilde{Q}}_n^* \exp(in\omega_1 t) \right] \tag{4.14}$$

We have omitted the oddball wave-number $n = N/2 + 1$. Assuming now that the coefficients have been interpolated to the computational grid, each time step of the computation would require a Fourier reconstruction at each grid node for time t. This reconstruction procedure can be completed at the beginning of each time step evaluation. The base flow quantities are then effectively prescribed, and the computation of RHS can be carried out.

We tested this reconstruction method on base flow data obtained from the numerical simulations of Chapter 3. We computed the discrete Fourier transform in time of shear layer SL1 (see Table 3.3 over two oscillation periods. The Fourier transform was taken over two periods to average out the effects of any subharmonic modes. 32, 64, and 128 samples in time were taken in the three test cases. After removing the modes due to the subharmonic, we reconstructed the time accurate data using Equation 4.14. Figure 4.1 shows the vorticity field for the three cases compared to original time domain data. We conclude that for these shear layers, at least 64 samples per oscillation period is necessary for a smooth representation in the base flow.

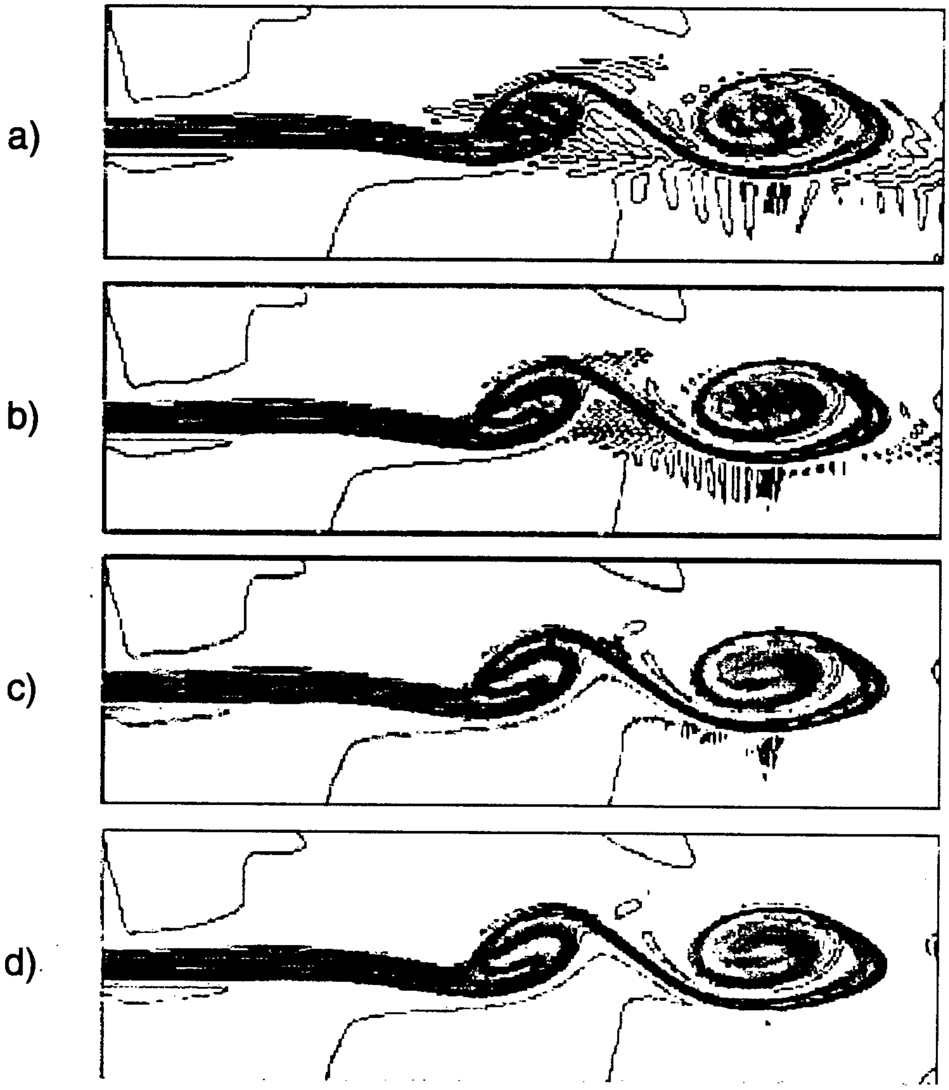

Figure 4.1: Reconstructed samples of SL1 shear layer based on Fourier coefficient reconstruction in Eq. 4.14. Original Fourier coefficients obtained from FFT over two periods with a) 32 samples, b) 64 samples, c) 128 samples. d) is the original time slice of SL1.

Chapter 5

Results of Linearized Euler Simulations

In this chapter we exploit the simplifications made in the linearized Euler analysis to explore a wider range of flow conditions. Of particular interest is to study further the effect of instability wave amplitude on the acoustic field. Our approach here is to first demonstrate that the linearized Euler analysis is capable of reproducing the instability-wave compression-wave interaction behavior observed when we solved the full Navier-Stokes equations. Data obtained from the free-shear layer DNS is used to define the base flow, whereas the compression wave is introduced as a boundary condition to the perturbed solution field. We also consider an alternative profile for the incident oblique wave which simplifies acoustic measurements while retaining the instability-wave thresholding behavior seen previously. This alternative profile does not reproduce the same acoustic directivity as the compression wave. A wide range of instability-wave cases are conducted with this profile. Finally, fully exploiting the capabilities of the linearized Euler analysis, we replace the realistic instability-wave base flow obtained from numerical simulations with an analytic mixing-layer model for saturated vortices. Although numerous simplifying assumptions are made in applying this approximate base flow, those assumptions are not found to interfere with the basic generation process and permit us to study it in even greater detail.

Grid Size	$Nx \times Ny$	$301/376^* \times 291$
Complete Domain Size	$(x_{min} : x_{max}) \times (y_{min} : y_{max})$	$(0 : 60/75^*) \times (-15 : 40)$
Interior Domain Size	$(x_{min} : x_{max}) \times (y_{min} : y_{max})$	$(9 : 50/65^*) \times (-12.33 : 35)$
Time Step	Δt	0.0238948
Filter Coeff.	α'_x, α'_y	$2.222/2.050^\dagger$, $2.050/2.222^\ddagger$
Filter Period	N_{filter}	every 10 Δt

Table 5.1: Parameters for numerical simulations. Exceptions for: *Cases G4 and G5; †Stuart vortex cases (Section 5.4); ‡Cases CW1-3. See Tables 3.3 and 3.4 for case designations. Interior domain refers to computational domain excluding boundary zones.

	Inflow	*Outflow*	*Top*	*Bottom*
U_{max}	—	1.0	—	—
ψ	—	10^{-3}	—	—
σ_{max}	1.0	0.5	2.0	2.0
N_{sponge}	$90/100^*$	100	20	20
L_{sponge}	$9.0/10.0^*$	5.0	10.0	2.67

Table 5.2: Boundary zone: Buffer zone and damping sponge settings. *Alternate settings for weakly forced cases (SL3 and D1; see Tables 5.3 and 5.4 for case designations).

A summary of the parameter settings used in the linearized Euler simulations presented in this chapter are given in Table 5.1. Boundary zone parameters are given in Table 5.2. Validations for these grids and filter parameters are documented in Appendix B.

5.1 Compression Wave Cases: Comparison to Navier-Stokes Solutions

The acoustic field produced in the Navier-Stokes solution of the instability-wave shock interaction problem is characterized by an apparent "leakage" phenomenon. For a steady shear layer, the incident shock wave is trapped by total internal reflection. For sufficiently high instability wave amplitude, however, the velocity field associated with the vortices becomes periodically arranged in such a way as to permit the wave to escape. By investigating this problem within the context of a linearized Euler analysis, we test the hypothesis that for this kind of sound generation to occur, only the effect of the unsteady shear layer on the shock, rather than the details of the shock, is important.

In the linearized Euler analysis, the impingement of a compression wave on a shear layer does result in an angular deflection of the shear layer. However, we will show later that this deflection is not necessary for the sound generation process we wish to reproduce. We will also indicate the numerical difficulty the deflection effect causes (as it did in the Navier-Stokes simulations), especially for the low amplitude instability wave base flow; we thereby motivate the use of an incident oblique Mach wave which does not impart an angular deflection in the shear layer.

To understand the effect of imposing an oblique compression wave on a shear-layer base-flow, it is instructive to examine first a steady flow case. In this example we use for the base-flow a parallel supersonic shear layer. The compression wave is represented entirely in the perturbed solution. Therefore, the perturbed solution must contain the all effects brought about the compression wave. The compression wave, imposed as a boundary condition, intersects the shear layer and must reflect as an expansion wave to satisfy the pressure compatibility condition there. The effect of the succession of compression and expansion waves is the turning of the downstream supersonic flow toward the shear layer. This is a global effect and requires that the shear layer turn parallel to this flow, as discussed in Section 2.5 and demonstrated for the DNS in Figure 3.8. However, in the linearized Euler representation, the prescribed base-flow shear-layer cannot adjust; consequently, the perturbation solution tends to compensate for this lack of turning by infusing a steady perturbation downstream of the interaction site. The effect is illustrated in Figure 5.1. The magnitude the perturbed solution in the compensation region can approach base-flow levels at large distances downstream. In the unsteady case, this adjustment region will contain unsteady disturbances which must be accommodated by the outflow boundary conditions. To reduce the effect of the deflection, we end the interior domain immediately downstream of the interaction site.

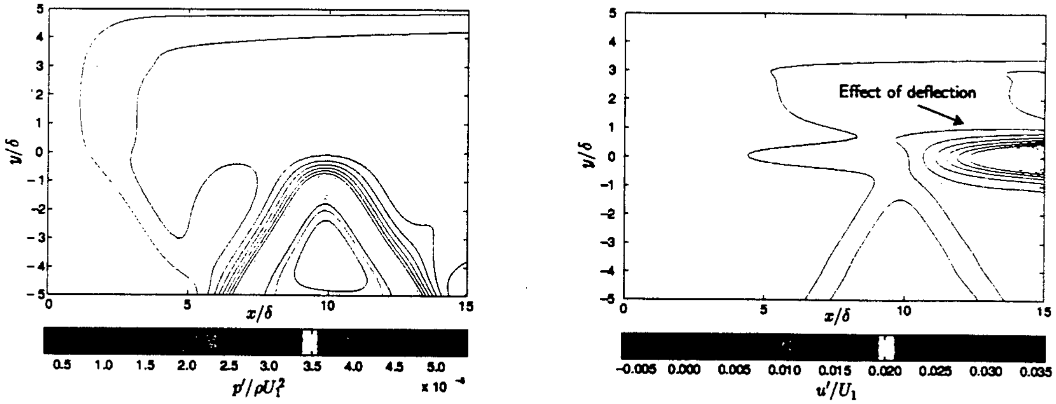

Figure 5.1: Perturbation field of compression wave ($w/\delta = 2.0$, $\Delta p/p_\infty = 0.01$) incident on steady shear layer (coordinates given as x/δ and y/δ). *Left*: pressure; *right*: streamwise velocity velocity. Deflection of shear layer is manifested in perturbation field, as seen in streamwise velocity.

cases	*wave type*	$\Delta p/p_\infty$	w/δ	*base flow*
CW1	compression	0.01	2	SL1
CW2	compression	0.01	2	SL2
CW3	compression	0.01	2	SL3

Table 5.3: Summary of linearized Euler analysis cases reported. Base flow SLn indicate forced, free shear layers defined in Table 3.3

We consider compression wave cases at $\Delta p/p_\infty = 0.01$ for base flows containing the forced shear layers documented in Section 3.2. We demonstrate that the linearized Euler analysis is an appropriate framework for investigating the screech-type source. In Figure 5.2 we show a series of visualizations of the perturbation field over one interaction cycle for the SL1 shear layer. This figure is the analog of Figures 3.9 and 3.16. Nearly all characteristics of the interaction process seen in the Navier-Stokes solutions are reproduced here. The compression wave undergoes large fluctuations. During its upstream excursion between the shear layer vortices, an acoustic compression front is released. The secondary traveling waves are also evident, though they do not produce significant radiation due to the proximity of the exit zone.

We also sample this field and compare a pressure trace to those obtained earlier in the Navier-Stokes Cases B1 and B2. We normalize the pressure trace to the compression wave amplitude in each case. As shown in Figure 5.3, the primary wave is reproduced, giving us confidence in the linearized Euler solution. As this matching is made for the normalized acoustic pressure, we also reinforce the previous finding that the acoustic field scales with the amplitude of the incident compression wave. As noted above the secondary acoustic features are not as prominent.

The variation in these traces as a function of observer angle θ is given in Figure 5.4. It is analogous to the Navier-Stokes Case B1 directivity plot in Figure 3.17. The overall trend seen in the linearized Euler result is similar to the Navier-Stokes result, including the contamination due to the shear layer deflection in directions approaching $\theta = 90°$.. In the case of the Euler result, the characteristically steep compression is followed by a less rapid expansion at angles approaching the upstream direction.

We also note the pressure-trace directional variation of Cases CW2 and CW3, in which base flows of reduced instability-wave amplitude are used. The trends observed Case CW1 are seen again in CW2 (see Figure 5.5) with a mild reduction in overall amplitude and some broadening in the wave-form. At $\theta = 90°$ the pressure trace differs from those at other angles, being dominated by a disturbance we attribute to the shear layer deflection. For the most weakly forced shear-layer base-flow case, CW3, we are unable to recover the sound from the instability-wave compression-wave interaction. The dilation field is shown at two times separated by one half period in

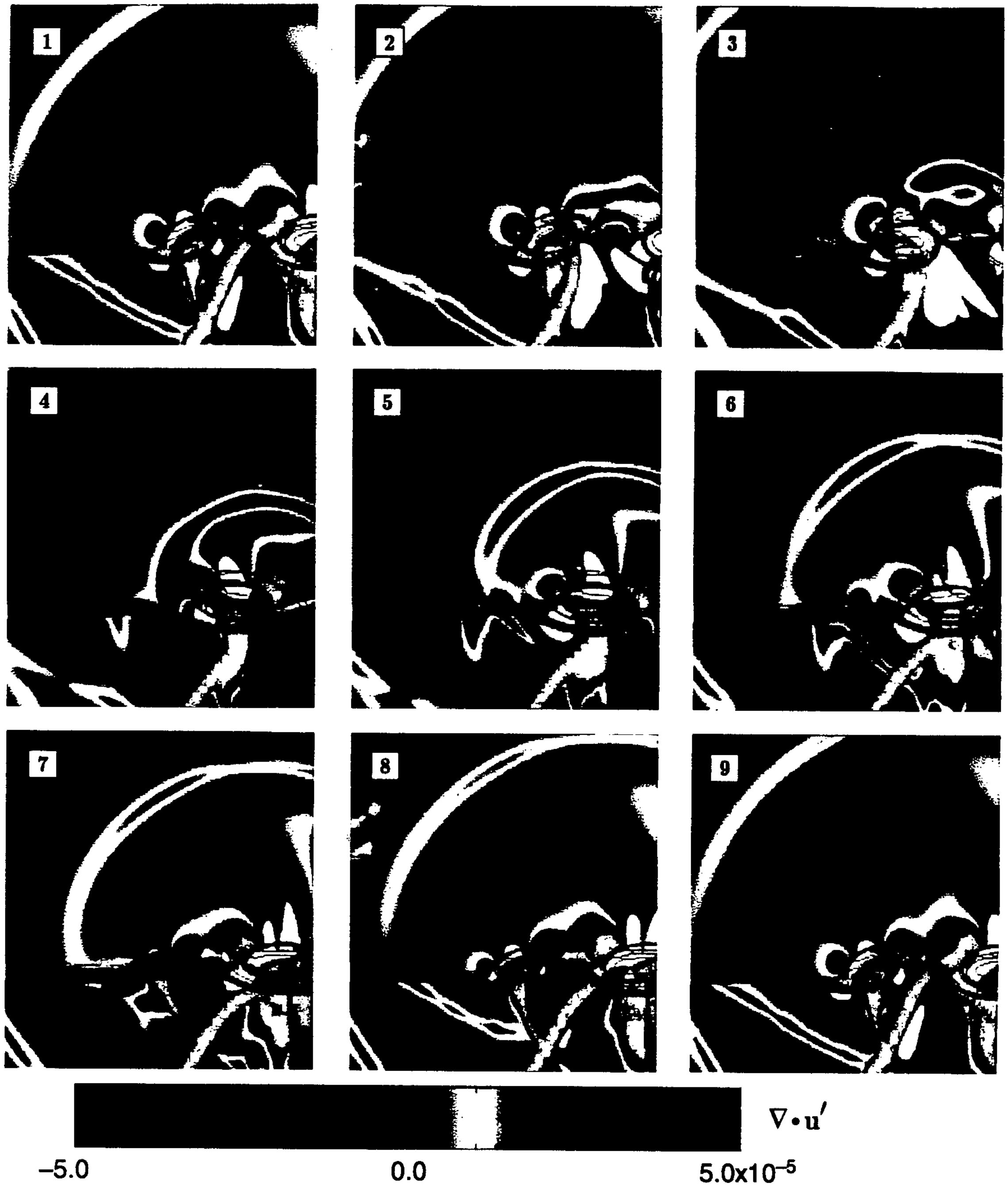

Figure 5.2: Instability-wave compression-wave interaction for linearized Euler simulation. Case CW1 (SL1 shear layer base flow and $\Delta p/p_\infty = 0.01$ compression wave amplitude). Dilatation field and vorticity field, with vorticity contour increments at $\Delta\omega/(U_1/\delta) = 0.1$.

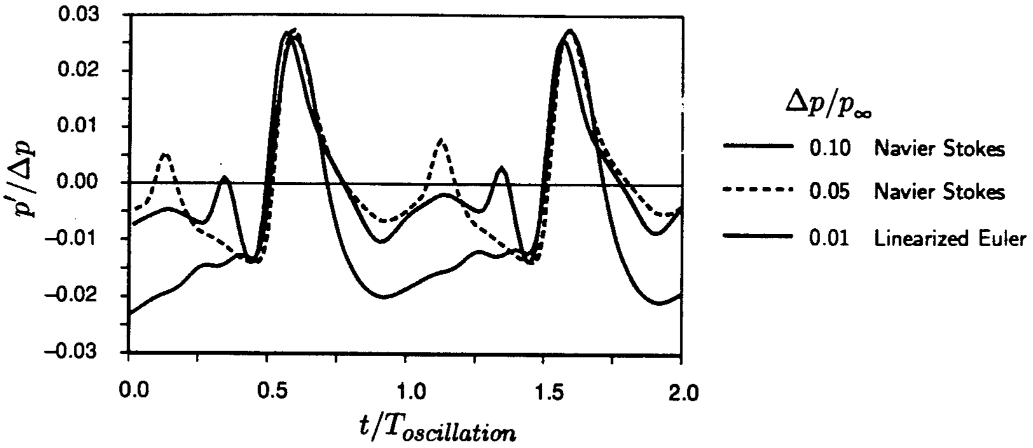

Figure 5.3: Comparison of acoustic pressure trace of linearized Euler result and Navier-Stokes results at $r/\lambda = 1.3$, $\theta = 135°$. Cases B2 ($\Delta p/p_\infty = 0.10$), B1 ($\Delta p/p_\infty = 0.05$) and CW1 ($\Delta p/p_\infty = 0.01$).

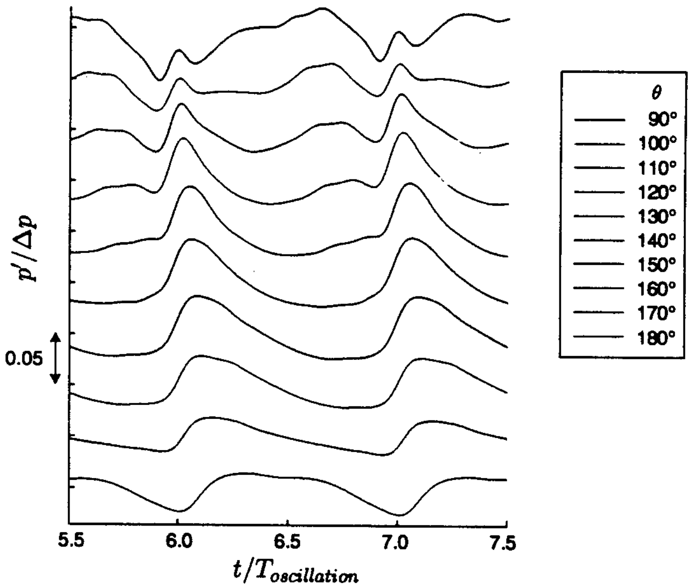

Figure 5.4: Case CW1: Pressure fluctuation traces normalized to compression wave amplitude for various observer angles θ at radius $r/\delta = 30$.

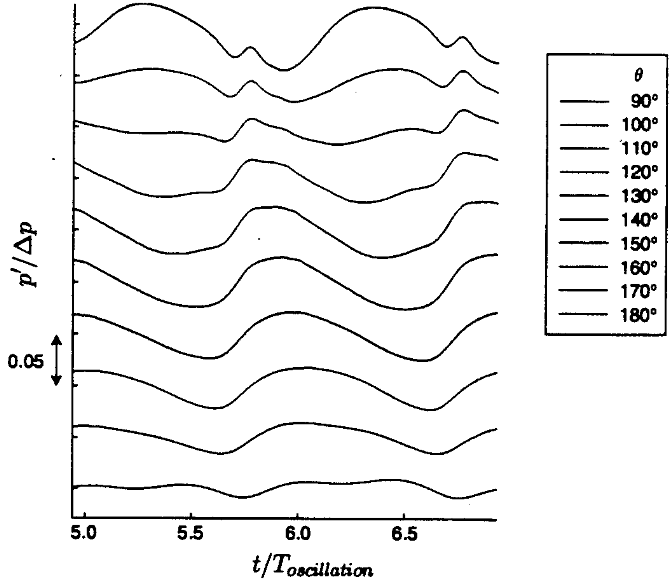

Figure 5.5: CW2: Pressure fluctuation traces normalized to compression wave amplitude for various observer angles θ at radius $r/\delta = 30$.

Figure 5.6. The fine scale circular wave-fronts are centered at a point downstream of the intended interaction site and are believed to be due to the traveling wave phenomenon. The broader wave phenomena originate from even farther downstream and are more clearly recorded in the time traces shown in Figure 5.7. The positive shift in the trace peak with viewing angle θ indicates that the actual interaction region is located downstream of the intended source. We have concluded that the performance of the inflow and outflow boundary conditions implemented in the presence of the shear layer deflection is insufficient to prevent feedback receptivity in the case of a weakly forced shear layer. The weakly forced shear layer is more susceptible to unintended instability wave growth manifested in the perturbation solution because its stability characteristics remain relatively unchanged in the base flow. Conversely, the strongly forced shear layer base flow reaches a saturated state quickly; the stability of its mean profile is significantly altered and less unstable at the forcing frequency at the interaction site.

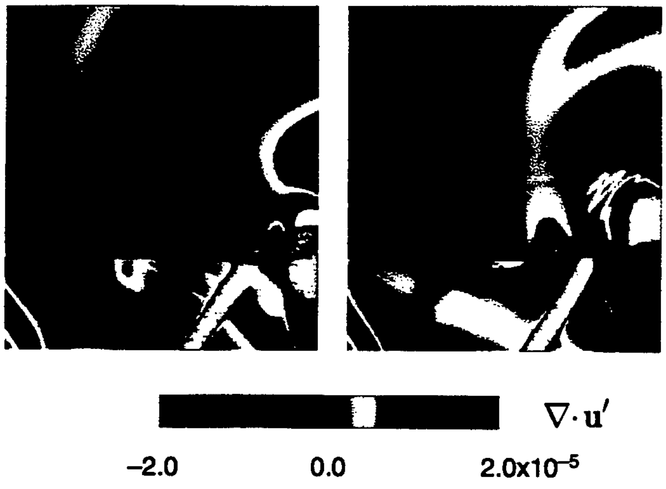

Figure 5.6: Instability-wave compression-wave interaction for linearized Euler analysis. Case CW3 (SL3 shear layer base flow and $\Delta p/p_\infty = 0.01$ compression wave amplitude). Dilatation field and vorticity field, with vorticity contour increments at $\Delta\omega/(U_1/\delta) = 0.1$.

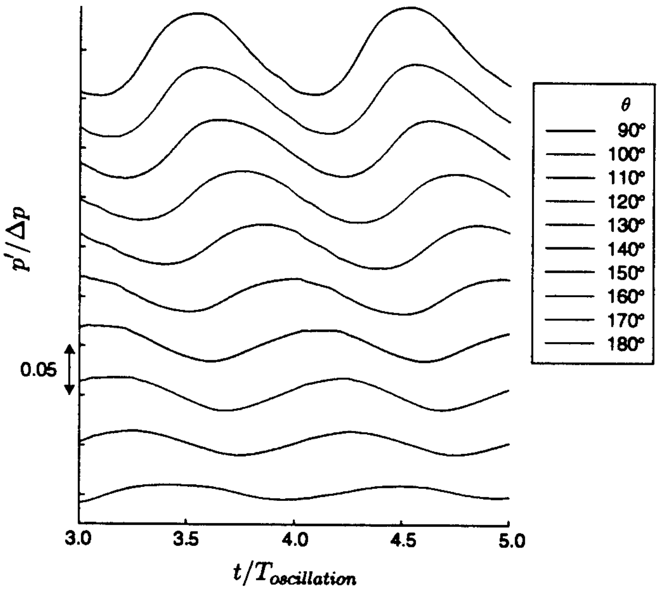

Figure 5.7: Compression wave, SL3: Pressure fluctuation traces normalized to compression wave amplitude for various observer angles θ at radius $r/\delta = 30$.

5.2 G-wave

We have demonstrated above that for the high amplitude shear layer the linearized Euler analysis reproduces the Navier-Stokes result for instability-wave compression-wave interaction. We have also encountered numerical errors in the Euler analysis which are not unlike those faced when extracting the acoustic near-field in the Navier-Stokes simulations. To summarize, the deflection of the shear layer by the compression wave introduces disturbances into the perturbation solution whose magnitude exceeds the levels for which the outflow boundary conditions were designed. In this section, we introduce linearized Euler simulations based on an alternative oblique wave profile, the Gaussian distribution, or G-wave. We show that the acoustic field produced by a Mach wave of this wave-form, when interacting with the forced shear layer, retains the characteristics of the radiation mechanism observed for the compression wave. Because the G-wave does not deflect the shear layer appreciably, we are able to measure the acoustic field with greater precision.

The G-wave is defined with the following shape function:

$$f(\xi) = Ae^{-(b\xi)^2} \tag{5.1}$$

where $A = 1.0$, $b = 2.14597$, and

$$\xi = \frac{x - x_{center}(y)}{w/2}, \tag{5.2}$$

$x_{center}(y)$ being the center-line of the G-wave. The function f, a Gaussian curve, is plotted in Figure 5.8. The parameter b assures that the width of the wave profile is based on the 1% of function's peak. The magnitude of the incident G-wave is measured in terms of its base-to-peak difference Δp, giving it the pressure distribution,

$$\Delta p'_{G-wave}(\xi) = f(\xi)\Delta p. \tag{5.3}$$

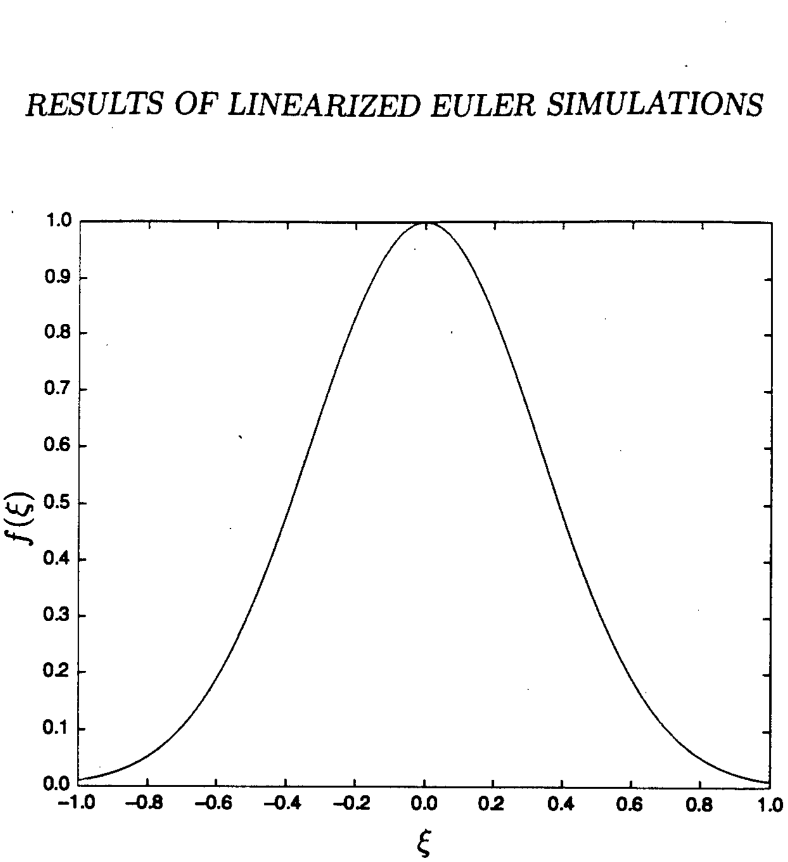

Figure 5.8: Shape function for defining the Gaussian "G-wave". The function width w is based on the 1% points (shown here as $\xi = -1$ and $\xi = +1$).

Supersonic small disturbance theory is then used to find fluctuations in other quantities. The G-wave is a combination compression-expansion wave. It will reflect from the shear layer as an expansion-compression.

The simulations we carried out with the G-wave verify that the large-amplitude instability-wave interaction mechanism remains valid for incident waves which have non-monotone profiles. Shocks, compression waves, and expansion waves which contain a monotonic pressure distribution were already considered. Given the increased "oscillation" complexity of the G-wave profile compared to the compression wave, we increased its standard width to $w = 4\delta$. Figure 5.9 is a visualization sequence over one oscillation cycle and is the G-wave counterpart of Figure 5.2. We emphasize that the visualized field in this case is pressure rather than dilatation, attesting to the improved numerical quality of the computed field. The now familiar interaction process involving the significant perturbation of the incident oblique wave and its apparent leakage through the shear layer is readily visible.

case	$\Delta p/p_\infty$	w/δ	*base flow*	x_{src}/δ	$K(x_{src})$
G1	0.04	4	SL1	40	0.526
G2			SL2		0.458
G3			SL3		0.241
G4	0.04	4	SL1	45	0.526
G5				42	0.528
G6				37	0.514
G7				35	0.498
G8				33	0.476
G9				32	0.463
G10				31	0.448
G11				30	0.429
G12				29	0.408
G13				28	0.383
G14				27	0.356
G15				26	0.327
G16				25	0.298
G17				20	0.166

Table 5.4: Summary of linearized Euler analysis G-wave cases. Base flow SLn indicate forced, free shear layers defined in Table 3.3.

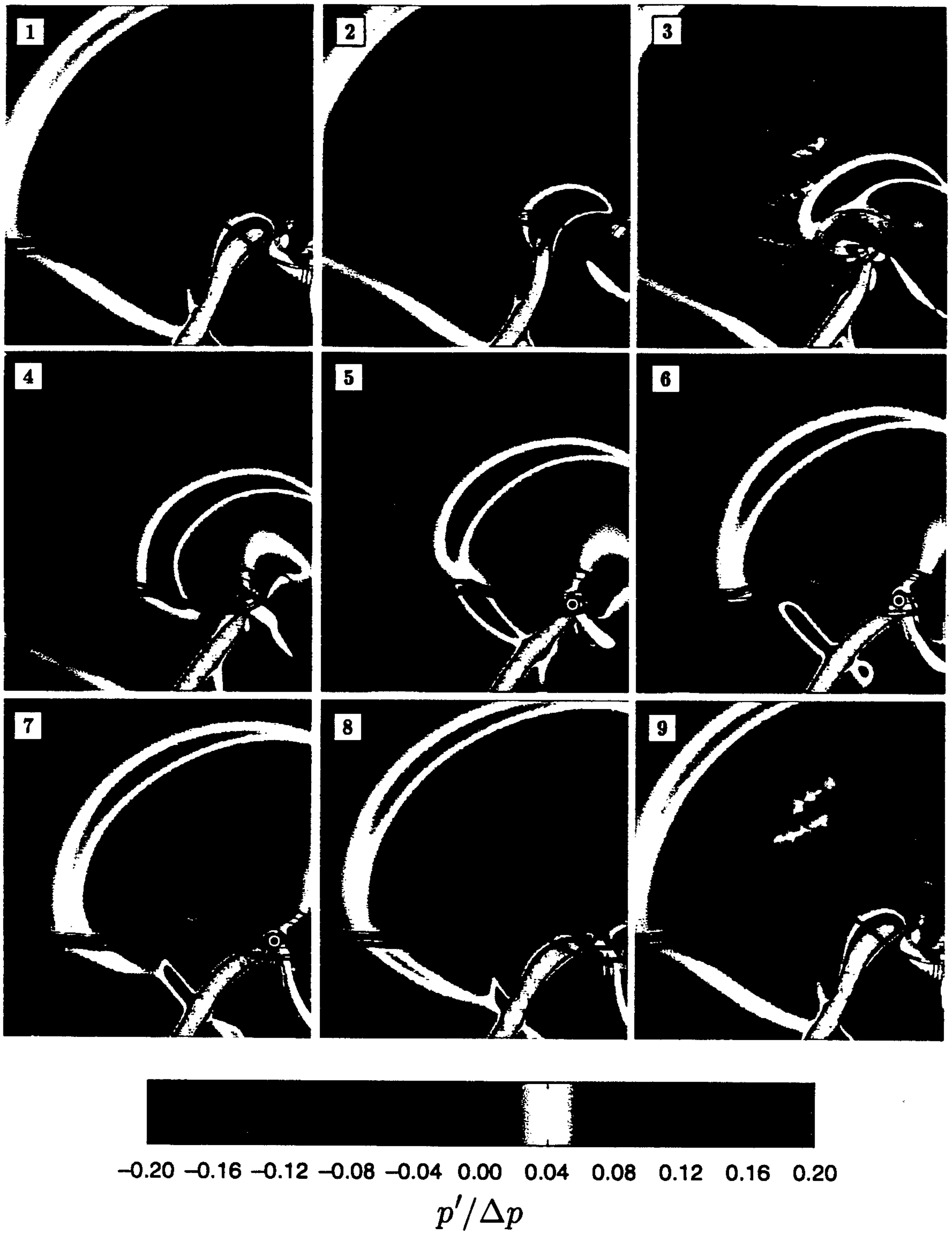

Figure 5.9: Pressure and vorticity for G-wave interacting with SL1 base flow instability wave (Case G1). The "reflection point" is indicated by the ⊙.

The improved visualization allows us to add detail to our description of the radiation process: for part of the cycle (Figure 5.9, frames 4–7) the incident wave impinges upon the vortex and is totally (internally) reflected. The reflection point remains "attached" to the vortex. As the vortex passes, the wave advances into the relatively irrotational region between vortices (frame 8), but the reflection point follows the curved vorticity contour of the vortex through the shear layer braid. Both the incident wave and the reflection are "dragged" through in a continuous fashion behind the reflection point (frames 8, 9, 1, and 2) and respond to the local velocity field by radiating outward in an arc. The reflection point continues outside the shear layer (frames 2–3), and there is no reflection point inside the shear layer until the incident acoustic-wave collides with the next vortex (frames 3–4). The collision causes the formation of a new reflection point (frame 4). The acoustic wave undergoes a severe refraction as it passes through the vortex (frames 3–4), focusing at some points and weakening at others. It extends back through the shear layer and advances upstream. With the encounter of the next vortex upstream (frames 5–6), a localized focusing again occurs. At this point (frames 6–9) the formation of the "secondary" traveling wave is apparent; it may be a remnant of the original acoustic wave. The traveling wave is an upstream-oriented, but in net, downstream traveling wave. The primary acoustic wave continues upstream, dragging the oblique Mach wave in the supersonic flow with it. The traveling wave continues downstream and arrives at the imposed G-wave just as it is colliding with the vortex. The traveling wave may be modified as it passes through the G-wave and continues downstream where it, too, interacts with the passing vortices to produce sound.

We note that the degree to which the wave-form of the G-wave is preserved in the acoustic field differs depending on direction of radiation θ. In Figure 5.10 we show pressure traces for the forward quadrant at nearly one acoustic wavelength from the source. There is some variation in the width associated with the G-wave in the acoustic trace with θ. The mean-to-peak amplitude variation, shown in Figure 5.15, also indicates significant variation, with peak radiation at $\theta = 120°$.

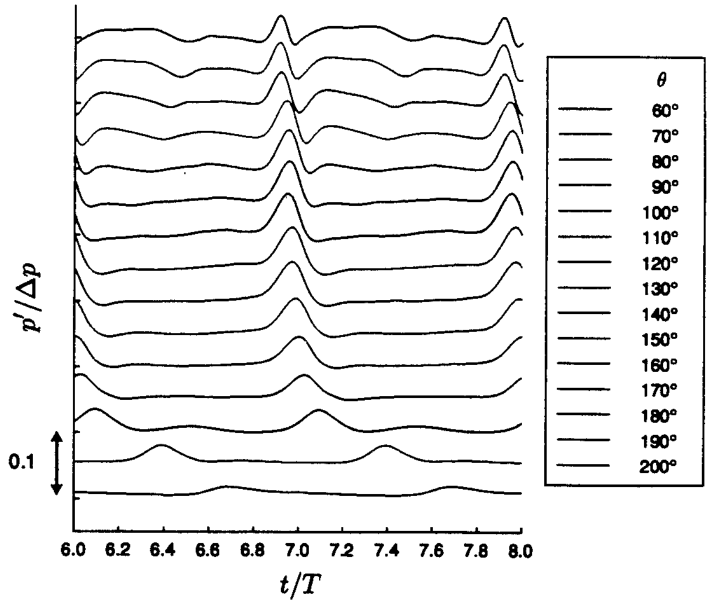

Figure 5.10: Fluctuating pressure trace in upstream quadrant for Case G1

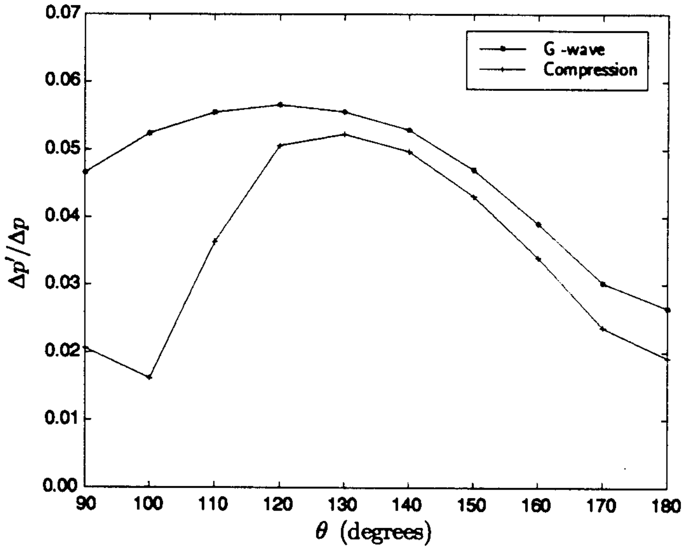

Figure 5.11: Directivity in upstream quadrant for G-wave case G1 and compression-wave case B1.

5.2.1 Instability Wave Amplitude

The reduction of fluctuations from unwanted sources in the solution field permits us to take a more detailed look at the dependence of the acoustic field on instability wave amplitude. In the Navier-Stokes simulations, we obtained indications that the acoustic radiation levels fall at rates disproportionately faster than our measure of the instability wave amplitude (Equation 3.1). A thresholding process was suggested but could not be quantified for lack of numerical fidelity in the simulations at low instability wave amplitude. The linearized Euler simulations with compression waves also failed to produce reliable results at the lower instability wave forcing case (SL3). With the G-wave results, we are able to identify three generally distinct regions of behavior with regard to the dependence of acoustic radiation amplitude on instability wave amplitude.

Instability Wave Amplitude: three base flows

We begin by comparing the over-all solution field for the three shear layer base flows that are subject to the G-wave oblique Mach wave. In Figure 5.12 Cases G1 and G2 both emit a field with a compact waveform that resembles the incident G-wave. This is seen more clearly in the fluctuation traces given in Figures 5.10 and 5.13. The actual spatial extent of the wave form is at least two times the G-wave width w in the directions sampled and exhibits a weak dependence on θ, increasing toward the upstream direction. Visualizations (such as Figure 5.9) indicate that the wave-form is most compact in the downstream direction.

The low instability wave amplitude case (Case G3) exhibits a vastly different radiation pattern. The acoustic pressure in Figure 5.14 shows the existence of several sources with different phases. In the middle angles ($\theta = 100°$ to $170°$), the alignment of the wave-forms suggest that the source is slightly down-stream of the center of the sampling probe arc ($x_{src} = 40$). At transverse angles ($\theta < 100°$), some of the waves clearly originate from farther downstream. Visualization indicates that traveling waves exist even at these low amplitudes in the supersonic flow (e.g., see Figure 5.17 in a somewhat different context). Although the primary source of interest

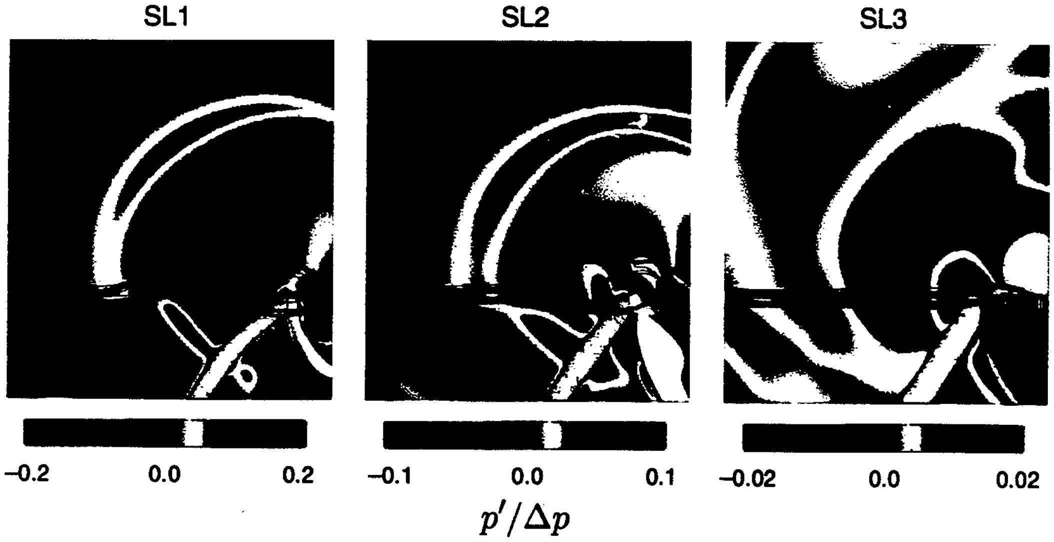

Figure 5.12: Pressure fluctuation normalized by G-wave pressure amplitude Δp for SL1 base flow (left), SL2 base flow (center), and SL3 base flow (right). Vorticity shown in green contours.

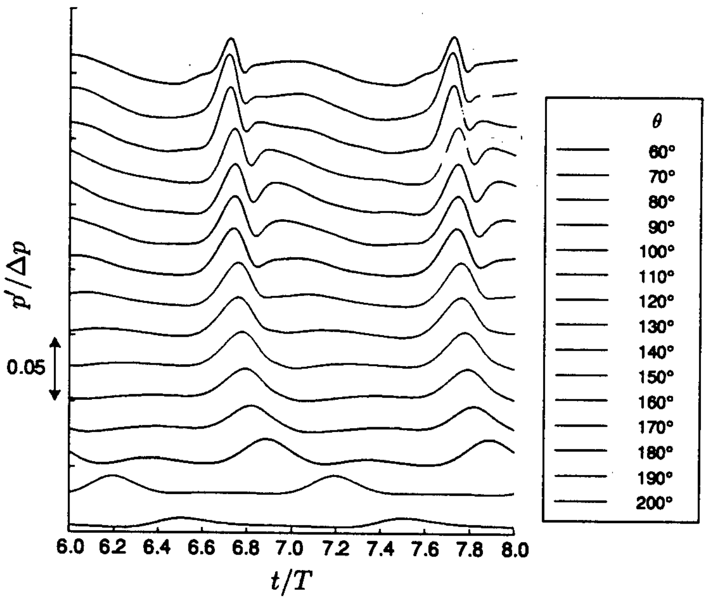

Figure 5.13: Fluctuating pressure trace in upstream quadrant for Case G2.

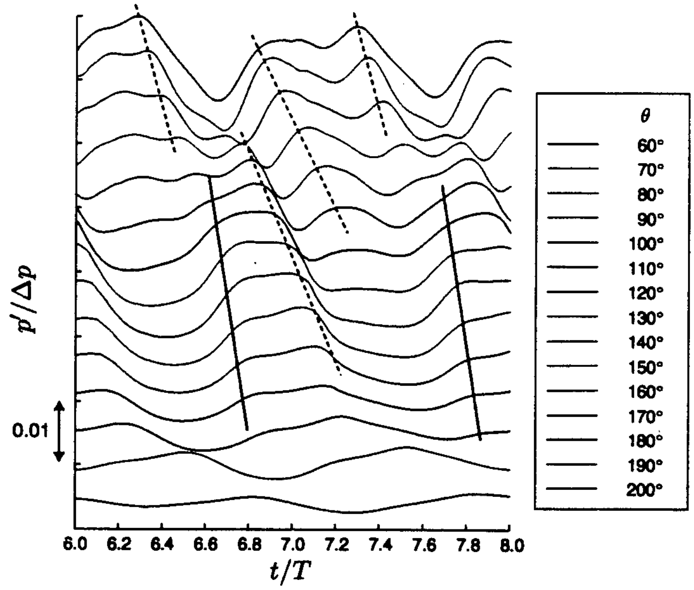

Figure 5.14: Fluctuating pressure trace in upstream quadrant for Case G3. Solid near-vertical lines indicate waves originating just downstream of interaction site; dashed lines are waves originating from farther downstream.

is prominent, it is possible that in the absence of the outflow boundary treatments, the secondary sources would dominate, given the rapid growth of the shear layer. The secondary sources notwithstanding, the primary features of this acoustic field are that it ceases to resemble to the incident wave and that its mean to-peak amplitude is significantly reduced. A comparison of the directivity of the three G-wave cases discussed here is given in Figure 5.15.

The dependence of the acoustic amplitude on instability wave amplitude K (Section 3.2.1) also agrees with the trend first observed in the direct numerical simulations. In Figure 5.16 we show the acoustic amplitude for various observer angle θ. For most θ given, a nonlinear reduction in acoustic amplitude is observed from Case G1 to Case G2. The reduction from G2 to G3 is not as inconsistent with a linear scaling. Even so, the results from these few base flows considered are insufficient to acquire a detailed understanding of the acoustic dependence on instability wave amplitude.

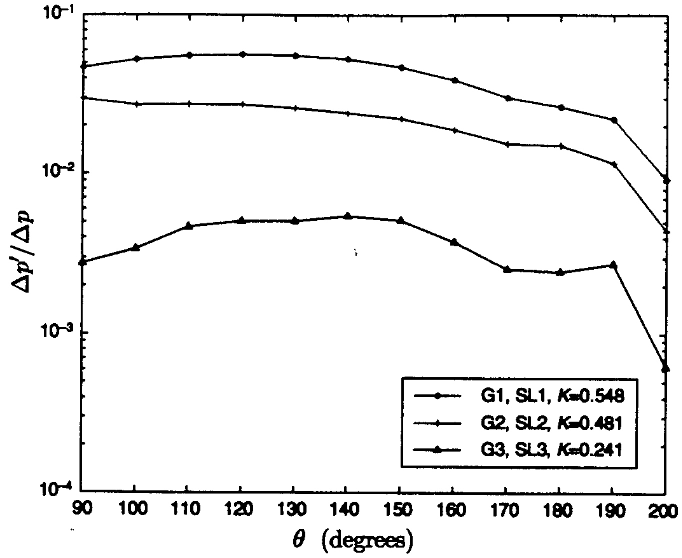

Figure 5.15: Mean-to-peak pressure amplitude directivity for three shear layer base flows (SL1–3), interacting with the G-wave.

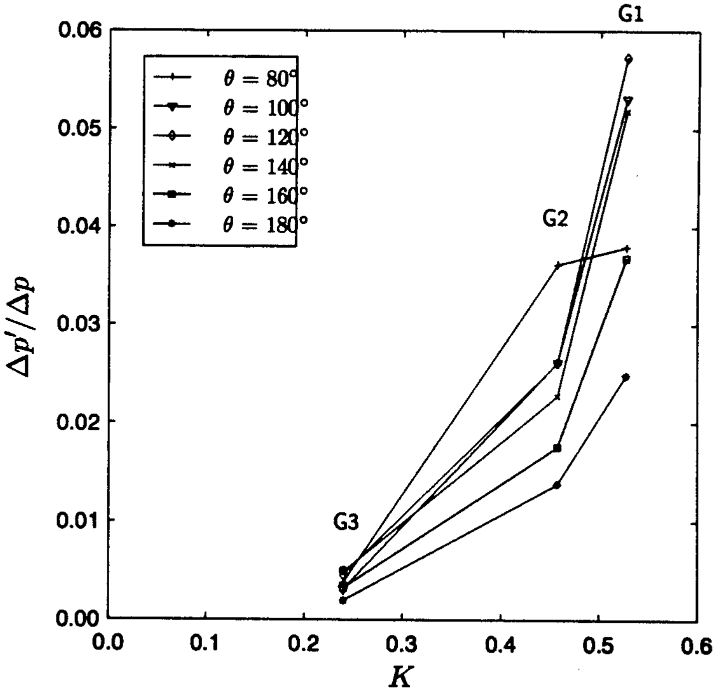

Figure 5.16: Mean-to-peak pressure amplitude as a function of instability-wave amplitude K.

Instability Wave Amplitude: single base flow

In an effort to elucidate the transition between high and low amplitude radiation, we carried out a series of simulations in which a single base flow case, SL1, was subject to the G-wave at a number of streamwise locations x_{src}. The details of these cases are summarized in Table 5.4. The acoustic field was sampled at $r/\delta = 30$ for a range of angles which is limited in the upstream direction at small x_{src}. It was noted that at points in the shear layer where the instability wave amplitude was very low, the sound field was dominated by secondary sources downstream of the source of interest; visualization such as in Figure 5.17 indicates that the traveling waves were responsible. In order to isolate the source of interest, the secondary sources were suppressed by placing an extra rectangular sponge at $x = x_{src} + x_{offset}$ as detailed in Figure 5.18, with $x_{offset} = 10$.

The result of this survey is shown in Figure 5.19. We first plot the acoustic mean-to-peak amplitude normalized to the incident G-wave amplitude $(\Delta p'/\Delta p)$ for $20 \leq x_{src} \leq 45$. In the same figure, we align the instability wave amplitude K and components K_u and K_v for the same region (cf. Section 3.2.1). We divide the acoustic amplitude curves into regions of "Low Amplitude", "Exponential", and "Saturation" to distinguish among different instability wave amplitude dependencies, as will be shown below. In the Low Amplitude region the acoustic amplitude is low; it corresponds approximately to the region in which the instability wave still grows exponentially in accordance with linear theory. Evidence in Section 5.4 suggests that the acoustic amplitude varies directly with instability wave amplitude here. In the Exponential region, the acoustic amplitude rises rapidly with source position. Meanwhile the instability wave growth rate diminishes. Finally in the Saturated region, the acoustic amplitude peaks locally at $x_{src} = 32$, decays slightly, then continues to increase with x_{src}. The local peak coincides approximately with the inflection point in K_u. The mean vorticity thickness of the SL1 shear layer (Figure 3.7) also reaches a local maximum here due to the initial roll-over of the shear layer vortex. The acoustic amplitude is found to reach its overall maximum at some θ in the vicinity of the peaks in K and K_u. The x_{src} at which this peak is reached is smaller for radiation

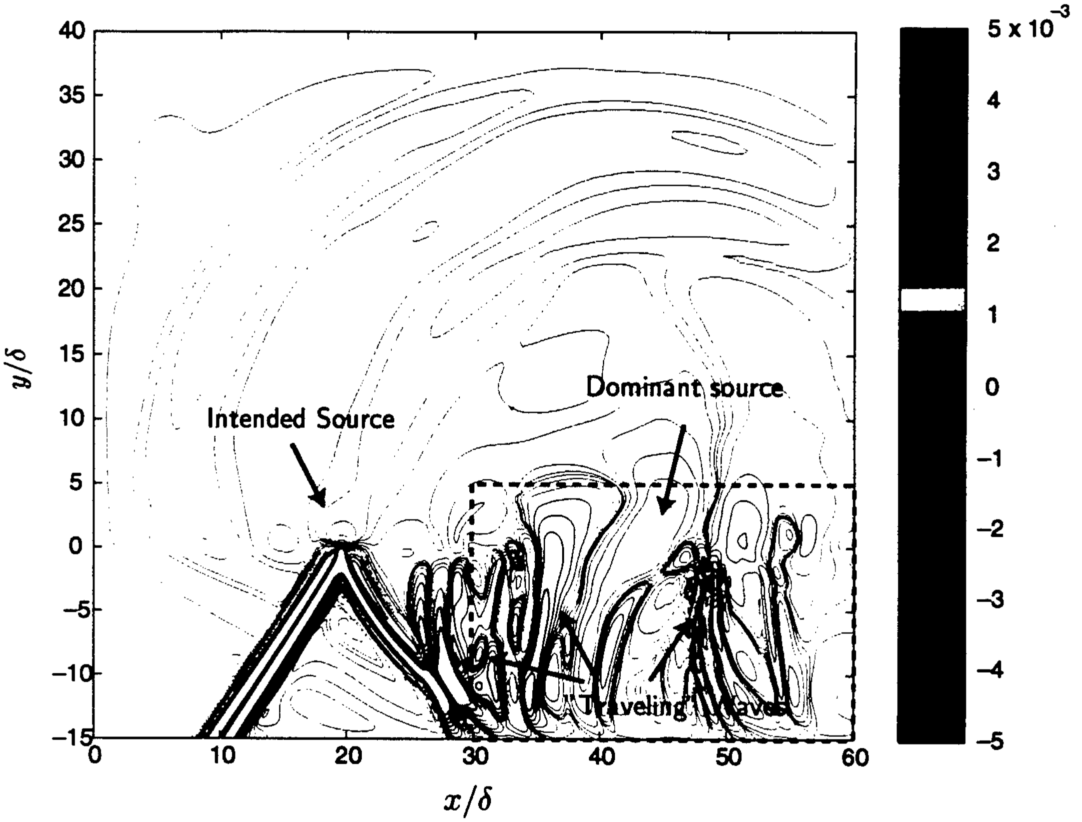

Figure 5.17: Raw pressure perturbation field $p'/\rho U_1^2$ for intended source location $x_{src}/\delta = 20$ before application of extra sponge. Visualization indicates presence of numerous "traveling" waves in supersonic stream, downstream of Mach wave reflection. Dominant source is deduced from center of concentric wave fronts in acoustic field. Location of extra sponge is indicated by the dashed line (see Figure 5.18).

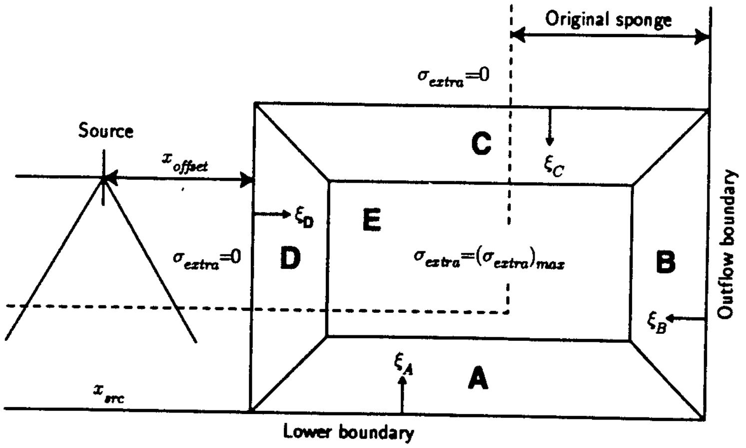

Figure 5.18: Extra sponge function detail. Sponge function is $\sigma_{extra} = \max(\sigma_{extra})\left[1 + \tanh(\xi/2)\right]/2$ along distance from sponge edge to 5δ into its interior in regions A, B, C, and D. In region E, $\sigma_{extra} = \max(\sigma_{extra})$. $x_{offset} = 10\delta$

directions approaching the upstream direction. The evolution of the directivity over the range of source locations is shown in Figure 5.20.

The dependence of acoustic amplitude on instability wave amplitude K is shown in Figure 5.21. The Exponential region is so named to indicate the approximately exponential dependence of acoustic amplitude with K. The acoustic amplitude grows by nearly an order of magnitude over a region in which K increases by only 50%.

The dependence of acoustic amplitude on K_v (Figure 5.23) also appears strongly exponential, whereas the dependence on K_u is clearly not (Figure 5.22). The near-multivalued tendency exhibited in Figure 5.22 suggests that in the Exponential region, K_v is the more relevant parameter influencing acoustic amplitude.

Ultimately, it is apparent that the instability wave amplitude cannot be tied uniquely to a single acoustic amplitude for the entire range of instability wave amplitude. In the Saturation region, *i.e.*, in region of leveling or diminishing K, K_u and K_v, acoustic amplitude continues to increase at some angles θ.

We note that the structure of the instability wave has changed from the small amplitude wave described in linear stability theory to a nonlinear vortex by the time

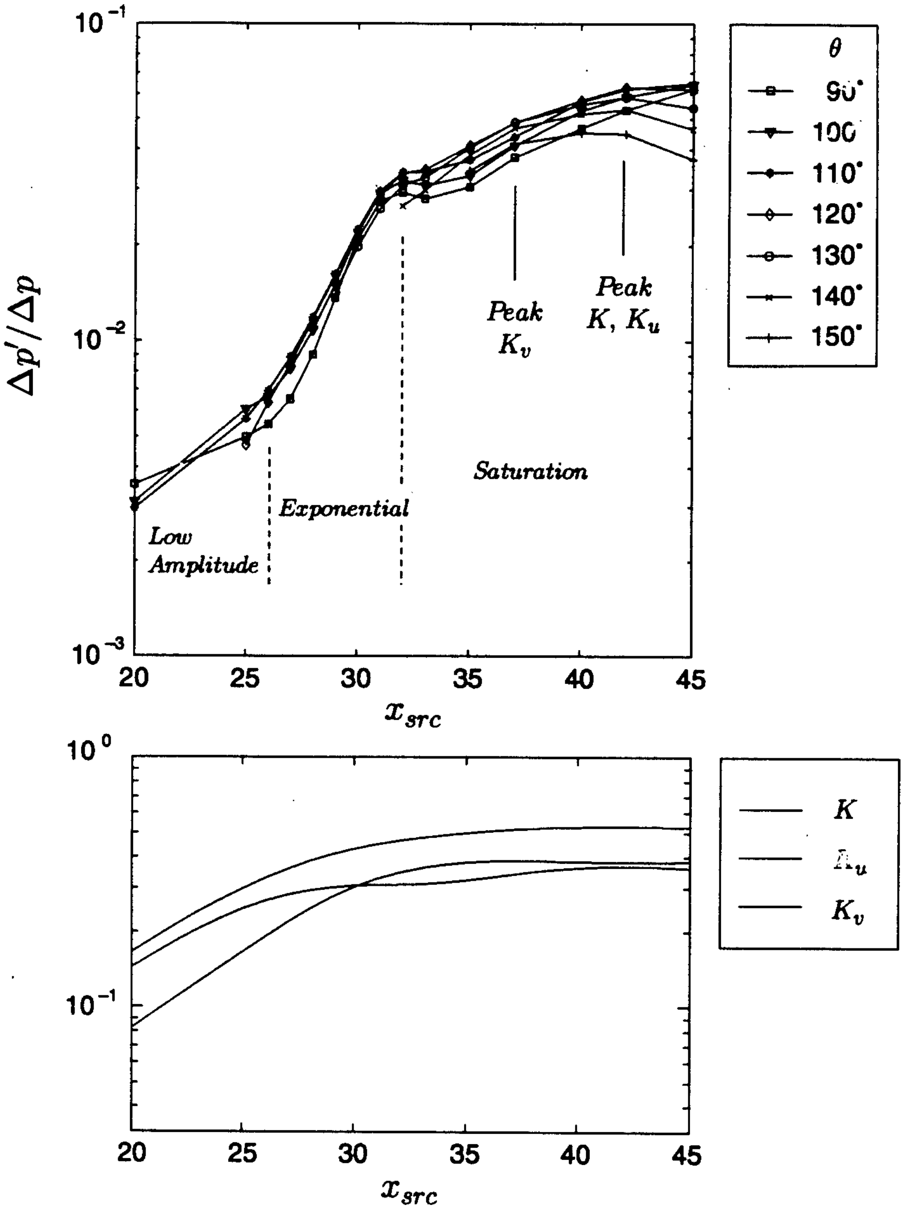

Figure 5.19: *Top*: Radiated acoustic pressure amplitude as a function of source location. *Bottom*: Instability wave amplitude for same source locations in SL1 shear layer.

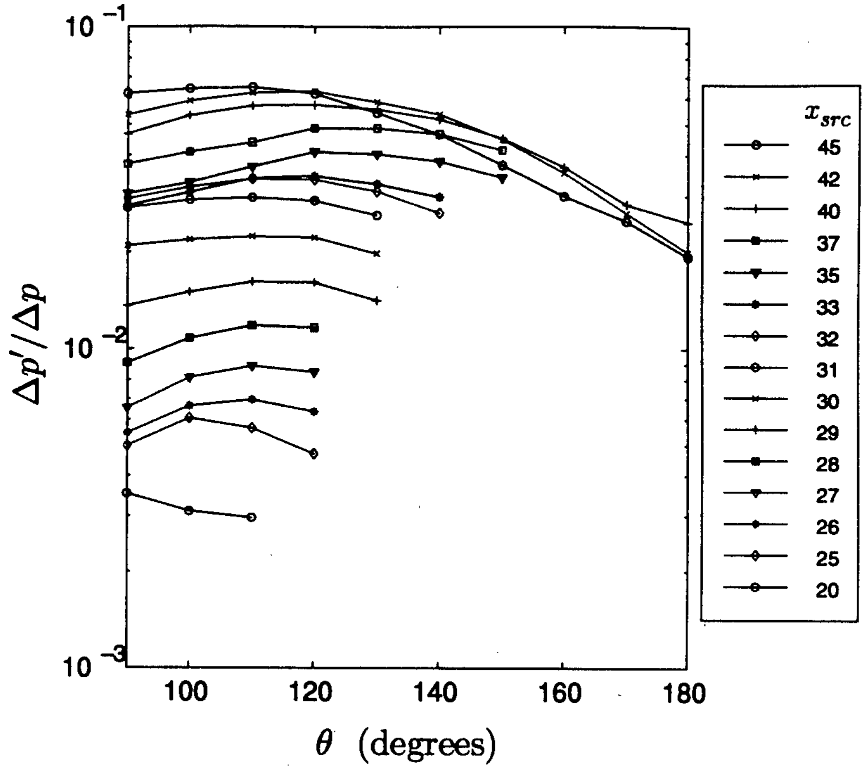

Figure 5.20: Radiated acoustic pressure amplitude versus observer angle θ about source. Acoustic amplitude is taken as mean-to-peak amplitude $\Delta p'$ normalized by G-wave amplitude Δp. Sampled at $r/\delta = 30$.

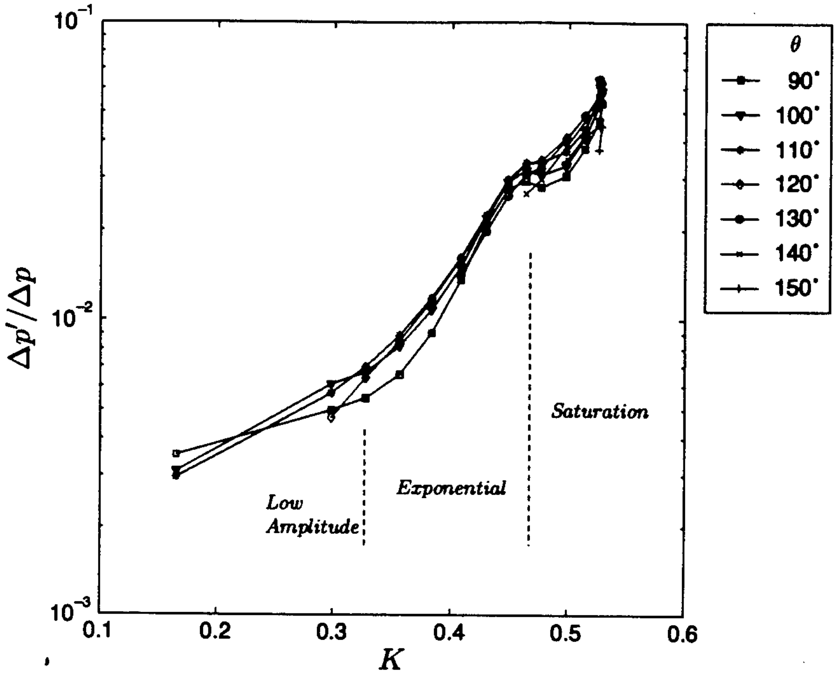

Figure 5.21: Radiated acoustic pressure amplitude versus instability wave amplitude K. Acoustic amplitude is taken as mean-to-peak amplitude $\Delta p'$ normalized by G-wave amplitude Δp. Sampled at $r/\delta = 30$ and $\theta = 90°$. Dashed lines divide curve into three regions of distinct behavior: "Low Amplitude" where radiation efficiency is low; "Exponential" where radiation levels grow exponentially with instability wave amplitude; and "Saturation", where radiation growth diminishes.

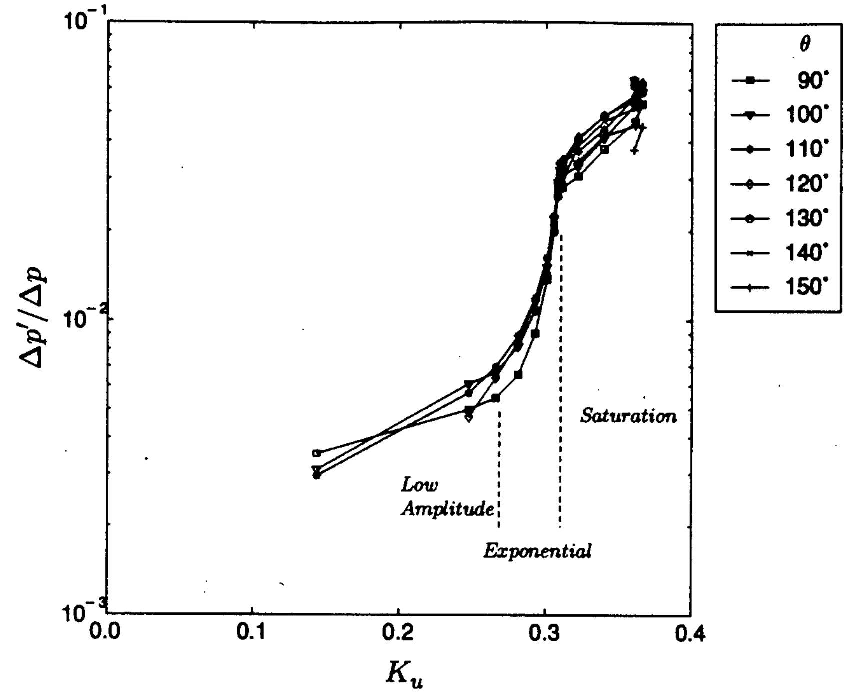

Figure 5.22: Radiated acoustic pressure amplitude as a function of instability wave amplitude component K_u.

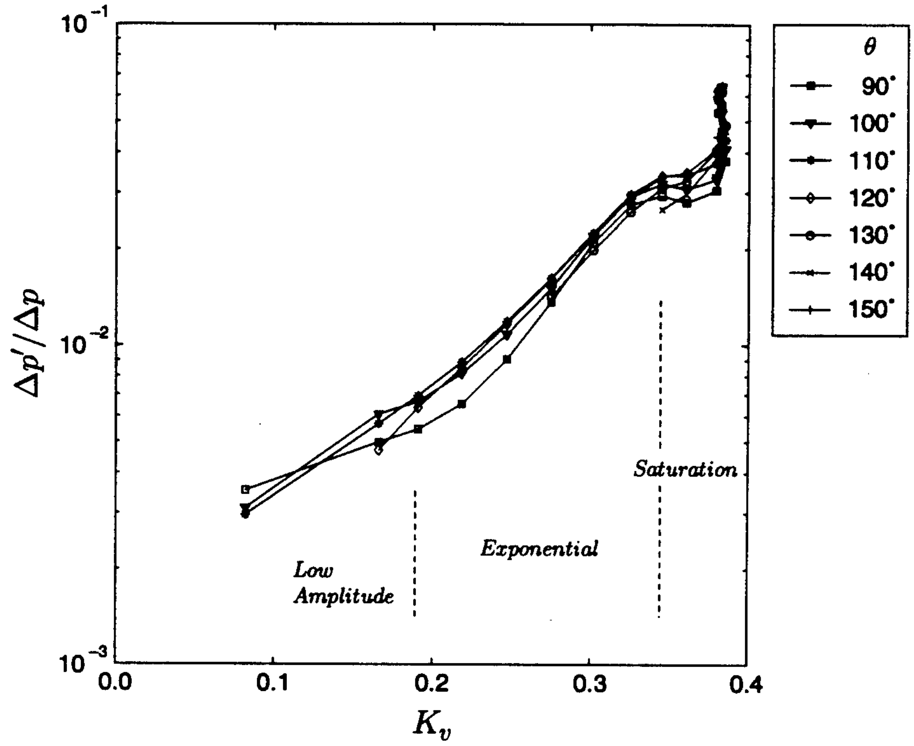

Figure 5.23: Radiated acoustic pressure amplitude as a function of instability wave amplitude component K_v.

it reaches the Saturation region. Hence parameters necessary to predict acoustic amplitude, and especially directivity, are likely to become more numerous and complex. The plots given in Figures 5.21, 5.22, and 5.23 stress this.

Within the Exponential region, the acoustic wave form undergoes a fundamental transition. As shown in Figure 5.24, the trace retains the shape of the incident G-wave at the upper extremes of the region ($x_{src} \approx 33$), and throughout the entirety of the Saturation region. However, for decreasing x_{src} or K, the Gaussian bump is absorbed into a more sinusoidal wave-form. We note that the low end of the exponential region is approximately the location at which the shear layer vortex begins to roll up. We noted earlier that the upper end of the exponential region (the local maximum in acoustic radiation) corresponds to the point at which the vortex experiences the initial "roll-over". In animated visualizations not presented here, we observe that part of the incident wave is transmitted while most of it is reflected back into the supersonic stream. Based on these observations the sound generation mechanism appears to be that of "leakage" or scattering of the incident wave at the upper end of the Exponential region—hence the compact wave form—whereas an entirely different mechanism is clearly dominant at the lower end. The transition process between these two mechanisms may be intimately related to the exponential growth in acoustic amplitude.

The evolution in wave form with instability wave amplitude observed above has some important ramifications with respect to previous interpretations of the screech sound field. As discussed in Section 1.2.2, the sound field of high aspect ratio rectangular screeching jets, which are nearly two-dimensional, has been observed to consist of a single, dominant "feedback shock". The reasons for the feedback shock being of compact wave form are not discussed in any of the studies in which it was observed. It is well known that the flapping mode of the rectangular screeching jet can be more intense than the flapping modes of the round jet [18]. It is proposed that the compact waveform of the feedback shock is due to the periodic leakage of the shock cell structure. In the flapping jet the instability waves are nearly saturated vortices. We have shown that the acoustic waves radiating from regions containing these high amplitude instability waves contain compact wave forms (resembling the incident wave);

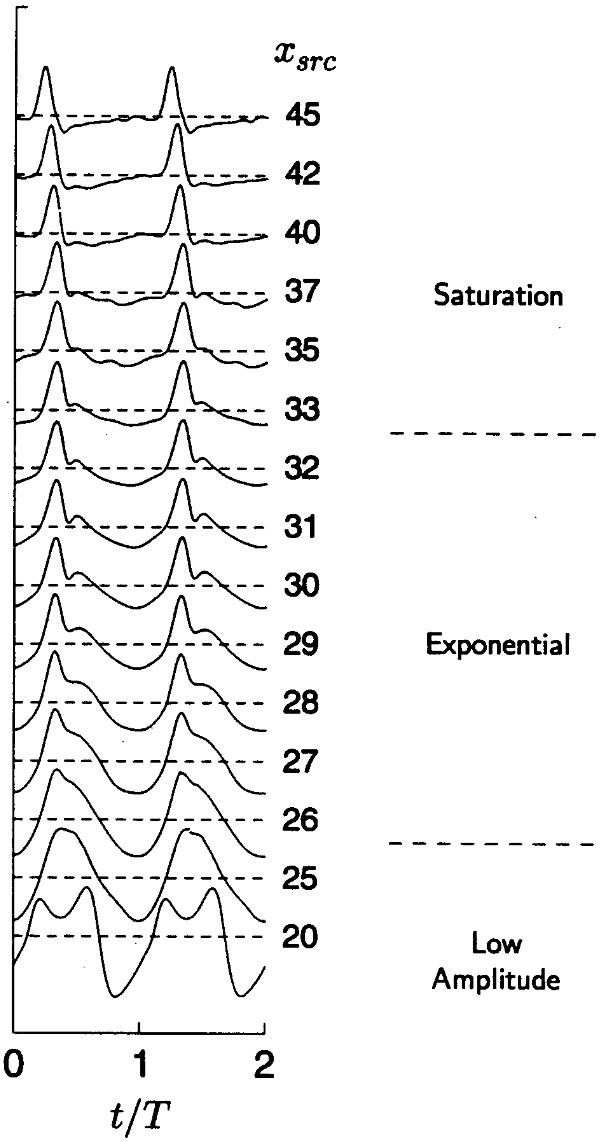

Figure 5.24: Acoustic pressure traces normalized to respective mean-to-peak amplitude (see Figure 5.19). Sampled at $r/\delta = 30$ and $\theta = 90°$. identified in Figure 5.21.

we have also shown that at lower instability wave amplitude, the sound emitted is more sinusoidal and of disproportionately lower amplitude. Hence, in the rectangular screeching jet, we would expect the rapid growth of the shear layer to favor the dominance of very few sources. On the other hand, in round jets, where the instability wave growth comparatively limited, the sources are of similar strength over the shock cell structure. The lower amplitude results in a sound field made up of the sinusoidal wave form. Together with the phased array property of the multiple sources, the uniformity in source strength and sinusoidal waveform lead to interference pattern responsible for the unique directivity of screech common reported.

5.3 Reduced mode representation of base flow

The temporal decomposition of the base flow as Fourier modes allowed us to study the sensitivity of high amplitude sound generation mechanism to the precise description of the shear layer. In particular, we compared the sound fields acquired from the interaction of the compression wave and a DNS base flow consisting of 1) its fundamental mode and 2) fundamental mode plus first harmonic, to the sound field of a fully represented DNS base flow. Visualizations such as in Figure 5.25, in which the base flow contains only the fundamental Fourier mode, clearly indicate that the same mechanism of sound generation is in effect, despite the highly modified base flow. The directivity is largely accounted for with the fundamental, as shown, in Figure 5.26. The addition of the first harmonic mode indicates eventual convergence toward the full representation. These results indicate that the fundamental sound generation mechanism can be recovered in a simplified representation of the base flow. This finding is exploited in the following section.

5.4 Stuart Vortex

The results in the previous section suggest that the radiation process is fundamentally that of scattering of the incident wave from instability waves of sufficiently high amplitude. The questions which remain are: What features or properties of the

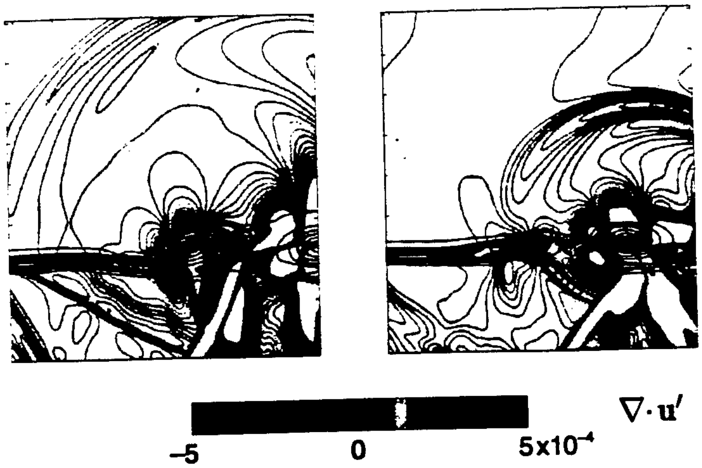

Figure 5.25: Visualization of reduced mode base flow for compression wave case. $Nk = 1$, SL1. See frames 1 and 5 of Figure 5.2 for the $N_k = 31$ counterpart.

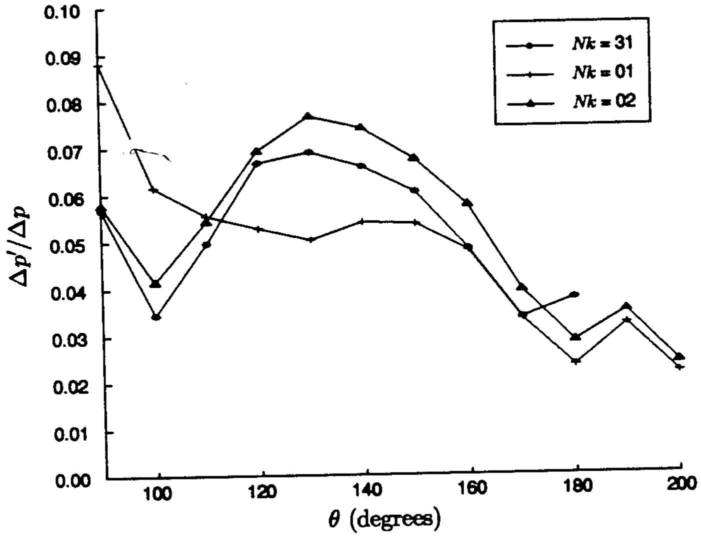

Figure 5.26: Reduced mode base flow for compression wave. Nk indicates the number of fluctuating modes retained; mean is considered $k = 0$. $Nk = 31$ represents maximum number of modes in data set.

instability wave field produces the windowing behavior? What explains the transition from the low amplitude behavior to the high amplitude, and finally, the saturated behavior?

As an alternative to an instability wave field based on numerical simulations, we consider instead one based on Stuart vortices [60]. The Stuart vortex mixing layer is a two-dimensional solution of the nonlinear incompressible Euler equations. The solution represents a periodic array of vortices convected in the mixing layer and for small amplitude becomes identical to the neutral wave of linearized stability theory. The vortex model has been the subject of an investigation into the two- and three-dimensional stability properites of coherent shear layers (Peirrehumbert and Widnall [35]). No compressible counterpart of this model is known.

In this section, we use the velocity field given by the Stuart vortex model to represent the instability wave field in the linearized Euler simulations. While this field is clearly not a solution to the compressible Euler equations, especially for large Mach number, it does represent a vortex laden shear flow. This flow is particularly useful for examining the effect of vorticity clumping. Given the degree of approximation, for simplicity we ignore thermodynamic variations.

5.4.1 Velocity Field

The velocity field is given as

$$\tilde{u} = \tilde{U}_c + \frac{C \sinh \tilde{y}}{C \cosh \tilde{y} + A \cos(\tilde{x} - \tilde{U}_c \tilde{t})} \tag{5.4}$$

$$\tilde{v} = \tilde{U}_c + \frac{A \sin(\tilde{x} - \tilde{U}_c \tilde{t})}{C \cosh(\tilde{y}) + A \cos(\tilde{x} - \tilde{U}_c t)} \tag{5.5}$$

where the tilde $\tilde{}$ indicates that the length scales have been normalized to streamwise instability wave number and the velocity scales have been normalized to half the velocity difference across the mixing layer. $\tilde{U}_c$ is the convection velocity of the vortices. The relationship between the amplitude parameters is

$$A = \sqrt{C^2 - 1} \tag{5.6}$$

Setting $A = 0$ results in a parallel shear layer with a $\tanh \tilde{y}$ profile. The $A = 0$ profile is wider than the shear layer which would realistically give rise to saturated vortices of the size, say, $A = 1$. A discussion of mean vorticity thickness is given below in Section 5.4.4.

We renormalize the velocity fields in Equations 5.5 and 5.5 to scales relevant to the our investigation by matching oscillation frequency ω and velocity difference $U_2 - U_1$. U_1 is taken as the velocity below the shear layer, and U_2 the velocity above. To rescale the velocities, we must take

$$\tilde{u} = 2u/(U_2 - U_1) \tag{5.7}$$

$$\tilde{v} = 2v/(U_2 - U_1) \tag{5.8}$$

$$\tilde{U}_c = U_c/(U_2 - U_1) \tag{5.9}$$

where for compatibility with the far fields, the convective velocity of the vortices must be the average of the velocities in the two streams:

$$U_c = (U_2 + U_1)/2 \tag{5.10}$$

The length scales are rescaled according to the streamwise wave number which maintains frequency compatibility for waves traveling at U_c. Therefore wave number $a = \omega/U_c$, and the coordinates are rescaled using

$$\tilde{x} = ax \qquad \tilde{y} = a(y - y_0). \tag{5.11}$$

Time is rescaled with

$$\tilde{U}_c\tilde{t} = \omega t. \tag{5.12}$$

If we define $b \equiv (U_2 - U_1)/2$, $\eta \equiv a(y - y_0)$, $\xi \equiv a(x - U_c t)$, and continue to require $U_c \equiv (U_2 + U_1)/2$, the renormalized velocity field simplifies to

$$u = U_c + b\frac{C \sinh \eta}{C \cosh \eta + A \cos \xi} \tag{5.13}$$

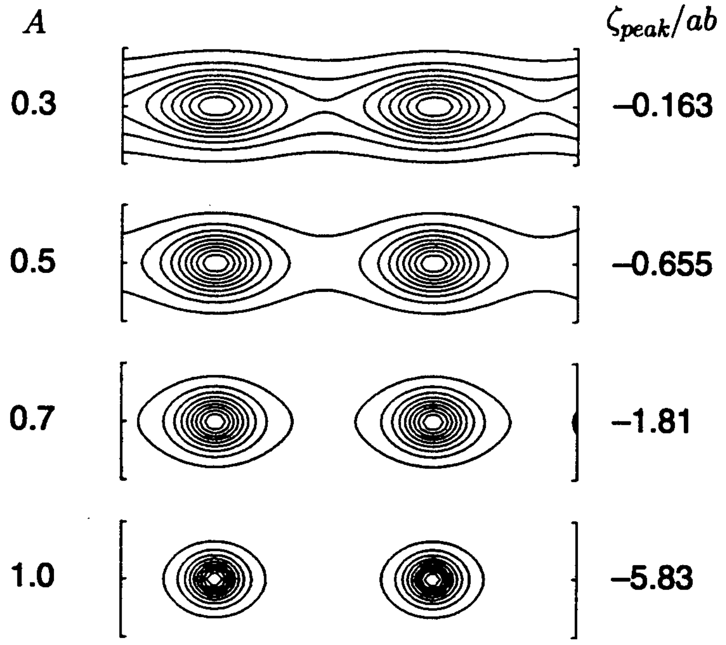

Figure 5.27: Contours of instantaneous vorticity for Stuart vortex mixing layer. Contour interval $\Delta\zeta = \zeta_{peak}/10$.

$$v = b\frac{A\sin\xi}{C\cosh\eta + A\cos\xi} \tag{5.14}$$

5.4.2 Vorticity

The vorticity field is

$$\begin{aligned}\zeta &= \frac{\partial v}{\partial x} - \frac{\partial u}{\partial y} = \frac{d\xi}{dx}\frac{\partial v}{\partial \xi} - \frac{d\eta}{dy}\frac{\partial u}{\partial \eta} \\ &= ab\left[\frac{A\cos\xi - C\cosh\eta}{C\cosh\eta + A\cos\eta} + \frac{A^2\sin^2\xi + C^2\sinh^2\eta}{(C\cosh\eta + A\cos\xi)^2}\right] \qquad (5.15) \\ &= -\frac{ab}{(A\cos\xi + C\cosh\eta)^2} \qquad (5.16)\end{aligned}$$

In Figure 5.27 we plot contours of instantaneous vorticity for several values of vortex amplitude A. With increasing A, the vorticity is concentrated about the vortex cores; the vortices themselves become relatively compact.

5.4.3 Instability Wave Amplitude

The instability wave amplitude is defined as before in Equation 3.1. δ, the initial vorticity thickness of the DNS shear layer, is taken as the reference length to make comparisons possible. It does not correspond to the vorticity thickness of the Stuart vortex mixing layer. The fluctuation velocities u' and v' taken with respect to mean shear layer,

$$\overline{u} = \frac{1}{2\pi}\int_0^{2\pi} u(\eta,\xi)d\xi = U_c + b\frac{C\sinh\eta}{\sqrt{C^2\sinh^2\eta+1}} \tag{5.17}$$

$$\overline{v} = \frac{1}{2\pi}\int_0^{2\pi} v(\eta,\xi)d\xi = 0, \tag{5.18}$$

are

$$u' = u-\overline{u} = b\frac{C\sinh\eta}{C\cosh\eta + A\cos\xi} - b\frac{C\sinh\eta}{\sqrt{C^2\sinh^2\eta+1}} \tag{5.19}$$

$$v' = v-\overline{v} = b\frac{A\sin\xi}{C\cosh\eta + A\cos\xi} \tag{5.20}$$

Note the density is taken as constant. The instability wave amplitude K, as defined by Equation 3.1, is plotted in Figure 5.28 as a function of Stuart vortex amplitude A. We also plot the components K_u and K_v, which are defined by equation 3.3. Curve fits to these functions are given by

$$K(A) = 0.969222A - 0.0765651A^2 - 0.180070A^3 + 0.0635244A^4 \tag{5.21}$$

$$K_u(A) = 0.504203A - 0.0218720A^2 - 0.0812319A^3 + 0.0261107A^4 \tag{5.22}$$

$$K_v(A) = 0.798699A - 0.0721922A^2 - 0.156105A^3 + 0.0563288A^4 \tag{5.23}$$

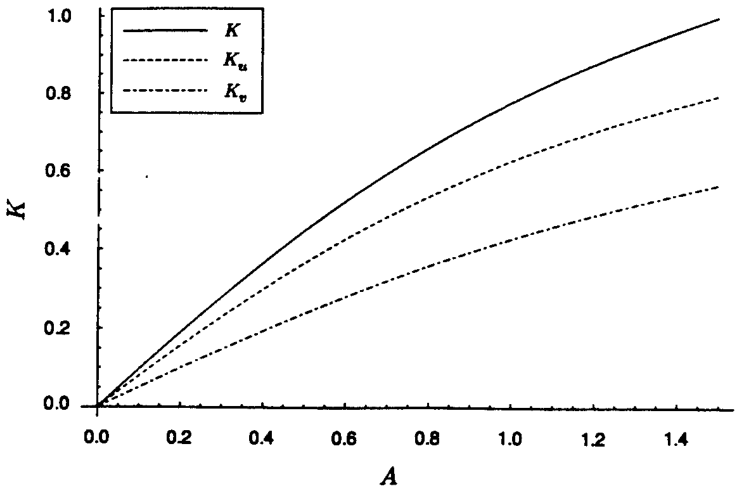

Figure 5.28: Instability wave amplitude K (Equation 3.1) and its components, K_u and K_v (Equation 3.3), for the Stuart vortex mixing layer. A is the amplitude coefficient.

5.4.4 Mean Vorticity Thickness

The mean vorticity thickness of the Stuart mixing layer based on $\overline{u}$ given in Equation 5.18 is

$$\delta_{Stuart} = \frac{|U_2 - U_1|}{|\partial\overline{u}/\partial y|_{max}} \tag{5.24}$$

$$= \frac{|U_2 - U_1|}{|ab\sqrt{A^2+1}|} \tag{5.25}$$

$$= \frac{|U_1 + U_2|}{\omega\sqrt{A^2+1}} \tag{5.26}$$

For the cases we consider, $U_1 = 1$, $U_2 = 0$, and $\omega = 0.1643$, giving $\delta_{Stuart}\Big|_{A=0}/\delta =$ 6.085. For $A > 0$ the mean vorticity thickness decreases as shown in Figure 5.29.

5.4.5 Comparison to previous results

We begin by comparing the acoustic field due to the interaction of the G-wave with the Stuart vortex base flow with the acoustic field due to interaction with the SL1 forced shear layer base flow. We consider matching instability amplitude parameters

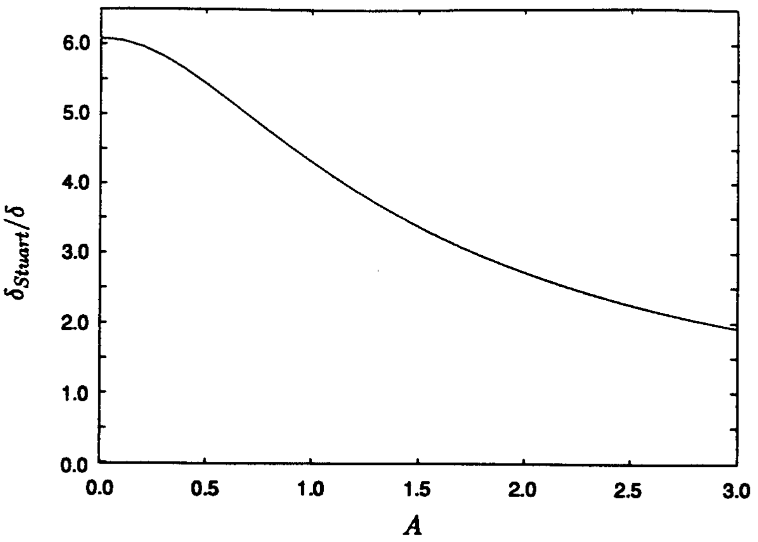

Figure 5.29: Vorticity thickness of Stuart vortex compared to initial vorticity thickness used in SL1 base flow for $\omega = 0.164345$.

SL1 Case	x_{src}	Matching i.w. Amp	$A(K)$ or $A(K_v)$	Stuart Case A
G1	40	$K = 0.526$	0.603	0.6
G10	31	$K = 0.448$	0.501	0.5
G8	33	$K_v = 0.361$	0.493	0.5
G11	31	$K_v = 0.349$	0.405	0.4

Table 5.5: Parameters based on instability wave amplitude for matching Stuart base flow results to those obtained with the DNS base flow.

of K and K_v between the base flow cases. The consideration of K_v is motivated by the observation (presented at the end of the next section) that the vertical velocity component is responsible for most of the radiation. The matched cases are outlined in Table 5.5.

At the source location $x_{src}/\delta = 40$ in the SL1 shear layer, $K = 0.526$. Matching this parameter in the Stuart vortex field requires that $A \approx 0.6$. Visualization obtained from this case (Figure 5.30) indicates that despite its simplifications, the Stuart model retains the properties necessary to produce the same kind of interaction and sound field seen in the DNS shear layers. The vorticity in the Stuart vortex field is more concentrated, though peak levels are comparable to the SL1 vortices.

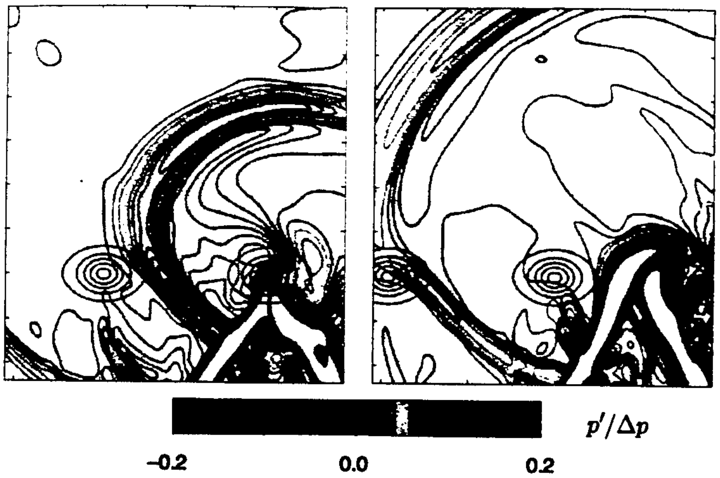

Figure 5.30: Visualization of interaction of G-wave with Stuart vortex base flow for $A = 0.6$. Vorticity contour increment is $\Delta\zeta/(U_1/\delta) = 0.1$.

Despite these similarities, we find that neither K nor K_v serve as a reliable parameter for matching instability waves and acoustic radiation levels among different base flows. In Figure 5.31 we compare the directivity of the acoustic field in a Stuart vortex case ($A = 0.6$ and $A = 0.5$) to their DNS base flow counterparts, matched based on K. For $A = 0.6$, the magnitude and peak directivity are comparable and would suggest that K is a good indicator of acoustic emission potential. However, in the acoustic results based on a matching at $A = 0.5$, there is a large difference in both peak directivity and overall magnitude. K_v also proves to be an unreliable predictor for acoustic amplitude. For the results presented in Figure 5.32 we match the base flows according to K_v. Large quantitative differences in the resultant fields are observed for both matching points ($A = 0.5$ and $A = 0.4$).

5.4.6 Variation with Stuart vortex amplitude

The analytic description of the Stuart vortex mixing layer enables us to investigate the instability-wave compression-wave interaction process and resultant acoustic radiation for a wide range of amplitude settings. We continue to use the G-wave to minimize

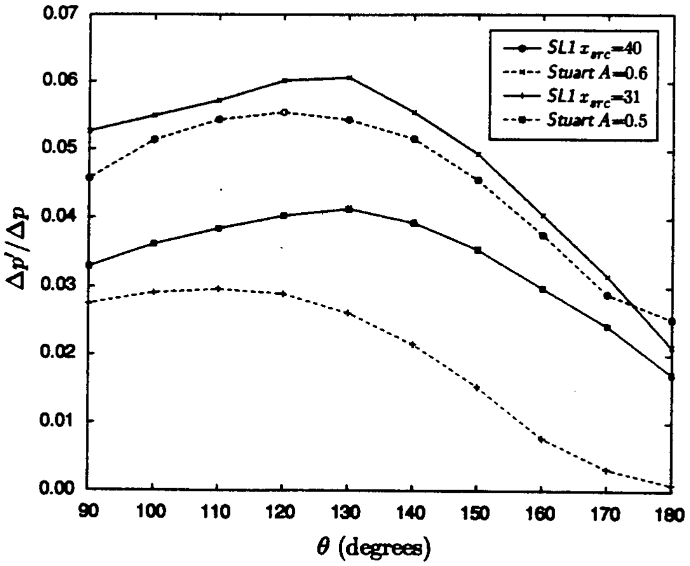

Figure 5.31: Acoustic directivity for base flow with matched K: SL1 Case G1 ($x_{src} = 40$) vs. Stuart vortex $A = 0.6$, and SL1 Case G10 ($x_{src} = 30$ vs. Stuart vortex $A = 0.5$).

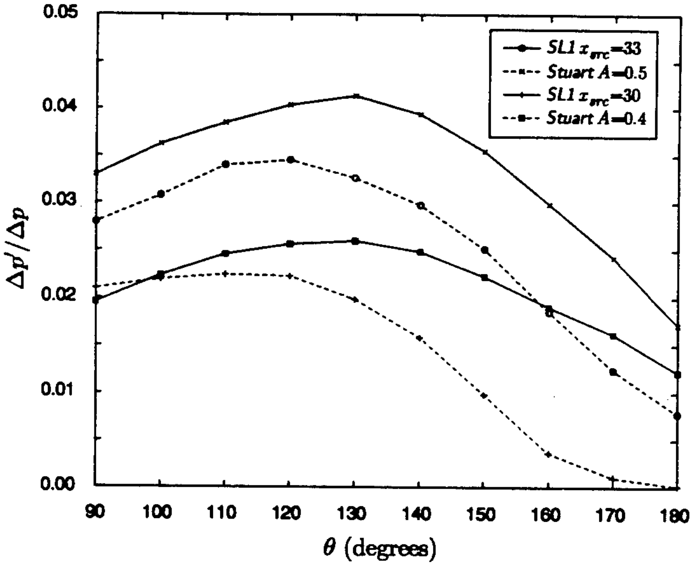

Figure 5.32: Acoustic directivity for base flow with matched K_v: SL1 Case G1 ($x_{src} = 33$) vs. Stuart vortex $A = 0.5$, and SL1 Case G10 ($x_{src} = 30$ vs. Stuart vortex $A = 0.4$).

deflection effects. The Stuart mixing layer amplitude parameter A is varied from 0.03 to 1.5.

The pressure field visualizations shown Figure 5.33 for several A indicate that there is a fundamental change in the sound generation mechanism with A. At $A = 0.05$, the Stuart mixing layer is only weakly unsteady. The incident G-wave undergoes only small changes in position and its reflection is well defined. The resultant sound produced is a small fraction of the incident wave amplitude, and its waveform is broad. With increased A, the vorticity in the mixing layer becomes more concentrated. Oscillations experienced by the incident wave increase, and the reflection is less well defined. At the same time, the acoustic amplitude rises, and the wave-form becomes more compact. By $A = 0.8$, the vortices are essentially discrete entities, causing the incident G-wave to experience large oscillations in position. The leakage mechanism as a means of producing the sound is apparent. As such the waveform of the sound field is very compact, the acoustic amplitude having risen still further. For very high A, the mixing layer vortices are tightly concentrated, and the G-wave reflection is essentially nonexistent in the steady sense. However, the acoustic field does not change appreciably from the $A = 0.8$ case, other than to exhibit stronger reflections from the interaction of the acoustic wave with upstream vortices. It is clear that acoustic saturation has occurred.

To explore the transition in the sound field in more depth, we examine the dependence of the amplitude, directivity, and wave form of the sound field on A. In Figures 5.34 and 5.35 we plot the acoustic amplitude for selected angles against A. As in the DNS base flow cases, we identify three regions of acoustic behavior: Linear (instead of "Low Amplitude"), Exponential, and Saturation. The logarithmic axes in Figure 5.34 are used to show that the acoustic amplitude varies linearly with A. The acoustic amplitude rises roughly exponentially with A until approximately $A = 0.7$, above which the acoustic field saturates and becomes comparatively invariant with A.

In Figure 5.36 we plot the directivity of the acoustic field. The direction of peak radiation shifts from upstream (approximately 130°) in the linear and exponential regions, to downstream (to angles no greater than $\theta = 90°$) after saturation.

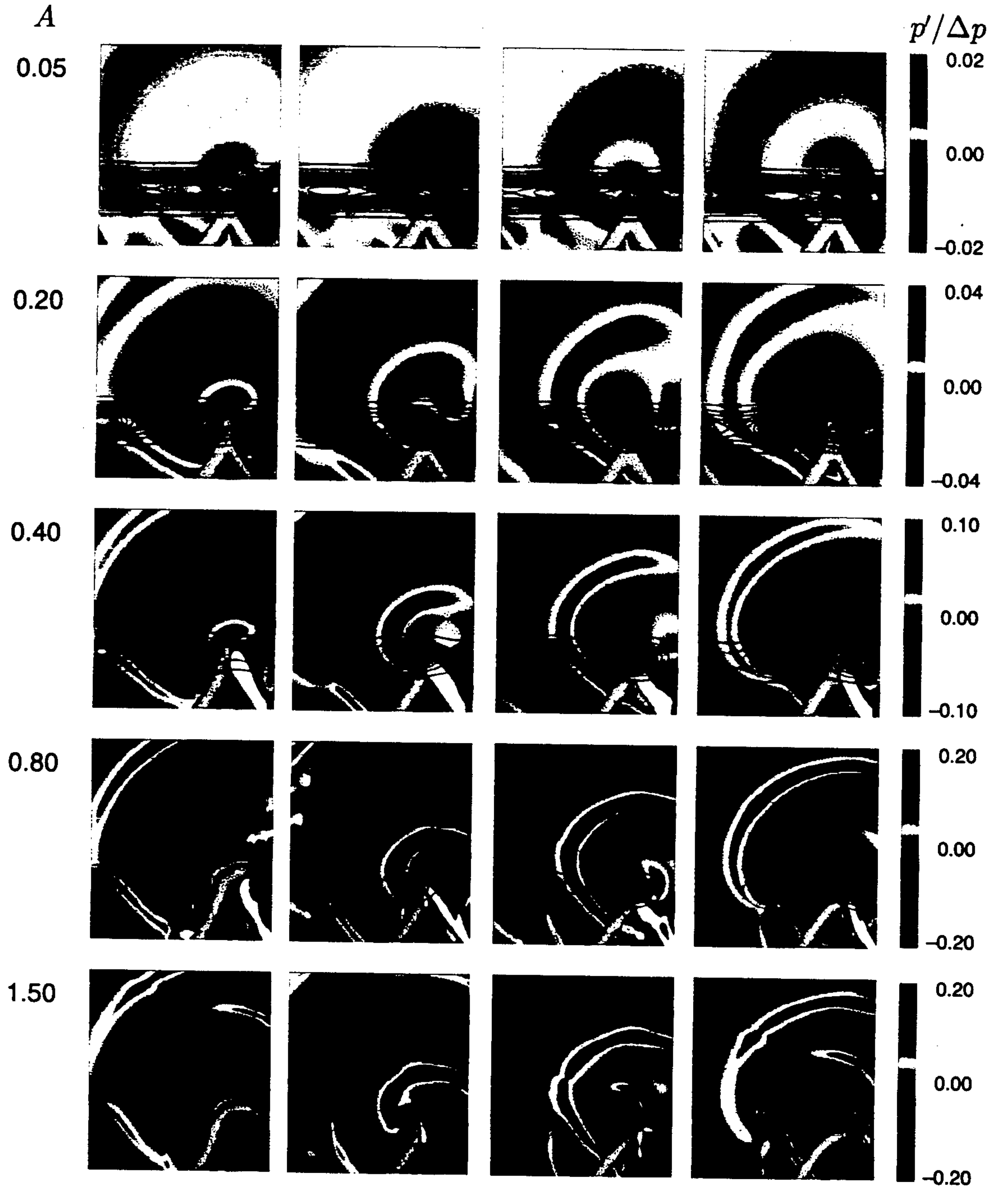

Figure 5.33: Visualization of perturbation pressure field and base flow vorticity at various Stuart vortex amplitude A.

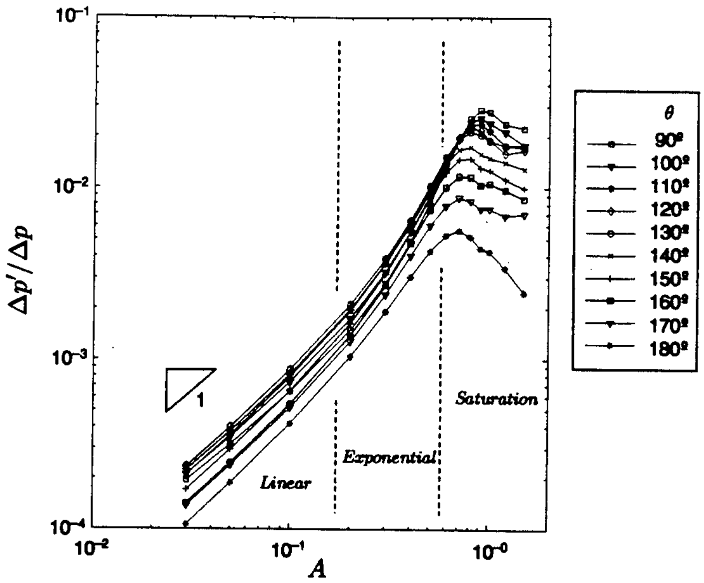

Figure 5.34: Dependence of acoustic amplitude on amplitude coefficient A. Log-Log scales to show linear dependence on A at low A.

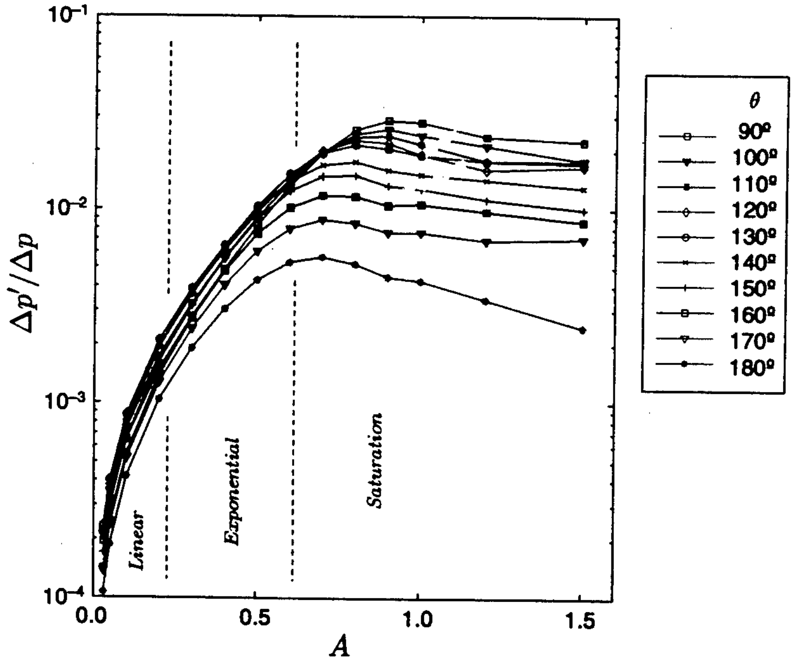

Figure 5.35: Dependence of acoustic amplitude on amplitude coefficient A

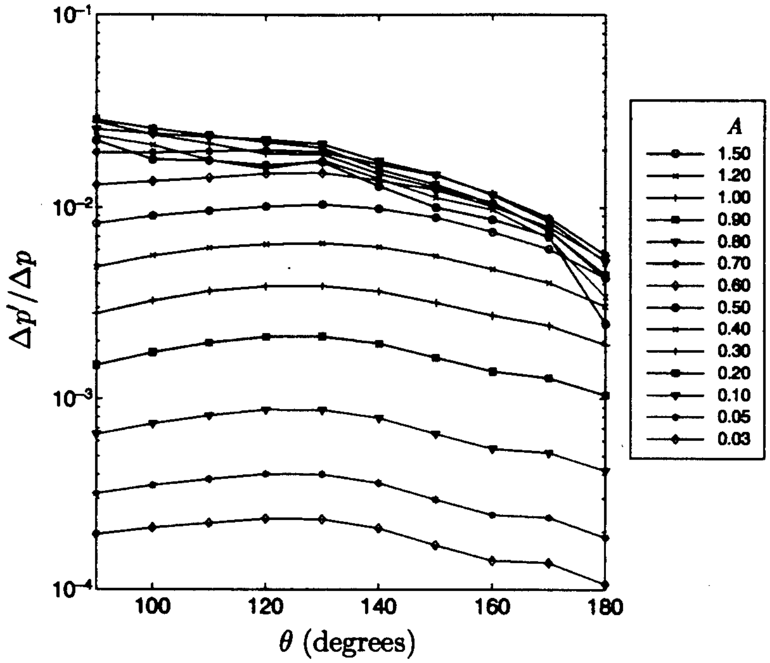

Figure 5.36: Acoustic directivity for interaction between Stuart vortex mixing layer and the G-wave for several values of amplitude coefficient A. Sampled at r/δ=30.

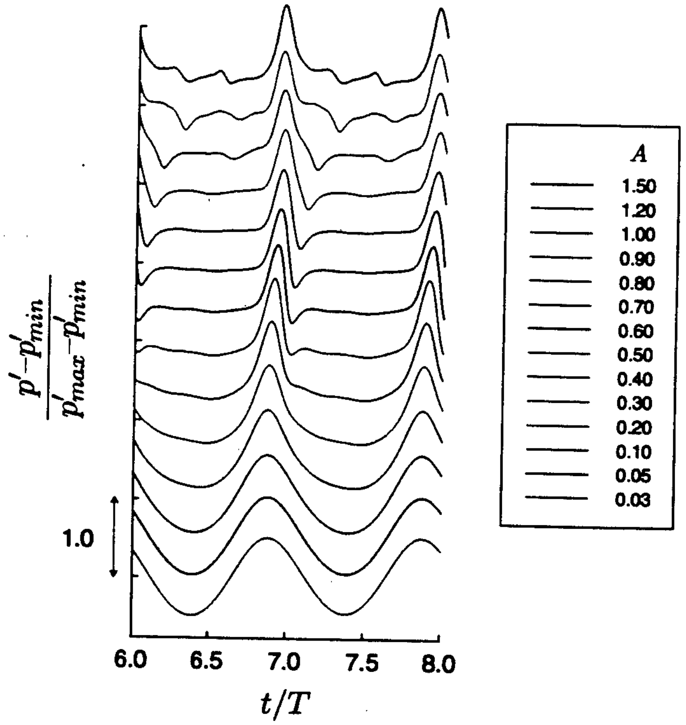

Figure 5.37: Comparison of traces at various values of vortex amplitude A.

The saturation phenomenon is also manifested in terms of wave form. Figure 5.37 illustrates how the waveform is essentially sinusoidal for low A, then acquires the G-wave pulse as A increases through the Exponential region ($0.2 \leq A \leq 0.7$) and maintains that wave-form in the Saturation region. Additional small disturbances appear at high A; these are identified as reflections arising from the radiated acoustic wave interacting with other freely propagating vortices.

Finally, we consider the individual suppression of fluctuation velocities u' and v' in the Stuart mixing layer model to obtain an indication of the relative importance of each component in the "leakage" process. Setting $A = 1.0$ to ensure saturated radiation conditions under normal circumstances, we set $u' = 0$ while retaining $v' \neq 0$ and then $v' = 0$ with $u' \neq 0$. We compare the results to the unsuppressed case for $A = 1.0$. As shown in the directivity plots in Figure 5.38, the vertical component of velocity alone actually enhances the radiation process at upstream θ. The acoustic

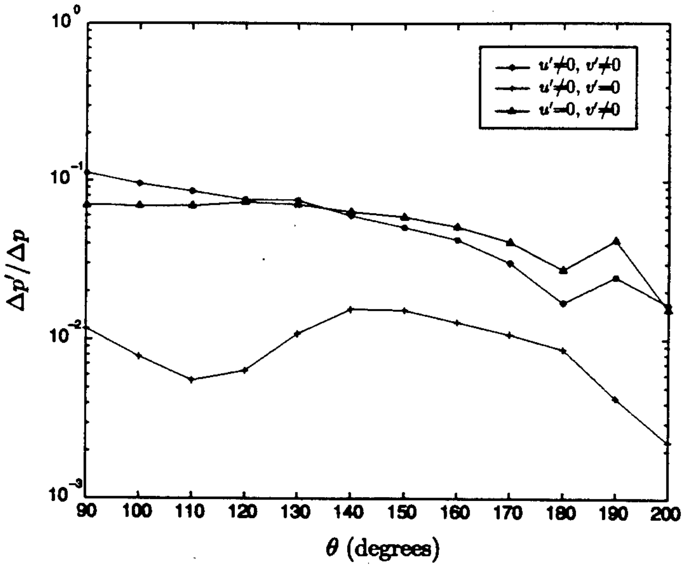

Figure 5.38: Comparison of directivity in which fluctuation velocity components u' and v' are successively suppressed.

field due to the streamwise velocity fluctuation u' alone, however, falls nearly an order of magnitude short at transverse angles θ.

5.4.7 Discussion of Stuart vortex results

In this section we considered the interaction of the G-wave with the Stuart vortex mixing layer. First, we established that despite the simplifications assumed in using the vortex model for a shear layer base flow, the basic mechanism for acoustic radiation at high amplitude is retained. For sufficiently high vortex amplitude A, the "leakage" mechanism for sound generation is observed. Only the details in overall acoustic amplitude and directivity are somewhat modified.

As with the base flow cases based on the Navier-Stokes shear layer SL1, we identified three regions of distinct behavior of the acoustic field with respect to a measure of instability wave amplitude. In Low Amplitude, or more precisely "Linear", region, we found that the acoustic amplitude varies directly with Stuart vortex amplitude A. In this region, the acoustic wave-form is sinusoidal. In the Exponential region $(0.1 \sim 0.2 \leq A \leq 0.7)$, the wave-form undergoes a transition from sinusoidal to one resembling the incident wave-form. The acoustic amplitude experiences exponential growth with A. In the saturation region ($A \geq 0.7$), the incident wave-form is sustained in the acoustic field without substantial change in acoustic amplitude. However, the directivity shifts from upstream ($\theta = 130°$) to downstream at high A.

It is clear that over the range of vortex amplitude A, the mechanism for sound generation experiences a transition. The sinusoidal wave-form in the acoustic field and linear dependence on A in the Linear region suggest that the mechanism is a simple linear interaction between the incident wave and the instability wave (e.g., as conceived by Tam [62]). In the Saturation region, the preservation of the incident wave-form in the acoustic field at high A supports the notion that the incident wave is periodically "leaked" through the shear layer through a scattering, or unsteady refraction, mechanism. The acoustic amplitude levels in the Saturation region are one to two orders of magnitude higher than in the Linear region. The acoustic amplitude rises exponentially with A between the two regions. If one assumes that in this Exponential region the scattering mechanism overtakes the linear mechanism with increasing A, then one may conclude that the scattering mechanism is in a sense a fundamentally more efficient method for sound generation.

Finally, one must ask how representative of the realistic (Navier-Stokes) shear layer is the Stuart vortex model. While generally similar behavior is observed between the acoustic fields generated using, respectively, the DNS and Stuart base flows, the details of the mixing layers themselves contain some important differences. First with increasing instability wave amplitude K, the vorticity thickness of the DNS shear layer increases. However, in the case of the Stuart vortex, vorticity thickness *decreases* with vortex amplitude A. Furthermore the vortices in the DNS shear layer saturate, i.e., they reach a maximum amplitude and have finite cores. In the Stuart model we can produce arbitrarily concentrated vortices by continuing to raise A beyond levels one would realistically expect to observe in the shear layer. The relationship between A and K is not linear at higher A, further skewing a direct comparison. Nevertheless, despite these differences, the great similarities observed in the overall acoustic radiation behavior give us confidence that the Stuart vortex results are valid enough for obtaining useful insight into the screech generation mechanism.

5.5 Summary of Linearized Euler Simulations

In this chapter we have shown that simulations based on the linearized Euler equations is an appropriate context for investigating the interaction of a compression wave and a realistic forced shear layer and the resultant acoustic field. The success of this approach indicates that the interaction process itself is largely the effect of shear layer on the incident wave and does not intrinsically depend on the modification of the shear layer by the incident wave. We were able to reproduce the "leakage" effect observed previously in the Navier-Stokes equations.

With the introduction of the G-wave, we were able to substantially increase the fidelity of our acoustic measurements while retaining similar interaction and radiation behavior. We conducted a detailed survey of the dependence of the acoustic field on the instability wave amplitude and were able to identify three distinct regions of behavior: 1) Low Amplitude, 2) Exponential, and 3) Saturation.

We investigated two simplifications to the base flow, first the modal reduction of its temporal Fourier representation, and then the introduction of the Stuart vortex mixing layer model. The use of the mean plus a single unsteady mode for the base flow was found sufficient to produce the "leakage" effect. Additional modes were found only to refine the directionality. The use of the Stuart model enabled us to explore the acoustic saturation process in greater detail. With the Stuart model we were able to reproduce the Exponential and Saturation regions found for the more realistic base flow, and found strong evidence that the behavior of the Low Amplitude region is indeed linear. We established that an absolute maximum radiation level exists.

Chapter 6

Geometrical Acoustics

We have used numerical simulations with varying degrees of idealization to refine our understanding of the sound generation process in a screech-type source. The generation process was studied over a range of instability wave and compression wave amplitudes. A thresholding and saturation process was observed whereby the radiated sound levels grow exponentially with instability wave amplitude up to a point. The acoustic field was found to scale with the amplitude of the incident compression wave.

In the process of modeling we simplify the description of a physical phenomenon by stripping away the less important aspects and are left with the fundamental mechanism responsible for its behavior. We have already taken steps toward a model of the instability-wave shock interaction. The first step was to replace the shock with a weak compression wave. With this we were able to regard the incident wave amplitude as a small parameter, where in the next step we decoupled it from the large amplitude shear layer disturbances in the linearized Euler simulations. A change of description of the compression wave to the G-wave helped reinforce the notion that processes such as thresholding can be regarded more in the light of acoustic scattering; the specifics of the incident wave are not important. A gross simplification of the shear layer through the use of the velocity field of Stuart vortex solution suggests that there is something intrinsic to a vortex laden mixing layer which permits the periodic "leakage" we observe.

In this chapter we explore a different approach to describing the instability-wave shock interaction and sound radiation phenomenon: geometrical acoustics. In geometrical acoustics, we build on the notion that the large amplitude, vortical nature of the flow field is important for explaining the sound generation as a scattering process. The shock is thereby modeled as a standing acoustic wave which travels through an unsteady flow field.

6.1 Methodology

We make use of classical geometrical acoustics for a time- and space-varying medium. The assumptions one makes in deriving the basic equations of geometrical acoustics are restrictive. The first assumption is that the length scales associated with variations in the base flow are large compared to the acoustic wavelength. This is known as the high wave number limit. This restriction is of practical importance when computing the amplitude of the acoustic field; greater uniformity in the base flow reduces the likelihood of caustics, that is, mathematical singularities caused by wave-front focusing. In our flow the length-scales associated with the instability waves are in fact comparable to the overall acoustic wavelength. However, the overall acoustic wavelength may not be the most relevant length scale. Instead, the length scales associated with the details of the shock, which are much smaller than the acoustic wavelength, may be more important. Still, wave-front focusing does occur, even in the steady case, and acoustic amplitude is not considered in the analysis of this chapter. A second assumption in geometrical acoustics is that the time scales associated with the unsteadiness of the base flow are long compared to the acoustic time scales. In our flow, this assumption is clearly violated as the convection Mach number of the instability waves is approximately 0.75. Nevertheless, it will be shown that the geometrical acoustics approach does yield compelling qualitative results.

6.1.1 Formulation of governing equations

The eikonal equation

$$\frac{\partial\Theta}{\partial t}+\mathbf{v}\cdot\nabla\Theta=-c|\nabla\Theta| \tag{6.1}$$

forms the basis of computing ray trajectories and wave fronts in geometrical acoustics. Θ is the phase function of the acoustic wave, and its gradient $\nabla\Theta$ is parallel to the wave-front normal, $\mathbf{n}$. $\mathbf{v}$ is the velocity field of the base flow and c is the base flow speed of sound. In general, both $\mathbf{v}$ and c vary in time and space.

A detailed derivation of the eikonal equation is given in Ostashev [31]. We give a brief summary of the derivation here. The eikonal equation arises from taking the Euler equations linearized about an unsteady mean flow and recasting the fluctuating quantities as harmonic functions in space and time:

$$(p', u_i', \rho', s') = (\hat{p}, \hat{u}_i, \hat{\rho}, \hat{s})\exp(ik_0\Theta) \tag{6.2}$$

Here, k_0 is the reference value of the wave number and $\Theta(\mathbf{R}, t)$ is the phase function ($\mathbf{R}$ being the position vector). A substitution of Equation 6.2 into the linearized Euler equations leaves a portion of the equations different from the remaining terms by factors of $k_0 l$ and $k_0 c_0/\Omega$, where l and Ω are the characteristic base flow length and frequency scales. In the high frequency limit we can assume that $k_0 l \gg 1$ and $k_0 c_0/\Omega \gg 1$, allowing us to consider solutions in terms of the small parameters $1/k_0 l$ and $\Omega/(k_0 c_0)$. Collecting terms according to "Debye series" expansions, based on these parameters, of the harmonic function coefficients, a recurrence relationship between coefficients of order k_0^n and k_0^{n-1} can be found. For equations of the order k_0^1, coefficients of order k_0^{n-1} do not exist and the right hand side of the equations vanish. The resulting equations form a linear system in the lowest order coefficients, which is homogeneous. For solutions to be nontrivial, the determinant of the coefficient matrix of this system must be zero, a condition guaranteed by the eikonal equation, Equation 6.1.

6.1.2 Solution of the governing equation

The eikonal equation is solved in a similarity coordinate following the sound wave. Such a strategy involves defining a Hamiltonian function H so that the differential equation can be written

$$H(\mathbf{R}, t, \Theta, \mathbf{b}, q) = 0 \tag{6.3}$$

where $\mathbf{b} \equiv \nabla\Theta$ and $q \equiv \Theta_t = \partial\Theta/\partial t$. The Hamiltonian function of choice (*e.g.*, see Zauderer [81], p. 82) is

$$H[\mathbf{R}, t, \Theta, \mathbf{b}, q] = \Theta - \Theta_0 - (\mathbf{R} - \mathbf{R_0}) \cdot \mathbf{b} - q(\mathbf{b})(t - t_0) \tag{6.4}$$

If we rewrite eikonal equation as

$$F[\mathbf{R}, t, \Theta, \mathbf{b}, q] = \left[\frac{\partial\Theta}{\partial t} + \mathbf{v} \cdot \nabla\Theta\right]^2 - c^2(\nabla\Theta)^2 = 0 \tag{6.5}$$

then we can define the five *characteristic equations*:

$$\begin{aligned}
\frac{d\mathbf{R}}{d\tau} &= F_{\mathbf{b}} && (6.6)\\
\frac{dt}{d\tau} &= F_q && (6.7)\\
\frac{d\Theta}{d\tau} &= \mathbf{b} \cdot F_{\mathbf{b}} + qF_q && (6.8)\\
\frac{d\mathbf{b}}{d\tau} &= -F_{\mathbf{R}} - F_\Theta \mathbf{b} && (6.9)\\
\frac{dq}{d\tau} &= -F_t - F_\Theta q && (6.10)
\end{aligned}$$

where τ is the characteristic variable. Evaluating the right hand side of these equations and renormalizing the coordinates by $dt/d\tau$, time t becomes the characteristic variable, and we obtain our governing characteristic equations.

$$\begin{aligned}
\dot{\mathbf{R}} &= \frac{d\mathbf{R}}{dt} = \mathbf{v} - \frac{c^2\mathbf{b}}{q + \mathbf{v} \cdot \mathbf{b}} && (6.11)\\
\dot{\Theta} &= \frac{d\Theta}{dt} = 0 && (6.12)
\end{aligned}$$

$$\dot{\mathbf{b}} = \frac{d\mathbf{b}}{dt} = \frac{(\mathbf{b}\cdot\mathbf{b})\nabla c^2}{2(q+\mathbf{v}\cdot\mathbf{b})} - (\mathbf{b}\cdot\nabla)\mathbf{v} \tag{6.13}$$

$$\dot{q} = \frac{dq}{dt} = \frac{(\mathbf{b}\cdot\mathbf{b})}{2(q+\mathbf{v}\cdot\mathbf{b})}\frac{\partial c^2}{\partial t} - \mathbf{b}\cdot\frac{\partial \mathbf{v}}{\partial t} \tag{6.14}$$

$$\tag{6.15}$$

where, again, $q = \frac{\partial\Theta}{\partial t}$ and $\mathbf{b} = \nabla\Theta$. Note that $q = \partial\Theta/\partial t \neq d\Theta/dt = 0$.

The solution to these equations represent the ray trajectories of acoustic waves. $\dot{\mathbf{R}}$ is the acoustic propagation velocity along a ray. Along the characteristic moving at $\dot{\mathbf{R}}$, phase Θ is constant, leaving $\dot{\Theta} = 0$.

6.1.3 Initial conditions

Specifying initial conditions for the governing equations requires one to take into account the orientation of the wave fronts and modify the initial ray trajectory according to the local flow conditions. We specify initial conditions for ray position $\mathbf{R}$; initial phase Θ is irrelevant, since Θ does not change along characteristics. Initial q and $\mathbf{b}$ are specified assuming the form of Θ is

$$\Theta(\mathbf{R},t) = \mathbf{k}(\mathbf{R},t)\cdot\mathbf{R} - \omega t \tag{6.16}$$

where $\mathbf{k}$ is the (local) acoustic wave number vector and ω is the (local) frequency, which is fixed provided that the source is stationary. In our implementation, the initial point of the ray is fixed to the laboratory frame and located uniform flow. As result $\mathbf{k} = \mathbf{k_0}$ is constant there and

$$\mathbf{b}_0 = \nabla\Theta\Big|_{t=0} = \mathbf{k_0} \tag{6.17}$$

since $\nabla\cdot\mathbf{R} = 1$. Similarly,

$$q_0 = -\frac{\partial\Theta}{\partial t}\Big|_{t=0} = -\omega_0 \tag{6.18}$$

The relationship between the initial frequency ω_0 and the wave number $\mathbf{k_0}$ is obtained through the dispersion relation

$$\omega = k_0 c + \mathbf{k_0} \cdot \mathbf{v} \tag{6.19}$$

Solving for k_0, we obtain

$$k_0 = \frac{\omega / c}{M \mathbf{n} \cdot \mathbf{m} + 1} \tag{6.20}$$

where $\mathbf{m} = \mathbf{v}/|\mathbf{v}|$, $M = |\mathbf{v}|/c$, and $\mathbf{n} = \mathbf{k_0}/k_0$ is the wave-front normal. For a uniform horizontal flow of Mach number M_1, the initial condition for the wave vector $\mathbf{b}$ becomes

$$\mathbf{b_0} = \mathbf{k_0} = k_0 \mathbf{n} = \frac{\omega / c}{1 + M_1 \cos\theta} \left[\hat{\mathbf{x}}_1 \cos\theta + \hat{\mathbf{x}}_2 \sin\theta \right] \tag{6.21}$$

where θ is the orientation of the wave-front normal $\mathbf{n}$, as measured from the downstream direction. The relative values of k_0 and ω, rather than the absolute values, are important. Equation 6.21 permits us to specify initial values of b_0 and q_0 in a uniform flow to form rays in any direction θ.

We note that when $M_1 > 1$, there is an apparent singularity in the above expression for $M_1 \cos\theta = -1$. Waves satisfying this condition are oriented precisely at the Mach angle $\mu = \sin^{-1}(1/M_1)$ and are therefore standing waves. However, because the waves are stationary, the frequency must be zero. Hence, for these conditions we require that the wave number be finite (but arbitrary) and of known orientation; *i.e.*, we specify that

$$q_0 = -\omega = 0 \tag{6.22}$$

$$\mathbf{b}_0 = \hat{\mathbf{x}}_1 \cos\theta + \hat{\mathbf{x}}_2 \sin\theta \neq 0 \tag{6.23}$$

This is the initial condition we use to represent the oblique shock in geometric acoustics.

6.1.4 Numerical solution of the eikonal equation

We now have a first order nonlinear system of differential equations (five equations for two-dimensional flow and seven equations for three-dimensional flow). The variables consist of two distinct types: the solution variables $\mathbf{R}$, $\mathbf{b}$, and q; and the base flow variables v and c. The base flow variables are specified from an existing precomputed data set (*e.g.*, from a simulation or model flow). In practice, we pre-compute $\mathbf{v}$, c^2, $\nabla\mathbf{v}$, ∇c^2, $\partial\mathbf{v}/\partial t$, and $\partial c^2/\partial t$.

The goal is to generate the ray paths $\mathbf{R}$ for a large series of starting points on the same wave front. We advance the solution to some end condition (such as maximum time or time steps) for each ray path, and store the positions $\mathbf{R}$. Let index m denote the ray, and index n denote the time step. Thus, we acquire an array of coordinates $\mathbf{R}_{m,n}$. $\mathbf{R}_{m,n}$ for fixed m and varying n represents the ray m. As Δt is in general variable for maximum integration efficiency, the wave fronts are obtained by interpolating in time $t(m,n)$ the ray position data.

We establish the initial conditions for each ray m as noted previously:

$$\mathbf{R}_{m,0} = \mathbf{R}_{m,0} \tag{6.24}$$

$$\mathbf{b}_{m,0} = \mathbf{k_0} = k_0\mathbf{n}_0 \tag{6.25}$$

$$q_{m,0} = \begin{cases} 0 & \theta = \cos^{-1}(-1/M_1) \\ -k_0(c + \mathbf{n_0}\cdot\mathbf{v}) & \text{otherwise} \end{cases} \tag{6.26}$$

where $\mathbf{n}_0$ is the unit normal to the initial wave front. For a stationary source, ω will remain constant across the initial wave-front.

The governing equations 6.11 through 6.14 have the form $\dot{\mathbf{Q}} = f(\mathbf{Q}_n, t_n)$. We integrate these equations using the Richardson extrapolation form of the fourth order Runge-Kutta method (as taken from [43]). The variable time step Δt afforded by this method assures an accurate solution while maintaining computational efficiency.

6.2 Steady flow examples

In the following we demonstrate the ray tracing code on two steady flow examples in preparation for representing the instability wave shock interaction problem with geometric acoustics. Both involve a horizontally oriented, steady, parallel shear layer with a hyperbolic tangent profile:

$$u_1 = U_1 + \frac{U_2 - U_1}{2}\left[1 + \tanh\left(\frac{y - y_0}{\delta/2}\right)\right] \tag{6.27}$$

$$u_2 = 0 \tag{6.28}$$

where $U_1 = 1$ and $U_2 = 0$ are the asymptotic velocities below and above the shear layer, respectively; y_0 is the shear layer center-line; and δ is the vorticity thickness. For these examples, we have ignored variation in the speed of sound c. We have normalized the vertical coordinate y by the shear layer thickness δ and taken $y_0 = 0$.

In the first example, we place a point source in a supersonic flow ($M = 1.2$) at $y/\delta = -2$. The Figure 6.1 we show the ray trajectories (in red) and wave fronts (black). By point source, we mean that the wave initial wave front forms a circle. The ray trajectories themselves are confined within a Mach cone (only the upper half of which we computed). Some ray trajectories pass into the shear layer, and then return to the lower stream; such rays experience total internal reflection. Some of these create Mach wave traces that travel obliquely to the shear layer and are completely analogous to those observed in the simulations. The overall wavefront development is very similar to that predicted by Howe [11].

In the point source example, rays are emitted in all possible directions for a supersonic flow. As a result, some rays were redirected via the refractive effect of the shear layer back into the supersonic flow, while others were transmitted across. In the next example we consider a standing plane wave in the presence of a steady shear layer. For the acoustic wave to be stationary, the flow must be supersonic. The orientation of the plane wave corresponds exactly to the Mach angle $\mu = \sin^{-1}(1/M)$. In Figure 6.3 we show such a oblique standing wave. Note in particular that the orientation of the wave front normal $\mathbf{n}$ is perpendicular to the ray trajectory $\mathbf{u} = \mathbf{v} + c\mathbf{n}$. For the

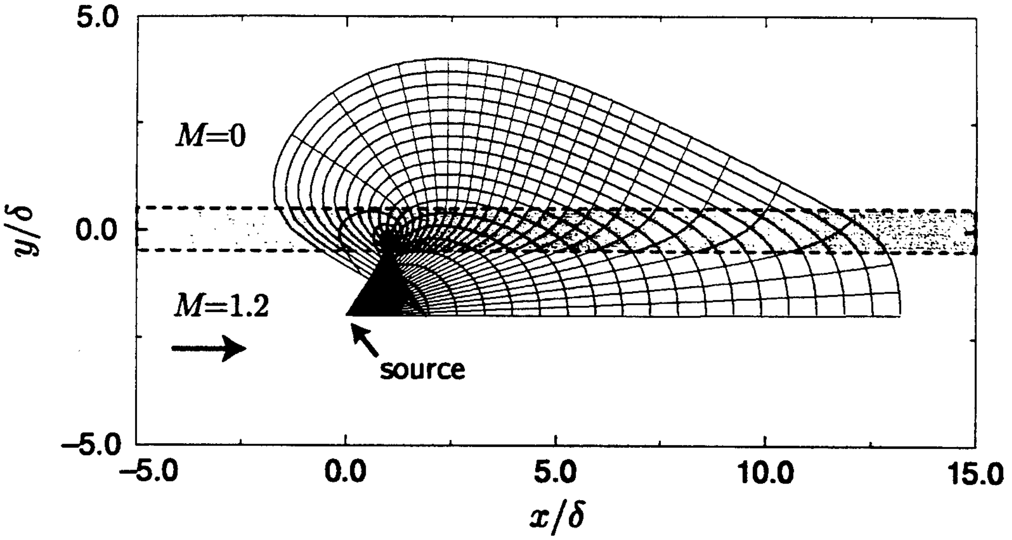

Figure 6.1: Point source on the supersonic side of shear layer. Red: rays, black: wave-fronts. Dashed line indicates center vorticity thickness of shear layer. Only upper half of rays are computed.

standing wave, the wave fronts are parallel to and coincident with the ray trajectories. The wave extends toward the shear layer at the Mach angle μ, but as it encounters the velocity shear, its orientation changes toward the vertical. Details of this region as given in Figure 6.4 show that the ray loops back on to itself in the vicinity of the sonic line, before proceeding back into the high speed flow. This extreme case of refraction is the mechanism for total internal reflection. Under steady supersonic conditions for which the other side of the shear layer is quiescent, the oblique standing wave must reflect in this manner, according to geometric acoustics.

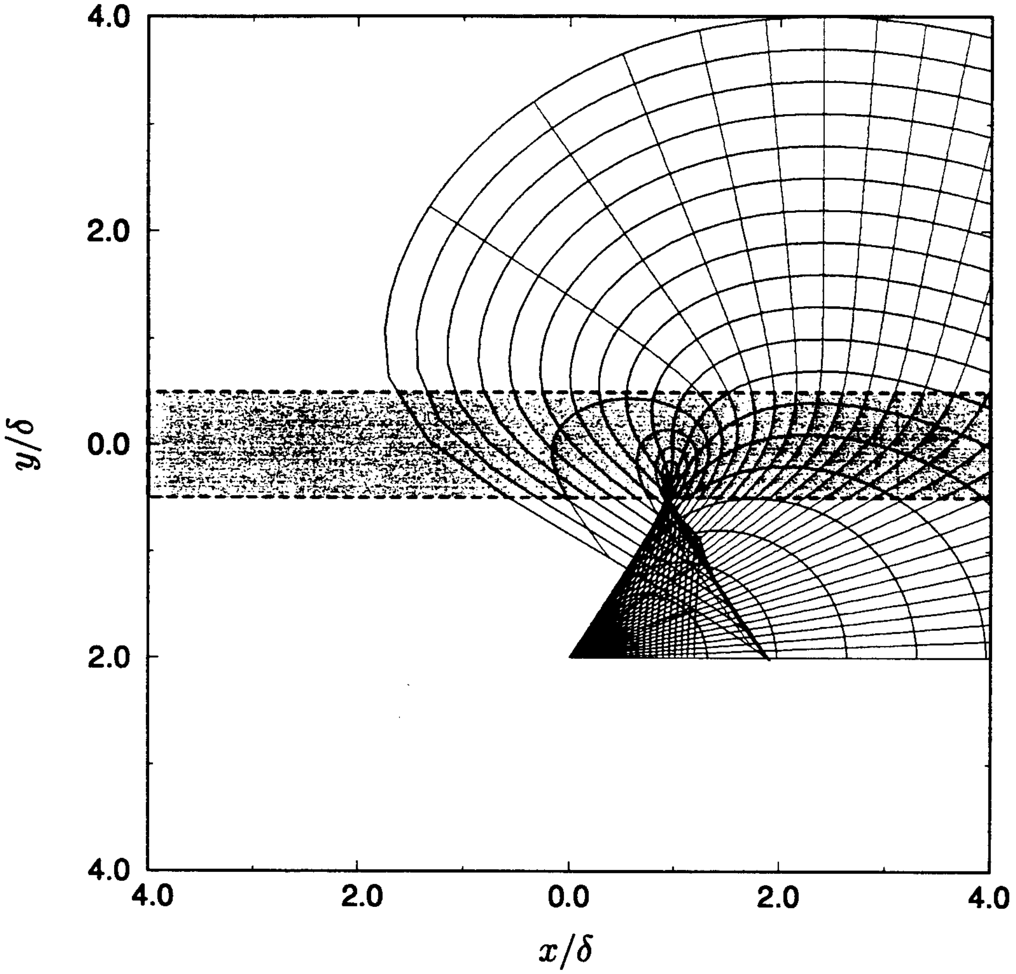

Figure 6.2: Detail of Figure 6.1.

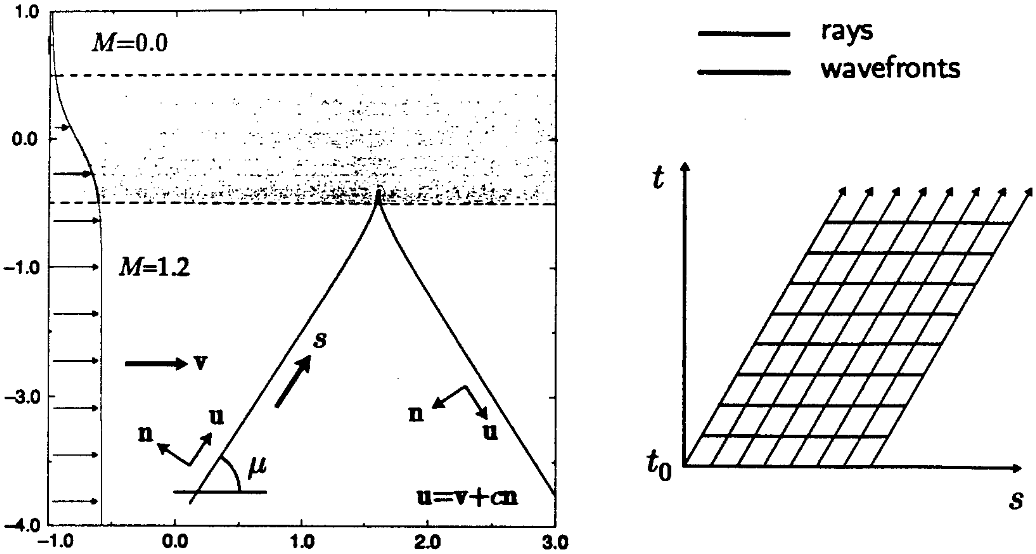

Figure 6.3: Standing oblique plane wave in supersonic side of shear layer. **u** is ray trajectory vector, **n** wave-front normal, **v** base flow. s is the spatial coordinate along the ray. At right, rays and wave fronts are shown in space-time. Projections of these onto x-y space collapse onto a single line, the standing wave-front.

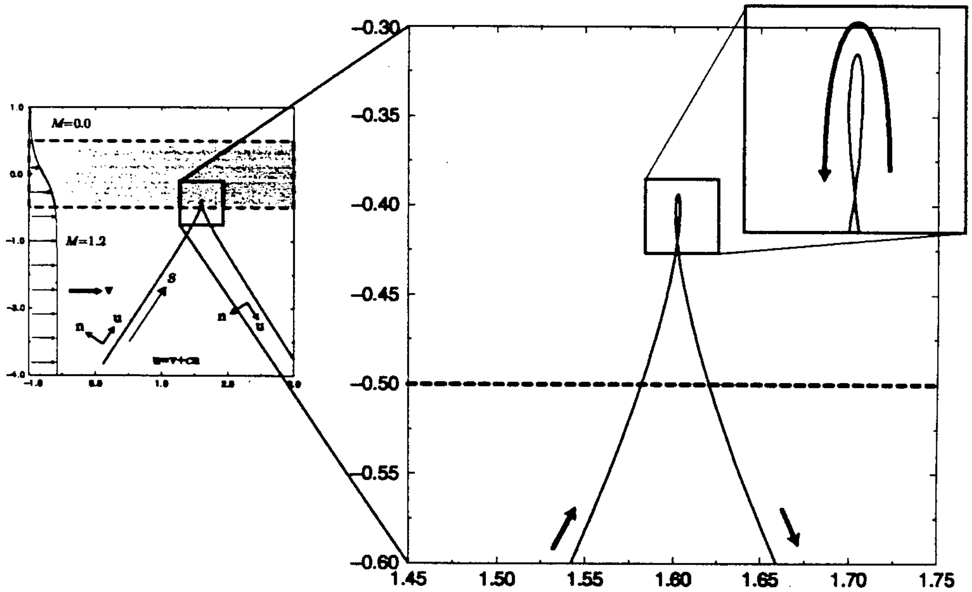

Figure 6.4: Detail of Figure 6.3. Standing oblique plane wave reflects due to refraction by velocity shear, causing ray (and wave-front) to loop.

6.3 Unsteady base flow

6.3.1 Basic behavior

Finally we carry out the geometrical acoustics analysis for unsteady base flow. The unsteady base-flow implemented is the idealized mixing layer of Stuart [60], as described in Section 5.4. Here we set the amplitude coefficient $A = 1.0$. Again, the Mach number of the high speed stream is taken to be $M_1 = 1.2$. 1024 rays were initialized on a line oriented at the Mach angle and intersecting the shear layer centerline at $x = 40$. The coordinate system is consistent with the linearized Euler cases. The initial points are spaced such that the ray initialized furthest from the shear layer will pass through the initial point of the ray closest to the shear layer in exactly one oscillation period. Rather than be spaced evenly between the first and last initialization points on the standing wave, the initial ray points are clustered so as to create a ray concentration where severe ray spreading occurs in the passage through the Stuart vortices. This clustering is similar to the grid node clustering of Section 2.6. Its settings were found through repeated trial with fewer rays (typically 32). The rays were integrated through two oscillation cycles. The large number of rays was chosen to improve wave-front resolution. 64 rays and 16 wavefronts (per cycle) were saved.

The rays are shown in Figure 6.5 and indicate that transmission has occurred across the shear layer, unlike the steady shear layer example shown in Figure 6.3. In Figure 6.6 we show waves spaced in 1/8 cycle increments. The wave fronts are very similar to those observed in the Stuart vortex linearized Euler simulations (see Figure 5.30).

The transmission of acoustic rays does not occur at every value of the Stuart vortex amplitude coefficient A. Figure 6.7 shows the onset of acoustic transmission as A is increased from zero, the case in which the shear layer is steady, to 1.0. In this figure, a set of rays representing the incident standing plane wave is arranged such that the rays arrive at the shear layer over one oscillation period. The $A = 0$ case, which corresponds to the steady shear layer, results in total internal reflection of the incident rays. As A is increased above zero, the initially weak, convecting vortices appear and

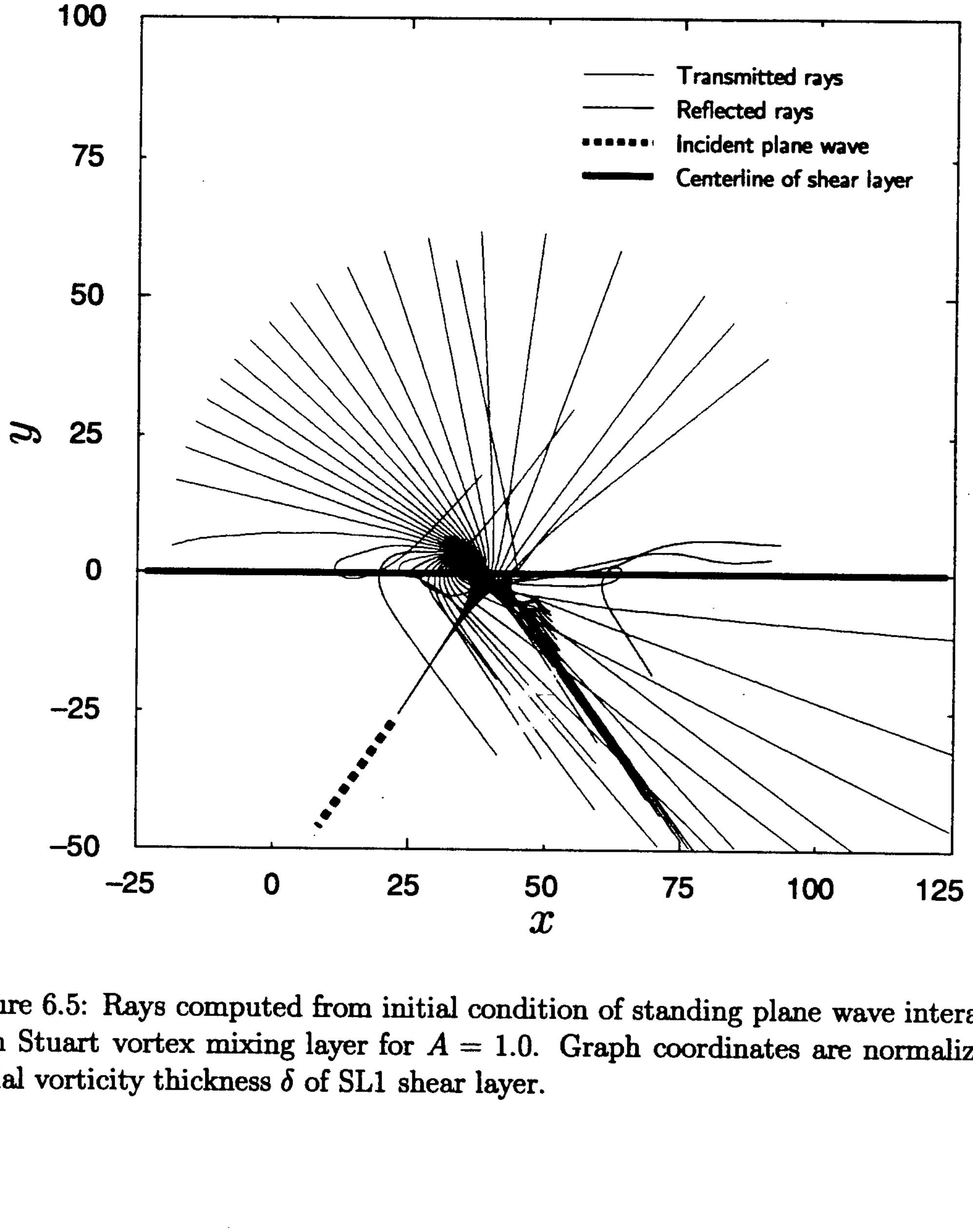

Figure 6.5: Rays computed from initial condition of standing plane wave interacting with Stuart vortex mixing layer for $A = 1.0$. Graph coordinates are normalized to initial vorticity thickness δ of SL1 shear layer.

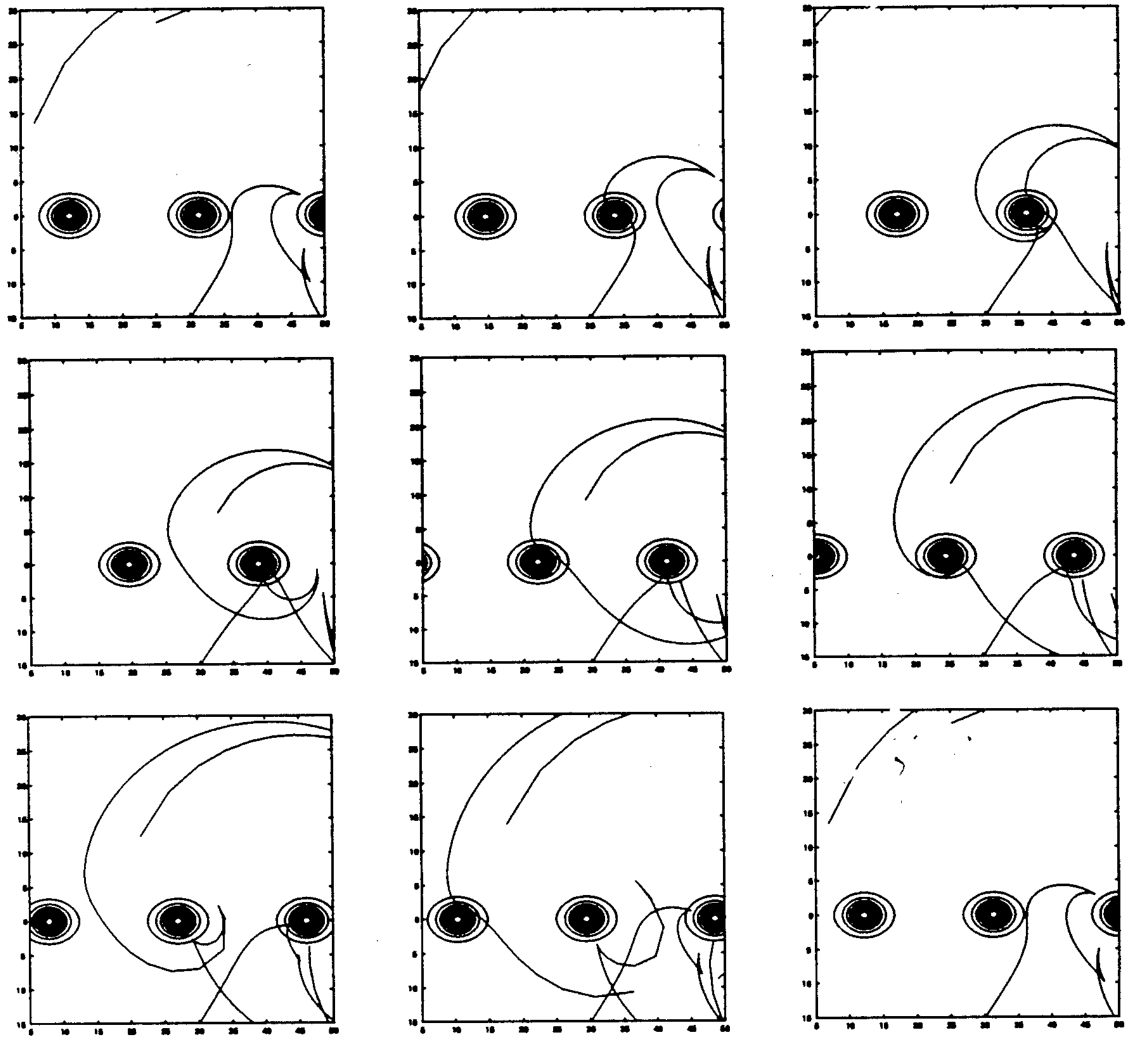

Figure 6.6: Wave front computed under same conditions as in Figure 6.5. Spaced every 1/8 cycle.

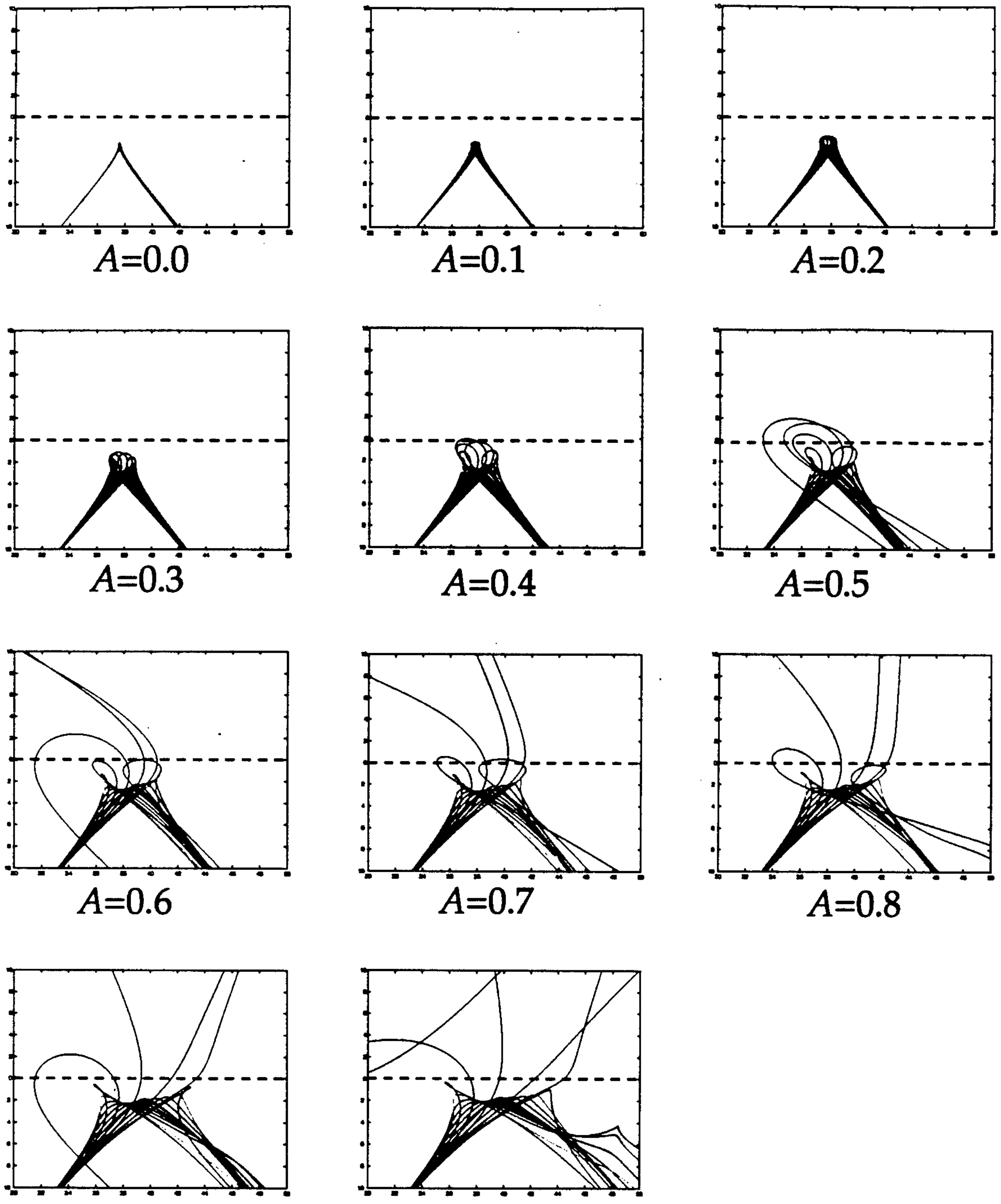

A=0.0 A=0.1 A=0.2

A=0.3 A=0.4 A=0.5

A=0.6 A=0.7 A=0.8

A=0.9 A=1.0

Figure 6.7: Rays representing standing wave incident on Stuart vortex mixing layer of various amplitude coefficient A. Dotted line represents centerline of shear layer.

impart deviations in the rays paths, depending on their moment of incidence; these deviations increase with A. Between $A = 0.5$ and 0.6, rays which pass entirely through the shear layer are detected. However, their transmission angles are confined to the upstream direction. As A is further increased, the range of transmission angles increases until it encompasses all possible angles at $A = 1.0$. We note that although there is an increase in the range of angles over which transmission occurs, the number of rays which are transmitted does not increase appreciably.

6.3.2 Transmission window: parameterizing the ray initial condition

To investigate further the relationship between transmission of acoustic rays and the Stuart vortex parameter A, we again consider rays corresponding to a standing acoustic wave in the supersonic stream. We wish to determine the fraction of rays among all possible such rays that are transmitted, and how this fraction varies with A. Although a given ray may be identified by its initial position (x_0, y_0) and time t_0, the uniformity of the velocity field away from the shear layer and the periodicity of the shear layer itself results in rays which are not unique. We can define the entire set of uniquely behaving rays by reducing the initial condition to a single phase parameter ξ.

Suppose we have a periodic instability wave of wave number a, convecting at velocity U_c. The unsteadiness of the instability wave can be removed by using a phase parameter ξ, where

$$\xi = a(x - U_c t) \tag{6.29}$$

Suppose now that the lower of the shear layer is supersonic at Mach number M and that an oblique standing wave is introduced from below. Since this wave is standing, it must form an angle with the flow equal to the Mach angle $\mu = \sin^{-1} M^{-1}$. Information in this standing wave will travel toward the shear layer at speed

$$c_{ray} = c\sqrt{M^2 - 1} \tag{6.30}$$

along the standing wave, where c is the speed of sound. The wave itself, which is also the initial ray path, is described by the line

$$\frac{y-y_0}{x-x_0}=\frac{1}{\sqrt{M^2-1}} \tag{6.31}$$

The standing wave is made up of a family of acoustic rays. If we consider the ray which is initialized at position and time (x_0, y_0, t_0), we can find the position of the ray in time:

$$\begin{aligned} x &= x_0+\frac{M^2-1}{M}c(t-t_0) && (6.32)\\ y &= y_0+\frac{\sqrt{M^2-1}}{M}c(t-t_0) && (6.33) \end{aligned}$$

Suppose now that we have a horizontal reference line $y = y_1$ which is crossed by the ray in the uniform part of the supersonic flow. At the time of crossing, the instability wave field is of phase $\xi = \xi_1 = a(x_1 - U_c t_1)$. We can find ξ_1 by solving for x_1 (Equation 6.31) and t_1 (Equation 6.33).

$$\begin{aligned} x_1 &= x_0+(y_1-y_0)\sqrt{M^2-1} && (6.34)\\ t_1 &= t_0+\frac{y_1-y_0}{c}\frac{M}{\sqrt{M^2-1}} && (6.35) \end{aligned}$$

or

$$\xi_1=a\left[x_0-U_c t_0+(y_1-y_0)\left(\frac{M(M-M_c)-1}{\sqrt{M^2-1}}\right)\right] \tag{6.36}$$

where $M_c = U_c/c$. Note that y_1 is arbitrary but constant.

In the event that the mixing layer is periodic with wave-number a, the uniqueness of an initial condition defined by the parameter ξ_1 in Equation 6.36 is only guaranteed for ξ_1 varying by less than 2π. Thus ξ_1 is a phase function and all unique initial conditions are defined for $0 \le \xi_1 < 2\pi$. In Figure 6.8 we plot lines of constant ξ_1 in the uniform portion of the supersonic velocity field at $t_0 = 0$, $M = 1.2$, $U_c = 0.5$, and arbitrary constant $y_1 = -30$. For reference, we also show contours of vorticity for the mixing layer at $t = 0$. The lines of constant ξ_1 are oriented such that to obtain

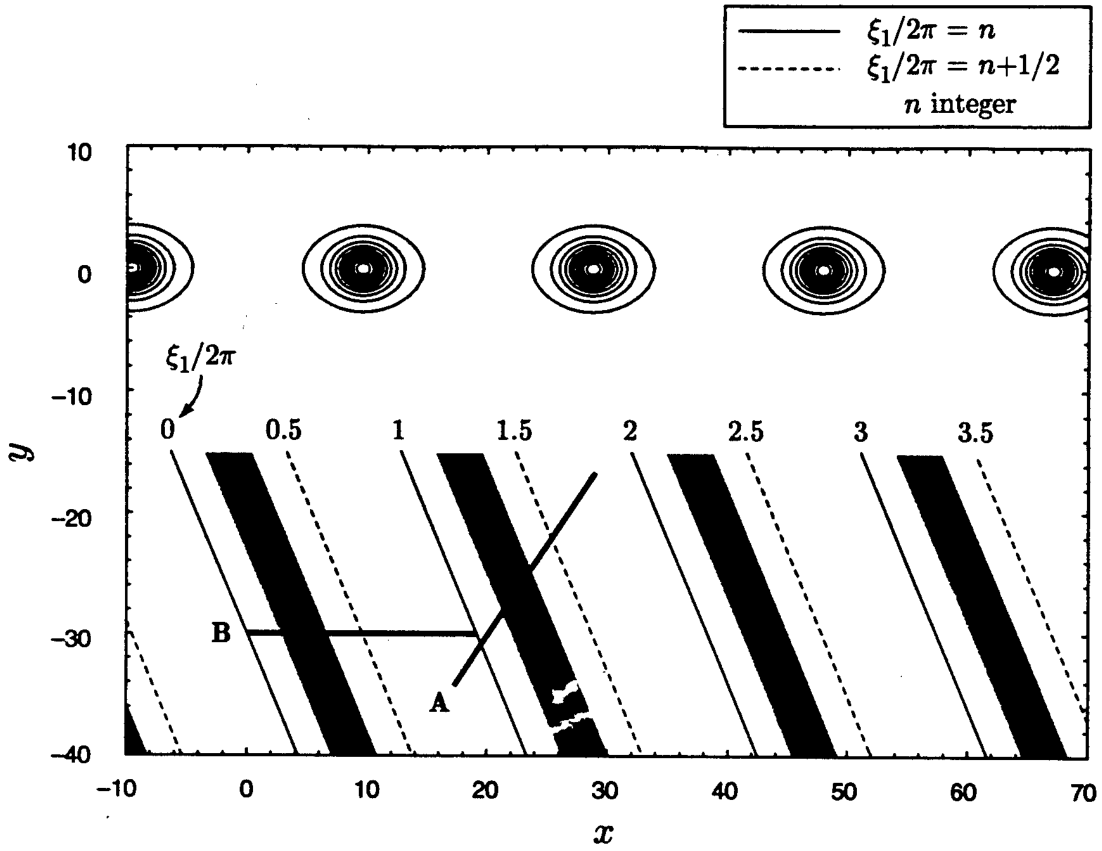

Figure 6.8: Initial condition phase map for ξ_1 as defined by Equation 6.36. $y_1 = -30$. $A = 1$. **A**: locus of ray initial conditions for case shown in Figures 6.5 and and 6.6. **B**: horizontal locus of ray initial conditions. Regions of light blue indicate all initial conditions which result in transmission.

the same ray behavior as one moves the initial condition away from the the mixing layer (along $-y$), one must also move the initial condition farther downstream. This can be understood from the fact that the convection speed of the vortices $U_c = 0.5$ exceeds the projection of the ray speed onto the horizontal axis.

$$(c_{ray})_x = c_{ray}\cos\mu = c\sqrt{M^2-1} \times \frac{\sqrt{M^2-1}}{M} = 0.306 \qquad (6.37)$$

In Figure 6.8 we superimpose on the phase contours the locus of points (labeled "**A**") that we used to form the initial conditions for the case shown Figures 6.5 and 6.6. We can show that transmission occurs for rays whose initial positions lie between the points $x = 28.98$, $y = -16.53$ and $x = 31.30$, $y = -13.14$. This corresponds to the phase function range $1.137 \leq \xi_1/2\pi < 1.352$, which due to periodicity is the same as $0.137 \leq \xi_1/2\pi < 0.352$. We define "transmission" for a ray as the condition in which the ray extends beyond $y = 8$ on the first pass through the layer. Note that some rays will cross the shear layer on the second pass, *i.e.*, after looping back into the supersonic side. The colored bands in Figure 6.8 indicate all the ray initial positions for which we expect transmission to occur.

Returning to our investigation of the dependence of the transmission on the vortex parameter A, we need now only consider varying the ray initial condition phase parameter ξ_1 from 0 to 2π to accommodate all unique rays. In this study, we achieve the necessary phases by holding $y_0 = -30$ (as a matter of convenience), again with $y_1 - 30$, and $t_0 = 0$. In choosing these initial conditions, note that the rays no longer originate from a single standing plane wave. The locus of initial conditions are labeled **B** in Figure 6.8. We track the minimum and maximum phase ξ_1 for which transmission occurs to obtain a transmission fraction $\psi = (\xi_{max} - \xi_{min})/2\pi$.

We ensure that for $y_0 = -30$ the ray initial conditions lie in the uniform part of the flow. In Figure 6.9 we show ray trajectories for initial conditions at various distances from the shear layer. We see that there is no change in ray trajectory for $y_0 < -30$, and only minor changes for $y_0 < -20$.

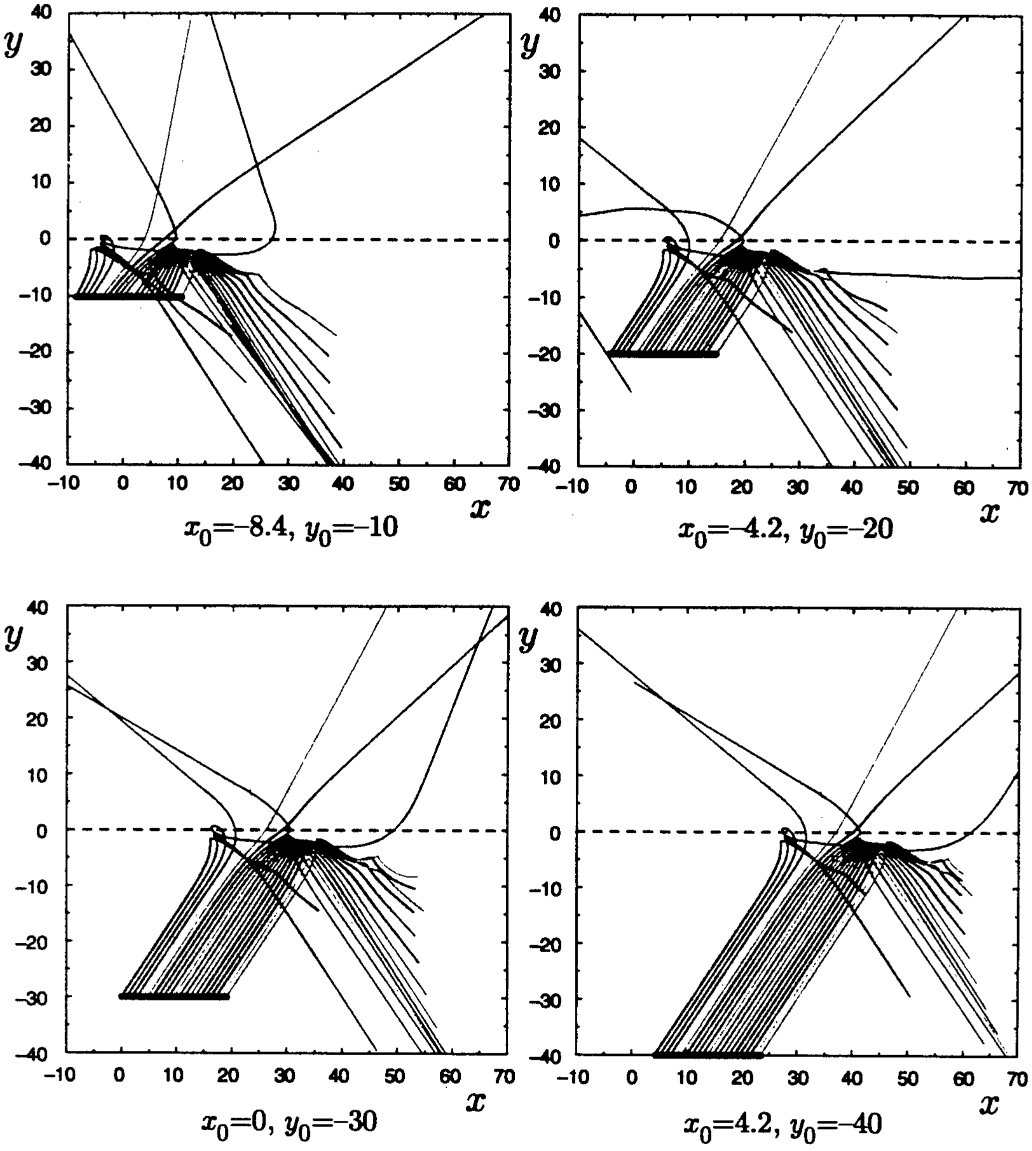

x_0=-8.4, y_0=-10

x_0=-4.2, y_0=-20

x_0=0, y_0=-30

x_0=4.2, y_0=-40

Figure 6.9: Ray trajectories for a series of initial conditions at various y_1 but the same range of ξ_1. to check for flow uniformity. Thick red lines indicate location of initial positions. Strong uniformity in transmitted ray trajectories found for $y_0 < -30$; near-uniformity for $y_0 < -20$.

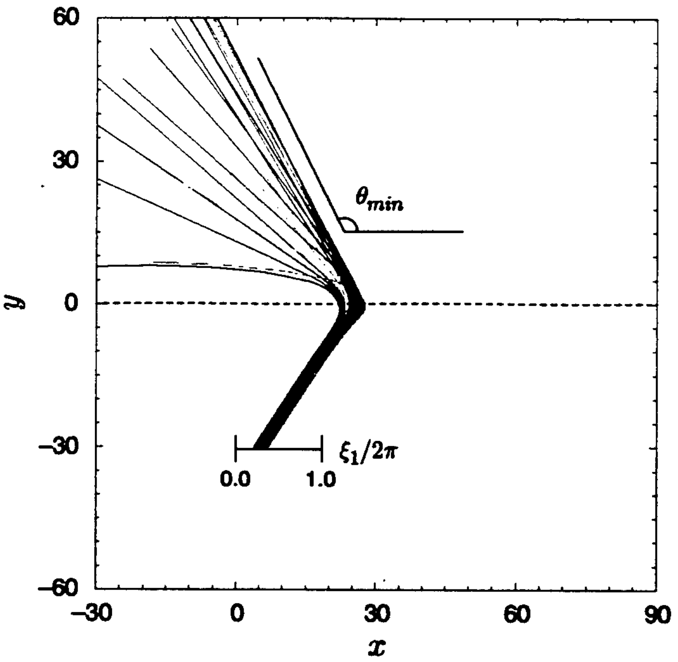

Figure 6.10: Transmitted rays representing standing plane wave(s) incident on Stuart vortex mixing layer of magnitude $A = 0.650$. Initial condition phase parameter varies from $\xi_1/2\pi = 0.199$ to 0.365.

6.3.3 Transmission Window: Results

In Figure 6.10 we show a set spanning the rays which cross the shear layer for $A = 0.65$. In this case transmission occurs for $0.199 \leq \xi_1/2\pi \leq 0.365$, giving a transmission fraction $\psi = 0.166$. Over the range of $0 \leq A \leq 1.2$ this transmission "window" is found to be nonexistent up to $A = A_{crit} = 0.54$, above which point it grows rapidly (Figure 6.11). The corresponding transmission fraction is shown in Figure 6.12.

As observed earlier, at vortex amplitude A just above the threshold of transmission A_{crit}, the range of transmission angles is limited to the upstream direction $\theta = 180°$. As A increases, the minimum transmission angle θ_{min} decreases to include the downstream direction. This trend is shown in Figure 6.13. Note however that the rays associated with $\xi_1 = \xi_{min}$ and $\xi_1 = \xi_{max}$ both have transmission angles in the upstream direction. The ray associated with θ_{min} is initialized at an intermediate phase $\xi_{min} \leq \xi_1 \leq \xi_{max}$, indicating that the wave front of the transmitted acoustic

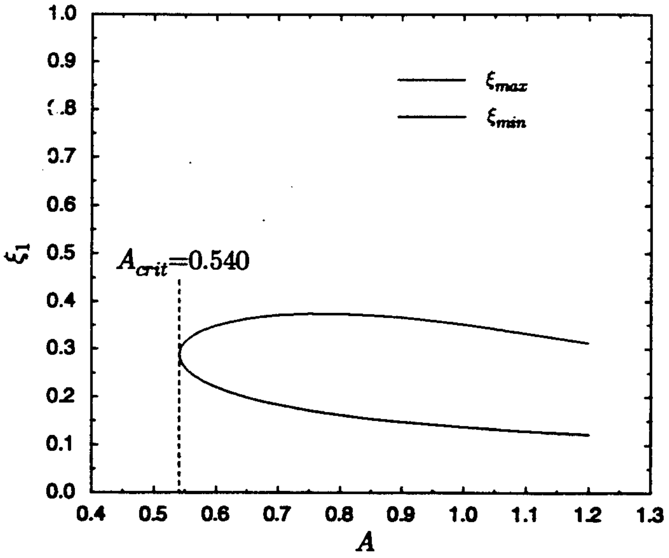

Figure 6.11: Minimum and maximum phase parameter $\xi/2\pi$ for which transmission is found to occur across Stuart mixing layer.

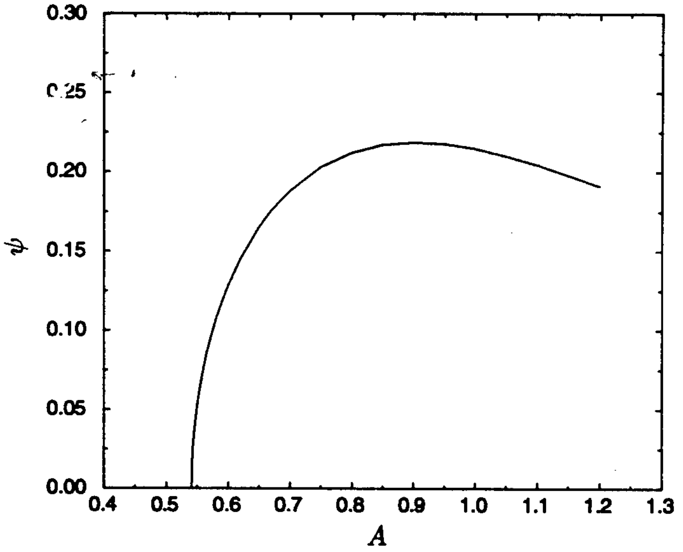

Figure 6.12: Fraction ψ of all possible rays (representing an oblique incident standing wave) which pass through Stuart vortex mixing layer.

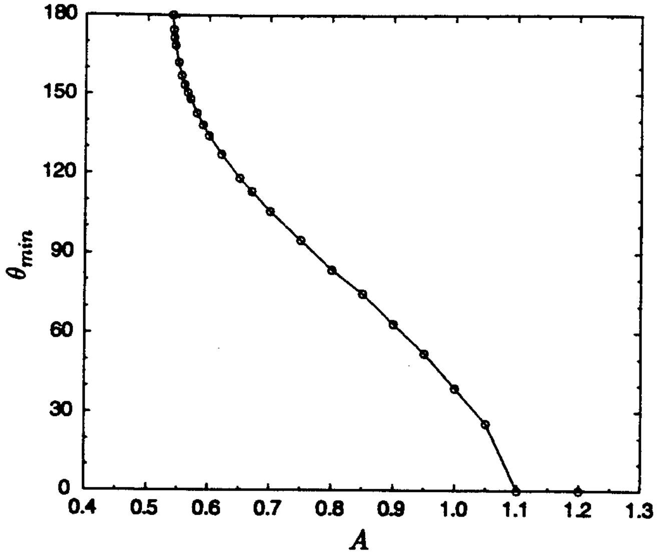

Figure 6.13: Minimum transmission angle for rays passing across Stuart vortex mixing layer.

rays folds back onto itself. This pattern, clearly observed in the wave-front visualizations of Figure 6.6, is the transmission of the entire incident plane wave reflection system through the shear layer. The same phenomenon was observed in the DNS Case A2, as seen in Figure 3.12.

Although the wave front visualizations of Figure 6.6 strongly support the notion that the acoustic radiation which results from shock instability wave interaction is governed by refractive behavior, certain details are inconsistent and suggest that geometrical acoustics provides only a partial explanation of the observed behavior. The first is the nature of the onset of transmission; this onset occurs suddenly and does not motivate the exponential rise in transmitted acoustic amplitude we observed in the linearized Euler simulations. The critical value of Stuart vortex amplitude A above which transmission occurs corresponds more closely to the region of saturation observed in the linearized Euler calculations. Finally, at the onset of transmission, the transmission angle in the geometrical acoustic cases is limited to the upstream direction. This range of transmission angles increases to include the downstream directions with A. However, this behavior is not observed in the simulations; transmission occurs in all directions. It is suggested that the refractive behavior best explains the sound generation mechanism for high instability wave amplitude. At lower amplitude other physical mechanisms, such as diffraction, may come into play, and further, explain the exponential dependence of acoustic amplitude on instability wave amplitude. The issue of incident wave width may also play a role in determining the dominant behavior.

6.3.4 Role of Unsteadiness

The issue of the role of the unsteadiness, as opposed to a frozen instantaneous field, in producing the conditions for refraction was also studied. The Stuart vortex mixing layer field consists of a velocity field pattern which translates at velocity U_c. Setting $U_c = 0$ allows one to "freeze" the velocity field pattern without modifying the far field values, albeit by producing an somewhat unphysical flow. We introduce a set of rays at fixed distance from the centerline of the layer and over one instability wavelength for various vortex amplitude A. As seen Figure 6.14, rays will not pass through the mixing layer under these frozen conditions. We conclude then that the unsteadiness brought about by the convection of the vortices, in addition to the vortex velocity field, is necessary for the periodic transmission we observe.

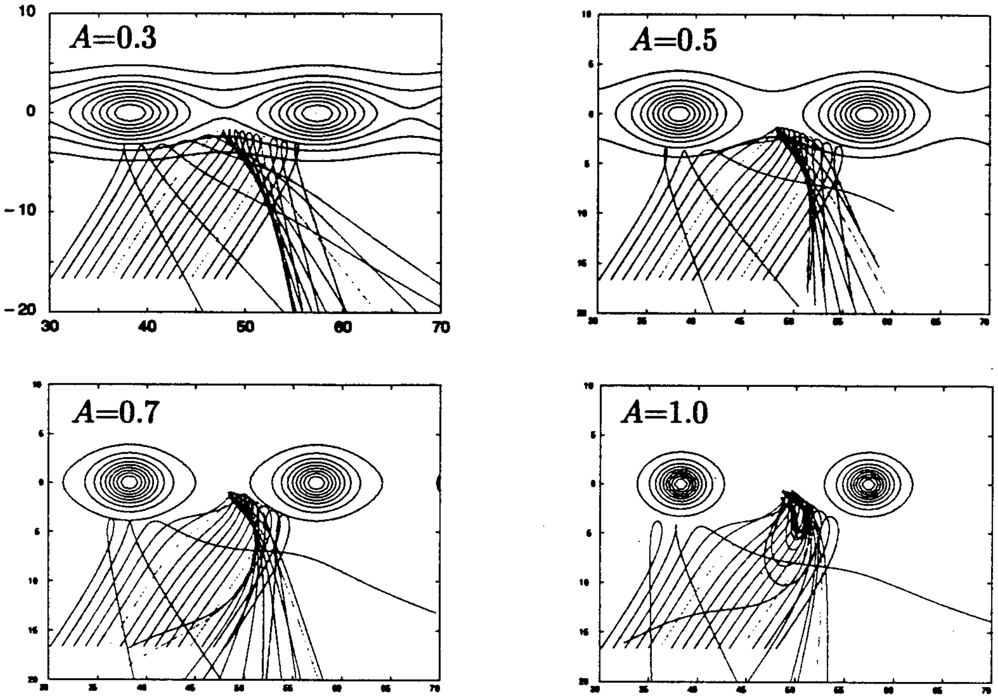

Figure 6.14: Rays incident on "frozen" (non-convecting) Stuart vortex mixing layer. Transmission is found not to occur.

Chapter 7

Conclusions

The objective of this work was to elucidate the mechanisms governing the generation of sound in supersonic jet screech. We investigated the behavior of an isolated screech-type source arising from large scale instability-wave shock interactions. To approximate the source in the absence of screech feedback, we devised a simplified model problem comprised of a forced, supersonic shear layer and an oblique shock. We simulated the instability wave shock interaction and measured the resulting sound. To study problem with fewest assumptions, we first solved the full Navier-Stokes equations. We then invoked a series of progressive simplifications to the model problem and studied the problem again at each step:

1. We reduced the shock to a weak compression wave within the Navier-Stokes framework.

2. We decomposed the problem into an unsteady base-flow from DNS and an incident/scattered perturbation field; we obtained these solutions using the linearized Euler equations.

3. We replaced the monotonic compression wave with a compact- profile Gaussian wave.

4. We replaced the DNS shear-layer base-flow with an idealized mixing-layer model.

5. Finally, we replaced the linearized Euler equations with the equations governing geometric acoustics for an unsteady base-flow.

Although not every detail carried over to the next level of simplification, we found the basic description of the sound generation process to remain the same. A composite of flow visualizations illustrating this commonality is shown in Figure 7.1. The conclusions based on these studies are listed below and grouped in terms of those obtained from DNS, the linearized Euler simulations, and geometrical acoustics.

Direct Numerical Simulations

- The passage of instability wave vortices across an incident shock results in large fluctuations in the shock. Coupled with these fluctuations is the generation of the sharp compression front of the acoustic wave, which occurs precisely as the shock travels upstream between the vortices in its oscillation cycle. The shock itself "leaks" through the shear layer at this point as the sound wave.

- The sound generated by the interaction exhibits sufficient upstream directivity to create an upstream-traveling, oblique Mach wave in the supersonic stream. The upstream directivity is significant because of screech feedback and its dependence on shear layer receptivity at the nozzle lip. It is clear that the amplitude in this direction is influenced by the details of the shear layer and the amount of refraction the acoustic wave undergoes on its way upstream. It is noted, however, that the upstream direction is not the direction for maximum directivity of a single source.

- The instability-wave shock interaction and sound emission behavior is essentially reproduced with weak compression waves, indicating that the nonlinearity of the shock is not required for the screech-type sound generation process to occur. The amplitude of the acoustic field is found to scale with the compression wave amplitude. These findings are the basis for the decomposition we perform in the linearized Euler analysis, and ultimately, geometrical acoustics.

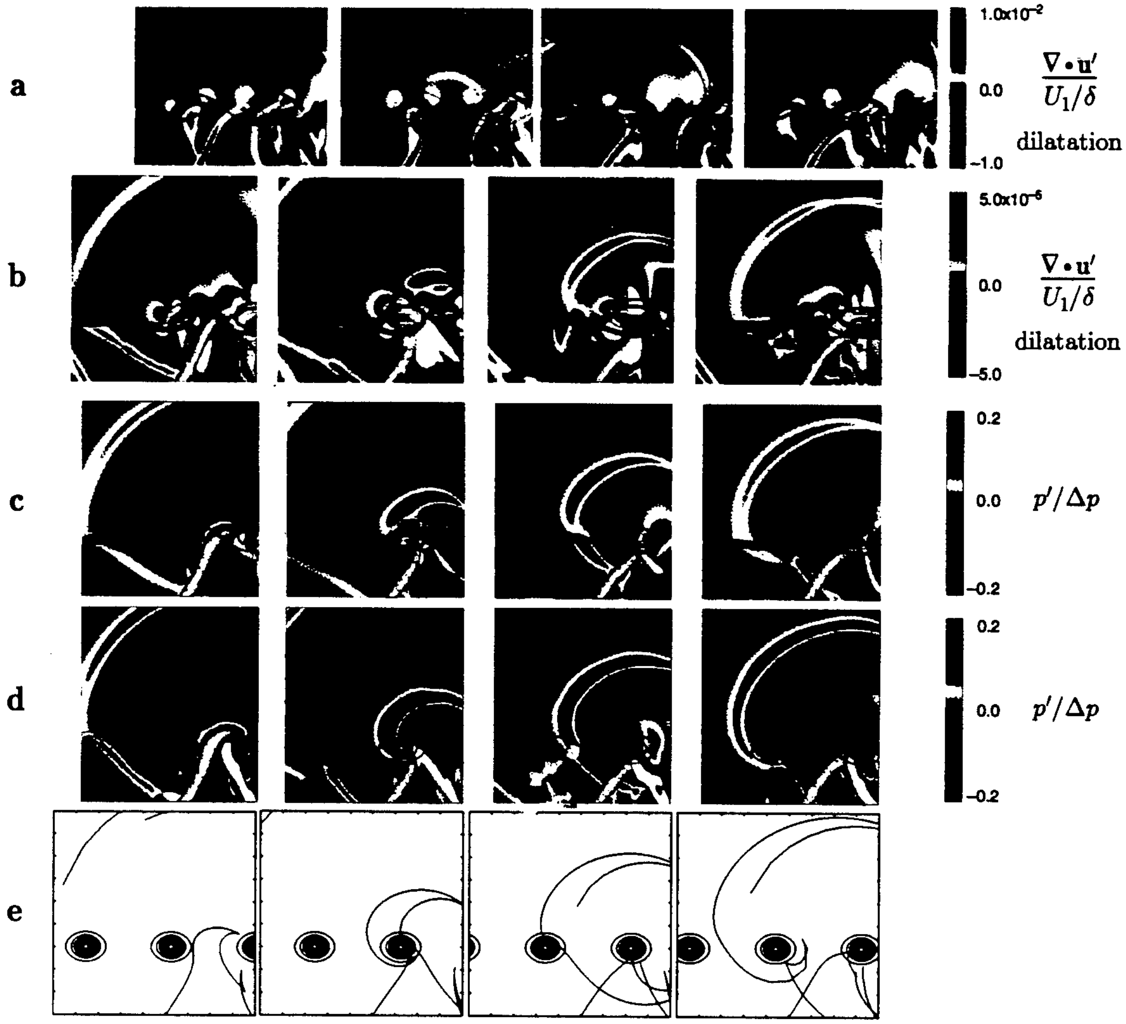

Figure 7.1: Visualization of sound generation as observed in (a) DNS, with incident compression wave; (b) linearized Euler, with DNS base flow, and incident compression wave; (c) linearized Euler, with DNS base flow, and incident G-wave; (d) linearized Euler, with Stuart vortex base flow, and incident G-wave; (e) geometrical acoustics with incident Mach wave.

- Slow, downstream-traveling waves are found to appear and persist in the supersonic stream and serve as secondary sources of sound via essentially the same interaction mechanism. The origin of these waves is not entirely clear, but they have been observed over the entire range of instability wave amplitudes. In some cases they appear to be the external sound field returning to the supersonic flow after refracting through an instability wave. At low instability wave amplitude they can become primary sound sources. These features are reproduced in both the linearized Euler analysis and geometrical acoustics.

Linearized Euler simulations about an unsteady base flow

- Numerical solutions of the Euler equations, linearized about an unsteady base flow obtained from DNS, are used to show that the screech generation process can be regarded as the scattering of an incident standing wave by instability waves. This may represent the first instance in which an unsteady base flow is used with the linearized Euler equations to study supersonic jet noise.

- The linearized Euler simulations are used to show that the sound generation process is governed by thresholding phenomenon, whereby the acoustic amplitude rises exponentially with instability wave amplitude until a saturation state is reached. There is also evidence of third regime of dependence at low instability wave amplitude. The reason for saturation is clear: the velocity field associated with the high instability wave amplitude is sufficient for complete leakage of the incident wave. The exponential growth with instability wave amplitude are believed to be related to the exponential decay of evanescent waves across a shear layer; "partial leakage" occurs in the exponential region.

- The velocity field is shown to be the critical feature of instability waves which result in the sound generation. Replacing the the DNS base flow with an incompressible vortex mixing layer solution with thermodynamic variations omitted is shown to reproduce much of the sound generation behavior, including the thresholding phenomenon. In particular, the vertical component of the vortex velocity fluctuation has been shown a greater enabler of the leakage than the horizontal component. The Stuart vortex mixing-layer has proven to be a useful tool for studying the dependence of the screech generation process on the velocity field due to its analytic description.

Geometrical Acoustics

- The sound generation process is reproduced with geometrical acoustics by integrating ray paths through a vortex laden shear flow. This result shows that the high amplitude screech generation process is fundamentally driven by the unsteady refraction of the incident shock and that "leakage" is an appropriate characterization.

- Geometrical acoustics may not be an appropriate framework for explaining the sound generation at low instability wave amplitude. As instability wave amplitude is reduced, the leakage process as predicted in geometrical acoustics is abruptly cut off. In the linearized Euler simulations, although an exponential reduction in acoustic level was observed, sound was still produced at instability wave amplitudes below the geometrical acoustics cut-off.

7.1 Recommendations for Future Work

- This present work obtained some basic results for the interaction of an instability wave and a shock. However, these results were limited. It is of interest to examine effect of the shock on the initial propagation of the acoustic wave. For sufficiently strong shocks, the leakage effect of sound production would suggest that these sound waves retain shock-like amplitudes in the near field. As we have observed significant interaction of the radiated field with the shear layer, strong traveling shocks may have a significant effect on the evolution of instability waves.

- We have identified three regimes of acoustic field dependence on the instability wave amplitude: low amplitude, exponential, and saturation. Based on the Stuart vortex results, we show that there is a linear dependence on instability wave amplitude at the low instability wave levels; this is consistent with broad-band shock noise observations and models. Can sound from these low amplitude interactions be reliably predicted with acoustic analogy models? Can such acoustic analogy models be extended to accommodate higher amplitude instability waves?

- In jets undergoing screech, the oscillation modes are typically asymmetric and involve significant cross-jet interaction. Furthermore, experiments [33] have shown more shock oscillation at the jet centerline than at the shear layer. What impact does having a true shock cell structure have on the shock noise generations mechanisms observed in the present work?

Appendix A

Compression Wave

In this appendix we describe the basis of the incident, oblique compression wave. The compression wave is implemented as a boundary condition in both the Navier-Stokes computations of Chapters 2 and 3 and the linearized Euler computations of Chapters 4 and 5. The Navier-Stokes description of the compression wave differs from the linearized Euler description in that finite amplitude effects are accommodated in the former (short of actual shock formation) but neglected in the latter. The following description applies to the Navier-Stokes version. The simplifications for the linearized Euler version are given at the end of this appendix.

A.1 Compression waves in the Navier-Stokes simulations

The compression wave is introduced over a region of sufficient width to prevent a shock from forming anywhere in the interior. The boundary condition prescription also assumes that the compression wave reflects from a steady shear layer and forms an expansion wave. A schematic of what occurs is shown in Figure A.1a.

A compression is introduced into the flow between points A and B at the lower boundary of the domain. The flow is supersonic, and is bounded by a shear layer, where the stream above the shear layer is assumed to be subsonic. The compression

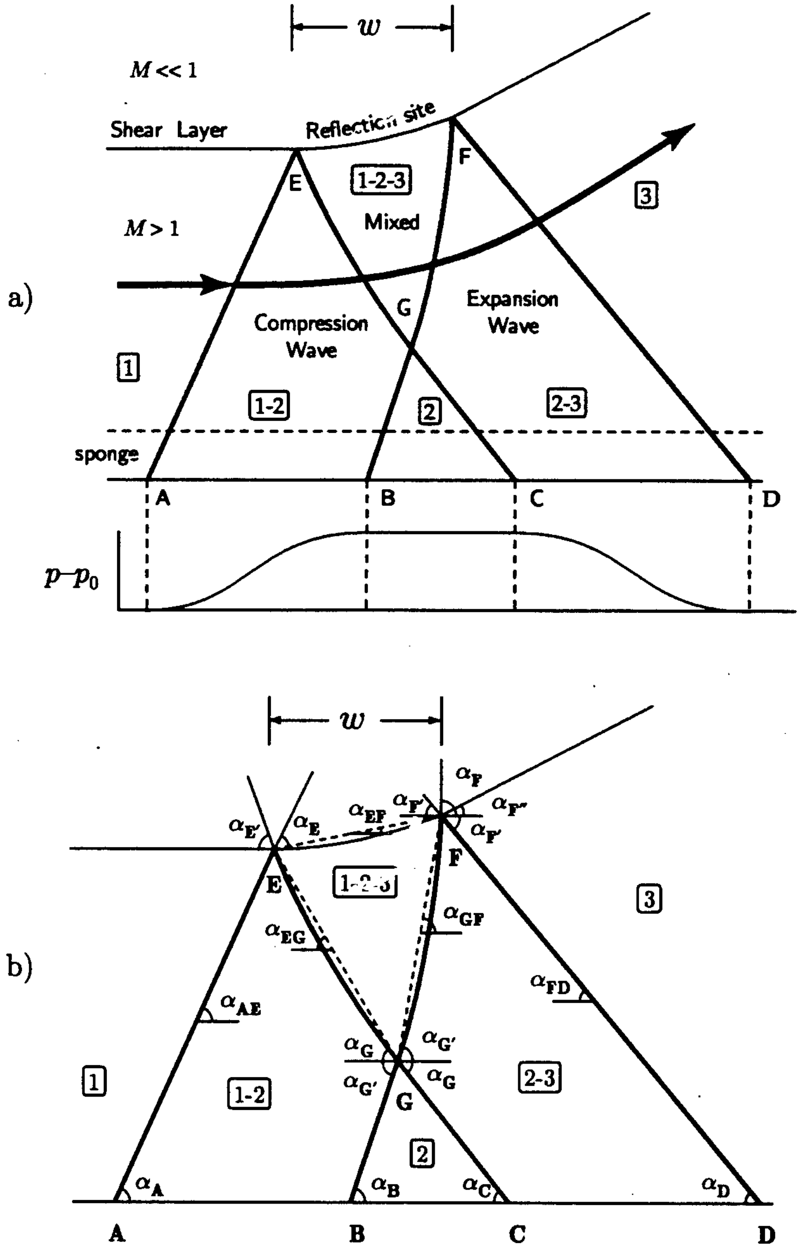

Figure A.1: Schematic of compression wave system. a) Layout, with width w defined as indicated. b) Detail of geometry with which layout is estimated.

wave extends into the supersonic flow obliquely until it encounters the shear layer. Since the compression wave cannot be supported beyond the sonic line of the shear layer, it must reflect back into the supersonic flow. Because the pressure field beyond the sonic line is uniform and equal to the pressure upstream of the compression wave, the reflected wave must maintain this pressure uniformity and therefore is an expansion wave. The expansion wave then extends back to the boundary at points C and D. A streamline which travels through the compression wave from region 1 is turned upward toward the shear layer in region 1-2. The streamline is again turned toward the shear layer as it passes through the reflected expansion wave in region 2-3. This turning causes the shear layer to be deflected away from the lower boundary.

The "width" of the compression wave is not defined at the domain boundary, but instead at the reflection site (see Figure A.1a). This length is denoted w. The wave system will consist of six distinct regions. These are (1) upstream supersonic flow; (1-2) compression wave alone; (2) region between compression wave and expansion wave; (1-2-3) region of both compression and expansion waves; (2-3) expansion wave alone; and (3) supersonic region downstream of the wave system.

The critical part of the boundary condition is located in the region between A and B, where the compression wave is imposed. The conditions prescribed here will determine the wave shape for the rest of the system. The boundary condition between C and D is primarily imposed to ensure compatibility with far downstream conditions (*i.e.*, region 3). In practice, the waves approaching the C-D region will be unsteady and in no way resemble the mean. Given that the C-D region need not be specified with any significant accuracy, we make certain approximations when producing the pressure distributions in that area. The first assumption is that the shear layer is a vortex sheet. The second is to approximate the reflection process itself with a crude use of the method of characteristics. In the Figure A.1b, we indicate all the points for which we control the orientation of the Mach wave characteristics (A through G), and angles associated with those characteristics.

We relate these characteristic angles in the following manner. We specify p_1 and p_2, the pressure upstream and downstream of the compression wave, respectively. Note that the pressure downstream of the entire wave system, p_3, is equal to the upstream pressure, p_1, due to the pressure compatibility condition across the shear layer. We assume that the pressure will vary in some smooth manner between regions 1 and 2 (*e.g.*, according to a hyperbolic tangent function). The Mach numbers are also noted, *i.e.*, M_1 is specified, and $M_3 = M_1$. In the region between the compression and the expansion, the Mach number M_2 is found from the pressure p_2 using the isentropic relations:

$$\frac{p_2}{p_1} = \left[\frac{1+\frac{\gamma-1}{2}M_2^2}{1+\frac{\gamma-1}{2}M_1^2}\right]^{\frac{\gamma}{\gamma-1}} \tag{A.1}$$

which gives

$$M_2 = \left[\frac{2}{\gamma-1}\left\{\left(\frac{p_2}{p_1}\right)^{\frac{\gamma-1}{\gamma}}\left(1+\frac{\gamma-1}{2}M_1^2\right)-1\right\}\right]^{\frac{1}{2}}. \tag{A.2}$$

We define the angle θ as the orientation of the streamline. Thus

$$\theta_1 = 0 \tag{A.3}$$

$$\theta_2 = \theta_1 + \nu(M_1) - \nu(M_2) \tag{A.4}$$

$$\theta_3 = \theta_2 + \nu(M_3) - \nu(M_2), \tag{A.5}$$

where $\nu(M)$ is the Prandtl-Meyer function, defined as

$$\nu(M) = \sqrt{\frac{\gamma+1}{\gamma-1}}\tan^{-1}\sqrt{\frac{\gamma+1}{\gamma-1}(M^2-1)} - \tan^{-1}\sqrt{M^2-1}. \tag{A.6}$$

The Prandtl-Meyer function applies for both compression and expansion waves in this case since both are required to be isentropic (*i.e.*, no actual shock formation). Care is to be taken to realize that the function must be used in opposite the conventional sense when applying it to compressions, as when we obtain θ_2.

We also define the Mach angles μ_1, μ_2, and μ_3 for the three regions using the local Mach number:

$$\mu = \sin^{-1}\left(\frac{1}{M}\right). \tag{A.7}$$

We can now define the specific geometry of the wave reflection structure. The Mach lines enclosing the region in which the compression and expansion waves overlap are generally curved; these lines are approximated as straight lines oriented at the average of the orientation at the adjoining endpoints. Other Mach lines are straight lines. The angles we use to approximate the Mach line orientations are then

$$\alpha_{AE} = \alpha_A = \mu_1 \tag{A.8}$$

$$\alpha_{EG} = \frac{\alpha_E + \alpha_G}{2} = \frac{\mu_1 + (\mu_2 - \theta_2)}{2} \tag{A.9}$$

$$\alpha_{BG} = \alpha_B = \mu_2 + \theta_2 \tag{A.10}$$

$$\alpha_{EF} = \frac{\alpha_{F''}}{2} = \frac{\theta_3}{2} \tag{A.11}$$

$$\alpha_{GF} = \frac{\alpha_{G'} + \alpha_F}{2} = \frac{(\mu_2 + \theta_2) + (\mu_3 + \theta_3)}{2} \tag{A.12}$$

$$\alpha_{GC} = \alpha_C = \mu_2 - \theta_2 \tag{A.13}$$

$$\alpha_{FD} = \alpha_D = \mu_3 - \theta_3 \tag{A.14}$$

We define a height h to denote the distance from the domain's lower boundary to the shear layer.

Vertex positions: let (x_{src}, y_{src}) denote the center of the source location (not taking the deflection of the shear layer into consideration). Then we can define coordinates of the wave structure relative to those points.

$$x_E = x_{src} - w/2 \tag{A.15}$$

$$y_E = y_{src} \tag{A.16}$$

$$x_F = x_{src} + w/2 \tag{A.17}$$

$$y_F = y_{src} + w \tan \alpha_{EF} \tag{A.18}$$

$$x_A = x_E - h/\tan \alpha_{AE} \tag{A.19}$$

$$y_A = y_{src} - h \tag{A.20}$$

$$x_D = x_F + h/\tan \alpha_{FD} \tag{A.21}$$

$$y_D = y_A \tag{A.22}$$

$$x_G = \frac{y_E - y_F + x_E \tan \alpha_{EG} + x_F \tan \alpha_{GF}}{\tan \alpha_{EG} + \tan \alpha_{GF}} \tag{A.23}$$

$$y_G = \frac{y_E \tan \alpha_{GF} + y_F \tan \alpha_{EG} + (x_E - x_F) \tan \alpha_{EG} \tan \alpha_{GF}}{\tan \alpha_{EG} + \tan \alpha_{GF}} \tag{A.24}$$

$$y_B = y_A \tag{A.25}$$

$$x_B = x_G - (y_G - y_B)/\tan\alpha_{BG} \tag{A.26}$$

$$y_C = y_A \tag{A.27}$$

$$x_C = x_G - (y_G - y_C)/\tan\alpha_{CG} \tag{A.28}$$

Once the overall geometry is set, we define a local coordinate system for each the compression and the expansion waves. This coordinate system takes advantage of the property that the flow will remain constant along characteristics (for each kind of wave); the region of overlap will be assumed outside the boundary zone region and will not be computed in detail.

The compression and expansion wave coordinates are

$$\xi_c = \frac{x - x_{AE}(y)}{x_{BG}(y) - x_{AE}(y)} \tag{A.29}$$

$$\xi_e = \frac{x - x_{GC}(y)}{x_{FD}(y) - x_{GC}(y)} \tag{A.30}$$

where $x_{AE}(y)$ is the leading edge Mach line of the compression wave, $x_{BG}(y)$ the trailing characteristic, and likewise for the expansion wave with $x_{GC}(y)$ and $x_{FD}(y)$, respectively. Those lines are given by

$$x_{AE}(y) = x_A + \frac{y - y_A}{\tan\alpha_{AE}} \tag{A.31}$$

$$x_{BG}(y) = x_B + \frac{y - y_B}{\tan\alpha_{BG}} \tag{A.32}$$

$$x_{CG}(y) = x_C + \frac{y - y_C}{\tan\alpha_{CG}} \tag{A.33}$$

$$x_{FD}(y) = x_D + \frac{y - y_D}{\tan\alpha_{FD}} \tag{A.34}$$

The pressure change through each the expansion and the compression then becomes a function of only ξ_c and ξ_e, respectively:

$$\theta'_c = +\psi(\xi_c)\Delta p \tag{A.35}$$

$$\theta'_e = -\psi(\xi_e)\Delta p \tag{A.36}$$

where $\Delta p \equiv p_2 - p_1$. The shape function $\psi(\xi)$ defines how the pressure is distributed across each of the compression and expansion waves. In our case we have defined the shape function using a hyperbolic tangent function,

$$\psi(\xi) = \frac{1}{2}\left[1 + \tanh\left(\frac{\xi - 1/2}{w_\psi}\right)\right] \tag{A.37}$$

where the transition width parameter

$$w_\psi = -\frac{1}{2\tanh^{-1}(2\epsilon_\psi - 1)} \tag{A.38}$$

is defined so that

$$\psi(0) = \epsilon_\psi \tag{A.39}$$

$$\psi(1) = 1 - \epsilon_\psi. \tag{A.40}$$

We have used $\epsilon_\psi = 1\%$.

Finally, to determine local flow conditions in terms of velocity we compute the local Mach number based on the local pressure

$$M_{local}(p_{local}, p_{ref}, M_{ref}) = \left[\frac{2}{\gamma - 1}\left\{\left(\frac{p_{local}}{p_{ref}}\right)^{\frac{\gamma-1}{\gamma}}\left(1 + \frac{\gamma - 1}{2}M_{ref}^2\right) - 1\right\}\right]^{\frac{1}{2}}. \tag{A.41}$$

We use this relation to compute "actual" Mach number

$$M = M_{local}(p_1 + p_c' + p_e', p_1, M_1) \tag{A.42}$$

and Mach number due to the compression and expansions alone, respectively:

$$M_c = M_{local}(p_1 + p_c', p_1, M_1) \tag{A.43}$$

$$M_e = M_{local}(p_1 + p_e', p_2, M_2). \tag{A.44}$$

M_c and M_e are used to compute the local turning angles using the Prandtl-Meyer functions:

$$\begin{aligned} \theta_c' &= \nu(M_1) - \nu(M_c) && \text{(A.45)} \\ \theta_e' &= \nu(M_e) - \nu(M_2) && \text{(A.46)} \end{aligned}$$

giving a total angle

$$\theta = \theta_1 + \theta_c' + \theta_e'. \tag{A.47}$$

With $p = p_1 + p_c' + p_e'$, temperature acquired through the isentropic relation

$$T = T_q \left(\frac{p}{p_1}\right)^{\frac{\gamma-1}{\gamma}} \tag{A.48}$$

and speed of sound $c = \sqrt{\gamma RT}$, the velocity field is acquired simply as

$$\begin{aligned} u &= Mc\cos(\theta) && \text{(A.49)} \\ v &= Mc\sin(\theta). && \text{(A.50)} \end{aligned}$$

Finally, the density field is acquired using the ideal gas law,

$$\rho = \frac{p}{RT}. \tag{A.51}$$

A.2 Simplifications for the linearized Euler simulations

In the linearized Euler simulations, the oblique compression wave is introduced as a perturbation to the base flow solution. In other words, the compression wave is introduced as a boundary condition of the perturbation field. Because we assume that the magnitude of the perturbation variables are much smaller than the magnitude of the base flow quantities, the linear assumptions are invoked. The presence of the compression wave system is assumed to have a negligible impact on the base

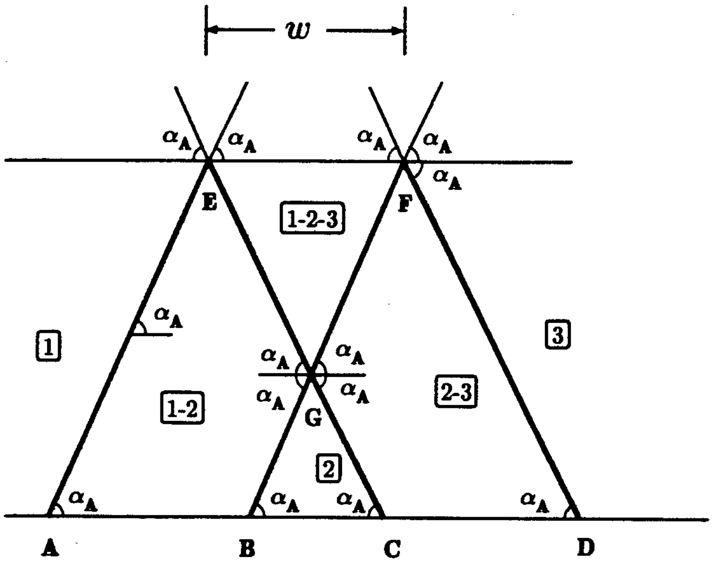

Figure A.2: Schematic of compression wave system for linearized Euler simulations. Note that α_A is the Mach angle for region 1.

flow. As a consequence, the orientation of the waves are determined solely by the properties of the base flow. In regions where flow properties are uniform, the Mach angles are fixed. Hence neglecting the deflection of the shear layer, approximating the shear layer as a vortex sheet, and assuming uniformity in the supersonic flow yields a simplified geometry for the wave system, as depicted in figure A.2. Flow properties are then obtained by translating the conditions applied at the boundaries along characteristics at the Mach angle toward the shear layer. The reflected expansion wave then assumes the the corresponding flow properties for downward propagating characteristics. In the linearized Euler simulations, a Gaussian profile is also invoked on the lower boundary. Because of the assumptions of linearity, the wave system is not sensitive to this modification. The procedures for determining the solution in the region in which the reflected waves intersect the lower boundary remain the same as for the compression/expansion wave system.

The relationships among the perturbation variables is determined through supersonic "thin airfoil" theory, wherein the deflections from the flow direction are assumed to be very small compared to the velocity magnitude. In this context, we relate the velocity fluctuations to the prescribed pressure fluctuations with

$$u' = \frac{1}{\rho_1 U_1} p' \tag{A.52}$$

$$v' = \frac{\beta}{\rho_1 U_1} p', \tag{A.53}$$

where $\beta = \sqrt{M_1^2 - 1}$. Density is obtained through the linearized isentropic relation,

$$\frac{\rho'}{\rho_1} = \frac{p'}{\gamma p_1} \tag{A.54}$$

The Mach wave angle is given by $\alpha_A = \mu = \sin^{-1}(1/M_1)$.

Appendix B

Validation

In this appendix we carry out grid and filter refinement studies. We test the grid resolution and Padé filter settings employed in the Navier-Stokes (Chapters 2 and 3) and linearized Euler simulations (Chapters 4 and 5). At the end of this appendix, we also verify that the linearized Euler simulations behave linearly, *i.e.*, that the solution scales directly with the flow "inputs".

The grid distribution is described in Section 2.6, and the filtering method is described in Section 2.2.5. In choosing the grid resolution, we are striking a balance between numerical accuracy and computational cost. We use the filter to remove unresolved, high frequency components of the numerical solution. In the case of the Navier-Stokes simulations, high frequency waves arise primarily from weak eddy-shocklets that appear above and below saturated vortices. In the case of the linearized Euler simulations, filtering supplies numerical dissipation to an otherwise numerically undamped scheme. Resolution also plays an important role in the behavior of the filter with respect to features that appear in the flow. The transfer function of the filter responds to the resolution of the feature with respect to the local grid rather than its physical scale. Hence, in validating grid resolution, we are also validating the filter parameters chosen.

B.1 Navier-Stokes simulations

With regard to resolution, the initial concern in the case of the Navier-Stokes simulations is that the shear layer development be accurately represented. When instability waves are small, the shear layer is essentially parallel and is dominated by the velocity gradient in the y-direction. The width of the shear layer is of the order of the initial vorticity thickness. As the vortices develop, the mean vorticity thickness increases four-fold (see Figure 3.7). Further, the regions between the vortices contain thin remnants of the shear layer (often called "braids"). Thus the grid must contain sufficient maximum resolution to resolve these small features, and this region of maximum resolution must be large enough to encompass the growth of the vortices.

In the following we compare SL1 shear layer computations carried out on meshes whose y-direction grid counts are $Ny = 291$ and $Ny = 446$. The smaller case corresponds to the grid size used in the computations presented in Chapter 3. The domain size in x and y remains fixed. Because the y-direction represents the critical direction with respect to resolution constraints, the x-resolution is also held fixed at $\Delta x/\delta = 0.1$ in this study.

Because the grid stretching and distribution parameters are identical, the y-resolution differs by a constant factor of $445/290 \approx 1.5$ over all y. The minimum and maximum y-direction grid spacing is $\Delta y/\delta$=0.0667 and $\Delta y/\delta = 0.444$, respectively. To retain the approximately the same CFL number (see Equation 2.37), we reduce the time step Δt by a factor of 1.5. Accounting for the increased grid size and the reduced time step, the increase in the computational expense of the $Ny = 446$ case is therefore $1.5^2 = 2.25$ times the $Ny = 291$ case.

Between the two grid cases, the Padé filter coefficient α' is held constant at 2.222. The number of time steps between filter application is increased from $N_{filter} = 10$ to 15 because the change in time step. To quantify the degree to which the higher resolution grid reduces the filtering effect for fixed filter coefficient α', we consider the following. The effect of increasing the spatial resolution by 1.5 is that of reducing the severity of filtering at a fixed grid wave number $k' \equiv k(\Delta y)_{Ny=291}$. Here we have defined the grid wave number k' with respect to the $Ny = 291$ grid to permit us to

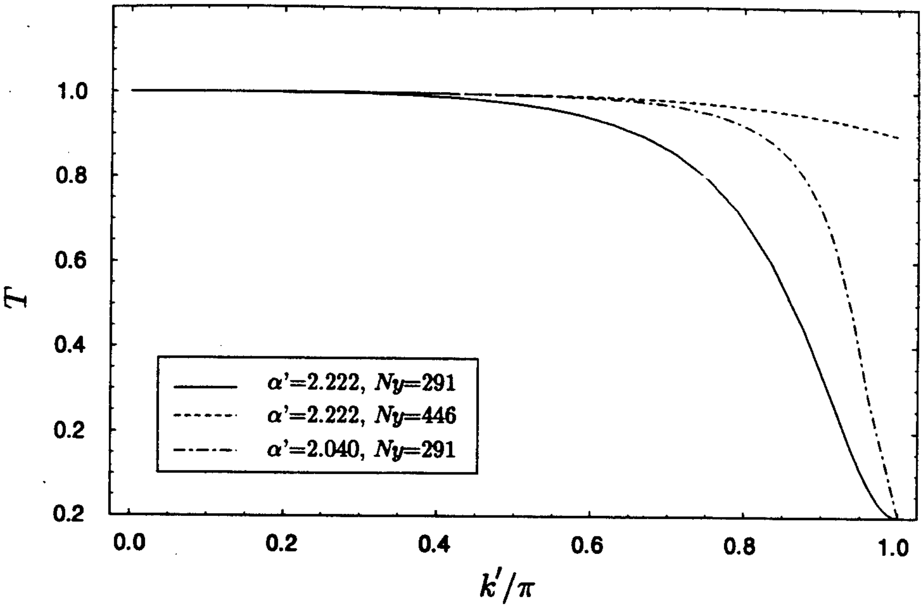

Figure B.1: Filter transfer function comparison.

compare the response of filter transfer functions in the two grid cases to features of the same size. In Figure B.1 we show the filtering transfer function T against fixed grid wave number k' for three cases. The first case (solid line) corresponds to the $Ny = 291$ case, which we use as a reference. The second case (dashed) corresponds to the $Ny = 446$ case. The third case (dash-dot) is explained below. We see that for fixed grid wave number, the increased resolution reduces the effect of the filter. This is more clearly seen when the transfer function is subtracted from unity, as shown in Figure B.2. The 50% increase in grid resolution reduces the influence of the filter by nearly an order of magnitude over the entire wave-number range. The third case (dash-dot) is the filter transfer function which duplicates (over the lower half of the grid wave number range) the effect of increasing the resolution by instead modifying the filter coefficient. We conclude that for the lower grid wave numbers, the 1.5 increase in grid resolution is analogous to reducing the filter coefficient α' from 2.222 to 2.04. Hence, the grid resolution validation also serves as a filter validation.

In Figures B.3 and B.4 we plot the instability wave amplitude (squared), as defined in Equation 3.1, for both $Ny = 291$ and $Ny = 446$. We obtain very good

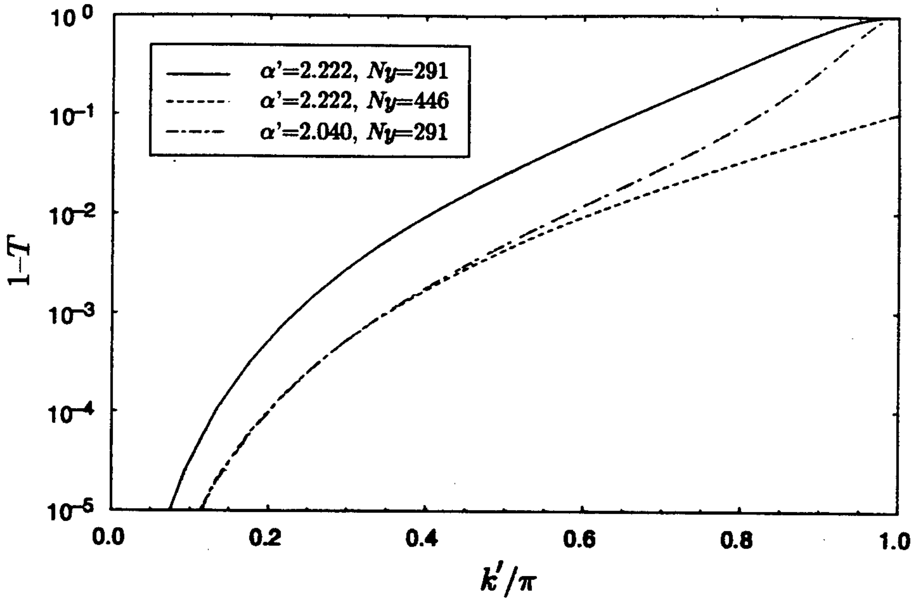

Figure B.2: Filter transfer function comparison, continued.

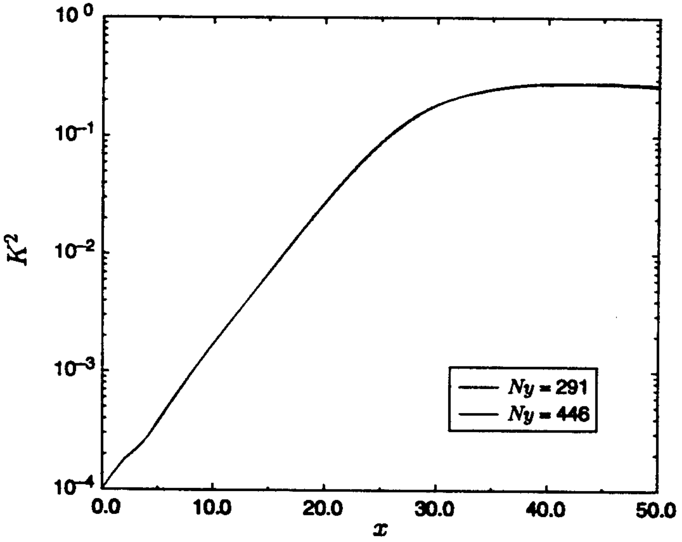

Figure B.3: DNS resolution and filter validation using instability wave amplitude K. Ny is the number of grid points in the spanwise direction.

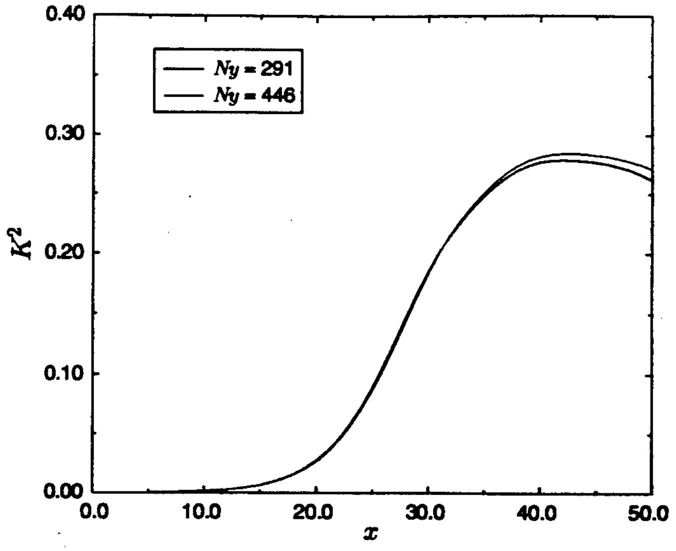

Figure B.4: DNS resolution and filter validation using instability wave amplitude K. Ny is the number of grid points in the spanwise direction.

agreement over the entire range of amplitude, from inflow to the saturated region. In the saturated region we do obtain a small discrepancy in amplitude, representing a maximum error of 1.8% in K (or 3.5% error in K^2). For the purpose of computing an unsteady, forced shear layer, this discrepancy is acceptable; the grid resolution and filter settings do not severely impact the computational results. We also find good agreement in the shear layer growth rates (see Figure B.5).

The second concern in the Navier-Stokes simulations is that the acoustic field be sufficiently resolved by the grid and uninfluenced by the filters. The grid falls to its lowest density ($\Delta y/\delta = 2.0$) in the y-direction near the upper boundary of the computational domain. Because the acoustic wave propagation is an inviscid and essentially linear process, at least in the region of lowest grid resolution, we carry out these validations in the context of the linearized Euler resolution and filter validations. The y-distribution of grid points is identical for all DNS and linearized Euler simulation cases. These validations are presented in the following sections.

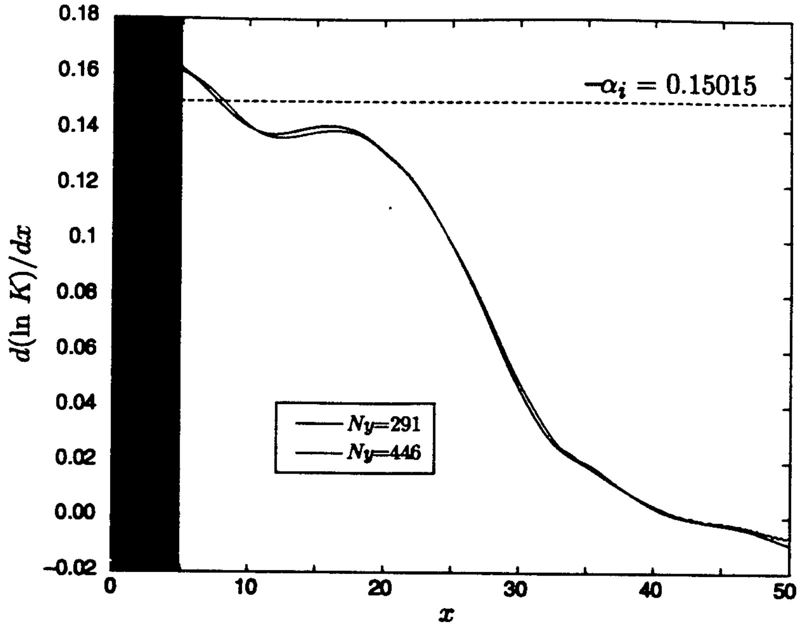

Figure B.5: DNS resolution and filter validation using growth rate of instability wave amplitude K. Ny is the number of grid points in the spanwise direction.

B.2 Linearized Euler simulations

In the linearized Euler computations, there are four classes of runs carried out: compression wave with DNS base flow, G-wave with DNS base flow, compression wave with Stuart vortex base flow, and G-wave with Stuart vortex base flow. These are summarized in Table B.1. The base flow is prescribed in the linearized Euler computations; therefore, in these validations we are checking only that the acoustic results are insensitive to the filter and resolution settings. Because of the variation in flow configurations among the classes, the limits of the computational method are stressed in somewhat different ways.

In the linearized Euler results presented in Chapter 5, we carried out the simulations using computational grids of $Nx = 301$ by $Ny = 291$, except as noted in Table 5.1. The mesh is held uniform in x, at $\Delta x = 0.2$ and stretched in the y direction according to the prescription given in Section 2.6. Note that the x resolution is half that used in the DNS, whereas the y mesh resolution is identical. The Padé filter

Base Flow	Compression wave	α'_x	α'_y	G-wave	α'_x	α'_y
DNS	(C-DNS)	2.222	2.222	(G-DNS)	2.222	2.050
Stuart	C-Stuart	2.222	2.222	G-Stuart	2.222	2.222

Table B.1: Classes of linearized Euler computations with reference filter settings. ( ) Validations not carried out.

coefficient α' is generally assigned independently in the x and y directions; these are indicated in Table B.1. We refer to these grid and filter settings as the reference settings. For these reference cases, the incident compression or G-wave is $\Delta p/p_\infty = 0.01$. To verify that the results are independent of these grid size and filter settings, we repeat select cases at finer grid sizes but with fixed coefficients settings. As discussed in the the DNS validation above, refining the mesh while holding the filter coefficient constant constitutes relaxing the filter strength.

A specific validation for the compression wave on the DNS base flow was not carried out because a DNS base flow on a refined grid was not readily available. For the compression wave validation, we rely on the C-Stuart case in which we can readily increase the base flow grid resolution due to its analytic description. Thus in Figure B.6 we compare the directivity of the compression wave at $r/\delta = 30$ from the apparent source at two grid resolutions: 301 × 291 and 601 × 581. The Stuart vortex amplitude $A = 0.7$. We find that the acoustic directivity changes by no more than 3%.

For the G-wave, a similar grid refinement is carried out on the same $A = 0.7$ Stuart base flow, using the same grid resolutions and filter coefficients as in the compression wave case. As shown in Figure B.7, the change in acoustic directivity changes by no more than 2.5%.

B.3 Linearity Check: the Linearized Euler Equations

The linearized Euler equations (Equations 4.10 through 4.12) are by definition linear in the perturbation field Q'_m, $m = 1, \ldots, 4$. The flow "inputs" consist solely of the

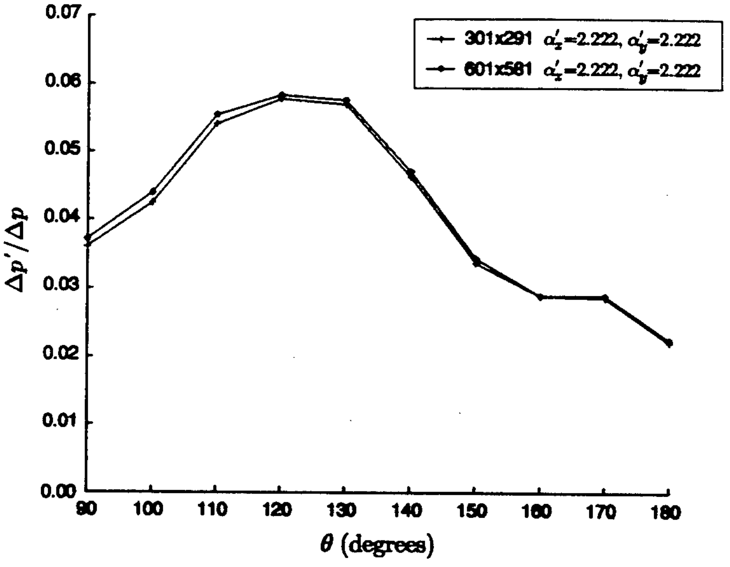

Figure B.6: Acoustic directivities in grid refinement study of incident compression wave on Stuart vortex base flow at $A = 0.7$.

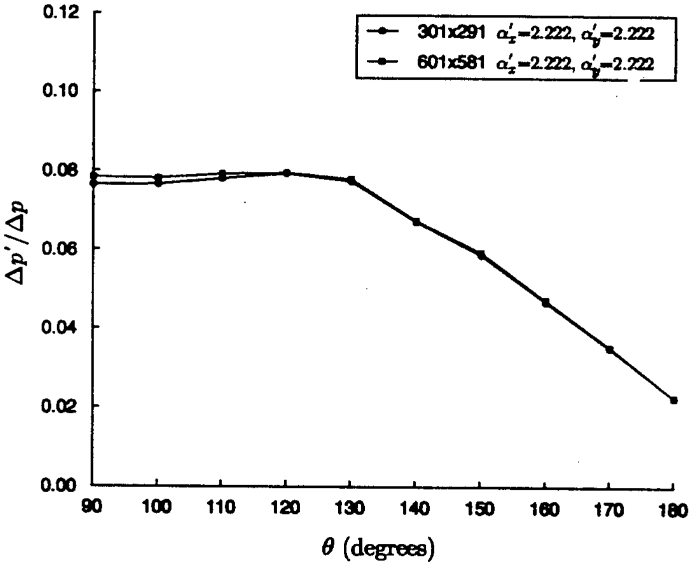

Figure B.7: Acoustic directivities in grid refinement study of incident G-wave wave on Stuart vortex base flow at $A = 0.7$.

boundary condition, namely, the incident Mach wave. This Mach wave is imposed at the lower boundary of the computational domain via the damping sponge. An acoustic field which scales directly with the imposed Mach wave amplitude would indicate that the solution is linear. To verify that the numerical solutions to the linearized Euler equations are linear, we carried out a series of computations with identical base flows and varied the amplitude of the incident Mach wave. The base flow is the Stuart vortex mixing layer, as defined in Section 5.4, with $A = 0.6$. The grid is identical to that used for the Stuart vortex base flow cases in Chapter 5. We compare a compression wave against an expansion wave, where the Mach wave amplitude is set to $\Delta p/p_\infty = +0.01$ and -0.01. We find the radiated acoustic field, normalized to their respective Mach wave amplitude, to be essentially identical but of opposite sign. Time traces of the acoustic field as normalized to the amplitude of the compression wave $\Delta p/p_\infty = +0.01$ are shown in Figure B.8. The departure from linearity is measured in terms of the following expression:

$$Error = \left| \frac{(p'_-/\Delta p_-) - (p'_+/\Delta p_+)}{\Delta p'_+/\Delta p_+} \right| \tag{B.1}$$

where the subscript indicates the sign of the incident wave. The error based on this definition is plotted against time in Figure B.9; the maximum of this error is plotted against observer angle in Figure B.10. We show that the error, though small for all angles, rises with upstream angle up to 10^{-3}. This degree of linearity is sufficient for the present computations.

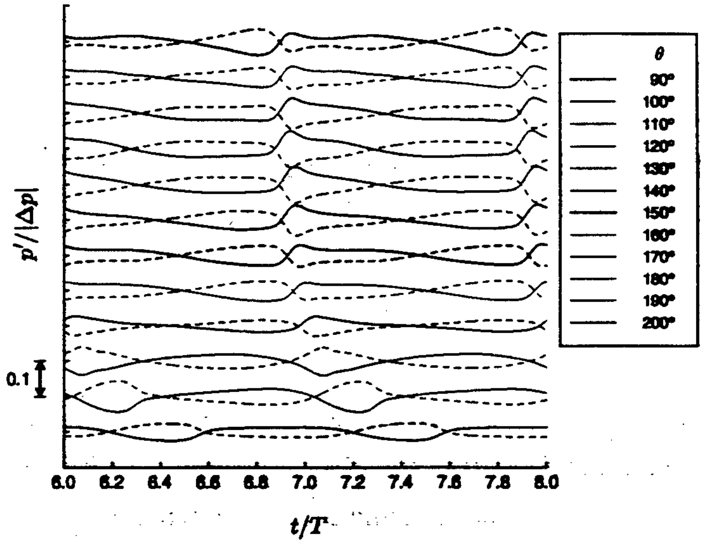

Figure B.8: Acoustic pressure traces resulting from interaction of Mach wave and Stuart vortex mixing layer. Vortex amplitude $A = 0.6$. Incident Mach wave type: —— compression wave ($\Delta p/p_\infty = +0.01$); – – – expansion wave ($\Delta p/p_\infty = -0.01$).

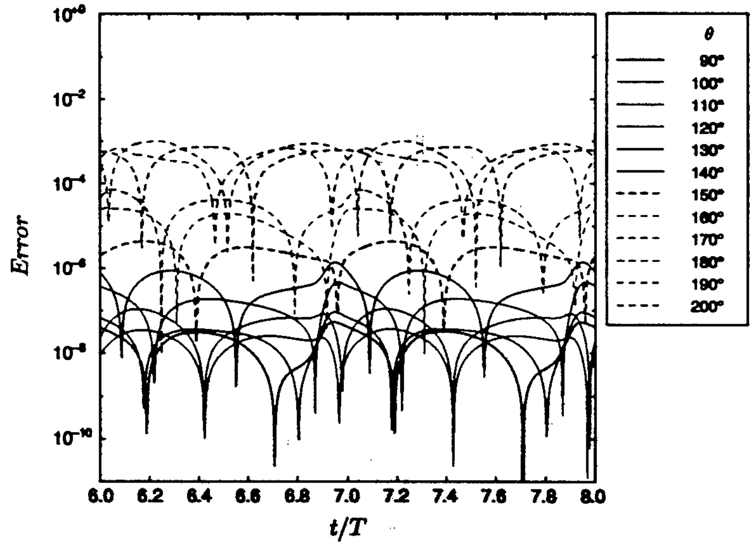

Figure B.9: Time history of relative error in normalized pressure fluctuation $p'/\Delta p$ for compression waves of $\Delta p = \pm 0.01$.

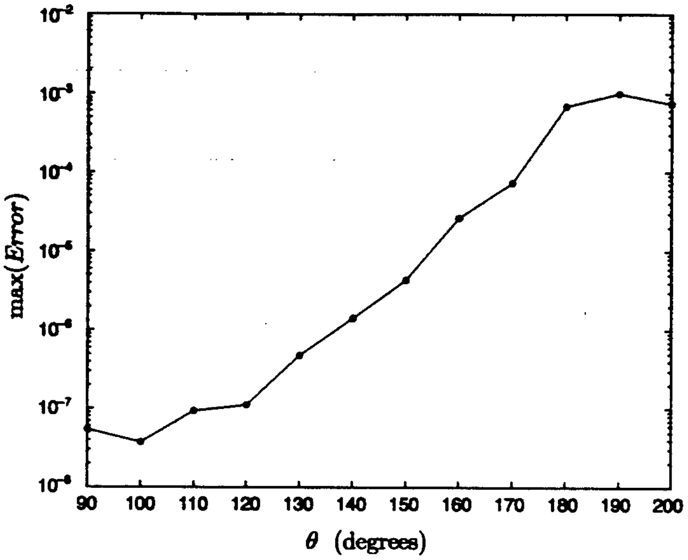

Figure B.10: Angular dependence of maximum relative error in normalized pressure fluctuation $p'/\Delta p$ for compression waves of $\Delta p = \pm 0.01$.

Bibliography

[1] A. B. Cain and W. W. Bower. Modeling supersonic jet screech: Differential entrainment and amplitude effects. In *AIAA 34th Aerospace Sciences Meeting and Exhibit*, number AIAA 96-0916, Reno, NV, January 15-18 1996.

[2] A. B. Cain, W. W. Bower, S. H. Walker, and M. K. Lockwood. Modeling supersonic jet screech. Part 1: Vortical instability wave modeling. In *AIAA 33rd Aerospace Sciences Meeting and Exhibit*, number AIAA 95-0506, Reno, NV, January 9-12 1995.

[3] M. D. Dahl and P. J. Morris. Noise from supersonic coaxial jets. Part 2: Normal velocity profile. *Journal of Sound and Vibration*, 200(5):665–699, 1997.

[4] M. G. Davies and D. E. S. Oldfield. Tones from a choked axisymmetric jet. I. cell structure, eddy velocity, and source locations. *Acustica*, 12:257–266, 1962.

[5] M. G. Davies and D. E. S. Oldfield. Tones from a choked axisymmetric jet. II. the self-excited loop and mode of oscillation. *Acustica*, 12:267–277, 1962.

[6] J. B. Freund. Proposed inflow/outflow boundary condition for direct computation of aerodynamic sound. *AIAA Journal*, 35(4):740–742, 1997.

[7] A. Hammitt. The oscillation and noise of an overpressure sonic jet. *Journal of the Aerospace Sciences*, 28(9):673–680, 1961.

[8] M. Harper-Bourne and M. J. Fisher. The noise from shock waves in supersonic jets. Technical Report CP 131, AGARD, 1974.

[9] A. Harten and S. Osher. Uniformly high-order accurate non-oscillatory schemes, I. *SIAM Journal Numerical Analysis*, 24:279–309, 1987.

[10] J. A. Hay and E. G. Rose. In-flight shock cell noise. *Journal of Sound and Vibration*, 11(4):411–420, 1970.

[11] M. S. Howe. Transmission of an acoustic pulse through a plane vortex sheet. *Journal of Fluid Mechanics*, 43:353–367, 1967.

[12] M. S. Howe and J. E. Ffowcs Williams. On the noise generated by an imperfectly expanded supersonic jet. *Philosophical Transactions of the Royal Society of London A*, 289:271–314, 1978.

[13] T.-F. Hu and D. K. McLaughlin. Flow and acoustic properties of low reynolds number underexpanded supersonic jets. *Journal of Sound and Vibration*, 141(3):485–505, 1990.

[14] M. Israeli and S. A. Orszag. Approximation of radiation boundary conditions. *Journal of Computational Physics*, 41:115–135, 1981.

[15] W. M. Jungowski. Influence of closely located solid surfaces on sound spectra radiated by gas jets. In *Proceedings of the Symposium on the Mechanics of Sound Generation in Flows*, pages 117–122, Gottingen, Germany, 1979.

[16] E. J. Kerschen and A. B. Cain. Modeling supersonic jet screech. Part 2: Acoustic radiation from the shock-vortex interaction. In *AIAA 33rd Aerospace Sciences Meeting and Exhibit*, AIAA 95-0507, Reno, NV, January 9-12 1995.

[17] A. Krothapalli. Revisiting screech tones: Effects of temperature. In *AIAA 34th Aerospace Sciences Meeting and Exhibit*, number AIAA 96-0644, Reno, NV, January 15-18 1996.

[18] A. Krothapalli, Y. Hsia, D. Baganoff, and K. Karamcheti. The role of screech tones in mixing of an underexpanded rectangular jet. *Journal of Sound and Vibration*, 106(1):119–143, 1986.

[19] T. K. Lee and X. Zhong. Spurious numerical oscillations in simulation of supersonic flows using shock-capturing schemes. *AIAA Journal*, 37(3):313–319, 1999.

[20] S. K. Lele. Compact finite difference schemes with spectral-like resolution. *Journal of Computational Physics*, 103(1):16–42, 1992.

[21] M. J. Lighthill. On sound generated aerodynamically. I. general theory. *Proceedings of the Royal Society of London A*, 211(1107):564–587, 1952.

[22] M. J. Lighthill. On the energy scattered from the interaction of turbulence with sound or shock waves. *Proceedings of the Cambridge Philosophical Society*, 49:532–551, 1953.

[23] Ganyu Lu and Sanjiva K. Lele. Numerical investigation of skewed mixing layers. Technical Report TF-67, Department of Mechanical Engineering, Stanford University, 1996.

[24] K. Mahesh, P. Moin, and S. K. Lele. The interaction of a shock wave with a turbulent shear flow. Technical Report TF-69, Department of Mechanical Engineering, Stanford University, 1996.

[25] R. R. Mankbadi, R. Hixon, S.-H. Shih, and L. A. Povinelli. Use of linearized euler equations for supersonic jet noise prediction. *AIAA Journal*, 36(2):140–147, February 1998.

[26] T. A. Manning and S. K. Lele. Numerical simulations of shock vortex interactions in supersonic jet screech. In *36th AIAA Aerospace Sciences Meeting and Exhibit*, number AIAA-98-0282, Reno, NV, Jan. 1998.

[27] T. A. Manning and S. K. Lele. Numerical simulations of shock vortex interactions in supersonic jet screech: an update. In *Proceedings of FEDSM '98: 1998 ASME Fluids Engineering Division Summer Meeting*, number FEDSM-5238, Washington, DC, June 1998.

[28] K. Meadows. A study of fundamental shock noise mechanisms. Technical Report TP-3605, NASA, 1997.

[29] T. D. Norum. Screech suppression in supersonic jets. *AIAA Journal*, 21(2):235–240, February 1983.

[30] T. D. Norum and J. M. Seiner. Broadband shock noise from supersonic jets. *AIAA Journal*, 20(1):68–73, January 1982.

[31] V. E. Ostashev. *Acoustics in Moving Imhomogeneous Media.* E. and F. N. Spon, 1997.

[32] D. C. Pack. A note on Prandtl's formula for the wavelength of a supersonic gas jet. *Quarterly Journal of Mechanics and Applied Mathematics*, 3:173–181, 1950.

[33] J. Panda. Shock oscillation in underexpanded screeching jets. *Journal of Fluid Mechanics*, 363:173–198, 1998.

[34] J. Panda, G. Raman, and K. B. M. Q. Zaman. Underexpanded screeching jets from circular, rectangular, and elliptic nozzles. In *A Collection of the 3rd AIAA/CEAS Aeroacoustics Conference and Exhibit Technical Papers*, number AIAA-97-1623, Atlanta, Georgia, May 12-14 1997.

[35] R. T. Pierrehumbert and S. E. Widnall. The two- and three-dimensional instabilities of a spatially periodic shear layer. *Journal of Fluid Mechanics*, 114:59–82, 1982.

[36] T. J. Poinsot and S. K. Lele. Boundary conditions for direct simulations of compressible viscous flows. *Journal of Computational Physics*, 101(1):104–128, 1992.

[37] L. J. Poldervaart, A. T. Vink, and A. P. J. Wijnands. The photographic evidence of the feedback loop of a two dimensional screeching supersonic jet of air. In *Proceedings of the 6th International Congress on Acoustics*, Tokyo, Japan, 1968.

[38] A. Powell. On edge tones and associated phenomena. *Acustica*, 3:233–243, 1953.

[39] A. Powell. On the mechanism of choked jet noise. *Proceedings of the Physical Society (London)*, 66:1039–1056, 1953.

[40] A. Powell. On the noise emanating from a two-dimensional jet above the critical pressure. *Aeronautical Quarterly*, 4(2):103–122, February 1953.

[41] A. Powell. The reduction of choked jet noise. *Proceedings of the Physical Society of London B*, 67(4):313–327, 1954.

[42] L. Prandtl. Stationary waves in a gaseous jet. *Phys. Z.*, 5:599–601, 1904.

[43] W. H. Press, S. A. Teukolsky, W. T. Vetterling, and B. P. Flannery. *Numerical Recipes in Fortran 77: The Art of Scientific Computing.* Cambridge University Press, 2nd edition, 1992.

[44] G. Raman. Cessation of screech in underexpanded jets. *Journal of Fluid Mechanics*, 336:69–90, 1997.

[45] G. Raman. Screech tones from rectangular jets with spanwise oblique shock-cell structures. *Journal of Fluid Mechanics*, 330:141–168, 1997.

[46] G. Raman. Advances in understanding supersonic jet screech: Review and perspective. *Progress in Aerospace Sciences*, 34:45–106, 1998.

[47] G. Raman. Supersonic jet screech: Half-century from Powell to the present. *Journal of Sound and Vibration*, 225(3):543–571, 1999.

[48] G. Raman and E. J. Rice. Instability modes excited by natural screech tones in a supersonic rectangular jet. *Physics of Fluids*, 6:3999–4008, 1994.

[49] G. Raman and R. Taghavi. Resonant interaction of a linear array of supersonic rectangular jets: an experimental study. *Journal of Fluid Mechanics*, 309:93–111, 1996.

[50] G. Raman and R. Taghavi. Coupling of twin rectangular supersonic jets. *Journal of Fluid Mechanics*, 354:123–146, 1998.

[51] H. S. Ribner. Cylindrical sound wave generated by shock-vortex interaction. *AIAA Journal*, 23(11):1708–1714, 1985.

[52] A. Rona and X. Zhang. Jet screech source model by CFD and acoustic analogy. In *Proceedings of FEDSM '99: 1999 ASME Fluids Engineering Division Summer Meeting*, number FEDSM99-7239, San Francisco, CA, July 18-23 1999.

[53] H. Schlichting. *Boundary Layer Theory*. McGraw-Hill, 1979.

[54] J. M. Seiner. Impact of dynamic loads on propulsion integration. In *Proceedings of AGARD Meeting on Structures*, Norway, May 3-7 1994. AGARD.

[55] J. M. Seiner, J. C. Manning, and M. K. Ponton. Model and full scale study of twin supersonic plume resonance. In *25th AIAA Aerospace Sciences Meeting and Exhibit*, AIAA-87-0244, Reno, NV, January 1987.

[56] J. M. Seiner and T. D. Norum. Experiments in shock associated noise of supersonic jets. AIAA-79-1526, 1979.

[57] H. Shen and C. K. W. Tam. Numerical simulation of the generation of axisymmetric mode jet screech tones. *AIAA Journal*, 36(10):1801–1807, 1998.

[58] C.-W. Shu and S. Osher. Efficient implementation of essentially non-oscillatory shock-capturing schemes. *Journal of Computational Physics*, 77:439–471, 1988.

[59] C.-W. Shu and S. Osher. Efficient implementation of essentially non-oscillatory shock-capturing schemes, ii. *Journal of Computational Physics*, 83:32–78, 1989.

[60] J. T. Stuart. On finite amplitude oscillations in laminar mixing layers. *Journal of Fluid Mechanics*, 29:417–440, 1967.

[61] H. Suda, T. A. Manning, and S. Kaji. Transition of oscillation modes of rectangular supersonic jet in screech. In *15th AIAA Aeroacoustics Conference*, AIAA-93-4323, Long Beach, CA, October 25-27 1993.

[62] C. K. W. Tam. Stochastic model theory of broadband shock associated noise from supersonic jets. *Journal of Sound and Vibration*, 116(2):265–302, July 22 1987.

[63] C. K. W. Tam. Computational aeroacoustics: Issues and methods. *AIAA Journal*, 33(10):1788–1796, 1995.

[64] C. K. W. Tam. Jet noise generated by large-scale coherent motion. In Harvey H. Hubbard, editor, *Aeroacoustics of Flight Vehicles: Theory and Practice*, volume 1: Noise Sources, chapter 6, pages 311–390. Acoustical Society of America through the American Institute of Physics, 1995.

[65] C. K. W. Tam. Supersonic jet noise. *Annual Review of Fluid Mechanics*, 27:17–43, 1995.

[66] C. K. W. Tam, K. K. Ahuja, and R. R. Jones III. Screech tones from free and ducted supersonic jets. *AIAA Journal*, 32(5):917–922, May 1994.

[67] C. K. W. Tam and D. E. Burton. Sound generated by instability waves of supersonic flows. Part 2: Axisymmetric jets. *Journal of Fluid Mechanics*, 138:273–295, 1984.

[68] C. K. W. Tam and K. C. Chen. A statistical model of turbulence in two-dimensional mixing layers. *Journal of Fluid Mechanics*, 92:303–326, 1979.

[69] C. K. W. Tam and F. Q. Hu. On the three families of instability waves of high speed jets. *Journal of Fluid Mechanics*, 201:447–483, April 1989.

[70] C. K. W. Tam, J. A. Jackson, and J. M. Seiner. A multiple-scales model of shock-cell structure of imperfectly expanded supersonic jets. *Journal of Fluid Mechanics*, 153:123–149, 1985.

[71] C. K. W. Tam, J. M. Seiner, and J. C. Yu. Proposed relationship between broadband shock associated noise and screech tones. *Journal of Sound and Vibration*, 110(2):309–321, 1986.

[72] C. K. W. Tam, H. Shen, and G. Raman. Screech tones of supersonic jets from bevelled rectangular nozzles. *AIAA Journal*, 35:1119–1125, 1997.

[73] C. K. W. Tam and H. K. Tanna. Shock associated noise of supersonic jets from convergent-divergent nozzles. *Journal of Sound and Vibration*, 81(3):337–358, 1982.

[74] K. W. Thompson. Time dependent boundary conditions for hyperbolic systems. *Journal of Computational Physics*, 68:1–24, 1987.

[75] Y. Umeda and R. Ishii. Oscillation modes of underexpanded jets issuing from square and equilateral triangular nozzles. *Journal of the Acoustical Society of America*, 95:1853–1857, 1994.

[76] S. H. Walker and F. O. Thomas. Experiments characterizing nonlinear shear layer dynamics in a supersonic rectangular jet undergoing screech. *Physics of Fluids*, 9:2562–2579, September 1997.

[77] R. Westley and J. H. Woolley. An investigation of the near noise fields of a choked axisymmetric jet. In *Proceedings of the AFOSR-UTIAS Symposium held at Toronto*, pages 147–167, May 20-21 1968.

[78] F. M. White. *Viscous Fluid Flow.* McGraw-Hill, 2nd edition, 1991.

[79] Alan A. Wray. Very low storage time-advancement schemes. Technical report, NASA Ames Research Center, Moffett Field, California, 1986. Internal Report.

[80] J. C. Yu and J. M. Seiner. Near field observations of tones generated from supersonic jet flows. *Journal of Sound and Vibration*, 205:698–705, 1983.

[81] E. Zauderer. *Partial Differential Equations of Applied Mathematics.* Wiley, 1989.